



Hydrogen-Water Isotope Exchange in a Trickle Bed Column by Process Simulation
and 3D Computational Fluid Dynamics Modelling

By

Mohammed Aldehani

A thesis submitted to Lancaster University in partial fulfilment
of the requirements for the degree of
Doctor of Philosophy

October 2016

Engineering Department
Faculty of Science and Technology
Lancaster University

Declaration

I declare that this thesis is the result of my own independent work/investigation, except where otherwise stated. Other sources are acknowledged by explicit references.

October 2016

**To my parents,
My wife,
and my brothers and sisters.**

Acknowledgements



My first and foremost thanks and praises are due to Allah (God) Almighty who has helped me and provided me with faith, patience and commitment to complete this research.

I would like to express my deep thanks and gratitude to my supervisor, Dr. Farid Aiouache, for his supervision, guidance, support and encouragement throughout this research.

I would also like to express my thanks to my fellow research students in the School of Engineering at Lancaster University for providing a pleasant and stimulating research environment. I really enjoyed the friendship that I developed with them while doing this research.

Special admiration and gratitude are due to my parents, wife, brothers and sisters whose prayers, love, care, patience, support and encouragement have always enabled me to perform to the best of my abilities.

Last but not least, I would like to thank all the people, members of my family and close friends, who have borne with me during the period of my PhD studies.

Abstract

Hydrogen is the most abundant chemical element in the universe and exists under three isotopic forms: protium, deuterium and tritium. Protium is commonly used in a variety of industries including electronics, metallurgy, chemistry and petrochemistry. Deuterium and tritium have taken more roles in both civil and defence nuclear industries and biomedical sciences. Today water treatment systems at nuclear sites remove many contaminating debris isotopes, with the exception of tritium. This is because tritiated waters have traditionally been particularly difficult and expensive to treat while they can spread easily if they escape into the environment. The topic of separation and purification of tritium and deuterium has a considerable value. Among the numerous separation methods of hydrogen isotopes, H_2 - H_2O liquid catalytic exchange has attracted interest because of its mild operating conditions, high efficiency, limited corrosion and toxicity. The method of hydrogen-water liquid catalytic exchange has many possible applications such as; producing and upgrading heavy water, producing light water and removing tritium from light and heavy waters for recycling to fusion reactors or for low level nuclear deposits.

This thesis presents the hydrogen-water isotope exchange reaction that is taking place co-currently and counter-currently through a trickle bed column. Numerical simulations were performed by process design and fluid flow modelling. The missing physical properties of deuterium, and particularly of tritium isotopologues in gaseous and water forms, were predicted and validated with existing literature data. Moreover, suitable operating parameters were approached allowing isotopic exchange to be performed under favourable performance. Intrinsic fluid flow studies by 3D modelling offered more understanding of various underlying phenomena taking place at the local scale and provided identification of main hydrodynamic characteristics in a trickle bed reactor including trends of pressure drop, liquid holdup and catalyst wetting efficiency. The activity of the catalytic process in terms of rate of conversion was discussed through the effect of operating conditions and was validated by a comparison with experimental data and literature.

Content

Declaration.....	ii
Acknowledgements.....	iv
Abstract.....	v
List of Figure.....	x
List of Table.....	xvii
List of Acronyms.....	xix
CHAPTER 1: Introduction.....	1
1.1 Research motivation.....	1
1.2 Overall aim and Objective.....	3
1.3 Methodology.....	4
1.4 Contribution of the Thesis.....	5
1.5 Thesis outline.....	7
1.6 Publications & Presentations & training related to this work.....	8
CHAPTER 2: Background.....	10
2.1 Introduction to hydrogen isotope separation.....	10
2.1.1 Hydrogen isotope.....	10
2.1.2 Significance of hydrogen isotope separation.....	12
2.1.3 Separation methods of hydrogen isotope.....	16
2.1.4 Overview of the applications of hydrogen isotope separation methods.....	25
2.2 Development of H ₂ -H ₂ O exchange technology.....	27
2.2.1 VPCE process.....	27
2.2.2 LPCE process.....	28
2.2.3 CECE process.....	30
2.2.4 Tritium removal process.....	31

2.3 Brief on applications, designs and preparations of hydrophobic catalyst.....	32
2.3.1 Application of hydrophobic catalyst.....	32
2.3.2 Design of hydrophobic catalyst.....	34
2.3.3 Preparation of hydrophobic catalyst.....	34
2.3.4 Overview of hydrophobic catalyst research around the world.....	35
CHAPTER 3: Methodology.....	39
3.1 Introduction.....	39
3.2 Aspen plus simulation part.....	39
3.2.1 Introduction.....	39
3.2.2 Thermodynamic model for computations.....	40
3.2.2 Aspen plus simulation of the multicomponent columns.....	41
3.3 CFD simulation part.....	42
3.3.1 Challenge of CFD modelling.....	42
3.3.2 Derivative framework for CFD modelling of PBRs.....	43
3.3.3 Packing geometry.....	44
3.3.4 Simulation process.....	44
3.4 Model Development.....	45
3.4.1 Packing generation by DEM.....	45
3.4.2 Meshing Modulation.....	47
CHAPTER 4: Kinetics and reactive stripping modelling of hydrogen isotopic exchange of deuterated waters.....	49
4.1 Introduction.....	50
4.2 Material and methods.....	52
4.3 Results.....	53
4.3.1 Kinetic study and composition trends.....	53

4.3.2 Effect of mass transfer rate on the separation efficiency of reactive stripping process.....	56
4.4 Summary of the chapter.....	76
CHAPTER 5: Analysis of fluid flow in a 3D trickle bed reactor.....	78
5.1 Introduction.....	78
5.2 Model equations and packed bed generation.....	80
5.2.1 Model equations.....	80
5.2.2 Packing generation by discrete element method (DEM) and packed bed design.....	82
5.2.3 Boundary conditions.....	84
5.3 TRB structure and non-uniform porosity distribution.....	86
5.4 Pressure drop.....	93
5.5 Liquid holdup.....	95
5.6 Particle wetting and liquid-solid covering.....	96
5.7 Results and Discussion.....	97
5.8 Summary of the chapter.....	116
CHAPTER 6: Analysis of hydrogen-water isotope exchange in a 3D trickle bed reactor.....	118
6.1 Introduction.....	119
6.2 LPCE mathematical model.....	120
6.2.1 H ₂ -H ₂ O exchange reaction.....	120
6.2.2 Mass Transfer model and expression of the activity of catalyst.....	124
6.3 Modelling Description.....	126
6.3.1 Model equations.....	126
6.3.2 Boundary conditions and solver details.....	128

6.3.3 Kinetic model of the gaseous phase exchange and analysis.....	129
6.4 H ₂ -H ₂ O catalytic exchange processing.....	133
6.4.1 Counter-current flow exchange.....	133
6.4.2 Co-current flow exchange.....	144
6.4.3 Impact of flow mode operation for the isotopic exchange process.....	151
6.5 Stability of the steady-state operations.....	157
6.6 CFD model validation.....	158
6.7 Summary of the chapter.....	161
CHAPTER 7: Conclusions and Recommendations.....	163
7.1 Review of the work.....	163
7.2 Recommendations for future research.....	166
APPENDIX A.....	168
APPENDIX B.....	170
APPENDIX C.....	171
REFERENCES.....	172

List of Figures

Figure (1.1) trickle/packed bed reactor study approach.....	5
Figure (1.2) the organization of thesis.....	8
Figure (2.1) schematic of hydrogen isotope atoms.....	10
Figure (2.2) electrolysis combines with chemical exchange.....	20
Figure (2.3) electrolysis combines with distillation.....	20
Figure (2.4) electrolysis.....	21
Figure (2.5) flow sheet of monothermal chemical exchange process.....	22
Figure (2.6) flow sheet of bithermal chemical exchange process.....	23
Figure (2.7) flow sheet of combined VPCE and CD process.....	27
Figure (2.8) flow sheet of combined LPCE and CD process.....	29
Figure (2.9) flow sheet of CECE process.....	30
Figure (3.1) overview of the property parameters are required to estimate.....	40
Figure (3.2) property methods available in a simulator.....	41
Figure (3.3) general guideline for selecting a property method.....	41
Figure (3.4) derivative framework for CFD modelling of a PBRs.....	43
Figure. (3.5) Generation of the random packing: raining process (a) and the resulting sphere packing (b).....	44
Figure (3.6) calculation procedure of analysis of CFD.....	45
Figure (3.7) randomly generated packings from PFC ^{3D}	46
Figure (3.8) building steps of a random packed bed reactor for COMSOL modelling.....	47
Figure (3.9) different sizes of meshes applied for a random packed bed reactor by COMSOL; (a) Large mesh and (b) small mesh.....	48

Figure (4.1) schematic representations of the three mass transfer models.....	50
Figure (4.2) scheme of the whole tomography apparatus.....	52
Figure (4.3) kinetic model for deuterium isotopic exchange.....	55
Figure (4.4) kinetic model for deuterium isotopic exchange.....	56
Figure (4.5) deuterium and tritium isotopologue properties in both hydrogen gas and water phases.....	63
Figure (4.6, a) Effect of pressure and temperature.....	67
Figure (4.7, b) Effect of gas to liquid flowrate ratio.....	68
Figure (4.8, c) Effect of reactive stages.....	68
Figure (4.9, d) Effect of mass of catalyst per stage.....	69
Figure (4.10, e) product distribution inside the LPCE column.....	70
Figure (4.11, a1-a2) product distribution by rate-based non-equilibrium phase model.....	74
Figure (4.12, b1, b2) product distribution by rate-based non-equilibrium phase model.....	74
Figure (4.13, c1-c2) product distribution by rate-based non-equilibrium phase model.....	75
Figure (4.14, d) product distribution and relevant reaction rates inside the LPCE column.....	76
Figure (5.1) Generated packing by DEM.....	83
Figure (5.2) simulation domain.....	84
Figure (5.3, a-b) Reduction procedure of volumetric 3D data of porosity.....	89
Figure (5.4) spatial distribution of angularly averaged porosity inside the packing for (a) AR2; (b) AR4.....	90

Figure (5.5) Radial porosity profile, $\varepsilon(r)$ before averaging at (a ₁) and (b ₁) and after averaging (a ₂) and (b ₂) compared with Mueller's model; AR2 (left) and AR4 (right).....	91
Figure (5.6). Axial porosity profile, $\varepsilon(z)$ before averaging at (a ₁) and (b ₁) and after averaging (a ₂) and (b ₂); AR2 (left) and AR4 (right).....	92
Figure (5.7) Effect of liquid velocity on pressure drop at different gas velocity.....	97
Figure (5.8) Effect of particle diameter on pressure drop at different liquid velocity.....	98
Figure (5.9) Effect of particle diameter and gas velocity on pressure drop at different liquid velocity.....	99
Figure (5.10) Comparison of effect of liquid velocity on pressure drop with literature data at gas velocity 0.22 (m/s).....	100
Figure (5.11) Comparison of effect of liquid velocity on pressure drop with data of Gunjal et al. (at gas velocity 0.22 (m/s)).....	101
Figure (5.12) Comparison of effect of gas velocity on pressure drop with Specchia and Baldi (at liquid velocity 0.003 (m/s)).....	101
Figure (5.13) Effect of liquid velocity on liquid holdup at different gas velocity.....	102
Figure (5.14) Effect of gas velocity on liquid holdup at different liquid velocity.....	103
Figure (5.15) Effect of gas velocity on liquid holdup with column height (at liquid velocity 0.003).....	104
Figure (5.16) Effect of gas velocity on liquid holdup with column height (at liquid velocity 0.015).....	104

Figure (5.17) Effect of gas velocity on liquid holdup with radial variation (at liquid velocity 0.003).....	105
Figure (5.18) Effect of gas velocity on liquid holdup with radial variation (at liquid velocity 0.015).....	106
Figure (5.19) Effect of particle diameter on liquid holdup at different liquid velocity.....	107
Figure (5.20) Effect of particle diameter on wetting efficiency at different liquid velocity.....	108
Figure (5.21) Comparison of effect of liquid velocity on wetting efficiency with literature data.....	108
Figure (5.22) liquid flow distribution of iso-surface at liquid and gas velocity of 0.003 (m/s) and 0.11 (m/s), respectively; AR2.....	109
Figure (5.23) liquid flow distribution of iso-surface at liquid and gas velocity of 0.003 (m/s) and 0.11 (m/s), respectively; AR4.....	110
Figure (5.24) Liquid flow regime and wetted area at liquid and gas velocity of 0.003 (m/s) and 0.11 (m/s), respectively; AR2 and AR4.....	111
Figure (5.25) Effect of flow mode operation on liquid holdup at gas velocity 0.11 (m/s).....	112
Figure (5.26) axial and radial dispersion along with flow dynamics; (a_1 , a_2), respectively for AR2.....	114
Figure (5.27) vertical slices of particle tracers at Pe of 3.78, 4.62 and 5.46, respectively for AR2.....	115
Figure (6.1) schematic representation of hydrogen-water exchange in the counter-current mode operation.....	133

Figure (6.2) influence of hydrogen flow on conversion rate, water flow rate 30 ml/h, temperature 333.15 K.....	135
Figure (6.3) colour map of HD concentration over catalyst surface in counter-current at gas velocity; 2.55 (ml/s) (left - 3D on cross-sectional and vertical planes) and 12.9 (ml/s) (right - 3D on cross-sectional and vertical planes).....	136
Figure (6.4) influence of water flow on conversion rate, hydrogen flow rate 12.9 ml/s, temperature 333.15 K.....	138
Figure (6.5) influence of reaction temperature on conversion rate, hydrogen flow rate 4.5 ml/s, molar flow ratio of hydrogen gas to water ($\lambda=0.5$).....	139
Figure (6.6) colour map of HD concentration over catalyst surface in counter-current at temperature; 303.15 (K) (left - 3D on cross-sectional and vertical planes) and 343.15 (K) (right - 3D on cross-sectional and vertical planes).....	141
Figure (6.7) influence of reaction temperature and varied gas/liquid ratio on conversion rate.....	142
Figure (6.8) influence of column height on conversion rate with molar flow ratio ($\lambda=0.5$).....	143
Figure (6.9) schematic representation of hydrogen-water exchange in the co-current mode operation	144
Figure (6.10) influence of hydrogen flow on conversion rate water flow rate 24 ml/h, temperature 333.15 K.....	145
Figure (6.11) colour map of HD concentration over catalyst surface in co-current at gas velocity; 5 (ml/s) (left - 3D on cross-sectional and vertical planes) and 13.33 (ml/s) (right - 3D on cross-sectional and vertical planes).....	146
Figure (6.12) influence of water flow on conversion, rate hydrogen flow rate 13.33 ml/s, temperature 333.15 K.....	147

Figure (6.13) influence of reaction temperature on conversion rate, hydrogen flow rate 8.63 ml/s, molar flow ratio of hydrogen gas to water ($\lambda=0.5$).....	148
Figure (6.14) colour map of HD concentration over catalyst surface in co-current at temperature; 303.15 (K) (left 3D on cross-sectional and vertical planes) and 343.15 (K) (right - 3D on cross-sectional and vertical planes).....	149
Figure (6.15) influence of the temperature on conversion rate with different molar flow ratio (λ).....	150
Figure (6.16) influence of column height on conversion rate with molar flow ratio ($\lambda=0.5$).....	151
Figure (6.17) influence of hydrogen flow on conversion rate in co-current and counter current mode, water flow rate 24 ml/h, temperature 333.15 K.....	154
Figure (6.18) influence of water flow rate on conversion rate in co-current and counter current modes, hydrogen flow rate 13.5 ml/s, temperature 333.15 K.....	154
Figure (6.19) influence of the temperature on conversion rate in co-current and counter current modes with molar flow ratio ($\lambda=0.5$).....	155
Figure (6.20) influence of the catalytic bed height on conversion rate in co-current and counter current modes, molar flow ratio ($\lambda=0.5$).....	155
Figure (6.21) influence of hydrogen flow rate on mass transfer coefficient in co-current and counter current modes, water flow rate 24 ml/h, temperature 333.15 K...	156
Figure (6.22) influence of water flow rate on mass transfer coefficient in co-current and counter current modes, hydrogen flow rate 13.5 ml/s, temperature 333.15K.....	156
Figure (6.23) influence of temperature on mass transfer coefficient in co-current and counter current modes with flow ratio ($\lambda=0.5$).....	157

Figure (6.24) influence of the time on stability, hydrogen flow rate 4.55 ml/s, molar flow ratio of hydrogen gas to water ($\lambda=0.5$).....	158
Figure (6.25) comparison of the influence of hydrogen flow rate on conversion rate, water flow rate 24 ml/h, temperature 333.15 K.....	159
Figure (6.26) comparison of the influence of water flow rate on conversion rate, hydrogen flow rate 13.3 ml/s, temperature 333.15 K.....	160
Figure (6.27) comparison of the influence of the temperature on conversion rate, hydrogen flow rate 8.63 ml/s, molar flow ratio of hydrogen gas to water ($\lambda=0.5$).....	160

List of Tables

Table (2.1) comparable property of hydrogen isotope atoms.....	10
Table (2.2) molecular weight and radius of hydrogen isotope.....	11
Table (2.3) basic parameters of hydrogen isotope.....	11
Table (2.4) physical properties of hydrogen isotope water.....	12
Table (2.5) vapour pressure ratios for isotopologues water species $P(H_2O)\backslash P(x)$	18
Table (2.6) separation factor between protium and deuterium in water.....	21
Table (2.7) separation factor between protium and deuterium in hydrogen.....	22
Table (2.8) comparisons among hydrogen isotope separation technology.....	24
Table (2.9) comparisons among method of heavy water production.....	26
Table (2.10) comparisons among hydrogen-water isotope separation technology.....	30
Table (2.11) comparisons among technology of removing tritium from heavy water ...	31
Table (2.12) the main parameter of CECE technology in pilot plant test	31
Table (2.13) the preparation technology of hydrophobic catalyst.....	36
Table (2.14) the main types of hydrophobic catalysts and mixed packing tested and selected for H_2 - H_2O isotopic exchange.....	36
Table (2.15) the main mixed catalytic packing types manufactured and tested in LPCE process.....	37
Table (3.1) setting parameters of DEM based modelling.....	46
Table (3.2) packing parameters for different ARs.....	47
Table (4.1) physical properties of tritium and deuterium isotopologues in water and hydrogen.....	60
Table (4.2) properties of tritium and deuterium isotopologues in water and hydrogen with temperature.....	61
Table (5.1-a). Boundary and subdomain condition for CFD model.....	84

Table (5.1-b). Simulation domain and its description.....	85
Table (5.2) Porosity trends for AR2 and AR4.....	89
Table (6.1) Boundary and subdomain condition for CFD model.....	128
Table (6.2) kinetic parameters.....	130
Table (6.3) binary diffusion coefficient.....	131
Table (6.4) effective diffusion coefficient.....	132
Table (6.5) Operating data for 3D CFD modelling.....	134
Table (6.6) Physical properties of the liquid and gas phases.....	134

Nomenclature

A	Cross-sectional area of the column [m^2]
a	Interfacial area per unit bubbling area for trays [-]
a_I	Total interfacial area per unit volume of liquid, vapour [m^2/m^3]
a_F	Specific area of the packing [m^2/m^3]
a_w	Wetted surface area per unit volume of the column [m^2/m^3]
C_p	Specific molar heat capacity [$\text{J}/\text{kmol K}$]
D	Diffusivity [m^2/s]
d_F	Nominal packing size [m]
d_p	Bed particle diameter [m]
d_s	Sphere diameter [-]
Fr	Froude number [-]
g	Acceleration due to gravity [$\text{m}\cdot\text{s}^{-2}$]
G'	Gas flow rate [mol/s]
G'/L'	Gas to liquid flowrate ratio [-]
G	Matrix of thermodynamic factors [-]
H	Liquid enthalpy [J/mol]
h	Vapour enthalpy [J/mol]
h'	Heat transfer coefficient [$\text{W}/\text{m}\cdot\text{K}$]
h_F	Height of a packed section [m]
K	Equilibrium constant between phases [-]
$k_{r,i}$	Kinetic rate constant of reaction i [$\text{mol}/\text{kg}\cdot\text{s}$]
k_i	Film mass transfer coefficient of species i [$\text{mol}/\text{m}^3\cdot\text{s}$]
K_{eq}	Equilibrium constant for isotope exchange [-]
$K_{g,overall}$	Gas/liquid rate constant

L'	Liquid flow rate [mol/s]
m_c	Mass of catalyst [kg]
N	Number of stages in the LPCE column [-]
n	Number of data points in the normalized standard deviation equation [-]
n_c	Number of components [-]
NM	Rate of mass transfer between phases [mol/s]
P	Total pressure [Pa]
P_c	Critical pressure [kPa]
q	Heat transfer rate between phases [J/s]
r_i	Rate of the isotopic exchange (mole/kg.s)
Re	Reynolds number [-]
$Sep_{D,e}$	Separation factor [-]
Sc	Schmidt number
T	Temperature [K]
T_B	Boiling point temperature [K]
T_c	Critical temperature [K]
V_c	Critical molar volume [cm ³ /mol]
V_b	Molar volume at the boiling point (cm ³ /mol)
We	Weber number [-]
x	Mole fraction in the liquid phase [-]
x'_D	Atom fraction of deuterium in the liquid water
y	Mole fraction in the gaseous phase
y_{eq}	Equilibrium composition of deuterium in hydrogen phase
y'_D	Atom fraction of deuterium in hydrogen phase
Z_c	Critical compressibility factor [-]

Greek symbols

λ	Thermal conductivity [W/m.K]
φ	Fugacity coefficient [-]
ϕ	Fractional hole area per unit bubbling area [-]
μ	Dynamic viscosity [Pa.s]
ν	Kinematic viscosity [cP]
ρ	Density [kg. m ⁻³]
σ	Liquid surface tension [N/m]
σ_c	Critical surface tension of packing [N/m]
δ	Kronecker delta: 1 if i=k, 0 otherwise
ε	Bed voidage [-]

Abbreviations

LPCE	Liquid phase catalytic exchange
CECE	Combined electrolysis and catalytic exchange
VPCE	Vapour phase catalytic exchange
AECL	Atomic energy of Canada limited
CANDU	Canadian deuterium uranium reactor
CEA	French atomic energy commission
TRF	Tritium removal facility
DDW	Deuterium depleted water
CD	Cryogenic distillation
WD	Water distillation
CE	Chemical exchange
TD	Thermal diffusion
PTFE	Polytetrafluoroethylene

SDB	styrene-divinylbenzene copolymer
VOC	Volatile organic compounds
CEPE	Chemical equilibrium - bulk gas/liquid physical equilibrium
CKEP	Chemical kinetics - bulk gas/liquid physical equilibrium
CKRN-E	Chemical kinetics - rate-based gas/liquid non-equilibrium
DIPPR	Design Institute for Physical Properties Research
HETP	Height equivalent to theoretical plate [m]
I.D.	Internal diameter [m]
MESH	Material balance, vapour–liquid equilibrium equations, mole fraction summations and heat balance
NSD	Normalized standard deviation (%)
RadFrac	Rate-based equilibrium separation process model
RateFrac	Rate-based non-equilibrium separation process model
SDBC	Styrene-divinylbenzene copolymer
SRK	Soave-Redlich-Kwong equation-of-state
CFD	Computational Fluid Dynamics
PBR	Packed Bed Reactor
TBR	Trickle Bed Reactor
MRI	Magnetic Resonance Imaging
FD	Finite Differences
FV	Finite Volumes
FE	Finite Elements
DEM	Discrete Element Method
AR	Tube-to-particle diameter Aspect Ratio (aspect ratio)
LDV	Laser Doppler Velocimetry
GMRES	Generalized minimal residual method

GCI	Grid convergence index
PT	Particle Tracking
PTM	Particle Tracking Method

Subscripts

D ₂	Deuterium gas
D ₂ O	Heavy water or (deuterium oxide)
T ₂ O	Tritium oxide or (super-heavy water)
DT	Deuterated tritium gas
DTO	Tritiated heavy water
HTO	Tritiated water
HD	Deuterated hydrogen
HDO	Deuterated water
HT	Tritiated hydrogen gas
T ₂	Tritium gas
<i>eq</i>	Equilibrium state
G	Gas
L	Liquid
V	Vapour
I	Interphase boundary between the gas and liquid

Chapter 1

Introduction

1.1 Research motivation

The style to design and analysis packed bed columns for physical separation processes is well-established and accessible in open literature. Though, for the case of reactive separation processes, an entirely generalized path for design and analysis might not be viable owing to the unique nature of the reactions concerned and the catalyst utilized in each case. The integration of reaction with the separation process minimizes the degrees of freedom and imposes further limitation on the process and tools design, and the congruity between the operating windows of both of these processes is hard to reach. This makes the design and development of this combination a more challenging assignment. There has been a significant number of publications on reactive separations mostly for reactive chromatography and reactive distillation. A simultaneous absorption and reaction is as well the topic of classical multiphase gas-liquid reactions when the reaction occurs between the liquid substrate and the dissolved gas. In spite of that, an opposite case of reactive stripping wherein, reaction happens in the vapour phase between the gas and the stripped-off component, is infrequent. An example of this reactive stripping process is H_2 - H_2O exchange used for the separation of hydrogen isotopes. The isotope exchange reaction is carried out in a trickle bed reactor (TBR) filled with a hydrophobic or wetproofed catalyst. The TBR is generally known as the catalytic chemical exchange (CE) column in which water and hydrogen are contacted in (co/or counter)-current mode through the catalyst bed to transfer deuterium or tritium from water to hydrogen by an exchange reaction that takes place in the gas phase.

The H_2 - H_2O liquid phase catalytic chemical exchange method has been highly investigated worldwide and been found as an efficient separation method for hydrogen isotopes. [202] The method can be used to produce deuterium depleted waters (DDW), heavy waters, tritium depleted waters for a recycle and purification of tritium from a thermal nuclear fusion reactor. [20, 133] Alternatively, the process of H_2 - H_2O vapour phase catalytic chemical exchange can achieve the same result but the method needs 200°C vapours, consumes more energy and has a complicated design of associated devices. [77] Compared to the widely used H_2O - H_2S exchange reaction and NH_3 - H_2 exchange reaction, method of H_2 - H_2O liquid phase catalytic exchange presents a high separation factor, is non-toxic and non-corrosive. Therefore, it is interesting to investigate further H_2 - H_2O liquid phase catalytic exchange and broaden its application to a number of research areas.

The work focuses on improving its efficiency by investigating in-depth local phenomena of fluid flow and mass transfer inside the liquid phase catalytic exchange (LPCE) column, thus increasing its viability in practical applications. The requirements to be the project to its achievements are well defined, as previous simulation studies have focused more broadly on overall process design, without considering the underlying effects of local fluid and mass transfer phenomena taking place inside the LPCE column. As the LPCE process is well-established, extensive research has already been completed in an attempt to improve and optimise its efficiency, both experimentally and via the use of process simulations. However, there is a lack of research that is still not sufficiently explored, particularly local events and thus the fluid flow in generally inside the trickle-type packed bed of the LPCE column, and their influence on local performance. This lack of knowledge is highly significant when attempting to draw overall conclusions on the observed performance at the column outlet. Therefore, in computational flow models, the effect of various issues influencing performance of the trickle bed reactors can be studied. It is however, essential to set experimental data available from literature related to TBR operation under similar operating conditions to validate, and quantify possible uncertainties as well to in predict flow and inherent mixing.

Having identified this clear shortfall in the previous research, this work is tailored to address it. An LPCE column is initially simulated by using a rigours process design model relevant to a counter-current reactive stripping. This model takes into account interfacial multi-component mass transfer, chemical reactions and thermodynamic non-idealities. The process model is implemented in the simulation tool of Aspen Custom Modeler. Also, in this work, underlying events observed in the process design covering both co-current and counter-current operation modes are investigated by three-dimensional (3D) computational fluid dynamics (CFD) modelling. The fluid flow characteristics inside the column and their impact on both local performance as well as overall performance at the outlet of the LPCE column are investigated.

1.2 Overall aim and objectives

This project aims to provide a detailed account to study hydrogen isotope separation by H₂-H₂O liquid phase catalytic exchange and to address the specific issues in a trickle-bed reactor (TBR). Despite several works devoted to the experimental investigation of hydrogen isotope separation, there is yet no universal agreement on the influence of interstitial phenomena on overall TBR hydrodynamics. Consequently, Aspen Plus process simulation and CFD modelling techniques were developed in this research to obtain better understanding of the effects of non-uniform local flow and mass transfers in a trickle-bed reactor.

Based on issues and shortfalls briefly discussed in previous section and a critical literature review to be introduced in Chapter 2, the following objectives were defined for this thesis:

1.2.1 Modelling the isotopic exchange between hydrogen and water in a reactive stripping column for the detritiation processing using the simulation software Aspen plus Custom Modeler and includes:

- Prediction of the missing physical properties of deuterium and tritium isotopologues in hydrogen gas and water forms and validation with existing literature data.
- Investigation of influence of important design parameters such as temperature, total pressure, gas to liquid flowrate ratio, pressure drop and size of the reactive stripping column on separation of deuterium and compared to the data in literature.

1.2.2 Application of 3D CFD modelling to investigate in-depth local phenomena of fluid flow in both co-current mode and counter-current mode, and thus evolution of local and overall performance. Previous simulation studies on isotopic exchange have focused broadly on overall process design, without considering the underlying effects of local phenomena taking place inside the reactor. This application includes:

- Development and validation of a comprehensive multiphase 3D CFD model, to simulate gas-liquid flow through a trickle bed reactor.
- Investigation of local insights into key flow characteristics of a TRB over a range of operating parameters for ARs (i.e., 2 and 4).
- Generation of CFD results to study influence of column structure and characteristics (i.e. LPCE diameter to particle diameter ratio), flow rates of gas and liquid on global hydrodynamics parameters such as pressure drop, liquid hold-up and mixing.
- Characterisation of different flow scales occurring in trickle and pulse flow regimes.
- Influence of particle diameter on partial wetting properties.

1.2.3 Application of 3D CFD modelling to investigate LPCE column performance, fluid flow and mass transfer models during the H₂-H₂O catalytic exchange in both co-current mode and counter-current mode operation. This application includes:

- Discussion on process performance in terms of isotopic exchange conversion (activity) under effects of operating conditions such as flow rate of hydrogen, flow rate of water, temperature and height of catalytic bed.
- Finally, validation of process models by comparison of the results against experimental data obtained in existing literature.

1.3 Methodology

The overall methodology used to study flow processes of hydrogen and liquid water occurring in (co/counter) current modes passing through a trickle column by using Aspen Plus and CFD simulations is shown in Figure (1.1). Various modelling approaches are applied to achieve the objectives and listed follows:

In the first part, the Aspen plus modular package was used to access the missing thermodynamic properties of the components involved the hydrogen exchange process and this was achieved by using scalar (fixed) and temperature-dependent properties. The properties of hydrogen isotopes gases as well as liquids were first predicted with rigorous models and implemented in the process simulation package to determine favoured operating parameters of temperature, pressure and gas to liquid flow ratios.

In the CFD part, a granular packing of dense spherical particles was built by simulation using the discrete element method (DEM) in order to mimic laboratory samples. The commercial particle flow code 3D (PFC^{3D}) was used to generate realistic packing samples of random structures with different packing arrangement of spherical particles. The packing geometry, which was defined by the 3D coordinates of particle centres, was then embedded into the commercial CFD package (Comsol) via 3DAutoCAD (Autodesk) processing.

Before computing the two-phase flow using CFD, one needs to generate a multidimensional porosity distribution at a certain sectional size for radial and axial profile. Therefore, the structure of the bed was studied to understand flow characteristics inside the void formed by different packing arrangements of spherical particles. After that, the computational model was extended to measure the hydrodynamic parameters such as pressure drops and liquid holdup in trickle flow regimes for two particle sizes. The model was able to capture some of the naturally occurring features in the pulse flow regime. Effect of parameters such as particle diameter and phase flow rates on reactor hydrodynamics was studied. A reactor model was developed in the Eulerian framework.

The CFD model was then extended further to simulate the performance of the reactor of H₂-H₂O liquid catalytic exchange process by predicting effects of flow rate, temperature, and height of bed on conversion rate, optimizing process parameters and understanding issues of CFD modelling of trickle bed reactors throughout the exchange process.

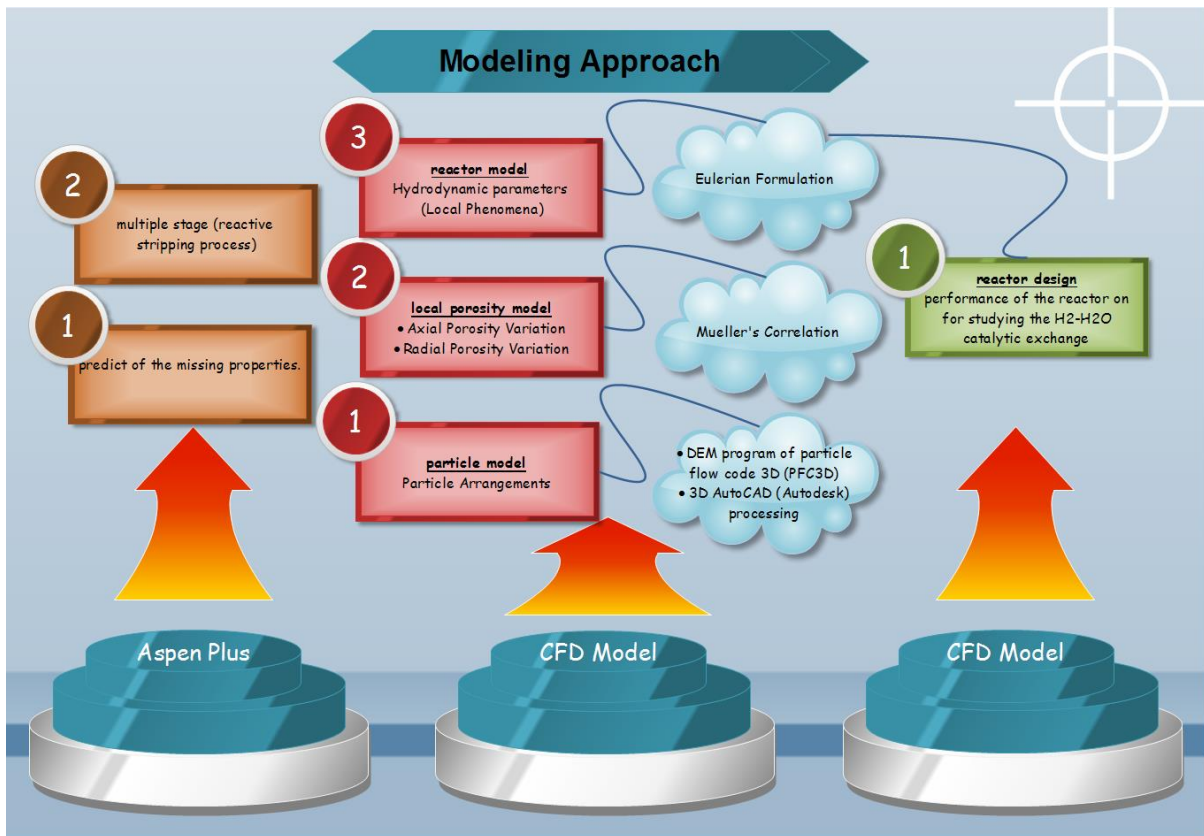


Figure (1.1) trickle/packed bed reactor study approach.

1.4 Contribution of the Thesis

This thesis provides a detailed account to study hydrogen isotope separation by H₂-H₂O liquid phase catalytic exchange in a trickle column by using Aspen Plus process simulation and CFD modelling techniques. Although there are still some unresolved issues, the overall understanding of hydrogen isotope separation and its flow characteristics inside the column reactors is now better understood than that was at the start of this work. Some of the significant contributions made throughout this work are summarized as follows:

- Most of the studies used simplified assumptions based on average physical and transport properties while neglecting the thermal properties of isotopologues such as (heat of vaporization, enthalpy, heat capacity and conductivity) and the underlying heat transfer phenomena. In reality, the liquid stream in the LPCE column is typically operated under a trickle flow and a partial wetting of the packing, causing both mass and heat dispersions and a boundary resistance to mass transfer between

liquid water and gaseous hydrogen. In addition, the methods for solving the multi-component reactive stripping/scrubbing system were mainly taken from the binary component approaches which are more or less straightforward extensions of methods that have been developed for solving conventional scrubbing/stripping column problems. Commercial software packages that carry advanced modelling methods and thermodynamic databases of prediction models for hydrogen isotopic exchange process have not been reported to our knowledge but some dedicated simulation tools were developed in house. Here a rigorous model which governs the coupling of mass and heat transport were presented and specific features of the reaction mixture and to investigate the synergic impact on isotope separation were demonstrated. The effects of transport and reaction kinetics on the transfer of deuterium between the liquid and gaseous phases were then investigated. The model was implemented into the simulation software Aspen plus, validated by comparison with published data, and extended to a sensitivity analysis on the effects of significant design and operating parameters on the column performance. A sensitivity analysis demonstrated the benefit of using this model to estimate missing physical properties developed for a variety of processes including tritium/deuterium rectification.

- Randomly packed beds are utilized in majority of industrially operated trickle bed reactors due to their simplicity in construction and loading process. From a phenomenological perspective, the structure of solid packing within the packed bed plays a significant role. Several physical phenomena involving dispersion, pressure drop, interstitial velocity, and local boundary layer formation over particle surfaces can be affected by complex geometry and it is often hard to identify them. Varied local packing arrangements exist in randomly packed bed reactors and the nature of voids formed between particles affects the flow structure inside the void and therefore controls the mixing, heat, and mass transport rates. Besides, it affects the static and dynamic liquid holdup in the bed. Therefore, CFD models based on a Phase of field approach were developed to gain an insight into interaction of liquid with gas through packed bed. The computational models were validated by comparisons against experimental data available from literature related to TBR operation under similar operating conditions. Simulation results were used to evaluate local phenomena on interaction of two phases over catalyst particles and to examine the sensitivity of spreading behaviour into a column reactor. Accordingly, the results of CFD assessments let us understand the reactor flow characteristics before computing the H₂-H₂O liquid phase catalytic exchange model. The CFD Model predictions were found to agree reasonably well with the numerical simulation and experimental results over a wide range of design and operating parameters.
- The H₂-H₂O catalytic exchange was successfully performed in a trickle bed type chemical

exchange column, and in both co-current and counter-current modes by the 3D CFD model. The effect of flow rate, temperature, height of bed and exchange methods on the performance of chemical exchange column were analysed and found to be significant. The computational methods by a rigorous design and analysis were presented and the results were helpful for designing and enhancing performance of the hydrogen isotope separation by H₂-H₂O liquid phase catalytic exchange process in a trickle column, and thus, providing data for engineering application.

1.5 Thesis outline

This thesis is organized in three Parts. In the first part, the prediction of the missing physical properties of deuterium and tritium isotopologues in hydrogen gas and water forms, and hydrogen isotope exchange via reactive stripping process was studied by using Aspen plus. In the second part, gas-liquid flow through simple trickle bed reactor was studied using 3D CFD modelling. In the third part, the 3D CFD modelling was applied to study the H₂-H₂O catalytic exchange performance. This thesis is organized as shown in Figure (1.2) and detailed as follows:

Chapter 2 provides a comprehensive literature review on previous research in this field. In this chapter we discuss the introduction of hydrogen isotope separation to various types of separation methods. In addition, the development of H₂-H₂O exchange technology is discussed along with brief overview on applications, designs and preparations of hydrophobic catalysts.

Chapter 3 describes the general methodology employed in the present work.

Chapter 4 introduces methods used to predict the missing physical properties of deuterium and tritium isotopologues for hydrogen and water forms. In addition, the methods used to implement the simulation of performance under favoured operating parameters of temperature, pressure and gas/liquid flow ratios into the simulation software Aspen plus Modeler are discussed.

Chapter 5 introduces a comprehensive 3D CFD model to simulate gas-liquid flow through packed beds. Random distribution of bed porosity is represented by a computational discrete element model. The mathematical model is embedded into a commercial CFD code. The model predictions are verified by comparing the simulation results of pressure drop and liquid holdup with previously published experimental data sets and computational results. The CFD model and the results are discussed in terms of elucidation of the role of local phenomena into the mixing and other transport events occurring in the trickle bed reactors and relevant interactions. As a result, the CFD simulation is expected to provide information about how these interactions would affect the gas-liquid performance of H₂-H₂O catalytic exchange.

The extension of computational models to simulate performance of H₂-H₂O catalytic exchange

inside a trickle bed are discussed in **Chapter 6**. In this Chapter, the 3D CFD model is applied to simulate the performance of the reactor and thus the activity of catalyst which can be described by measuring the conversion values throughout the catalytic bed. Effects of flow rate, temperature and height of bed on conversion rate of H₂-H₂O liquid catalytic exchange process are discussed and the results are validated with published experimental data.

Finally, in **chapter 7** relevant conclusions on the methodology followed in the work as well as the results obtained are summarised and recommendations for possible future works are discussed.

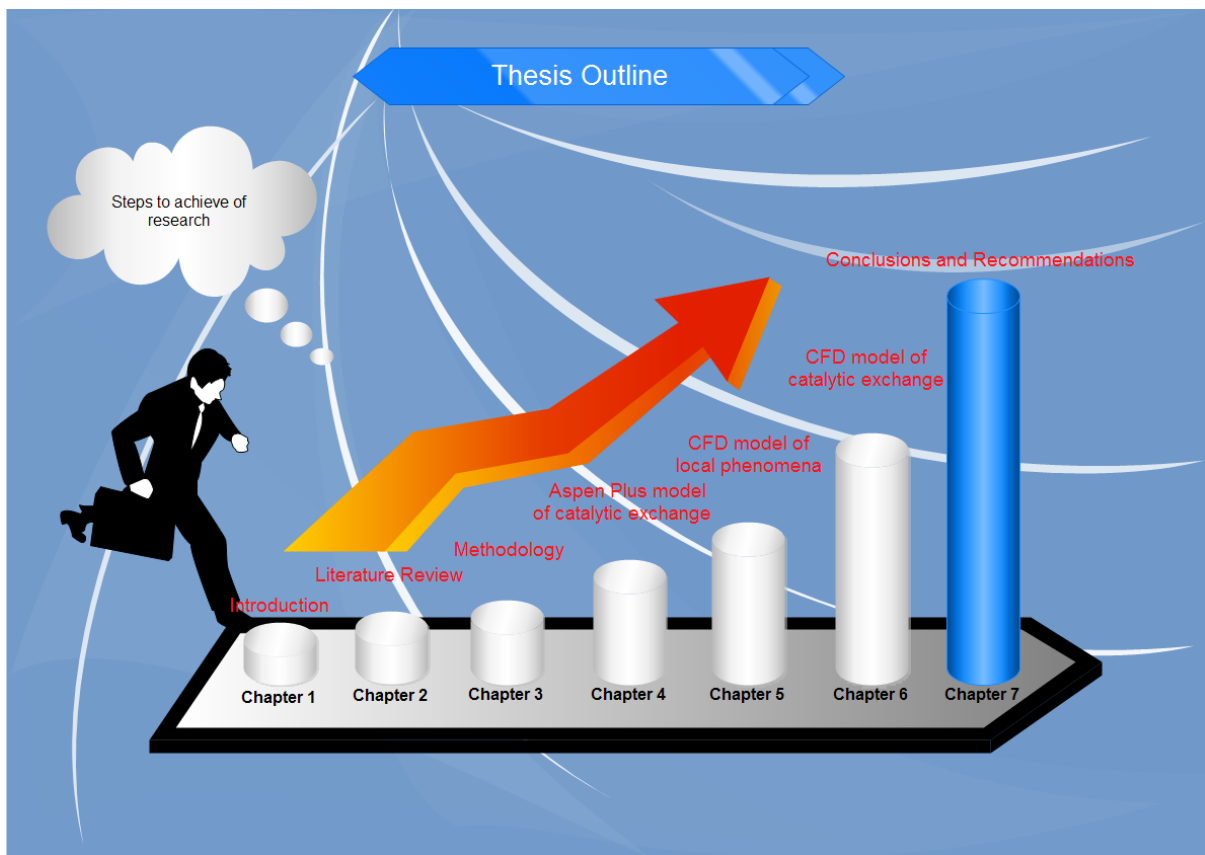


Figure (1.2) the organization of thesis.

1.6 Publications & Presentations & training related to this work

A papers were published from this work, the full details of these papers are found in the reference section [116, 125]. Other conferences and workshops associated with this work are given as follows:

Publications

1. Faris Alzahrani, **Mohammed Aldehani**, Hao Rusi, Michael McMaster, Daniel Luis Abreu Fernandes, Suttichai Assabumrungrat, Meabh Nic An tSaoir, and Farid Aiouache, "Gas flow

visualisation in low aspect ratio packed beds by three-dimensional modelling and near-infrared tomography”. *Industrial & Engineering Chemistry Research*. 2015, 54 (51), pp. 12714-12729.

2. **Mohammed Aldehani**, Faris Alzahrani, Meabh Nic An tSaoir, Daniel Luis Abreu Fernandes, Suttichai Assabumrungrat and Farid Aiouache,” Kinetics and reactive stripping modelling of hydrogen isotopic exchange of deuterated waters. *Chemical Engineering and Processing: Process Intensification*. 2016, 108, pp. 58-73.

Presentations

1. **Aldehani, Mohammed**, the Faculty of Science and Technology Christmas Conference (December, 2013).
2. **Aldehani, Mohammed**, Simulation of waste water processing by water/hydrogen exchange in fusion reactors, ChemEngDayUK at University of Manchester, 7-8 April 2014.
3. **Aldehani, Mohammed** et al., Hydrogen catalytic exchange by dual hydrophobic and hydrophilic catalyst, European Symposium on Chemical Reaction Engineering (ESCRE) Conference at Germany, 27-30/10/2015.

Training

1. Training course for COMSOL under title “introduction to COMSOL Multiphysics” @ University of Cumbria on 15 January 2014.
2. Training course in EndNote @ Lancaster University 04 February 2014.
3. COMSOL workshop under title under title “introduction to COMSOL Multiphysics” @ Lancaster University on 28 January 2015.
4. A Webinar under title (Reaction Engineering with Advanced simulation) @ London on 24 September 2015.
5. A seminar under title (The role of hydrogen in the carbon-catalyst reaction: the example of amorphous carbon conversion to graphene), @ Lancaster University on 28 January 2015.
6. High performance computing-based computational fluid dynamics for offshore renewable energy workshop @ Lancaster University on 7-8 April 2016.
7. A seminar under title (Photoconductivity methods in the study of semiconductors) @ Lancaster University on 13 April 2016.

Chapter 2

Background

2.1 Introduction to hydrogen isotope separation

2.1.1 Hydrogen isotope

Among the known families of chemical elements, hydrogen isotopes have the most different relative atomic mass and strongest isotope effect. [1]

2.1.1.1 Hydrogen isotope atoms

Generally, there are three isotopes of the element hydrogen: protium, deuterium, and tritium (^1H , ^2H , and ^3H) with nucleus proton (p), deuteron (d), and triton (t), respectively. Hydrogen and deuterium are stable isotopes while tritium is a radioactive isotope by β^- decay and a half-life period of 12.32 years, as listed in Table 2.1. [1] All three are naturally occurring isotopes and additional properties of isotope atoms are listed in Table (2.1).

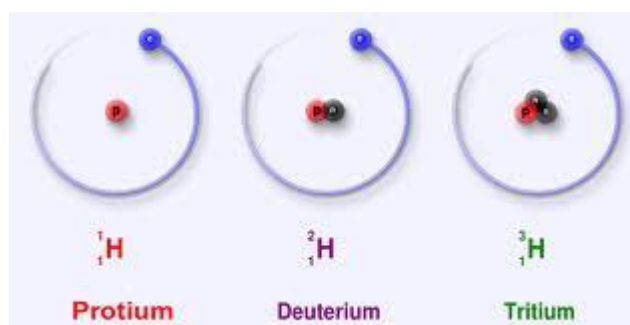


Figure (2.1) schematic of hydrogen isotope atoms.

Table (2.1) comparable property of hydrogen isotope atoms. [1]

Names and Symbols of Isotopes	Hydrogen (H)	Deuterium (D)	Tritium (T)
Names and Symbols of Isotopes Nucleus	Proton (p)	Deuteron (d)	Triton (t)
Isotopic Mass (10^{-3} kg/mol)	1.007825	2.014102	3.016050
Nucleus Invariant Mass (kg)	$1.6726 (10^{-27})$	$3.3436 (10^{-27})$	$5.0061 (10^{-27})$
Nuclear Spin	1/2	1	1/2
Magnetic Moment (J/T)	$1.41062 (10^{-26})$	$4.33066 (10^{-27})$	$1.50457 (10^{-26})$
Electric Dipole Moment (cm^2)	0	$2.77 (10^{-31})$	0
Binding Energy (MeV)		2.226	8.48
Decay Mode	Stable	Stable	β^- decay
Half-Life (y)			12.32

2.1.1.2 Hydrogen isotope molecules

Hydrogen is diatomic molecule. Two hydrogen isotope atoms form one hydrogen molecule by the covalent bond. The three naturally occurring hydrogen isotopes (hydrogen, deuterium, and tritium) form six known isotopic species of molecular hydrogen; H₂, HD, HT, D₂, DT, and T₂. [1] Table (2.2) shows the molecular weight and radius of hydrogen isotope molecules and Table (2.3) shows some physical properties of the hydrogen isotopes. This table shows that, with exception to the molecular radius, a linear increase of physical properties along the molecular weights. This is an interesting trend that could be exploited to predict the missing physical properties of hydrogen isotopes.

Table (2.2) molecular weight and radius of hydrogen isotope. [1]

Molecules	H ₂	HD	HT	D ₂	DT	T ₂
Molecular Weight (10 ⁻³ kg/mol)	2.015650	3.021927	4.023875	4.028204	5.030152	6.032100
Radius (10 ⁻¹⁰ m)	0.7414	0.7413	0.7414	0.7417	0.7417	0.7414

Table (2.3) basic parameters of hydrogen isotope. [1]

Molecules	H ₂	HD	HT	D ₂	DT	T ₂
Molecular Weight	2.016	3.022	4.025	4.029	5.032	6.034
Boiling Point (K)	20.39	22.14	22.92	23.67	24.38	25.04
Triple Point (K)	13.96	16.60	17.62	18.73	19.71	20.62
Triple Point Pressure (mmHg)	54.0	92.8	109.5	128.6	145.7	162.0
Critical Temperature (K)	33.24	35.91	37.13	38.35	39.42	40.44
Critical Pressure (mmHg)	9,736	11,134	11,780	12,487	13,300	13,878
Dissociation Energy (eV)	4.476	4.511	4.524	4.553		4.588
Zero Point Energy (per cm)	2,171.4	1,884.3		1,542.4		

2.1.1.3 Hydrogen isotope waters

H and D are stable hydrogen isotopes. One water molecule includes two hydrogen atoms, so there are two ways to substitute H with D; D₂O and HDO. H₂O is called light water and D₂O and HDO are called heavy water and semi-heavy water, respectively. Table (2.4) shows some physical properties of the hydrogen isotope waters. Unfortunately, a large number of physical properties are still missing in the open literature and these will be a subject of study in the following chapters. Otherwise similar trends to hydrogen isotope in gases are observed, that is, a linear increase of the physical property of the molecular weight.

Table (2.4) physical properties of hydrogen isotope water. [1]

Molecule	H ₂ O	D ₂ O	T ₂ O
Molecule Weight (10 ⁻³ kg/mole)	18.014924	20.027478	22.031372
Melting Point (°C)	0.00	3.81	
Triple-Point Temp (°C)	0.010	3.82	4.49
Triple-Point Pressure (mmHg)	4.58	5.02	4.92
Temperature of Maximum Density (°C)	3.984	11.185	13.403
Maximum Density (g/cm ³)	0.999973	1.10585	1.21501
Boiling Point (°C)	100.00	101.42	101.51
Density (at 25 °C, g/cm ³)	0.99701	1.1044	1.2138
Dielectric Constant (at 25 °C, debye)	78.39	78.06	
Surface Tension (at 24 °C, dyne/cm)	71.97	71.93	
Viscosity (at 25 °C, cp)	0.8903	1.107	
Ionization Constant (at 25 °C)	1.27 (10 ⁻¹⁴)	1.95 (10 ⁻¹⁵)	~ 6 (10 ⁻¹⁶)

2.1.2 Significance of hydrogen isotope separation

In modern society, hydrogen isotopes (hydrogen, deuterium, and tritium) play very important roles in many industries. However, over exposure, deuterium and tritium can cause health issues to humans. In order to improve safety and efficiency of hydrogen isotope applications, hydrogen isotope separation is therefore highly needed.

2.1.2.1 Applications of hydrogen energy

Hydrogen is the most abundant and widely distributed resource on the earth. Hydrogen is also an important industrial raw material as well as major secondary energy source and applications include:

(1) Fuel combustion

As high-energy fuel, the maximum fuel value of hydrogen is 121061 kJ/kg, which is much higher than petrol 44467 kJ/kg and ethanol 27006 kJ/kg. Liquid hydrogen is heavily used in the aerospace industry because the propellant is typically composed of liquid hydrogen and liquid oxygen which can generate the specific impulse as high as 390 s. [2-4] As engine fuel, hydrogen is superior to petrol and diesel in many aspects of physical properties.

(2) Petrochemical industry

Hydrogen is one of the crude materials in the modern petrochemical industry. It is mainly used for hydrodesulfurization, hydrocracking, as well as hydrotreatment of C3 distillate and petrol, hydrodealkylation of C6~C8 distillate, etc. [5-7] Hydrogen is also widely used to manufacture fine chemicals and produce intermediates of medicines, dyes, and pesticides. [8]

(3) Electronic industry

In the processing of large-scale electronics, a high purity and super high-purity hydrogen are needed as a basic gas to prepare mixed gases. High purity hydrogen is also needed to produce electron tubes, ionic tubes, hydrogen thyratrons, picture tubes, laser tubes, etc. [9] Amorphous silicon solar batteries have been widely applied to many areas and the production of such batteries needs high purity hydrogen. [10-12] The manufacture of optical fibres also needs hydrogen and the development of optical fibres has significantly promoted the market of hydrogen. [13]

(4) Applications in other industries

In the metallurgical industry, hydrogen acts as a reducing agent of metallic oxides into metal forms as well as a shielding gas to protect metals during the processing at high temperatures. In the food processing industry, natural cooking oil is processed by addition of reaction between hydrogen and active double bond of the oil molecules, allowing thus oil to be stored stably with minimized bacterial growth. [14] Liquid hydrogen has a good cooling capacity and can be used to cool electric generators and nuclear reactors in the fields of electric power and atomic energy, respectively. [1]

2.1.2.2 Application of deuterium

High purity deuterium was initially applied to military field such as deuterium fluoride (DF) chemical laser weapon, nuclear weapon and so on [15-17]. Later, high purity deuterium was used as a civil material for the processing of deuterated optical fibres, special light bulbs, deuterium lubricating oils and semiconductor toughening, nuclear medicine and nuclear agriculture. Deuterium has a number of commercial and scientific uses. These include:

- (1) DF laser is a strong laser weapon and deuterium is an important raw material for DF laser. Purity of deuterium directly affects beam quality of laser. As a result, high purity deuterium must be used.
- (2) High purity deuterium is needed for the manufacture of military nuclear weapons such as hydrogen bomb, neutron bomb, and ship-carried laser cannons.
- (3) To obtain usable nuclear energy, nuclear fusion must be controllable. The first step to achieve controllable nuclear fusion is to heat nuclear fuels such as deuterium and tritium to a very high temperature. Deuterium used for controllable thermonuclear reaction must have a very high purity, a very small amount impurity will greatly increase the radiation damages, and hence high purity deuterium must be produced.
- (4) The other existing form of deuterium is heavy water (deuterium oxide, D₂O). The special value of deuterium oxide is shown in the application of nuclear energy technologies, including good slowing properties and little absorption of neutrons. Reactors that used deuterium oxide as a moderator are called deuterium oxide reactors. Among thermal-neutron reactors, deuterium oxide

reactors need the least amount of natural uranium and strong adaptability to fuel. The Canada Deuterium Uranium (CANDU) nuclear power plant can produce plutonium-239 for nuclear weapon while generating electrical energy. [18]

With the development and innovation of technology, deuterium will be more widely used. Demand for deuterium will be increased and therefore, how to obtain deuterium with high purity will be a hot research topic.

2.1.2.3 Application and risk of tritium

(1) Application of tritium

High purity tritium is critical as a nuclear material to produce nuclear weapons that contain tritium [19]. There are traces only of tritium in nature owing to its relative short life activity, so the tritium used nowadays to produce thermonuclear weapons and other research activities is obtained via nuclear reactor processing. Currently, there are several ways to obtain tritium; (1) tritium can be generated via nuclear reaction between a neutron and lithium in a thermal-neutron reactor; (2) tritium can be generated from deuterium by capture of one neutron in a deuterium oxide reactor; (3) tritium can also be recycled from parts containing tritium. However, tritium obtained from these methods is not sufficiently pure, leading to additional purification techniques. [20]

Further, tritium and its labeled compounds play an important role in the field of industry, hydrology, geology and several areas of research. Tritium and its labeled compounds are also a significant research tool in life science research, [21] such as the mechanism of enzyme, cell biology, molecular biology, receptor-binding research, analysis of radiological immunology, and diagnosis and treatment of cancer. Tritium is also used to produce light emitting tritium tube. Therefore, preparation, purification and separation of tritium are very significant steps and are still highly researched topics at both academic and development stages. [21]

(2) Risk of tritium

Tritium is low energy β radiator and can only reach 0.005 mm in the skin. So the harm of external irradiation is very little and human can be easily protected. The damage caused by tritium is mainly because of internal irradiation. Tritium gas (e.g. HT, DT) enters human body by lung and most tritium gas will be exhausted quickly. The blood will absorb 1.6% tritium gas. The half-life of tritium in the blood is 1 hour and 0.004% of such tritium will be transformed into HTO. Reaction (2.1) shows how tritium gas transforms in the blood. [22]



Water containing tritium is very harmful to human. In nature and deuterium oxide reactor plants, the most common chemical forms of tritium water are HTO and DTO. Tritium water has similar chemical

properties with water and can easily enter the body via lung, skin, and food. Once entered into the body, HTO and DTO can reach an exchange balance rapidly with body fluids. Tritium enters human tissues and cells and participates in body metabolism as an element in the body, as a result, will cause long-term damage to tissues and organs. [23]

Countries have different regulations for tritium. For example, in Japan, the maximum permitted to discharge in to the environment is 90Bq/cm³ for air, 60Bq/cm³ and 0.005Bq/cm³ for water and water vapour, respectively [24].

As it can be concluded from above, purification and separation of tritium is not only good for various industrial and research activities but also reduces risk to the human health.

2.1.2.4 Risk of heavy water

It is well known that heavy water is a very important raw material in the nuclear industry. Unlike normal water, heavy water cannot feed lives. Heavy water has similar chemical properties to light water but not physical properties. It is difficult to dissolve heavy water into organic liquids. Heavy water has boiling point 101.42°C (light water boiling point 100°C), density 1.1 g/cm⁻³ (light water density 1 g/cm⁻³), and viscosity 1.1 cp (light water viscosity 0.9 cp). [1]

Heavy water and light water have totally different affection on living entities. Scientific studies showed deuterium was harmful to the survival and propagation of living entities and was risky to living entities no matter the amount in water. The good thing is that living entities have adapted natural water with 150 ppm deuterium. If deuterium is higher than 150 ppm in water, it is risky to living entities.

As early as 1974, deuterium has been found as a factor for ageing. Goodall K B, proposed an important theory that deuterium produced extra stress on DNA helix structure and caused phase shift, breakage, and replacement of double helix and disorder, resynthesis, and mutation of RNA. Living entities have no resistance to deuterium and once deuterium enters living entities, it is very hard to get cleared. So high amounts of deuterium have a negative effect on inheritance, metabolism, and enzymes of the human body. Higher amount of deuterium are more toxic to living entities. Therefore, living entities, including humans, a variety of plant and animal, are always under the poisoning of deuterium by different degrees. [25]

Some other studies [26-28] showed that deuterium could affect the mitosis of organisms, damage DNA repair enzymes and cause DNA disorder. Because cells will keep inheritable properties after mitosis, the DNA damage would be carried for a lifetime. Heavy water reacts with DNA and affects the activity of genetic factors and causes malignant tumors [29-31].

Reports showed that deuterium inhibited activity of biological enzymes. Reaction rate of biological enzymes for DNA replication decreased to half in heavy water [32]. Other studies showed mice died when heavy water reached a concentration 35% in the body [33-35].

2.1.3 Separation methods of hydrogen isotope

Isotopes have same electronic configuration and similar chemical properties. So it is difficult to separate isotopes. However, the difference of mass number of hydrogen isotopes is relatively large and there are some differences in the physical and chemical properties of hydrogen isotopes and therefore, it is relatively easier to separate hydrogen isotope. [36]

There are many methods to separate hydrogen isotopes and these can be divided into two major categories; chemical and physical methods. Chemical methods mainly include electrolysis, chemical exchange, and chromatography. Physical methods mainly include thermal diffusion, gaseous diffusion method, cryogenic distillation, and low temperature adsorption. Although laser method includes chemical processes, but the principle method is based on a physical mechanism. [36]

2.1.3.1 Physical methods

2.1.3.1.1 Thermal diffusion (TD)

This method is widely used for the separation of gas isotopes and is based on the mechanism that a temperature gradient will cause a concentration gradient of different gas components in mixed gases. [37-41] Based on the definition of separation constant, equilibrium separation constant of the thermal diffusion separation column can be expressed by equation (2.2):

$$Sep_{eq} = \frac{\left(\frac{C_1}{1-C_1} \right)_{top}}{\left(\frac{C_1}{1-C_1} \right)_{bot}} = e^{\frac{H}{K_c+K_d}L} \quad (2.2)$$

Where Sep_{eq} is the equilibrium separation constant; C_1 is the concentration in a random spot in the column; L is the total length of thermal diffusion separation column; H is the coefficient of transport by thermal diffusion; K_c is the coefficient of transport by convection currents; and K_d is the coefficient of transport by ordinary diffusion. H , K_c , and K_d are constants. Usually, $H/(K_c+K_d)$ can be written as $2A$, and equation (2.2) can be expressed by equation (2.3):

$$Sep_{eq} = e^{2AL} \quad (2.3)$$

Equation (2.3) is the expression of equilibrium separation constant of thermal diffusion separation column in steady state conditions.

Only when separation constant (2A) is increased, isotopes with high purity can be obtained. Based on the theory, the optimized separation conditions are: low temperature of cold wall, large temperature ratio, small radius ratio, small radius of cold wall, and high processing pressure.

Compared with other separation methods, the thermal diffusion separating method has several merits: simple setting, no rotation parts, easy cascading, high separating constant in a single column, easy operation, and little residue in column, so it was widely used in the early separation research. But thermal diffusion separating method was consuming a large electric energy, had low production ability and was only suitable for small to medium-scale isotope separations. [36]

2.1.3.1.2 Gaseous diffusion

The gaseous diffusion method was developed based on diffusion laws of mixed gas molecules. When gas molecules go through small pores, capillaries, or porous media, the diffusion process will produce basic separation effect.

Ideal separation constant of gaseous diffusion method for a dual gases system is the square root of molecular weight ratio of heavy molecule to light molecule. For H_2+HT (T_2) system, the max value is 1.732. Under experimental conditions however, the penetration constant ratio of T_2 and H_2 was 2.12 ± 0.03 when they went through palladium alloy membrane and the penetration constant ratio was irrelevant to temperature in the range 350~550 °C. The phenomena led a number of research interest. [42-43]

Scholar Izumoji, Y. et al. from Japan reported that at 300 K and 7 atm, very high separating factor was obtained when hydrogen isotopes went through palladium alloy membrane. They also hypothesized palladium alloy containing 8% tritium could further optimize the separation properties. [44] Currently, hydrogen isotope separation with this method is still in laboratory research stage.

2.1.3.1.3 Distillation

Distillation is a classic separation method for liquid mixtures. Basically, distillation can be divided into the simple distillation and the rectification. Hydrogen isotopes and their oxides have different volatilities at the same temperature. [36]

For a dual-isotope mixture, the separation constant of distillation is the ratio of saturated vapour pressure of two gases in the ideal condition and will not be affected by abundance of gases. Isotope separating effect usually decreases with increased temperature, so low temperature distillation has a high separation efficiency. In the field of hydrogen separation, water distillation (WD) and low temperature liquid hydrogen rectification or cryogenic distillation (CD) have been successfully applied. [36]

(a) Water distillation (WD)

Currently, some laboratories in Canada, America, and India have built plant for deuterium oxide (D_2O) with production ability higher than 100 tons per year. They all use water distillation to concentrate deuterium oxide in the final step.

Different countries have carried out experiments over wide temperature ranges to measure the separation factor of concentrated deuterium during water distillation. They all concluded that if deuterium oxide was an ideal solution [45], the separation factor would be related to the saturated vapour pressure ratio of H_2O and deuterium or tritium isotopologues as shown in Table (2.5).

Table (2.5) vapour pressure ratios for isotopologues of water species $P(H_2O)/P(x)$. [45]

Temperature	T_2O	DTO	D_2O	HTO	HDO
25	1.193	1.175	1.154	1.095	1.075
50	1.134	1.123	1.110	1.065	1.053
100	1.064	1.060	1.052	1.030	1.026

Water distillation is safe and easy to operate but has several drawbacks such as small separation factor, energy consumption, high cost of operation, and low recovery (2~3%). So it is uneconomical for initial stages of separation and may be used in the medium and final stage of separation and concentration. [36]

(b) Low temperature liquid hydrogen rectification or cryogenic distillation (CD)

Urey et al. first found deuterium from liquid hydrogen in 1931 [46]. Afterwards, liquid hydrogen rectification was widely used to separate deuterium in Germany, US, Japan, Canada, China, Romania and other countries. [47-52] Demonstrated by practice, low temperature liquid hydrogen rectification is a very effective method to separate hydrogen isotopes.

The advantages of liquid hydrogen distillation are: high separation factor, low energy consuming, high production ability, short start time, flexible design and low molecular of working material. The boiling points of H_2 , HD and D_2 are 20.39 K, 22.14 K and 23.67 K respectively, and the separation factor of H_2 - D_2 and H_2 -HD are 2.67 and 1.7, respectively.

Separation factor of tritium and deuterium isotopes at 24 K during liquid hydrogen distillation are $Sep_{H-T} = 4.7$ and $Sep_{D-T} = 1.34$, respectively. Therefore, this method can be used for separating tritium from hydrogen isotopes at affordable costs. [36]

The main disadvantage of liquid hydrogen distillation are: low operating temperature, high request of heat insulation, high technical difficulty, large amount of residue, and high request of raw material purity. [36]

2.1.3.1.4 Low temperature adsorption

Low temperature adsorption relies on refrigerating porous adsorbent such as activated carbon and molecular sieves. Through physical adsorption process, gas molecules are captured and separated from impurities. When gas mixture passes low temperature molecular sieves or activated carbon at 77K, all impurities in the DT gas are adsorbed from helium (He) as carrier gas. [53]

Separation of hydrogen and deuterium has been highly investigated by adsorption separation. [54-56] At 77 K and 1 atm, the separation factor of hydrogen and deuterium by activated carbon adsorption reached 1.2. At 75~90 K and 1 atm, by silica and molecular sieve adsorption was about 1.3~1.47 and 1.77~2.54, respectively. At 80 K, separation factor of hydrogen and deuterium by palladium adsorption was 3.5. At liquid nitrogen temperature, molecular sieve can reach interesting separation factors of D₂, HD, H₂, and others isotopologues. Low temperature molecular sieve adsorption is nowadays a mature technique that occurs at 77 K and is featured with easy maintenance, no solid waste and less environmental pollution. [57]

2.1.3.1.5 Laser technique

The laser method is an isotope separation method based on a combination of laser technology and nuclear technology. To date, many important isotopes have been separated by the laser method. The mechanism is to use laser with a proper wavelength to excite specific isotope component without affecting other components. Then, excited isotopes and unexcited isotopes can be separated by their different chemical and physical properties before energy transfer happens. [36] Hydrogen isotopes present different relative mass and apparent shift on their spectra, making separation by the laser technique a promising technology. [58-59]

2.1.3.2 Chemical Methods

2.1.3.2.1 Electrolysis

Electrolysis of water is the first application to produce deuterium oxide (D₂O) at large industrial - scale [60]. The technique offers a high separation factor and easy processing but it consumes much electric energy. The mechanism is to use direct current to electrolyse water with the presence of electrolytes. The process can be expressed by reaction (2.4):



When water contains deuterium, hydrogen discharge happens first on the electrolyte because of the mobility difference between hydrogen ion and deuterium ion and the larger overvoltage of deuterium compared to that of hydrogen. Therefore, in the electrolysis of water, the generated hydrogen gas contains depleted deuterium while deuterium is concentrated in the enriched solution. When the electrolysis method is used to separate hydrogen isotopes, separation factor of hydrogen-deuterium is about 3~12, separation factor of hydrogen-tritium is about 10, and separation factor of deuterium-tritium is about 2 (at 60°C). [36] Separation factor is significantly affected by cathode material, electrolysis solution properties and conditions of the electrolysis. In industry, when electrolysis method is used for enrichment of heavy water, iron is used as the cathode. Purer iron and smoother surface of pole result in higher separating factor.

It is usually more efficient to combine electrolysis (Figure (2.4)) and chemical exchange method (Figure (2.2)) or electrolysis and distillation method (Figure (2.3)) [61-63]. Both combined methods have advantages such as small process volume, high separation factor, easy operation and low loss, making its consumption of energy cost-effective.

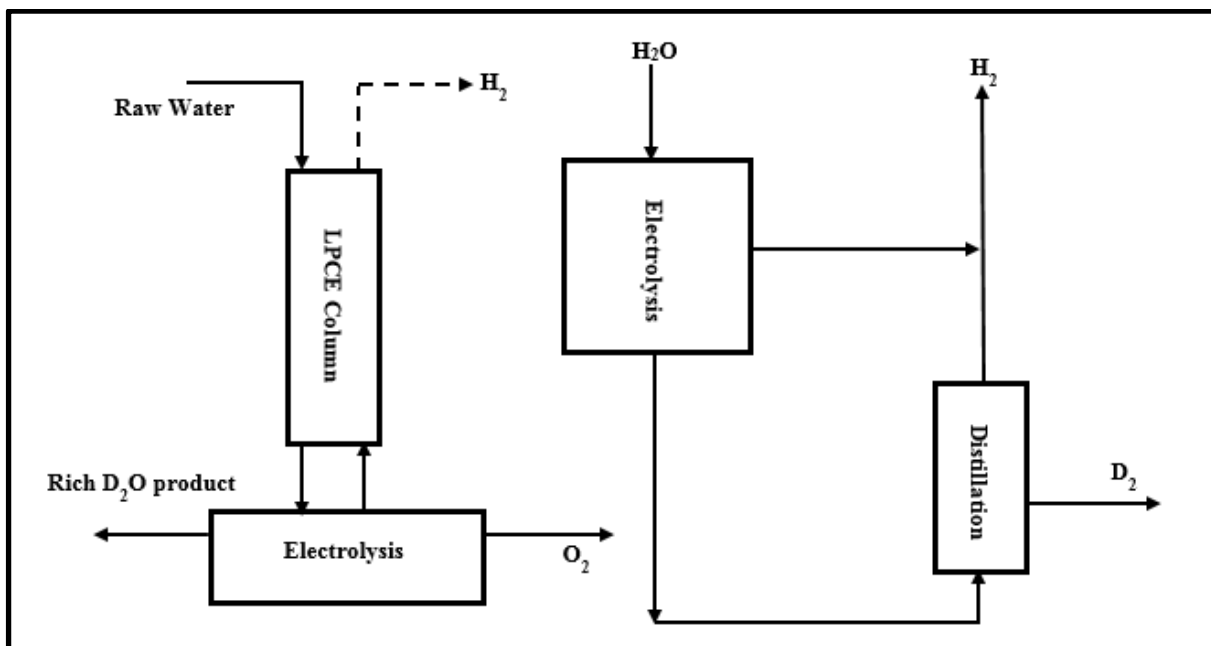


Figure (2.2) electrolysis combined with chemical exchange. Figure (2.3) electrolysis combined with distillation.

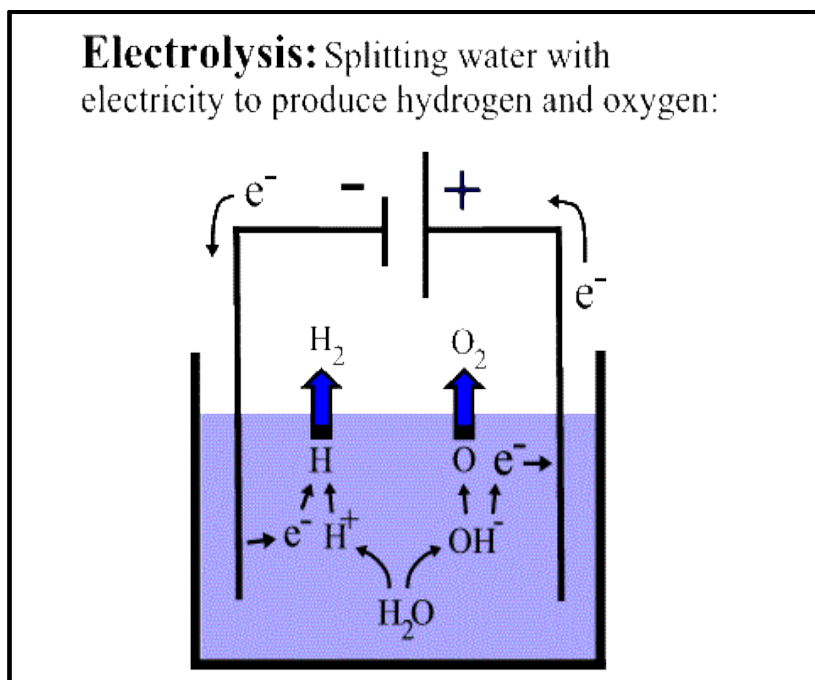


Figure (2.4) electrolysis.

2.1.3.2.2 Chemical exchange

Chemical exchange is a special method of isotope separation and is based on difference in distribution preference of isotopes in the chemical components to achieve separation of different purposes. When two chemical compounds of the same element react under certain conditions, isotopes of the element will have different contributions to unreacted reagents and reacted products.

To separate hydrogen isotopes, the chemical exchange method can be divided into two categories: one includes water, such as $\text{H}_2\text{O}-\text{H}_2$, $\text{H}_2\text{O}-\text{H}_2\text{S}$, $\text{H}_2\text{O}-\text{NH}_3$; the other includes hydrogen gas, such as NH_3-H_2 , $\text{CH}_3\text{NH}_2-\text{H}_2$. [64]

Table (2.6) lists the separation factor between hydrogen and deuterium from water based reactions and Table (2.7) lists the separation factor between hydrogen and deuterium from hydrogen gas based reactions. Values in the table show the corresponding relations between the separation factor and temperature change, and lists some ratio of separation factors at several temperatures. It is clear to see that conducting a dual-temperature chemical exchange would reach larger separation factors. [64]

Table (2.6) separation factor between protium and deuterium in water. [64]

Reactant	Product	Separation factor Sep						Sep_{25}/Sep_{125}
		0°C	25°C	50°C	100°C	125°C	200°C	
$\text{H}_2\text{O}+\text{HD}$	$\text{HDO}+\text{H}_2$	4.53	3.81	3.30	2.65	2.43	1.99	1.57
$\text{H}_2\text{O}+\text{HDS}$	$\text{HDO}+\text{H}_2\text{S}$	2.6	2.37	2.19	1.94	1.84	1.64	1.29
$\text{H}_2\text{O}+\text{NH}_2\text{D}$	$\text{HDO}+\text{NH}_3$	1.02	1.00	1.00	0.99	0.99	0.99	1.01

Table (2.7) separation factor between protium and deuterium in hydrogen. [64]

Reactant	Product	Separation factor <i>Sep</i>						standard ratio*
		-50°C	-25°C	40°C	60°C	100°C	125°C	
HD+NH ₃	H ₂ +NH ₂ D	6.6	5.91*	3.30	2.99*	2.55	2.34	1.97
HD+CH ₃ NH ₂	H ₂ + CH ₃ NHD	7.90*	2.37	3.60*	-	-	-	2.19

H₂O-H₂S exchange reaction happens fast and does not need catalyst while other exchange reactions need catalyst to increase the reaction rate. Potassium methylamide catalyst (CH₃NHK) is an effective catalyst for CH₃NH₂-H₂ exchange reaction [20] while a hydrophobic catalyst is needed for H₂O-H₂ exchange reaction. [65-71].

The chemical exchanges are usually carried out via monothermal or bithermal methods. The monothermal method means that chemical exchange occurs at a single temperature. For example, in the exchange reaction of H₂O-H₂ or NH₃-H₂, ammonia and water can be decomposed into hydrogen gas by thermal energy or electric energy (thermal exchange) at constant temperature. [64] Figure (2.5) shows monothermal exchange process.

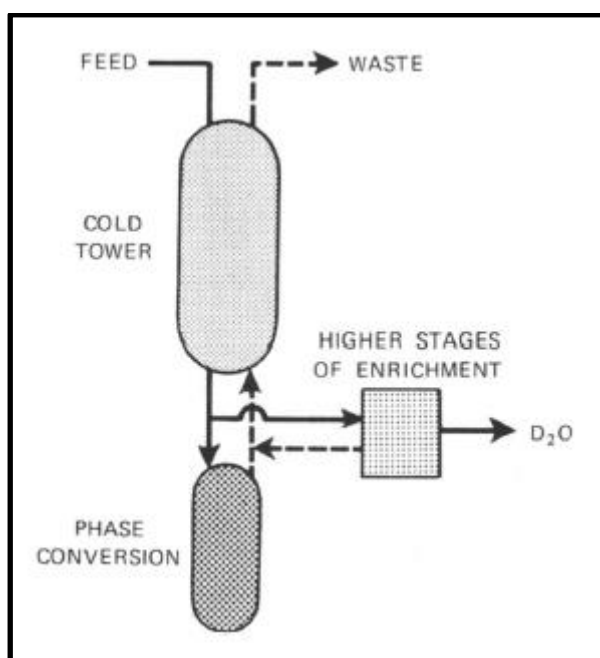


Figure (2.5) flow sheet of monothermal chemical exchange process. [64]

The bithermal exchange occurs at different temperatures. The gaseous and liquid components react and exchange in the reaction tower by the changes of reaction equilibrium constant. In the cold tower, heavy components usually concentrate in the liquid phase and in the hot tower, heavy components concentrate in the gaseous phase [64]. Concentrated gas or liquid can be obtained and transferred to the next stage for further concentration. To achieve a high separation, parallel connection of bithermal

towers are necessary. The number of parallel connections will be determined by the separation requirements; separation factor, ratio of gas to liquid flow rates (G/L), temperature and pressure. Figure (2.6) shows the bithermal exchange process.

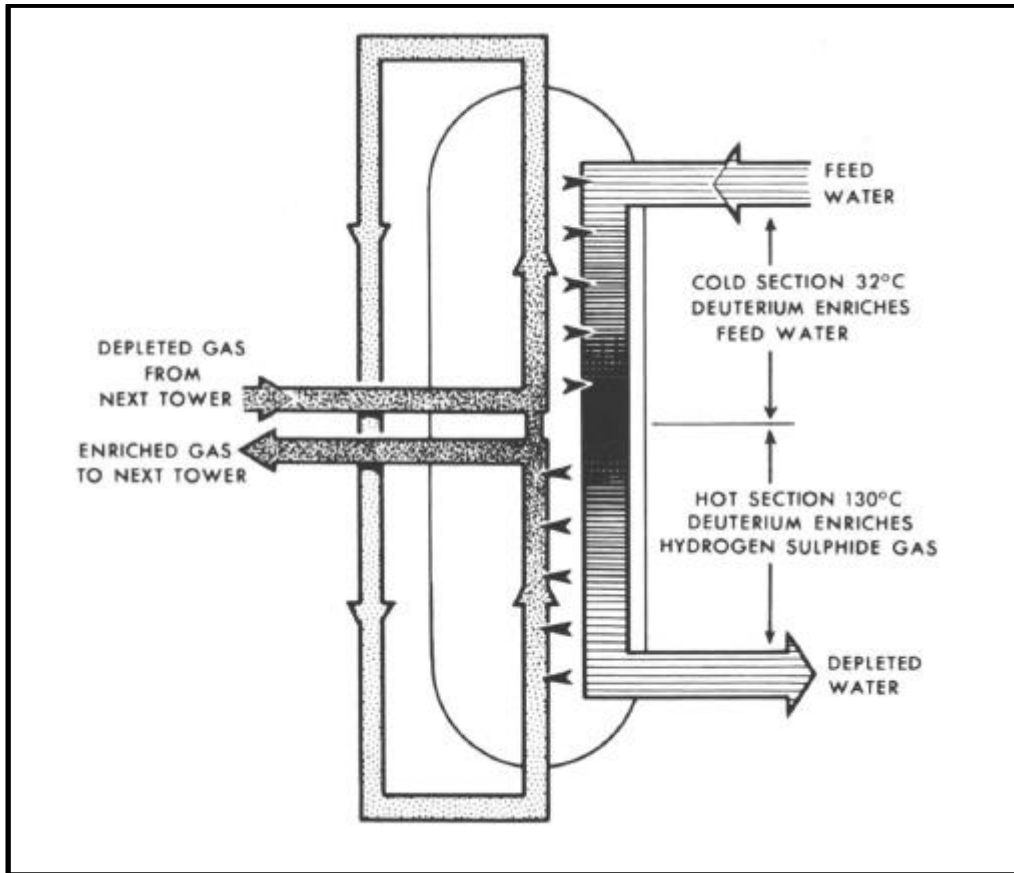


Figure (2.6) flow sheet of bithermal chemical exchange process. [64]

The major merits of chemical exchange are represented by the easy preparation of work material, the large separation factor and the strong dependency relationship between temperature and separation factor. [20, 64]

2.1.3.2.3 Chromatography

The earliest usage of displacement chromatography to separate hydrogen isotope appeared in 1960. [72] The advantages of this method are: easy separating mechanism and setting, fast separating, good for large-scale separation, and easy operation. Displacement chromatography is based on that many metal and alloys can react with hydrogen reversibly and form metal hydride. There is an isotope effect when metal hydrides are formed and among the known metal hydrides; palladium-hydrogen has the strongest hydrogen isotope effect. [36]

Hydrogenation of palladium starts with the adsorption of hydrogen molecules by palladium surface. Hydrogen molecules are then dissociated to atoms and hydrogen atoms dissolve into palladium. With increased hydrogen atoms in palladium, phase transition happens and hydride forms. Different from hydrogen, when deuterium and tritium are dissolved to palladium, they have different ground states in the crystal lattice because of their different atomic mass (energy level of ground state: tritium > deuterium > hydrogen). Different energy levels result in different macroscopic effects of the reaction; for the amount of released heat (tritium < deuterium < hydrogen); for the isothermal curve of hydrogen absorb/release, tritium has highest pressure and hydrogen has lowest pressure. These are the hydrogen isotope effects of palladium-hydrogen system. [36, 73]

The hydrogen isotope effect of palladium-hydrogen system also includes selective adsorption and release of palladium. The adsorption preference of palladium is hydrogen > deuterium > tritium and release preference of palladium is tritium > deuterium > hydrogen. The hydrogen isotope effect of palladium-hydrogen system decreases with increased temperature. So at lower temperature, the isotope effect will be stronger. [36, 73]

Technical comparison of the above separation methods are listed in Table (2.8).

Table (2.8) comparisons among hydrogen isotope separation technology. [20, 36 and 64]

Separation technology	Separation factor (α)			Energy consumption (kW)	Advantage	Disadvantage	Recovery (%)
	H-D	H-T	D-T				
Thermal Diffusion	1.05				simple equipment setting, easy operation	small scale, large energy consumption	>95
Water distillation (WD)	1.04 (333K)		1.01 (333K)	1000	easy operation	small separation factor, large heat consumption	2~3.5
Low temperature liquid hydrogen distillation	2.67 (24K)	4.7 (24K)	1.34 (24K)	800	high separation factor	difficult to handle large-scaled liquid hydrogen	>95

Laser	~10000					high separation factor, high utilization rate of raw material	immature production in industrial scale	>90
Electrolysis	3~8	6~12	~2	950		high separation factor	large energy consumption	~10
H₂O-H₂S bithermal exchange	2.36 (300K)	3.37 (300K)	1.42 (300K)	80		high separation factor, large flow of raw material	high toxicity and corrosivity of H ₂ S, difficult process control needed	~20
H₂-H₂O bithermal exchange	3.69 (303K)	6.54 (303K)	1.7 (303K)	50		high separation factor, non-toxic, noncorrosive	hydrophobic catalyst	~50
Combined electrolysis catalytic Exchange (CECE)	3.87 (298K)	5.6 (298K)	1.6 (298K)	900		high separation factor, non-toxic, noncorrosive	needed hydrophobic catalyst	~70
Palladium-hydrogen gas-solid chromatography	2.0		1.4	110		high separation factor, easy operation	only for small scale, large energy consumption	>9

2.1.4 Overview of the applications of hydrogen isotope separation methods

To date, the main purposes of hydrogen isotope separation are to produce deuterium oxide, (D₂O) and purify and recycle tritium. Demonstrated by practice among various methods, H₂O-H₂S bithermal exchange and H₂-NH₃ (bi)/thermal exchange are suitable for commercialization. [20, 64] Most countries use these two methods for deuterium oxide plants. Table (2.9) lists the process of deuterium oxide production in several countries. [74]

Table (2.9) comparisons among method of heavy water production. [74]

Method	Advantage	Disadvantage	Economy	Operating or constructing heavy water plant
Water distillation (WD)	Independent, easy operation, reliable	High consumption of vapor	Only suitable for final stage concentration	Nangal, India, with an annual output of heavy water 14 tons.
H₂O-H₂S bithermal exchange	Independent, mature technology, no need of catalyst	Low recycle rate of deuterium, corrosive, long process, high consumption of energy	Suitable for big plant (annual output over 100 tons)	<ol style="list-style-type: none"> 1. Savannah River, US, with an annual output of heavy water 450/180 tons. 2. China, with an annual output of heavy water 30 tons. 3. Port Hawkesbury, Canada, with an annual output of heavy water 400 tons. 4. Bruce A, Canada, with an annual output of heavy water 800 tons. 5. Bruce B, Canada, with an annual output of heavy water 800 tons. 6. Bruce D, Canada, with an annual output of heavy water 800 tons. 7. Glace Bay, Canada, with an annual output of heavy water 400 tons. 8. RAPP-Rana, Canada, with an annual output of heavy water 800 tons. 9. Kota, India, with an annual output of heavy water 100 tons.
H₂-NH₃ exchange	Mature technology, high recycle rate of deuterium, low consumption of energy	Dependent, need catalyst	Suitable for plant with annual output around 60 tons	<ol style="list-style-type: none"> 1. Vadodara, India, with an annual output of heavy water 67 tons. 2. Tuticorin, India, with an annual output of heavy water 71 tons. 3. Talcher, India, with an annual output of heavy water 63 tons.
Electrolysis		High consumption of energy	Only suitable for final stage concentration	Rjukan, Norway, with an annual output of heavy water 14-20 tons.

2.2 Development of H₂-H₂O exchange technology

The separation of hydrogen isotopes by H₂-H₂O chemical exchange process is attractive since it offers a high separation factor, is non-toxic and non-corrosive. The raw material of reaction is water. Hydrogen gas is obtained via electrolysis of water. This method has low cost and is very attractive to scientists. The major drawback is its slow reaction rate. To obtain usage exchange rate, catalysts are needed. H₂-H₂O chemical exchange can be divided into three categories by its process of exchange; high temperature vapour phase catalytic exchange (VPCE), liquid phase catalytic exchange (LPCE), and combined electrolysis catalytic exchange (CECE).

2.2.1 VPCE process

Vapour phase catalytic exchange (VPCE) was developed by the French atomic energy commission (CEA) and applied to the plant located at Grenoble, France. In the 1980's, modified VPCE was applied to power the reactor located at Darlington, Canada, to remove tritium from deuterium oxide (Tritium Removal Facility, TRF). [75] Figure (2.7) shows the flow sheet of the combined VPCE and cryogenic distillation (CD) process.

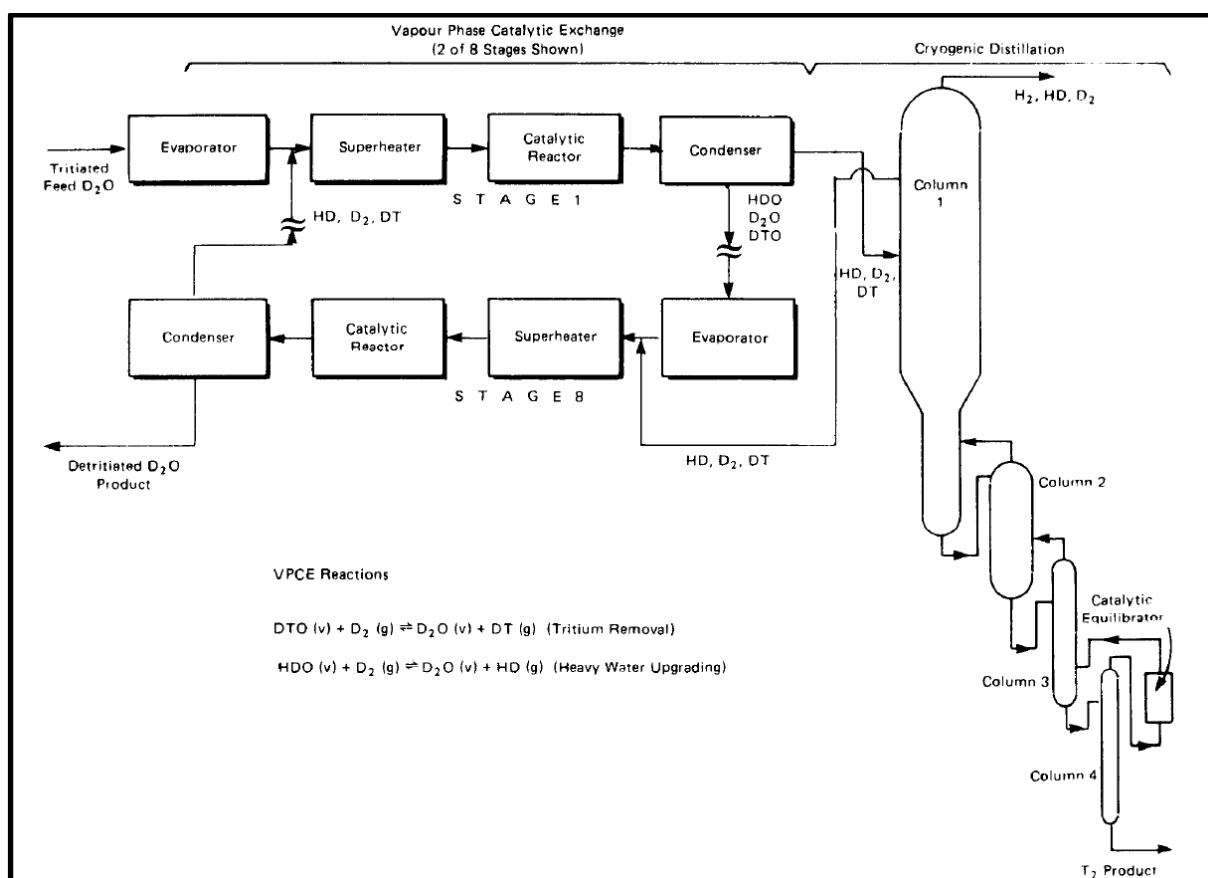


Figure (2.7) flow sheet of combined VPCE and CD process. [76]

Tritium and hydrogen containing deuterium oxide is first heated to a vapour. Under a certain pressure, deuterium oxide vapour mixes with D₂ at 200 °C and then enters the exchange column filled with a noble metal catalyst. HDO and DTO exchange with very pure D₂, the reactions are expressed by reaction (2.5) and (2.6).



At 200 °C, equilibrium constant of reaction (2.5) is 1.78.



At 200 °C, the equilibrium constant of reaction (2.6) is 0.82.

In these two vapour phase catalytic exchange reactions, the ratio (L/G) of the liquid phase flow rate (L) and vapour phase flow rate (G) must be lower than the equilibrium constant of exchange reaction to achieve mass transfer of hydrogen and tritium from liquid phase to vapour phase. [77] VPCE reactions use hydrophilic catalysts and are conducted at 200 °C to avoid activity reduction of hydrophilic catalysts affected by the condensation of water vapour. Tritium containing deuterium oxide needs repeated vaporization and condensation at 200 °C. The equipment and process are very complicated and consume much energy. [77]

2.2.2 LPCE process

The VPCE process has two drawbacks. One is that water needs to be vaporized by heat in every stage and to be condensed to water at ending stage, which consumes much energy; the other is that VPCE cannot conduct counter-current flow exchange.

In the 1980s, a hydrophobic catalyst was successfully produced, which made it possible to conduct low temperature liquid phase catalytic exchange. Different from vapour phase exchange, liquid phase catalytic exchange (LPCE) does not need the vaporization of water and vapour-liquid phase catalytic exchange can use (counter/co)-current flow exchange.

For liquid phase catalytic exchange (LPCE), deuterium oxide is in liquid phase and a catalyst bed uses combined filling of hydrophobic catalyst and hydrophilic catalyst. The system has vapour-liquid-solid co-existing phases and is a complicated mass transfer reaction process. Figure (2.8) shows the flow sheet of the LPCE-CD process. [78]

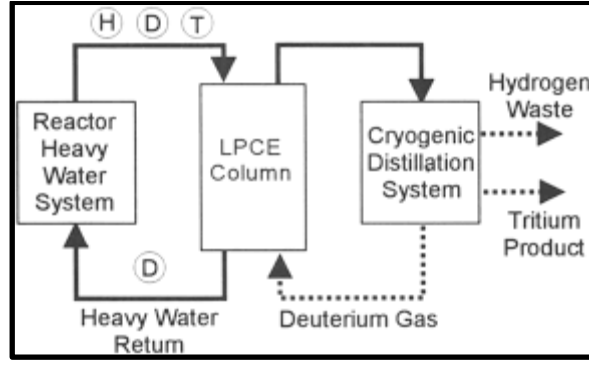


Figure (2.8) flow sheet of combined LPCE and CD process. [78]

For a system containing a small amount of deuterium, reaction (2.7) illustrates the isotopic exchange;



The relationship between separation factor and temperature can be expressed by equation (2.8) using an empirical model [20];

$$\ln Sep_{D,eq} = -0.2143 + 368.9/T + 27870/T^2 \quad (2.8)$$

For a system containing more than 99.5% deuterium, reaction (2.9) shows the isotopic exchange;



The relationship between separation factor and temperature can be expressed by equation (2.10),

$$\ln Sep_{D,eq} = -0.36 + 413.8/T + 15465/T^2 \quad (2.10)$$

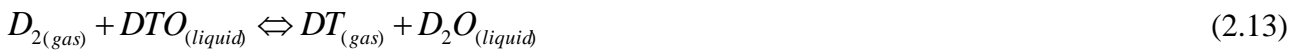
For a system containing a small amount of tritium, reaction (2.11) shows the exchange isotopic;



The relationship between separation factor and temperature can be expressed by equation (2.12);

$$\ln Sep_{T,eq} = -2.426 + 774/T + 0.292 \ln T \quad (2.12)$$

Reaction (2.13) shows the exchange reaction to remove tritium from deuterium oxide,



The relationship between separation factor and temperature can be expressed by equation (2.14),

$$\ln Sep_{D/T,eq} = -0.1474 + 191.5/T \quad (2.14)$$

Compared to VPCE, LPCE has the following advantages: high separating factor, easy setting and process, easy sealing of the system, easy operation, low reaction temperature, low energy consumption and vapour/liquid phases can be conducted counter-currently, achieving multi-stage reactions in a single reaction column.

2.2.3 CECE process

Combined electrolysis catalytic exchange (CECE) is a hydrogen isotope separating method with a very high efficiency. Electrolysis plays roles in both phase transition and hydrogen isotope separation. The heavy isotope is concentrated in the liquid phase and the light isotope is concentrated in the vapour phase. Catalytic exchange process pre-concentrates certain hydrogen isotope to achieve a higher purity of hydrogen containing deuterium oxide or concentration of tritium from tritium containing deuterium oxide. [79] Figure (2.9) shows the flow sheet of the CECE process.

The CECE process is different from VPCE and LPCE. the CECE process transits phase and pre-concentrates hydrogen isotopes at the same time. CECE has a very high separation factor and is highly investigated by scientists. [80] Table (2.10) shows how the VPCE, LPCE, and CECE differentiate in terms of the separation factor and operating conditions.

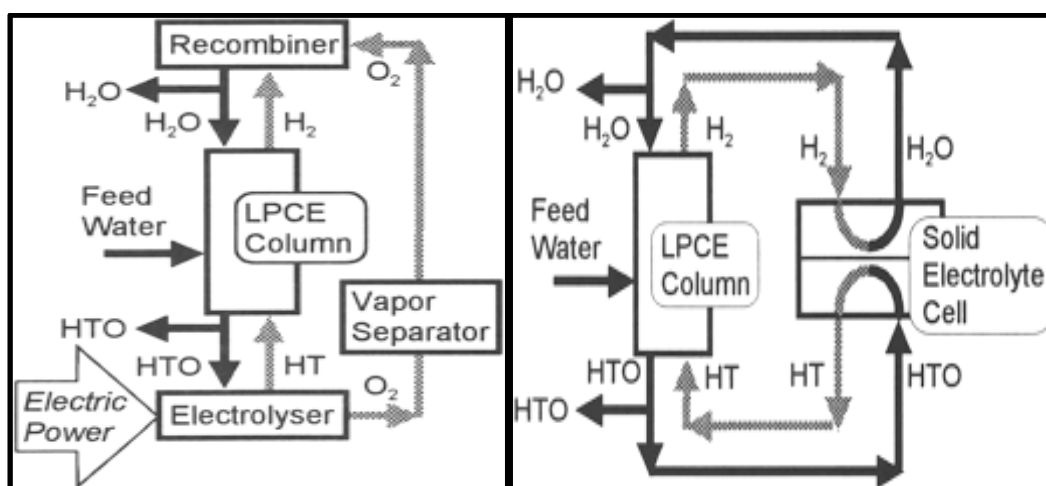


Figure (2.9) flow sheet of CECE process. [78]

Table (2.10) comparisons among hydrogen-water isotope separation technology. [20, 36 and 64]

Exchange process	Separation factor			Advantage	Disadvantage
	H-D	H-T	D-T		
VPCE	1.78 (473)		0.82 (473K)	Easy mechanism, easy preparation of catalyst	Complicated process and setting, high energy consumption
LPCE	3.8 (298K)	6.83 (298K)	1.67 (298K)	High separating factor, easy process and setting, low energy consumption	Need hydrophobic catalyst
CECE	3.87 (298K)	5.6 (298K)	1.6 (298K)	High separating factor, non-toxic, non-corrosive	Need hydrophobic catalyst

2.2.4 Tritium removal process

Heavy water reactors produce tritium 7.4×10^{13} Bq/MW every year. For example: a high-flux reactor in France, the saturation concentration of radioactive tritium heavy water up to 310×10^{12} Bq/L, the saturation concentration of radioactive CANDU-6 reactors moderator tritium is $(2.2 \sim 3.6) \times 10^{12}$ Bq/L. Radioactive tritium concentration in heavy water saturation of the heavy water research reactor experiments can also reach 1.1×10^{12} Bq/L [81]. As a result, it is necessary to remove tritium, and handle safety measures. The process to purify and recycle tritium from heavy water is similar to that of separation of deuterium from natural water. Table (2.11) lists several processes to remove tritium from different countries [82-89].

Table (2.11) comparisons among technology of removing tritium from heavy water.

Country	Unit	Process	Scale
France	Institut Laue-Langevin (ILL), Grenoble	VPCE	Experimental Facility
Canada	Ontario Hydro, Darlington	VPCE	Factory
Canada	Atomic Energy of Canada Limited (AECL)	LPCE-CD	Pilot Plant
India	Bhabha Atomic Research Centre (BARC)	VPCE	Pilot Plant
Canada	Chalk River Nuclear Laboratory (CRNL)	CECE	Demonstrated Facility
Russia	St.-Petersburg Nuclear Physics Institute (PNPI)	CECE	Industrial Scale

Currently, Mound laboratory in the US, AECL, Germany, Japan, Russia and Mol laboratory in Belgium all use CECE to investigate removal of tritium from heavy waters and light waters. Table (2.12) lists the main parameters of CECE technology in pilot plant tests [81].

Table (2.12) the main parameter of CECE technology in pilot plant test. [81]

Country	Catalyst	Reaction bed		Temperature (°C)	Processing capacity (kg/h)	Application
		height (m)	diameter (cm)			
US	Pt/C/PTFE (~Φ6 small pellet)	7.5	2.5	26~33	14.4	remove-tritium from light water
Canada	Pt/C/PTFE (~Φ6 small pellet)	8.3	6.3	22~27	36~45	remove -tritium from heavy water, recycle tritium
Belgium	Pt/C/PTFE (~Φ3x2 ring)	2.0	3.0	20~80	1.66	remove -tritium from light water
German	Pt/C/PTFE (~Φ10x2 ring)	6.2	44.0	88	180	remove-tritium from light water

Russia	Pt/SDB (~Φ0.8 small pellet)	6.9	10.0	40~80	2.5	Concentrate heavy water
Japan	Pt/SDB (~Φ1 small pellet)	12	7.0	70	30	Concentrate heavy water

2.3 Brief overview on applications, designs and preparations of hydrophobic catalysts

2.3.1 Applications of hydrophobic catalyst

Core technology of petroleum refining and petrochemical engineering is catalysis and the soul of catalytic technology is catalyst. At the beginning of 20th century, discovery of synthetic amine-iron catalyst promoted the development of coal industry. In 1950s, the discovery of polymerization catalysts led to the establishment of petrochemical industry and polymer industry.

In modern chemical industry, more than 90% chemical reactions are finished with catalyst. From the 1970s, catalysts started to be applied in energy chemical engineering and environmental chemical engineering. With the development of the nuclear industry, many countries carried out studies on H₂-H₂O liquid phase catalytic exchange to remove tritium and produce heavy water. The key of H₂-H₂O liquid phase catalytic exchange is the hydrophobic catalyst. [102]

Hydrophobic catalysts are used for reactions with water containing reagent, product, or reaction media. The mechanism is that the hydrophobic catalyst can avoid any liquid water blocking the micropore of carrier, which assists gaseous reagents such as hydrogen gas and volatile organics to enter active center of catalyst smoothly. Catalytic reactions with hydrophobic catalysts can happen at room temperature or slightly above room temperature. These reactions have low energy consumption and have high potential of application and include:

2.3.1.1 LPCE process

The LPCE is mainly used for hydrogen isotope separation. Specifically, the LPCE can be used to remove tritium from heavy water, production of heavy water and process of tritium containing waste. With hydrophobic catalysts, hydrogen gas and liquid water can conduct isotope exchange directly. [20, 36 and 64]

2.3.1.2 Hydrogen-oxygen reaction

Hydrogen-oxygen reaction to produce water can be catalysed in two ways; at high temperature and room temperature. High temperature catalysis needs hydrophilic catalyst and the reaction temperature needs to be maintained above 200 °C. Room temperature catalysis needs hydrophobic catalysts and the reaction temperature is usually below 80°C. [20, 36 and 64]

(1) De-hydrogenation reaction

Many nuclear reactions produce extra hydrogen gas, such as cooling water leakage from nuclear reactor, corrosion of metals and radical decomposition of water. Used fuel of nuclear reactors and other radical materials are usually stored in water containing containers, where hydrogen gas is generated from water decomposition by radiation. Batteries of conventional submarines generate much hydrogen gas during discharging. Oxygen produced by water electrolysis in nuclear submarines also generates much hydrogen gas. [90-91] Hydrogen-oxygen reaction can eliminate and reduce the risk of extra hydrogen gas.

During nuclear fusion reaction, tritium gas usually leaks and enters the operation environment. Hydrogen-oxygen reaction can turn tritium from vapour to liquid, which is a reliable way to control tritium pollution. [20, 36 and 64]

(2) CECE process

CECE is a combined technology of H₂-H₂O isotope exchange and electrolysis. The method is widely investigated because of its high separation factor and near room temperature reaction conditions. Hydrogen gas obtained from catalytic exchange column needs to react with oxygen by electrolysis with the water generated from the exchange column top reflux. [92] Hydrogen consumption is different by hydroxide reaction. Different from de-hydrogenation by hydrogen-oxygen reaction, CECE process produces more hydrogen gas and much heat, so the hydrophobic catalyst needs good heat resistance and thermal conductivity.

(3) Hydrogen-oxygen fuel cell

The mechanism of hydrogen-oxygen fuel cell is to generate electricity through the chemical reaction with hydrogen gas as raw material and oxygen as oxidant. The side products are heat and pure water. Hydrogen-oxygen reaction has to use hydrophobic catalyst to react at low temperature. [93]

(4) H₂O₂ (Hydrogen peroxide) preparation

H₂O₂ is usually prepared by anthracenequinone ordered oxidation-reduction reaction. The drawback of this method is the loss of quinone after oxidation. Preparation of H₂O₂ by direct oxidation of hydrogen and oxygen has been an attractive alternative. [94] The problem with this method is to find a suitable hydrophobic catalyst.

2.3.1.3 Low temperature oxidation of organic compounds

(1) Oxidation or partial oxidation of volatile organic compounds

Volatile organic compounds (VOC) are a major issue in air pollution. Hydrophobic catalysts can catalyse VOC at low temperature to finish oxidation or partial oxidation with low consumption of fuel. [95]

(2) Oxidation of organic compounds in aqueous solution

Wastewater can be oxidized with catalyst to turn the toxic compounds into carbon dioxide (CO₂) and water. Usage of hydrophobic catalyst makes it possible to carry out reaction at low temperature [96], which shows a promising potential for wastewater processing industry.

2.3.1.4 Catalytic reduction of NO_x

NO_x is a common air pollutant from factories and automobile exhausts. Similar to SO₂, NO_x is a major cause of acid rain. In order to control NO_x, hydrophobic catalyst can be used to reduce NO_x to nitrogen and water at low temperature. [97-99]

2.3.2 Design of hydrophobic catalyst

The design of hydrophobic catalysts mainly includes selection of active components and carriers and establishment of hydrophobic environment.

2.3.2.1 Active components

For LPCE, the design of catalyst should consider the adsorption ability to H₂, H₂O, and O₂. Active components of catalyst are usually made by group VIII metals like Pt.

2.3.2.2 Carrier

There are many kinds of effective carriers, such as; polytetrafluoroethylene, styrene polymer, activated carbon, aluminum oxide and ceramics. Activated carbon and aluminum oxide are hydrophilic carriers while the hydrophobic carriers are commonly made by resins or polymers, such as polytetrafluoroethylene (PTFE) and styrene-divinylbenzene copolymer (SDB). [100]

2.3.2.3 Establishment of hydrophobic environment

When hydrophobic carriers carry active components, there is no need of extra hydrophobic processing, but when hydrophilic carriers carry active components, it is necessary to process carriers before or after loading with hydrophobic polymer such as PTFE. Polymers have high molecular weight, so polymers cannot enter the micro-pore in the carriers and form a layer of hydrophobic membrane on the surface of catalyst, which is permeable to gaseous molecules but not polar liquids. [70, 100]

2.3.3 Preparation of hydrophobic catalyst

For the preparation of hydrophobic catalyst, national laboratories of many countries have hold dedicated patents, especially for the key technology. The principal different between them consist of metal and supported mixing kinds, water-proofing methods and active metal deposition methods. The main direction of studies consists of both the increase of stability and catalytic activity, the reduction of active metal content and development of interior structure of the catalytic exchange column. [101]. The main methods for preparation of the hydrophobic catalysts are [101]:

- Coating of the conventionally supported platinum catalysts (e.g. Pt/Al₂O₃; Pt/carbon) with the water repellent agents such as silicone or Teflon emulsion.
- Deposit Pt directly on hydrophobic support such polytetrafluoroethylene (PTFE) or styrene divinylbenzene copolymer (SDB).
- Mixing Pt powder with conventional catalysts powder and pelletizing the mixture.
- Bonding powdered supported Pt catalysts to a variety of column packing.

2.3.4 Overview of hydrophobic catalyst research around the world

In 1972, Stevens et al. from Chalk River nuclear laboratory published the first patent on the hydrophobic catalyst for H₂-H₂O liquid phase catalytic exchange. [102] This catalyst was made by depositing highly dispersed Pt on γ -Al₂O₃ carrier and then covering with silicone polymer membrane. Since this membrane is hydrophobic, the catalyst could keep its activity with the presence of water. Although the catalyst was not ideal in term of catalytic activity, stability and usage life, the invention was the first hydrophobic catalyst concept, which made it possible to conduct LPCE and other water containing multi-phase catalytic reaction under low temperatures.

Later, to improve the hydrophobic catalyst and H₂-H₂O exchange process, Canadian scholars Stevens, Rolston, DEN Hartog, Butler, Hammerli, Chuang, and others had done a lot of research on hydrophobic catalysts, expanded the hydrophobic catalyst applications around and promoted the development of the catalyst preparation process [103-107].

Besides Canada, Japan, Russia, Belgium, India, Romania and Korea also conducted research in the field of hydrophobic catalysts. To develop Japanese heavy water industry, many companies and research institutes had participated. Asalura et al., [108] from Energy Research Institute of Hitachi Corporation, Shimizu et al., [109] from isotope laboratory of Japan power reactor-nuclear fuel company, Isomura et al., [110] from Research Institute of Physical Chemistry, Okuno et al., [78] from Research Institute of Nuclear Energy have developed different hydrophobic catalysts and conducted extensive research on the improvement of H₂-H₂O exchange process.

Andreev et al., from Isotope Technology Department, Mendeleev Chemical Technological Institute of Moscow, investigated resin-based hydrophobic catalyst and used it for liquid phase catalytic exchange (LPCE). [111]

Bruggeman from Belgium [85] and Ionita from Romania [112] all developed their hydrophobic catalysts for H₂-H₂O liquid phase catalytic exchange.

Table (2.13) lists the preparation process of hydrophobic catalysts from some countries. The main hydrophobic catalysts prepared and tested in H₂-H₂O isotopic exchange (LPCE process) are listed in Table (2.14). [101]

Table (2.13) the preparation technology of hydrophobic catalyst [101].

Country	Process	Advantages	Disadvantages
Japan, Russia, Korea	The active components were directly immersed in the in hydrophobic polymers (e.g. styrenedivinylbenzene)	High catalytic activity, good resistance to radiation	Poor chemical stability
India	The active components were carried by hydrophilic carriers (e.g. activated carbon) and then hydrophobic material (e.g. Teflon suspension) was coated to the carriers.	High catalytic activity, Good chemical stability	Complicated preparation process
Canada, US	Active component-Pt was carried by activated carbon, and then mixed with Teflon suspension to prepare Pt/C/PTFE emulsion. The emulsion was coated to strong carriers (e.g. metal wire, ceramics)	High catalytic activity, good mechanical properties	Complicated preparation process
Germany, Belgium	Active components were carried by hydrophilic carriers (e.g. activated carbon) and then mixed with hydrophobic material (PTFE resin) mechanically. The carrier was then molded to obtain catalyst.	Good mechanical properties, simple preparation process	Low utilization of active components

Table (2.14) the main types of hydrophobic catalysts and mixed packing tested and selected for H₂-H₂O isotopic exchange [101].

Country	Tested catalyst types and metal content (wt %)	Selected catalyst type and metal content (wt %)	The stability of the catalyst
Canada	0.5% Pt / Al ₂ O ₃ 0.4% Pt / PTFE 0.1-0.4% (Pt / C)/PTFE (emulsion) Pt / zeolite Pt / SiO ₂	0.1% Pt/C/PTFE	After 170 days running the catalyst lost 13 % off initial activity
India	1% (Pt /C)/PTFE 1% (Pt/Al ₂ O ₃)/PTFE 1% (Pt/zeolite)/PTFE	1% Pt/C/ PTFE	Minimum some weeks
Japan	1.5% Pt/PTFE 0.1-2% Pt/SDBC 1.2-1.4% Pt/SDBC-(film type) Pt /FC-PTFE Pt/Al ₂ O ₃	0.5% Pt/SDBC (Kogel catalyst)	Operation of 13 years in separated bed reactor process without any regeneration
Germany	0.4% Pt/C/PTFE	0.4% Pt/C/PTFE	No information

Romania	0.1-2% Pt/C/PTFE 0.1-2% Pt/SDB 0.1-2% Pt/SDB/PS 0.5% Pt/SDB/PTFE	0.45% Pt/C/PTFE	One year half in LPCE process, without any regeneration
Belgium	over 30 different types Pt; Pd; Ni; Pt-NI; Pt-Pd; deposited on carbon or TEFLON	1% Pt/C/PTFE	5000 hours
Russia	0.8% Pt/Polysorb, Pd/Al ₂ O ₃	0.8% Pt/Polysorb	2700 h
USA	0.1% -Pt/C/PTFE (Canadian catalyst)	0.1% Pt/C/PTFE	Over 120 days

As can be noticed in Table (2.14), two main types of hydrophobic catalysts have been selected to promote isotopic exchange by LPCE process: (a) Platinum on Carbon and Teflon (Pt/C/PTFE), improvement and applied in varied ways in Germany, Belgium, Romania and Canada; (b) Platinum on styrene divinylbenzene (Pt/SDB) copolymer, improvement and applied in Japan, Russia and Korea. Although not all specifics or operation conditions for the selected catalysts are not sufficiently detailed in the papers or patents by the authors. It is apparent from this table that the best active metal for the catalyst is doubtlessly platinum and the best hydrophobic support-material or water proofing agent is polytetrafluoroethylene (PTFE). In addition, a number of laboratories have developed numerous types of mixed catalytic packing which vary in composition, design, form, physic-textural parameters and operating conditions as shown in Table (2.15) [101].

Table (2.15) the main mixed catalytic packing types manufactured and tested in LPCE process [101].

Country	The type of selected packing	Operation parameters	LPCE column sizes
Canada	1) A matrix of platinized hydrophobic carbon and PTFE deposited on corrugated screening and wound with alternate layers of hydrophilic cotton cloth.	Atmospheric pressure Temperature = 293.15 K Water flow = 19.8 kg/h Liquid/gas ratio (λ) = 0.91	Diameter = 100 mm Height = 10 m (6 m height of catalytic bed)
	2) Random packing consisting of 50% 0.37% Pt/C PTFE catalyst and 50% hydrophilic packing	Temperature = 298.15 K Hydrogen flow rate = 1 m/s Pressure = 100 KPa	
Japan	1) Separated beds of 0.5%Pt/SDBC catalyst and Mac Mahon hydrophilic packing in which the liquid water is not in contact with the catalyst.	Atmospheric pressure Temperature = 350.15 K	Diameter = 140 mm Height = 7 ~ 12 m
	2) 1.5% Pt/PTFE rings (7 x 3 x 0.8 mm) and	Atmospheric pressure, Temperature = 293.15 ~ 323.15 K	Diameter = 30 mm, height of catalytic

	mists water (particle size 5 m) in con-current with H ₂ gas.	Water flow rate = 1~ 6.10 ⁻² g/s	bed = 8 cm
Romania	Laboratory scale: Alternated beds of 0.45% Pt/C/PTFE and thermo-chemical activated metal hydrophilic packing. Experimental TRF: Compact packing; 2 % Pt/C/PTFE and ordered stainless steel packing.	Atmospheric pressure Temperature = 333.15 K Temperature = 343.15 Pressure = 1.3 ~ 1.5 bar	Diameter = 80 mm Height = 3 m Diameter = 100 m Height = 5 m
Belgium	67% etched Dixon packing and 33% Pt/C/PTFE catalyst.	Atmospheric pressure Temperature: 313.15 k Water flow rate: 2 ~ 20 mol/m ² s	Diameter = 30 mm Height = 2 m
Russia	Alternated beds of granulated platinum /Polysorb catalyst and hydrophilic metallic packing (Levin's packing)	Pressure = 0.13 ~ 4.0 MPa Temperature = 293.15 ~ 333.15 K Hydrogen velocity = 0.14 Nm ³ /m ² s	Diameter = 96 mm Height = 7.3 m
USA	Ordered packing consisting of Pt/C/PTFE dispersed on corrugated stainless steel screen mesh with a cotton fabric overlaid on the screen and wound in a cylindrical shape	Temperature = 333.15 Water flow = 0.3 ~ 0.6 l/h Gas flow = 0.5 ~ 0.7 m ³ /h Gas velocity: 0.109 m/s Liquid/gas ratio = 1	Diameter = 2.5 cm Height = 7.5 m
Korea	Industrial TRF Separated beds of CY Sulzer packing and 1 % Pt/SDBC.	Temperature = 343.15 ~ 346.15 K Pressure = 120 ~ 145 KPa	Diameter = 600 mm Height = 20 m (two columns)

Chapter 3

Methodology

3.1 Introduction

Chemical engineers use process simulation to carry out a diversity of important tasks. These tasks range from calculations of mass and energy balances of flow to prediction of the performance of process alternatives that can save millions of pounds. [113] With a view to understand the computations which are used in this study, a summarized description of the used software tools is given.

3.2 Aspen Plus Simulation part

3.2.1 Introduction

An engineer can quickly set a complicated flowchart and all the process conditions because of computers nowadays allow estimation, sizing, optimization and dynamic calculations which in the past required a large mainframes of computers. These simulations were often built by a group of specialists, including a physical property specialist. Presently, universal simulators like Aspen Plus, are easier to use and can be more powerful than a process dedicated software. [113]

Aspen Plus is a process simulation software which is used to predict the behaviour of chemical reactions, steps and relevant sizing of reactors using basic engineering relationships, such as mass and energy balances, phase and chemical equilibrium, as well as rate correlations. Throughout a well-defined unit operations and thermodynamic models, reliable thermodynamic data and realistic operating conditions are achieved. Aspen Plus uses numerical models to predict the performance of real plants. Aspen Plus can address quite complex processes, including chemical reactors, multiple-column separation systems of chemically reactive compounds. Aspen Plus can assist to design high quality plants with low plant design time and can raise profitability in existing plants by improving the size and operations of present processes. [113]

Today, a single engineer can define the basic simulation specifications, including the physical properties, in quite short time. Missing or insufficient physical properties, even so, can undermine the rigor of a model or even restrain from implementation into the simulation. That some required details are found missing is not an omission in the simulator. In addition, for most compounds, physical property parameters are not known for every thermodynamic model or for all temperature and

pressure ranges. As a result, models have been built with assumptions and procedural limits which ought to be improved. [113].

3.2.2 Thermodynamic Models for Computations

In Aspen Plus, all unit operation models need property values to generate the results. It is important to make sure that the properties of pure components and mixtures are being estimated suitably. Actually, selecting the appropriate method for estimating properties is one of the most important steps that will influence the remnant of the simulation. As a result, it is significant to carefully consider the choice of methods to estimate the various properties. [114]

The estimation methods are stored in the so-called a “Property method & options”. A property method is a set of estimation methods to calculate a number of thermodynamic and transport. The next properties are required in the Aspen Plus physical property computations; thermodynamic (fugacity, enthalpy, entropy, Gibbs free energy and molar volume) and transport (viscosity, thermal conductivity, diffusion coefficient, and surface tension). Besides, Aspen Plus saves a considerable database of interaction parameters which are used with mixing rules to estimate mixtures properties. [114] These mentioned above are called main properties, and at least one is required to do mass and energy balances in a unit operation. With regard to simulations such as those that involve both mass and energy balance calculations, a user should provide the following parameters; molecular weight (MW), critical temperature (T_C), normal boiling point (T_B), critical pressure (P_C), critical volume (V_C), acentric factor (ω), critical compressibility factor (Z_C) and extended Antoine vapour pressure equation (PLXANT). The following chart (3.1) list the overview of the property parameters are required for a rigorous estimation. [114-115]

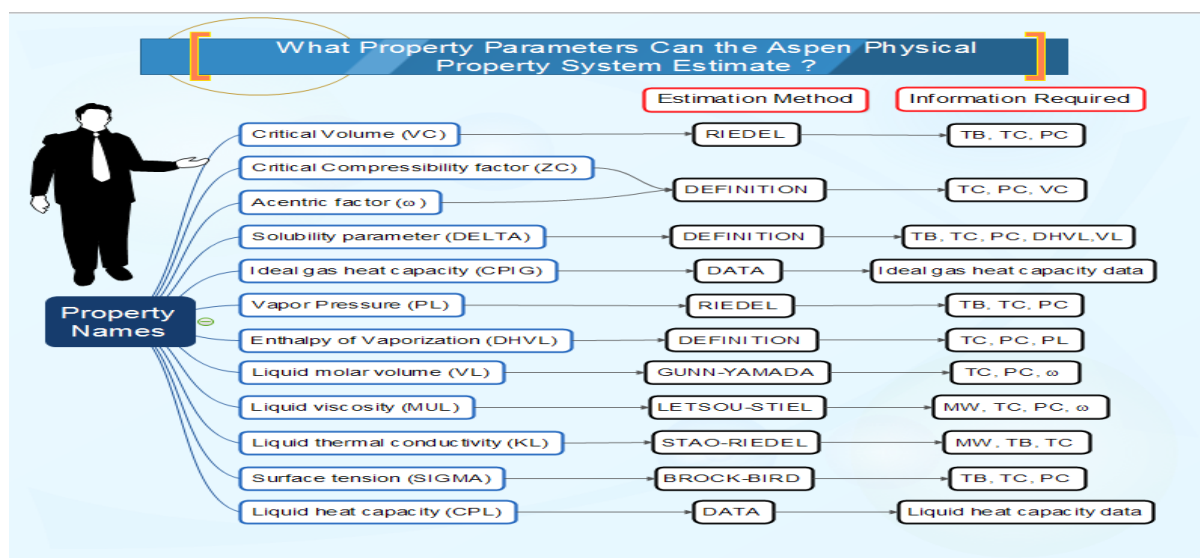


Figure (3.1) overview of the property parameters are required to estimate.

Property methods calculation options can be selected from the Properties, under the Methods folder as shown in figure (3.2). [114] After selecting a property method, there is a number of estimation equations for the different properties. In our case we selected, from the right hand side of the Property methods & models box, the Soave modified Redlich-Kwong equation of state (EOS) which is given by:

$$P = \frac{RT}{(V_m + c - b)} - \frac{a}{(V_m + c)(V_m + c + b)}$$

Where a, b, and c are component specific parameters. The values of these parameters are stored in Aspen Plus database for pure components or calculated using mixing rules for mixtures. Over all, to simulate non-databank components or have components for which parameters are missing, a general guideline by reference to the chart in figure (3.3) is followed. [114]

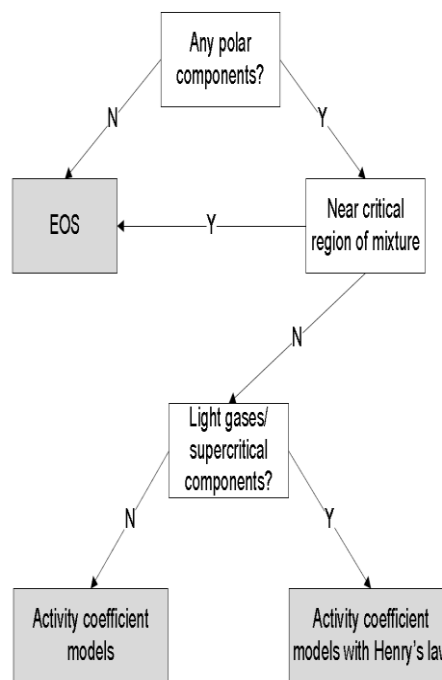
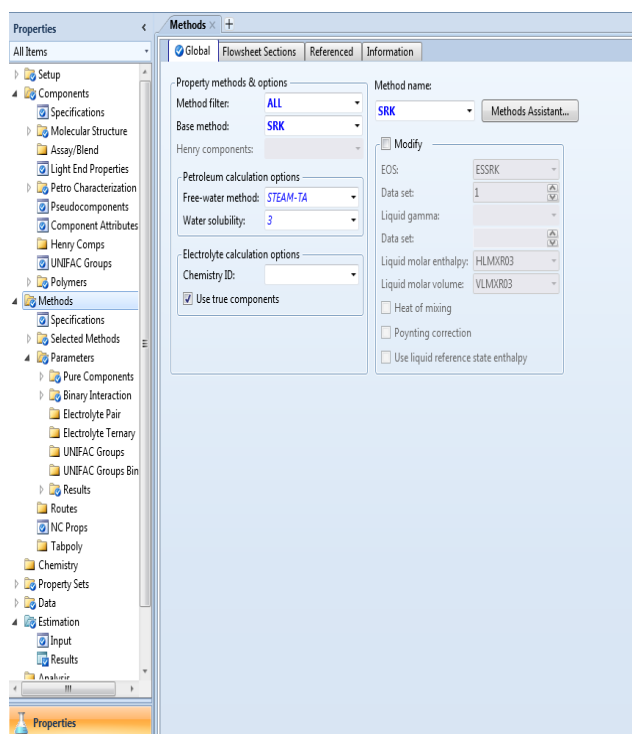


Figure (3.2) property methods available in a simulator. [114] Figure (3.3) general guideline for selecting a property method. [114]

3.2.3 Aspen plus simulation of the multicomponent columns

In an Aspen Plus simulator, thermodynamic processes are ‘go-through-in-blocks’ that may be; mixers/splitters, separators, exchangers, columns, reactors and pressure changers or even user defined models among others. These are called unit operations and they carry out specific purposes based on feed input, operating conditions and thermodynamic models. The reactants, products and energy transfer through the unit operations and interactions with the external domain happen by the material

and energy streams. The following blocks will be used for simulations in this study; equilibrium-based model (RadFrac) and rate-based model (RateFrac) columns. [114]

The RadFrac model, which assumes thermodynamic equilibrium between bulk gas and liquid phases in the column, does not require setting of the packing properties, while in the RateFrac model, the separation process was treated as a heat and mass transfer process and it is assumed that the equilibrium only exists at the gas/liquid interface. The mass and heat transfer resistances are considered according to the film theory, by directly accounting for interfacial fluxes, the film model equations and associated flow dynamics. Compared to RadFrac, RateFrac simulates the reactive stripping/scrubbing process more accurately, including the effects of the size of the column and the properties of packing internals on the process. The RateFrac also determines liquid holdup, pressure drops, interfacial area and mass transfer coefficients. These data are usually derived from laboratory experiments, which are very limited, or from relevant correlations. In this study, the RadFrac model was firstly used to estimate the key operating parameters for maximum separation efficiency of deuterium and then was extended to the RateFrac model. [116]

3.3 CFD Simulation part

3.3.1 Challenges of CFD Modelling

The 3D modelling of the flow field and transport using actual or computer-generated bed shapes has been growing through the past few years, as it offers comparable spatiotemporal resolution with 3D experimental methods, such as tomographic techniques (i.e., X-ray computer tomography, magnetic resonance imaging (MRI), laser doppler velocimetry (LDV), etc.) [117-118]. From the 3D simulation results, profiles of radial porosity, velocity, temperature, and dispersion are becoming accessible from a sufficient amount of data, while a limited number of experiments are used. Laboratory experiments on local velocity profiles were visualized for liquid flow by Giese et al.,[119] using the refractive index matching technique and by Gladden et al.,[120] using MRI, ascertaining many simulation works on fluid flow in porous media of different structures (spheres, cylinders, ordered, disordered, monodisperse and polydisperse, and so on). The approaches using 3D modelling are still, however, limited by requirements of large memories and computational power. [118] Current simulations, consisting of hundreds to over a thousand packed particles, still require large computation time, leading to simulations being carried out for small or laboratory scales. [121-122]

With the advent of fast computational machines through the past decade, computational fluid dynamic (CFD) models have gained tremendous potential in addressing a wide range of fluid flow issues with significant numerical accuracy. More strict simulation approach based on a new type of simulation procedures, e.g. the direct 3D simulation of the flow inside the actual 3D geometry of the bed

consisting of discrete individual particles instead of a pseudo-homogeneous porous medium have been developed. [117] The availability of refined mathematical models and the perpetually increasing performance of computers will make detailed 3D simulations more feasible. However, although it is possible to simulate the flow field inside a packing consisting of a few particles, it is still not possible to implement 3D simulation of a complete full-scale industrial packed bed reactor with an adequate resolution in a reasonable amount of time. [117]

In general, we should rather regard this approach as a tool for the analysis of the complicated processes on a formerly unreachable level of detail, draw consequences and establish cross-links between the detailed simulation and the traditional modelling approaches via incorporating the gained knowledge from the first to the latter. Therefore, the challenge is to analyse and to take advantage of the great deal of detailed local information obtained from 3D simulations. Main advantage from using 3D is improvement of physical insight into the local processes, which allows for a more fundamental understanding of how global characteristics are influenced. These insights may then be used for critical evaluations and convenient modifications of classical modelling approaches.

3.3.2 Derivative framework for CFD modelling

Experimental methods are the foundation of any theoretical analysis. However, these are sometimes replaced by modelling methods if experiments are limited by data size and range, field disturbance, personal safety, measurement accuracy and costs. Realizing a specific CFD and showing the results on screen will give insights into the packed bed reactor which may not be accessible by physical probes. The general method for approaching a simulation problem of fluid flow associated with mass and heat exchanges and also a chemical reaction in a packed bed reactor is outlined in the flow chart of Figure (3.4). [123]

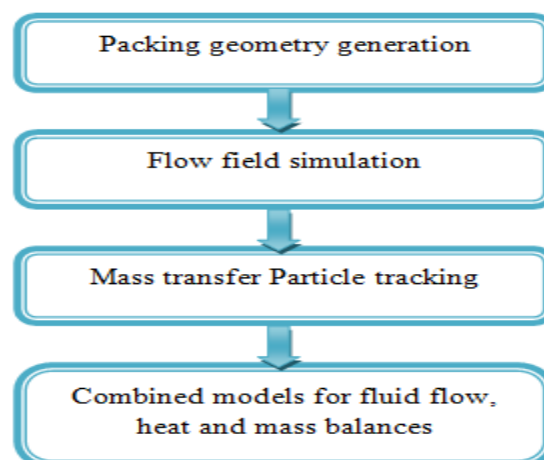


Figure (3.4) derivative framework for CFD modelling of a PBRs

First step is simulation of the packing geometry. Comparison of the relevant features of the generated random packing such as, average porosity and radial porosity profile with experimental data shows that the applied simulation approach produces realistic packing that matches experimental data well. [123]

3.3.3 Packing geometry

The most common style of a packed-bed is the random configuration of particles in a confining cylindrical tube. In many cases, the catalyst particles are spherical serving as representative model geometry. A fast and effective way to generate and discretize the 3D structure of a packed bed is an indispensable essential for a systematic investigation of local transport phenomena. Briefly, imitating the technical filling method, spherical particles are first randomly placed into a cylindrical tube as shown in Figure (3.5, a). After this raining method, the packing is compressed by rearranging the spheres with an increased probability into gravity direction (see Figure 3.5, b). [121]

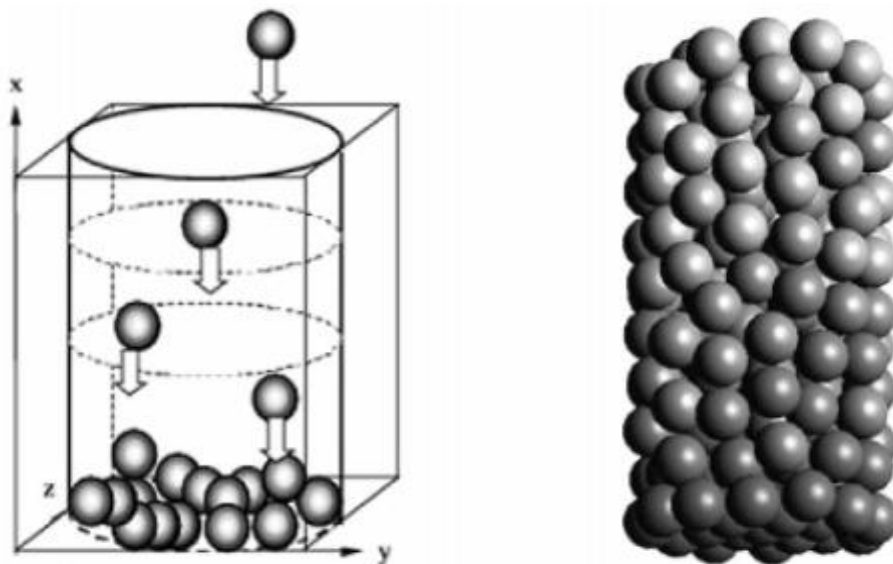


Figure. (3.5) Generation of the random packing: raining process (a) and the resulting sphere packing (b) [121]

3.3.4 Simulation Process:

To understand the simulation process and the steps involved in it. Usually, the CFD work includes three steps which can be surmised as follows:

1. **Pre Processing:** This is the first step in solving any CFD is used to definition of the geometry of the region, flow parameters and the boundary conditions which are needed for the relevant physical models to be used.
2. **Solver:** Once the problem is set-up for a defined boundary conditions, a solver (different popular commercial software's available like; FLUENT, CFX, POLYFLOW or Comsol Multiphysics®) will

be used to solve the governing equations of the phenomena (flow, species transport, chemical reaction subject to the conditions provided, etc.). There are various numerical methods used by the solver; finite difference (FD), finite element (FE) and finite volume (FV).

3. **Post-processing:** it is a final step which is used to interpret, analysis the data, and also to show the results in graphical and easy to read format by using various plots and tools. The figure (3.6) gives series of the steps that would be associated with analysis.

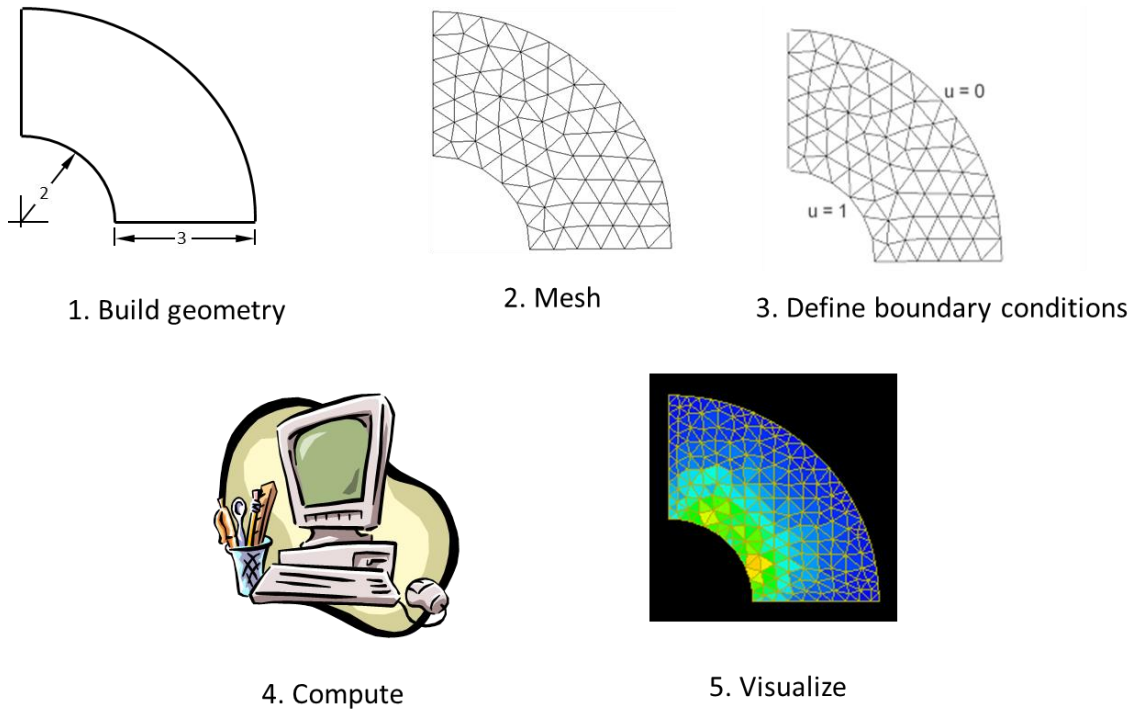


Figure (3.6) calculation procedure of analysis of CFD

3.4 Model development

CFD simulations of laminar flow, mass transfer and reaction were carried out in a series of 3D tubes, which were of different aspect ratios (ARs) (i.e.2 and 4). A granular packing was built by DEM in order to construct a densely spherical particles based packing. The numerical sample is very similar to the experimental close-packed materials and its solid fraction can be adjusted by tuning friction or cohesion properties between particles [124].

3.4.1 Packing generation by DEM.

A granular packing of densely spherical particles was built by means of DEM in order to mimic experimental samples. The 3D DEM code was written in the built-in FISH programming language of particle flow code 3D (PFC^{3D}) and was used to generate realistic packing samples of random structures with AR2 and AR4, as shown in Figure (3.7). The structure of the packing was a function of properties of both the container and the particles, including the stiffness, the density, and the

friction coefficients between the particles or the particles and the confining wall. The compaction process was carried out until the maximum unbalanced contact force between particles reached a value of the order 10^{-7} N, resulting in a packing at static equilibrium. [125]

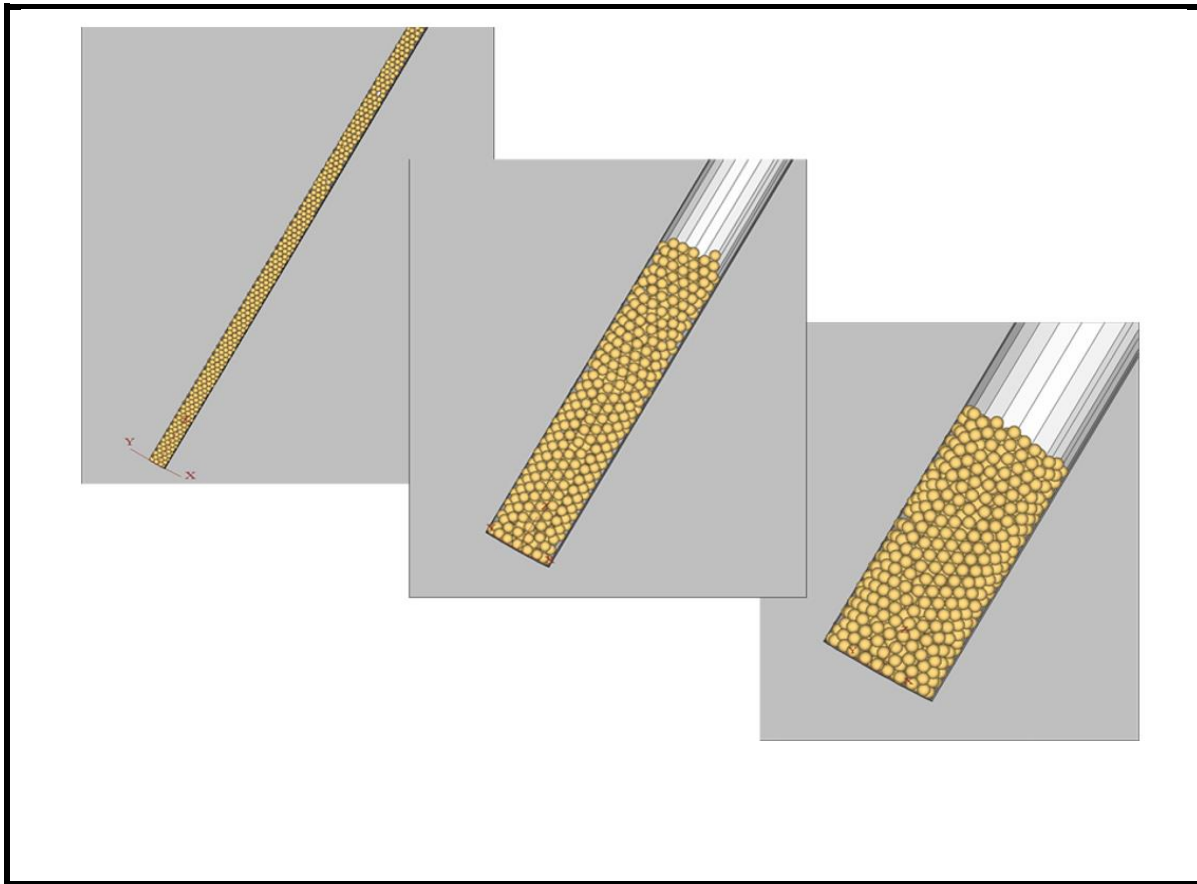


Figure (3.7) randomly generated packings from PFC^{3D}

The stiffness coefficients of the wall and the particles were varied for maximum density of the packing. The overall setting parameters are listed in Table (3.1).

Table (3.1) setting parameters of DEM based modelling

	Wall parameters	Particle parameters
Normal stiffness coefficient	10^{13} N/m	2.5×10^8 N/m
Tangential stiffness coefficient	10^{13} N/m	2.5×10^8 N/m
Friction coefficient	0.2 (-)	0.2 (-)
Density	-	3900 kg/m ³

The packing geometry, which was defined by the 3D coordinates of particle centres, was then embedded into the commercial CFD package COMSOL Multiphysics 4.4 via 3D AutoCAD (Autodesk) processing. Then COMSOL Multiphysics 4.4 with interface function LiveLinkTM for AutoCAD was able to import the packing and generate a 3D solid structure and of course was made ready to use for simulation in COMSOL, allowing a dedicated meshing to take place by using a

computer with 512 GB RAM. Figure (3.8) summarizes all building steps of a random packed bed reactor for COMSOL modelling.

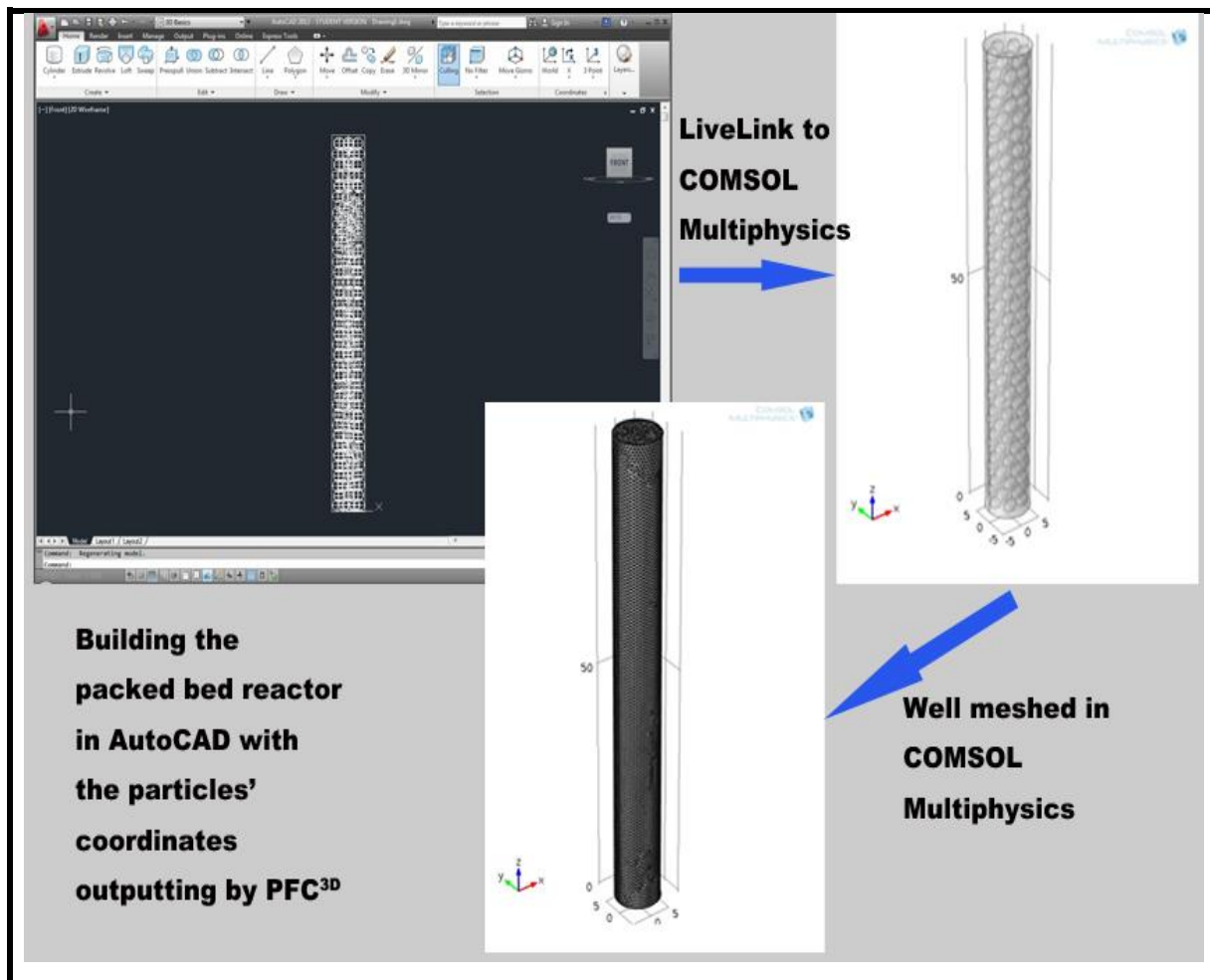


Figure (3.8) building steps of a random packed bed reactor for COMSOL modelling

The parameters of each generated packing is illustrated in Table 3.2 for AR2 and AR4 (all the models were built in unit of mm).

Table (3.2) packing parameters for different ARs.

Diameter of tube, D=10 mm			
Aspect Ratio	Diameter of particles d_p (mm)	Number of particles	Height of packings (mm)
2	5	12	25
4	2.5	118	25

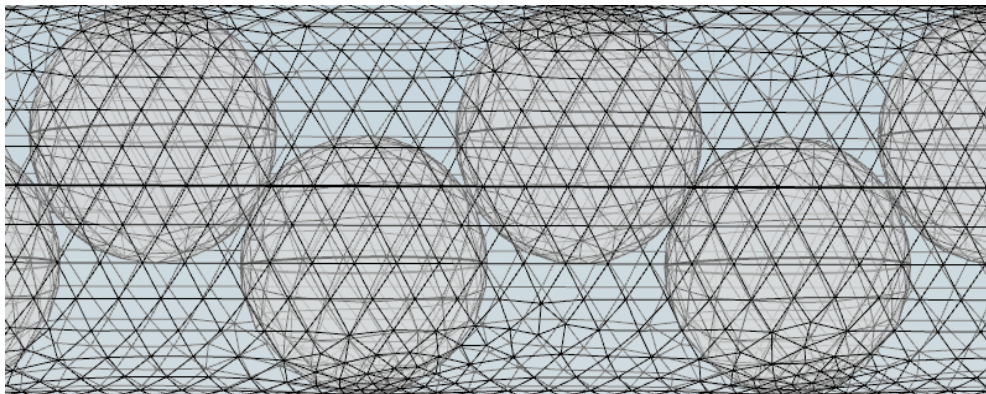
3.4.2 Meshing Modulation:

One of the important steps during the modelling and simulation of phenomena using CFD codes after build the geometry is creating a mesh for the investigated zone. A well meshed model has a significant importance in CFD simulation. It is very important prepare high-quality mesh for modelling .In fact,

the mesh plays a very crucial role for the calculation of simulations and is therefore, necessary to find an optimum balance between the number of cells and the hardware requirements for computing. Also, the balance between accuracy, computation time and file size was considered in this work. This consideration will influence the user's choice of mesh which is specified in the geometry creation step.

The automatic meshing in COMSOL Multiphysics was the first choice, but sometimes and especially for large AR, some manually settings of meshes were required. Since the smaller the mesh is, the more accurate the data is. The 'normal' meshes were set at first for every simulation model, and then the mesh size was decreased while making sure that the output data keep the same quality until the meshes reach their lowest limits and this means (mesh-independent). In this step, any further refinement of the mesh quality will not yield any further convergences in the model solution. However, although a more accurate result is obtained with a smaller mesh but this will require greatly increase computation times and much larger file size. Figure (3.9) shows different images of two different sizes of meshes.

(a)



(b)

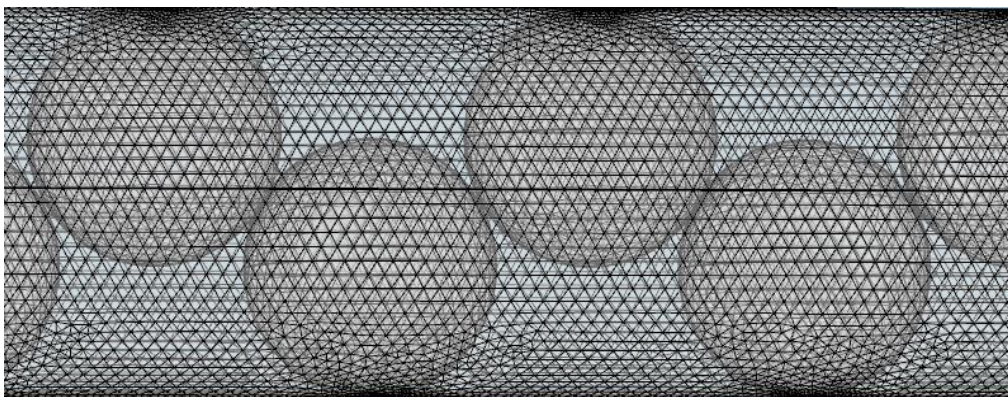


Figure (3.9) different sizes of meshes applied for a random packed bed reactor by COMSOL, (a) Large mesh and (b) small mesh.

Chapter 4

Kinetics and reactive stripping modelling of hydrogen isotopic exchange of deuterated waters

Application of commercial software packages that carry advanced modelling methods and thermodynamic databases of prediction models for hydrogen isotopic exchange process have not been reported to our knowledge but dedicated simulation tools were developed in-house [126-130]. In this chapter, we present the applicability of the rigorous rate-based model of the commercial package Aspen plus Custom Modeler (AspenTech, 2013), as a promising tool to investigate the coupling of mass and heat transport, specific features of the reaction mixture and the synergic impact on isotope separation of the catalytic exchange process in a reactive stripping column. Taking advantage of extensive experimental results in literature on hydrogen isotopic exchange by stripping/scrubbing, this chapter presents the experimental results of chemical kinetics of the gaseous catalytic exchange, the results of modelling of reactive stripping process, including effects of significant design and operating parameters on the column performance. The methodology used is as follows: (1) the gaseous phase catalytic exchange is carried out independently and in the absence of the scrubbing process using a water-proofed platinum/SDBC resin catalyst. A kinetic model for the overall rate of exchange process was developed, and relevant parameters estimated based on data generated using deuterium. (2) The missing physical properties of deuterium and tritium isotopologues for hydrogen and water are predicted by using existing thermodynamic models, geometric mean interpolation and linear correlation of the critical properties. (3) The effects of transport and reaction kinetics on the transfer of deuterium between the liquid and gaseous phases was investigated by three types of models based on coupling as shown in Fig.1: the chemical equilibrium and the bulk gas/liquid physical equilibrium (CEPE) controlled model (Figure 4.1 (a)), the chemical kinetics and the bulk gas/liquid physical equilibrium (CKPE) controlled model (Figure 4.1 (b)) and the chemical kinetics and the rate-based gas/liquid non-equilibrium (CKRN-E) controlled model (Figure 4.1 (c)). The results are discussed and validated by comparison with published data.

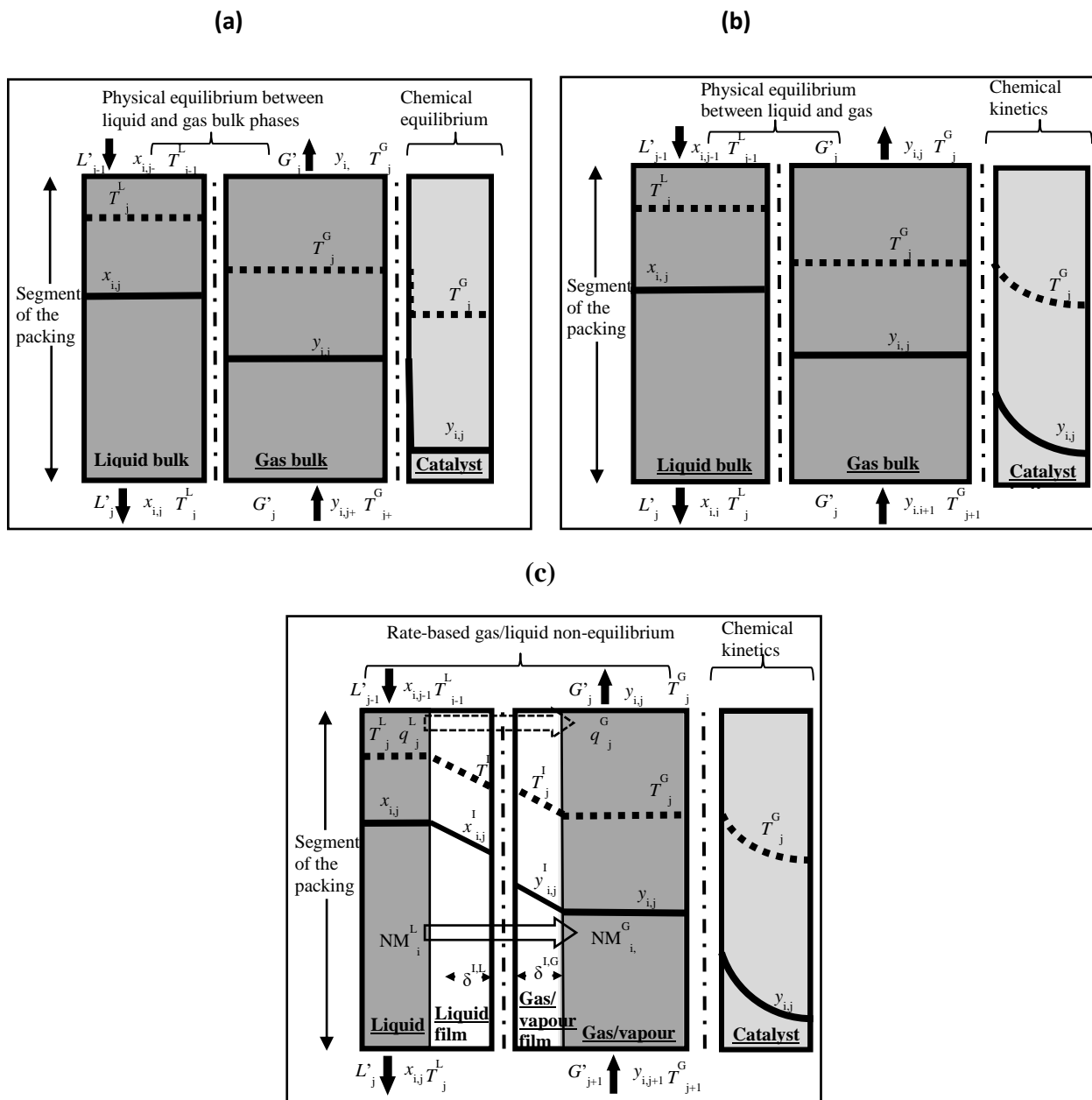


Figure (4.1) schematic representations of the three mass transfer models: (a) Chemical equilibrium and gas/liquid physical equilibrium (CEPE) model, (b) Chemical kinetics and gas/liquid physical equilibrium (CKPE) model, (c) Chemical kinetics and rate-based gas/liquid non-equilibrium (CKRN-E) model.

4.1 Introduction

Various technologies have been developed for water detritiation, including combined electrolysis and chemical exchange (CECE), liquid hydrogen distillation, cryogenic adsorption, palladium membrane diffusion, thermal diffusion, laser separation and electrochemical isotope separation [131-133]. The CECE process combines a water electrolysis unit and a liquid phase exchange (LPCE) column in which the catalytic hydrogen exchange reaction and the vapour/liquid scrubbing process occur. In the CECE, the contaminated water is first fed into an electrolyzer where it is split into gaseous oxygen

and hydrogen gases (H_2 , HD, T_2 , D_2 , HT and DT). The stream of hydrogen mixture is then directed up the LPCE column where it counter-currently interacts with water that is flowing down the catalytic packing column. As the liquid water trickles down the column, it becomes enriched in tritium while hydrogen gas becomes depleted, which causes an exchange of the HT/HD/ T_2 / D_2 /DT gas with the scrubbing water to produce concentrated tritiated and deuterated waters (i.e. HDO_L , HTO_L , DTO_L , T_2O_L or D_2O_L) while H_2 is vented to the atmosphere. This catalytic exchange process is driven by two sets of isotopic exchange reactions: (1) a gaseous catalytic exchange between the hydrogen mixture and the stripped off water vapour (H_2O_V ; reaction 4.1) and (2) the vapour-liquid concentration of the heavy water vapour isotopologues mixture HDO_V / HTO_V / DTO_V in liquid water (H_2O_L ; reaction 4.2).



This leads to the overall reaction:



The combined process, therefore, takes advantage of the wet scrubbing of HTO_V / HDO_V / DTO_V (produced by reaction 4.1) by H_2O_L (as shown in reaction 4.2) and the reactive stripping of H_2O_V (produced by reaction 4.2) by hydrogen (as shown by reaction 4.1) to promote the rates and the equilibrium boundaries of both reactions.

Most of the studies used assumptions based on average physical and transport properties while neglecting the thermal properties of isotopologues such as (heat of vaporization, enthalpy, heat capacity and conductivity) and the underlying heat transfer phenomena. The liquid stream in the LPCE column is typically operated under a trickle flow and a partial wetting of the packing, causing both mass and heat dispersions and a boundary resistance to mass transfer between liquid water and gaseous hydrogen. The methods for solving the multi-component reactive stripping/scrubbing system were mainly taken from the binary component approaches which are more or less straightforward extensions of methods that have been developed for solving conventional scrubbing/stripping column problems. Until recently, the trends of mass transfer rates of reaction (4.3), which lumps both the gaseous phase of reaction (4.1) and gas/liquid mass evaporation/condensation (reaction 4.2) in a wet scrubbing/stripping column, have been the general objectives of most modelling studies. In studies on packed columns, the effects of the flow dynamics, counter-current stream ratios, temperature, pressure and type of packing internal have been recurrently cited [66].

4.2 Materials and methods

The kinetics tests were carried out by following the kinetics of transfer of deuterium from water vapour to hydrogen gas (i.e. the reverse reaction of Eq. 4.1) as it is more affordable to feed the CECE column with deuterated liquid water than deuterated hydrogen gas. Directed by experiments illustrated in previous studies on fluid flow in the isotopic exchange process, the resistance to external mass transport was reduced by setting the minimum flowrate of H_2O_v and H_2 to $300 \text{ cm}^3/\text{min}$ and the internal mass transport inside catalyst was reduced by using particles as small as $0.08\text{--}0.10 \text{ mm}$ [133]. The kinetic tests of the catalytic exchange were carried out in a packed bed reactor as shown in Figure (4.2). The tube was made of fused quartz with a 12 mm internal diameter and filled with 0.75 g of hydrophobic Pt/SDBC resin (average pore size $110\text{--}175 \text{ \AA}$, surface area $900 \text{ m}^2 \text{ g}^{-1}$ and 2% impregnated platinum) as reported by Nic An tSoir et al. [125]. The catalytic system was initially reduced under 25 mol. % of H_2 and then purged with nitrogen. Typically, a D_2O_v composition of 12.0 mol. % (relative humidity (RH) of 60.1%) was introduced at atmospheric pressure by bubbling a mixture of H_2 (20 mol. % in N_2) at $338 \text{ cm}^3/\text{min}$ and temperature of 333 K using a controlled evaporator mixer (Bronkhorst). All pre- and post-packed tube pipes were insulated and heated to the operating temperature. Thermocouples were placed in front and behind the packed bed. In addition, a humidity sensor (Exo Terra Digital Hygrometer, accuracy 2% at $\text{RH} > 10\%$) was placed at the exit of the experimental setup. The output products were measured using a Pfeiffer Omistar GSD O mass spectrometer equipped with a quadrupole analyser.

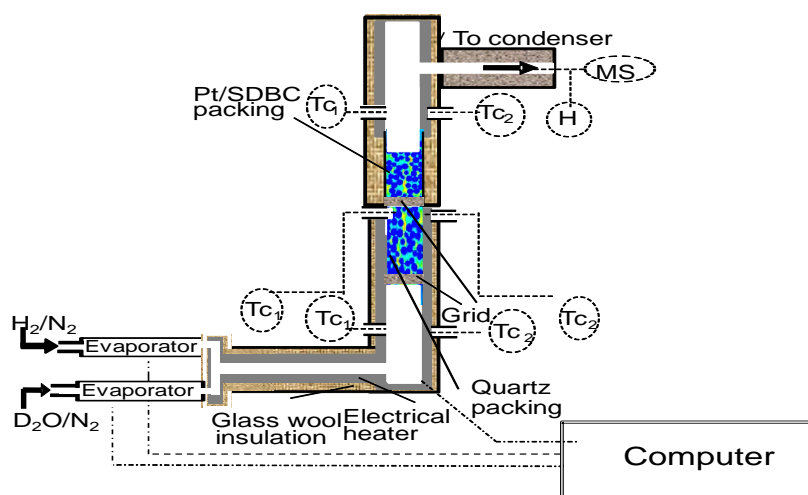


Figure (4.2) scheme of the whole tomography apparatus, packed bed tube diameter: 12 mm, thickness of both tubes: 1 mm, Evaporator (Bronkhorst) = Mass flow controller (N_2), air-actuated switching valve, distilled water bath; H: Humidity sensor; TC_1 = Thermocouples (monitoring), TC_2 : Thermocouples connected to programmable temperature controllers; MS: Mass spectrometer.

4.3 Results

4.3.1 Kinetic study and composition trends

The development of kinetic study of isotopic exchange was carried out because the rate of kinetic model impacts the driving forces of concentrations and temperature that are responsible of mass transfer rates in the reactive stripping process. Two approaches are available in the literature on the kinetics of the isotopic exchange: the first uses a lumping model where trends of gathered atomic concentration of deuterium per phase (gas or vapour) are considered while the second proceeds with trends of concentration of each species in the gaseous phase mixture regardless the nature of the phase. Herein, the later approach was considered and investigated under gaseous/vapour operations only. Most of the studies in the literature presented kinetic models that consider reaction (4.1) only. Associated side reactions and intermediate isotopologues were however demonstrated in our previous works [133-135] and were validated by a recent study by Roland et al. [136]. Kawakami et al. [137] and Sagert and Pouteau [138] studied the kinetics of the gas-phase exchange reaction (reaction 4.1) with the deuterium isotopologue over supported platinum catalysts and proposed a reaction mechanism based on the Langmuir-Hinshelwood approach. Kumar et al. [139] investigated the impact of external and internal mass transports on the intrinsic kinetics of catalytic exchange in absence of the gas/liquid scrubbing. Strong pore diffusion was observed, leading to internal effectiveness factors ranging from 13 to 20 %, while the external mass transfer resistance was negligible at the operating conditions. Roland et al. [136] reported rate coefficients for the isotope exchange reactions between deuterium gas and water vapour taking place at the surface of a stainless steel vessel. Time transients of D_2O_V and HDO_V , produced via isotope exchange reactions in the mixture of D_2 , H_2 , and D_2O_V , H_2O_V , HD and HDO_V , were measured. The results were adequately represented by the kinetic model in the form of coupled rate equations and the validity of the model was reported to be limited to low pressure environments and large gas (D_2) to water ratios. In a previous work, we used the gas phase hydrogen catalytic exchange to visualize mass, heat and fluid flow distributions in a gas-solid packed bed reactor. The packed bed was filled with Pt/SDBC. The derived transient changes of H_2O_V , HDO_V and temperature of the vapour phase hydrogen isotopic exchange reaction, between heavy water vapour (D_2O_V) and hydrogen gas, were described by 3D distributions inside and at the exit of a packed bed reactor [125, 133]. Herein, the kinetics of reaction (4.1) were investigated by observing the evolution of the six molecular species of hydrogen gas (H_2 , HD and D_2) and water vapour (H_2O_V , D_2O_V and HDO_V) involved in the overall catalytic process. Although a total of six reactions between the water vapour isotopes and hydrogen have been reported by Roland et al. [136], only three reactions were, in fact, independent as confirmed by Roland et al. [136]. Two of these reactions were determined to be under kinetic control.

Figure (4.3, a) shows transient composition profiles of the water vapour (H_2O_v), isotopologues (D_2O_v and HDO_v) and hydrogen gas isotopologues (HD and D_2) by using inlet compositions of D_2O_v and H_2 of 12.0 and 25.0 mol % in N_2 , respectively, and temperature of 333 K. The steady-state compositions were achieved after 50 minutes. It is interesting to see that compositions of HD and HDO compounds followed similar trends, while amounts of D_2 were negligible, demonstrating a similar operating mechanism for the gaseous and vapour components. The production of water, even in small amounts ($\sim 2\%$), demonstrates that its production occurs via D_2 release. Deuterium was released from D_2O_v by single and double de-deuteriations: the first into HDO_v and HD , and the second into H_2O_v and D_2 . D_2 was completely consumed while HD was partly consumed by H_2O_v into HDO_v . Therefore, the model of Roland et al. [136] is still valid but reduced to three reactions (i.e. reactions 4.4-4.6) where reactions (4.4) and (4.6) were assumed to be under kinetic control and reaction (4.5) under a quasi-equilibrium state [136].



The sum of these reactions (the reverse reaction of Eq. 1) leads to Eqs. (4.7.1) and (4.7.2).



The kinetics of gas phase catalytic exchange have been generally modelled by the surface Langmuir–Hinshelwood (LH), Eley–Rideal (ER) or linear adsorption mechanisms where the hydrogen and water molecules are dissociatively adsorbed at common or separate active sites. The high dilution of deuterium in water and hydrogen gas, along with relevant high adsorption capacities, led the rate for each surface reaction to be assumed to be first-order in coverage for each species [139]. The reaction rates, r_j , for reactions (4.4) and (4.6) are illustrated by Eqs. (4.8) and (4.9), respectively.

$$r_4 = k_{r,4} \left(\frac{y_{D_2O_v}}{y_{H_2O_v}} - \frac{1}{K_{eq_4}} \frac{y_{D_2}}{y_{H_2}} \right) \quad (4.8)$$

$$r_6 = k_{r,6} \left(\frac{y_{HD}}{y_{H_2}} - \frac{1}{K_{eq_6}} \frac{y_{HDO_v}}{y_{H_2O_v}} \right) \quad (4.9)$$

Where y_i is the mole fraction of species i in the gaseous phase (i.e. hydrogen and vapours). The quasi-equilibrium state of reaction (4.5) is taken into consideration by means of the mass action law:

$$K_{eq_5} = \frac{y_{HD}^2}{y_{D_2} y_{H_2}} \quad (4.10)$$

For the three reactions (4.4-4.6), the equilibrium constants K_i were obtained from Gibbs free-energy which was predicted in section 4.3.2.1 on property estimations and these equilibrium constants were compared with those reported by Yamanishi et al. [140], as shown in Figure (4.3, b).

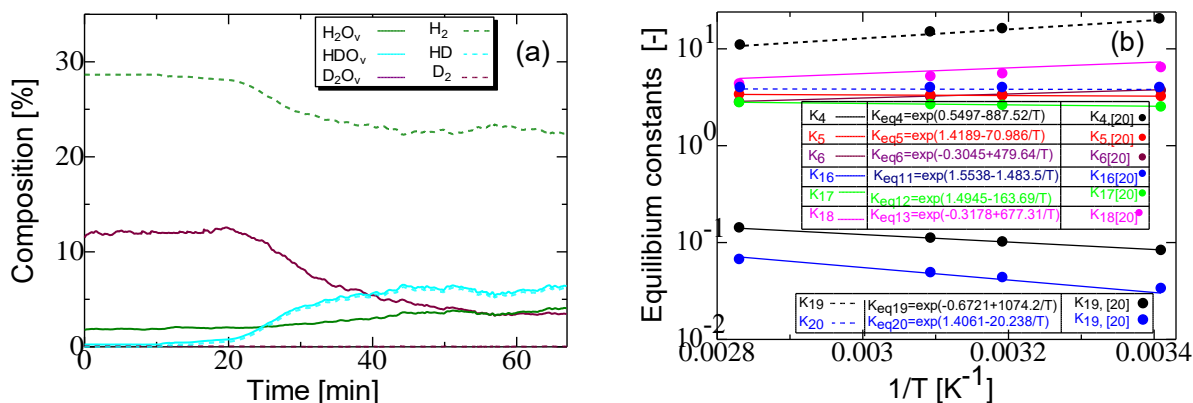


Figure (4.3) kinetic model for deuterium isotopic exchange. (a) Transient composition profiles of deuterium isotopologues in both hydrogen gas and water vapour, feed flow rate: 0.338 L/min, compositions of D_2O , H_2 and N_2 : 12, 25 and 63 %, respectively, temperature: 323 K, (b) chemical equilibrium constants with temperature.

A plug flow packed bed gas–solid model was developed where dispersions inside the packing were assumed negligible. The minimization of the sum of squares of residuals was performed by the non-linear least squares method, using the Marquardt method to adjust the kinetic parameters. The validity of the kinetic model was verified by calculating the relative deviation between experimental data and predicted results from the kinetic model. Data fittings are illustrated by Figure (4.4, e) for catalytic tests performed at various residence times and temperatures. The model clearly captures the trends in the data and fits the steady-state variations of the gas compositions well. The Arrhenius plots of the two kinetic constants $k_{r,4}$ and $k_{r,6}$ are given in Figure (4.4, e) along with the activation energies and pre-exponential factors of each reaction. The activation energy for the hydrogen exchange from the D_2O_v reaction is slightly higher than that of HDO. This explains why the formation of HDO_v/HD is so prominent, accounting for the majority of products at the end of each reaction. The activation energy values are within the range of reported values [139, 141], taking into account the weakening effect of platinum on hydrogen interactions due to the polarization by the SDBC resin. Figures (4.4, c) and (4.4, d) confirm that HD and H_2O_v , as intermediate component in the reaction mechanism (Eqs. 4.4-4.6), present the highest compositions of HD at low conversions of D_2O_v while HDO_v production increased constantly at high conversions. This result clearly anticipates the potential merit of using a gas/liquid counter-current flow of D_2O_L and H_2 in an LPCE column, in which D_2O_v is maximized along the column, and thus would maintain a high production of HD and low conversion

to condensable components (H_2O_v and HDO_v) as illustrated in the following section on the reactive stripping process by the equilibrium and non-equilibrium controlled models.

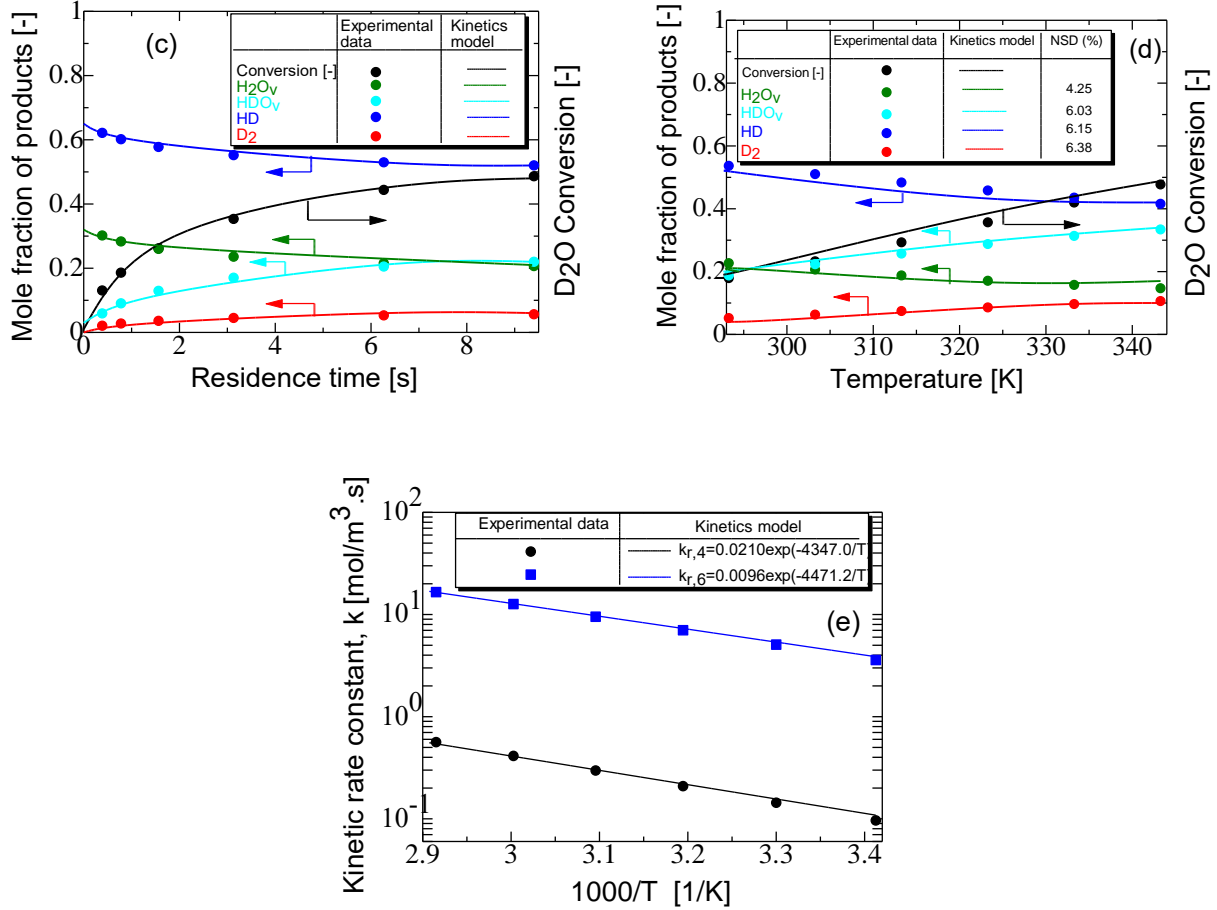


Figure (4.4) kinetic model for deuterium isotopic exchange. (c) Steady-state composition profiles of products of deuterium isotopologues with residence time in both hydrogen gas and water vapour, compositions of D_2O , H_2 and N_2 : 12, 25 and 63 %, respectively, temperature: 323 K, (d) Steady-state composition profiles of products of deuterium isotopologues with temperature in both hydrogen gas and water vapour, Feed flow rate: 0.338 L/min, compositions of D_2O , H_2 and N_2 : 12, 25 and 63 %, respectively, temperature: 323 K, (e) Arrhenius plots of chemical rate constants.

4.3.2 Effect of mass transfer rate on the separation efficiency of reactive stripping process

The application of the kinetic model of section 4.3.1 to the reactive stripping of deuterium from liquid water was validated by comparison with experimental data from literature. The reactive stripping extends the vapour/liquid phase exchange (Eq. 4.2) of D_2O_L to the products HDO_v and H_2O_v of the gaseous catalytic exchange (Eqs. 4.7.1. and 4.7.2, respectively)



Summation of Eqs. 4.7.1, 4.7.2, 4.11.1 and 4.11.2 leads to the overall Eqs. 4.12.1 and 4.12.2.



The overall exchange rate constant of isotopic exchange between hydrogen gas and liquid water (Eqs. 4.12.1 and 4.12.2) was assessed by averaging the overall exchange rate of deuterium composition along the column height and illustrated by Eqs. 4.14.1 and 4.14.2. [142]

At a given height of a column of height Z , the exchange rate is expressed by Eq. 4.13.

$$Gdy = K_{g,overall} (y_{D,eq} - y_D) dZ \quad (4.13)$$

Which after integration throughout the entire column leads to Eq. 4.14.1.

$$K_{g,overall} = \frac{G'}{h_F} \frac{(y_{D,out} - y_{D,in})}{(y_{D,eq} - y_D)_{out} - (y_{D,eq} - y_D)_{in}} \ln \frac{(y_{D,eq} - y_D)_{out}}{(y_{D,eq} - y_D)_{in}} \quad (4.14.1)$$

$$y_D' = \frac{y_{D_2} + \frac{1}{2} y_{HD}}{y_{H_2}} \quad (4.14.2)$$

Where y_D' represent the atom fraction of deuterium in hydrogen gas, h_F is the height of the full packing, $K_{g,overall}$ is the overall exchange rate constant based on the gas phase and y_{eq} is the composition of deuterium that would be in equilibrium with the deuterium composition of the water at that same height in the column.

A universal equilibrium model for a maximum separation efficiency and a non-equilibrium model based on a description of a single stage section representing a packing segment of a column were developed. Unlike the universal equilibrium model, the non-equilibrium model required the gas and liquid phases to be balanced separately. Both the equilibrium-based model and the rate-based model, denoted RadFrac and RateFrac modules, respectively, in the Aspen Plus process software, were used to simulate the hydrogen exchange process. The equilibrium model, which assumes thermodynamic equilibrium between bulk gas and liquid phases of reaction (4.2) in the column, did not require setting of the packing properties, while in the rate-based model, the separation process was treated as a heat and mass transfer process and was assumed that the equilibrium only exists at the gas/liquid interface. The mass- and heat-transfer resistances were considered according to the film theory, by directly accounting for interfacial fluxes, the film model equations and associated flow dynamics. Both models were combined with the relevant reactions and missing physical properties of single components as well as relevant mixtures. The equilibrium model was used to estimate the key operating parameters for maximum separation efficiency of deuterium and then the model was extended to the rate-based model.

4.3.2.1 Estimation of missing physical properties

Accurate values of thermo-physical properties are needed for the equilibrium and rate-based simulations. Despite their usefulness, measurements of the thermodynamic and transport properties of hydrogen isotopes in both hydrogen (HD , D_2 , HT , DT and T_2) and hydrogen oxide (HDO , D_2O , HDO , DTO and T_2O) forms, and the effects of operating pressure and temperature on these parameters, are scarce in open literature, particularly for tritium isotopologues. [143] In the last 25 years, few thermodynamic property studies have been conducted on deuterium. An equation of state for tritium is not available in the literature and experimental measurements on tritium are rather rare. Souers [1] published a review on the properties of cryogenic hydrogen and the estimated physical and chemical properties of deuterium and tritium. Since this last analysis, there have been great advances in computer technologies and equation fitting techniques, implying a need for an updated property review. [143] In addition, available database on properties of aforementioned components is limited and conspicuously incomplete in commercial process simulation packages. This is important for modelling the hydrogen isotopic exchange since unlike the isotopes of other elements, the relatively large mass differences between H, D, and T cause appreciable differences in the properties of their compounds, and even sometimes in the properties of relevant allotropes such as the ortho- and para-forms of hydrogen gas. [143]

Herein, it is not intended to investigate in detail the properties of deuterium and tritium, but instead we aimed to contribute to an open database for these isotopes (D, T), in both hydrogen gas and water forms, to be used for the isotopic exchange process. This database, as illustrated in Table (4.1), was added to the property set package of Aspen Plus by using experimental data available in the literature or predicted by using (1) existing thermodynamic models, (2) interpolation using the geometric mean of well-known data of analogous isotopologues [145] and (3) linear correlation of the critical properties (critical pressure, critical temperature and critical volume), Pitzer's acentric factor and the corresponding-states principle. [36, 146-150] The results are illustrated in Tables (4.1) and (4.2) and Figures (4.5, a-e). The property models for each component are defined in Tables (4.1) and (4.2). Figures (4.5, a) and (4.5, b) which show trends with temperatures of vapour pressure and enthalpy predicted by the Soave-Redlich-Kwong (SRK) equation of state of both water and hydrogen forms of deuterium isotopologues (D_2 , HD , $\text{D}_2\text{O}_\text{L}$ and HDO_L) and tritium isotopologues (T_2 , HT , $\text{T}_2\text{O}_\text{L}$ and HDO_L). These results are in agreement with those given in the steam and hydrogen gas tables by Richardson et al. [143] Other thermodynamic and transport properties of deuterium isotopologues, and their changes with temperature, were fitted to well-known literature models: dynamic viscosity using the Design Institute for Physical Properties (DIPPR) model and validated by data reported by Hill from Richardson et al. [143]; thermal conductivity using DIPPR model and validated by data

from Richardson et al.[143] and Matsunaga [151]; surface tension using Crabtree and Siman-Tov's model; and binary diffusivity using Wilke-Chang's model for liquid isotopologues and Chapman-Enskog-Wilke-Lee's model for gas isotopologues and validated using Kumar's results [139]. The trends of these physical properties are presented in Figure (4.5, a-d).

As previously discussed, the thermodynamic and transport properties of tritium isotopologues are limited in the open literature as they are experimentally difficult, expensive and tedious to evaluate. We proceeded therefore with Friedman's model which validates a linear trend of physical properties of analogous isotopologues along with the root of molecular weights [152]. The results achieved on deuterium isotopologues were therefore extended to each three isotopologues in hydrogen gas and water forms of tritium by using the plot of physical property versus the reciprocal of the square root of their molecular weights. Figures (4.5, e₁) and (4.5, e₂) shows profiles of critical properties, boiling point and molar volumes for both H₂O and H₂ isotopologues, respectively, and clearly demonstrate averaged standard deviations of 2.5 and 2.1%, respectively and a good fit with the Friedman model. Extension to tritium-based isotopologues for vapour pressure, molar volumes, enthalpy, Gibbs free energy, viscosity and surface tension were added to Figures (4.5, a-d). It is interesting to note the formation of non-ideal vapour isotopologue mixtures and negative deviation from Raoult's model, particularly at low concentrations of T₂O_v and D₂O_v and low temperatures (Figure (4.5, a)). The presence of the intermediates HTO_v and HDO_v tends to promote non-ideality. The impact of hydrogen bonds at low temperatures along with the vapour pressure of HDO and HTO_v of values which are different from the arithmetic mean of H₂O_v/D₂O_v and H₂O_v/T₂O_v pairs, respectively, might be responsible for such positive deviations. [152]

Table (4.1) physical properties of tritium and deuterium isotopologues in water and hydrogen*

Property**	H ₂ O	D ₂ O	HDO	H ₂	D ₂	HD	T ₂ O	HTO	DTO	T ₂	HT	DT
<i>API</i>	10.000	-3.730	3.135	340.000	340.000	340.000	-12.929	0.801	-8.398	340.000	340.000	340.000
<i>DGFORM</i>	-228.572	-234.585	-55.715	0.000	0.000	-0.350	-56.618	-56.030	-56.456	0.000	-0.280	-0.396
<i>DHFORM</i>	-241.818	-249.199	-58.639	0.000	0.000	0.071	-60.701	-58.938	-60.120	0.000	0.160	0.020
<i>DHVLB</i>	40.694	41.447	40.677	0.214	1.192	1.044	41.952	41.199	41.704	0.332	1.094	1.292
<i>FREEZEPT</i>	273.150	276.960	1.905	13.950	18.732	-256.550	6.363	2.553	5.105	-251.214	-255.996	-252.792
<i>MUP</i>	1.850	1.780	1.815	0.000	0.000	0.000	1.733	1.803	1.756	0.000	0.000	0.000
<i>MW</i>	18.015	20.027	19.021	2.016	4.028	3.022	22.029	20.022	21.028	6.030	4.023	5.029
<i>OMEGA</i>	0.345	0.366	0.355	-0.216	-0.145	-0.180	0.380	0.359	0.373	-0.097	-0.168	-0.121
<i>P_c</i>	22064.000	21671.000	21867.500	1313.000	1661.700	1484.000	21407.690	21800.690	21537.380	1895.329	1546.629	1780.258
<i>RKTZRA</i>	0.243	0.237	0.240	0.321	0.315	0.318	0.232	0.239	0.235	0.311	0.317	0.313
<i>SG</i>	1.000	1.107	1.054	0.300	0.300	0.300	1.179	1.072	1.144	0.300	0.300	0.300
<i>T_B</i>	373.15	374.57	374	20.39	23.654	22.29	375.671	374.251	375.203	25.991	22.727	24.914
<i>T_C</i>	647.096	643.89	645.644	33.19	38.35	36.06	641.892	645.098	642.95	41.957	36.797	40.254
<i>V_B</i>	18.831	18.853	18.842	28.568	25.114	26.841	18.868	18.846	18.861	22.800	26.254	23.940
<i>V_C</i>	55.947	56.300	56.124	64.147	60.263	62.000	56.536	56.184	56.420	57.661	61.545	58.942
<i>VLSTD</i>	18.050	18.130	18.045	53.558	53.558	53.558	18.184	18.104	18.157	53.558	53.558	53.558
<i>Z_C</i>	0.229	0.228	0.229	0.305	0.314	0.312	0.227	0.228	0.228	0.320	0.311	0.317

*: Property values in bold characters were added to Aspen plus data base.

** : Nomenclature of properties: *API* : Standard API gravity [-], *DGFORM*: Free energy of formation at 298 K [kJ/mol], *DHFORM*: Enthalpy of formation at 298 K [kJ/mol], *DHVLB*: Enthalpy of vaporisation at the boiling point [kJ/mol], *FREEZEPT*: Freeze point [K], *MUP*: Dipole moment [Debye], *MW*: Molecular weight [g/mol], *OMEGA*: Pitzer acentric factor [-], *P_c* [kPa], *RKTZRA*: Parameter for the Rackett liquid molar volume model [-], *SG*: Standard specific gravity at 298 K, *T_B*: Boiling temperature [K], *T_C*: Critical temperature [K], *V_B*: Liquid molar volume at boiling point point [cm³/mol], *V_C*: Critical volume [cm³/mol], *VLSTD*: Standard liquid molar volume at 298 K [cm³/mol], *Z_C*: Critical compressibility factor[-]

Property	HDO	HD	H ₂ O	D ₂ O	H ₂	D ₂	T ₂ O	HTO	DTO	T ₂	HT	DT
CPIGDP (Ideal gas heat capacity) $C_p^{i,g} [cal/mol.K] = C_1 + C_2 \left(\frac{C_3/T[{}^0C]}{\sinh(C_3/T[{}^0C])} \right)^2 + C_4 T[{}^0C]^2 + C_4 \left(\frac{C_5/T[{}^0C]}{\sinh(C_5/T[{}^0C])} \right)^2$ for $C_6 \leq T[{}^0C] \leq C_7$												
C ₁	33.48	27.621	33.48	33.48	27.621	30.132	33.8985	33.48	33.8985	32.2245	32.2245	31.3875
C ₂	27.2025	9.6255	26.784	27.621	9.6255	9.6255	28.458	27.621	28.0395	10.044	10.044	9.6255
C ₃	10763.4	10320.21	10924.94	10449.95	10320.21	10525.28	10131.89	10606.88	10288.4	10662.54	10662.54	10595.2
C ₄	11.2995	3.7665	8.7885	15.903	3.7665	-2.9295	20.5065	13.8105	18.414	-7.1145	-7.1145	-5.022
C ₅	1160.3	567.6	1169.0	1143.5	567.6	368.0	1126.4	1151.9	1134.8	234.3	234.3	300.1
C ₆	-173.2	-23.2	-173.2	-173.2	-23.2	-173.2	-173.2	-173.2	-173.2	-273.7	-273.7	-224.2
C ₇	3267.1	1226.9	2000.0	5726.9	1226.9	1226.9	8223.8	4497.0	6994.0	1226.9	1226.9	1226.9
DHVLDP (Heat of vaporisation) $\Delta H_{vap} [cal/mol.K] = C_1(1 - T_r)^{C_2 + C_3 T[{}^0C] + C_4 T[{}^0C]^2 + C_5 T[{}^0C]^3}$ for $C_6 \leq T[{}^0C] \leq C_7$, $T_r = \frac{T[{}^0C]}{T_c[{}^0C]}$												
C ₁	59.5107	1.0881	56.5812	65.16045	1.0044	1.1718	70.8939	62.31465	68.0481	1.29735	1.12995	1.21365
C ₂	0.74	0.36	0.61	0.98	0.70	-0.31	1.22	0.86	1.10	-0.99	0.02	-0.65
C ₃	-0.79	-1.10	-0.63	-1.11	-1.82	0.28	-1.44	-0.95	-1.28	1.69	-0.41	1.00
C ₄	0.45	1.07	0.40	0.56	1.45	0.35	0.67	0.51	0.62	-0.39	0.71	-0.03
C ₅	0.00	0.00	0.00	0.00	0.00	0.00	0.00	0.00	0.00	0.00	0.00	0.00
C ₆	1.31	-257.58	0.01	3.82	-259.20	-254.42	6.37	2.56	5.12	-251.22	-256.00	-252.80
C ₇	372.86	-238.21	373.95	370.74	-239.96	-234.80	368.59	371.80	369.65	-231.34	-236.50	-233.05
DNLDP (DIPPR liquid density) $\rho_p^l [mol/cm^3] = C_1 + C_2 \tau^{0.35} + C_3 \tau^{0.66} + C_4 \tau + C_5 \tau^{1.33}$ for $C_6 \leq T[{}^0C] \leq C_7$, $\tau = 1 - \frac{T[{}^0C]}{T_c[{}^0C]}$												
C ₁	0.4844	272.6596	0.4877	0.4781	412.5610	1.0868	0.4716	0.4812	0.4748	1.0868	136.8732	1.0868
C ₂	0.0014	4.2176	0.0015	0.0011	6.3903	0.0000	0.0009	0.0012	0.0010	0.0000	2.1088	0.0000
C ₃	0.0000	0.0243	0.0000	0.0000	0.0368	0.0000	0.0000	0.0000	0.0000	0.0000	0.0122	0.0000
C ₄	0.0000	0.0001	0.0000	0.0000	0.0001	0.0000	0.0000	0.0000	0.0000	0.0000	0.0000	0.0000
C ₅	0.0000	0.0000	0.0000	0.0000	0.0000	0.0000	0.0000	0.0000	0.0000	0.0000	0.0000	0.0000
C ₆	-0.2518	257.0070	0.0100	-0.7600	259.2000	252.7500	-1.2759	-0.5059	-1.0218	252.7500	254.8785	252.7500
C ₇	358.37	-245.754	360	355.2	-242.15	-252.75	351.984	356.784	353.568	-252.75	-249.252	-252.75
KLDIP (DIPPR liquid thermal conductivity) $\lambda^l [kcal/hr.m.K] = C_1 + C_2 T[{}^0C] + C_3 T[{}^0C]^2 + C_4 T[{}^0C]^3 + C_5 T[{}^0C]^4$ for $C_6 \leq T[{}^0C] \leq C_7$												
C ₁	0.58125	317.0138	0.58125	0.58125	479.6475	1.27875	0.58125	0.58125	0.58125	1.27875	159.1463	1.27875
C ₂	0.0	4.8825	0	0	7.44	0.0	0.0	0.0	0.0	0.0	2.44125	0
C ₃	0.0	0.0	0.0	0.0	0.0	0.0	0.0	0.0	0.0	0.0	0.0	0.0
C ₄	0.0	0.0	0.0	0.0	0.0	0.0	0.0	0.0	0.0	0.0	0.0	0.0
C ₅	0.0	0.0	0.0	0.0	0.0	0.0	0.0	0.0	0.0	0.0	0.0	0.0
C ₆	-0.3	-257.0	0.0	-0.8	-259.2	-252.8	-1.3	-0.5	-1.0	-252.8	-254.9	-252.8
C ₇	358.4	-245.8	360.0	355.2	-242.2	-252.8	352.0	356.8	353.6	-252.8	-249.3	-252.8

Table (4.2) properties of tritium and deuterium isotopologues in water and hydrogen with temperature.

Property	HDO	HD	H ₂ O	D ₂ O	H ₂	D ₂	T ₂ O	HTO	DTO	T ₂	HT	DT
KVDIP (DIPPR vapour thermal conductivity) $\lambda^s [J / s.m.K] = C_1 T[{}^{\circ}C]^{C_2} / \left(1 + C_3 / T[{}^{\circ}C] + C_4 / T[{}^{\circ}C]^2 \right)$ for $C_6 \leq T[{}^{\circ}C] \leq C_7$												
C ₁	5.73E-06	0.001.85	0.0000062	0.0000048	0.0026	0.00028	0.0000039	0.0000052	0.0000043	-0.0013	0.0010	-5.2E-04
C ₂	1.412464	0.827548	1.3973	1.4419	0.7452	0.9874	1.471782	1.427182	1.457064	1.149674	0.90747	1.069748
C ₃	0	-60.2534	0	0	12	-200.51	0	0	0	-342.892	-130.382	272.7634
C ₄	0	7414.38	0	0	0	21807	0	0	0	36417.69	14610.7	29221.38
C ₅	0	0	0	0	0	0	0	0	0	0	0	0
C ₆	1.2952	-179.359	0.01	3.79	-251.15	-40	6.3226	2.5426	5.0752	101.4705	-109.68	31.791
C ₇	775.129	1292.85	800	726.85	1326.85	1226.85	677.8395	750.9895	701.979	1159.85	1259.85	1192.85
MULDIP (DIPPR liquid viscosity) $\ln \eta^l [cP] = C_1 + C_2 / T[{}^{\circ}C] + C_3 \ln T[{}^{\circ}C] + C_4 T[{}^{\circ}C]^2 + C_5 / T[{}^{\circ}C]^2$ for $C_6 \leq T[{}^{\circ}C] \leq C_7$												
C ₁	-140.0	-3.1	-45.9	-140.2	-4.8	0.0	-140.0	-140.0	-140.0	3.2	-1.6	1.6
C ₂	7440.0	16.3	3703.6	7435.6	24.7	0.0	7440.0	7440.0	7440.0	-16.5	8.2	-8.4
C ₃	20.5	-0.2	5.9	20.5	-0.3	0.0	20.5	20.5	20.5	0.2	-0.1	0.1
C ₄	0.0	0.0	0.0	0.0	0.0	0.0	0.0	0.0	0.0	0.0	0.0	0.0
C ₅	2.0	6.6	10.0	2.0	10.0	0.0	2.0	2.0	2.0	10.0	10.0	10.0
C ₆	3.8	-259.2	0.0	3.8	-259.2	-252.8	3.8	3.8	3.8	-259.2	-259.2	-259.2
C ₇	365.0	-240.2	373.0	365.0	-240.2	-252.8	365.0	365.0	365.0	-240.2	-240.2	-240.2
MUVDIP (DIPPR vapour viscosity) $\eta^g [cP] = C_1 T[{}^{\circ}C]^{C_2} / \left(1 + C_3 / T[{}^{\circ}C] + C_4 / T[{}^{\circ}C]^2 \right)$ for $C_6 \leq T[{}^{\circ}C] \leq C_7$												
C ₁	0.0000175	0.000204	0.0000171	0.0000182	0.00018	0.00025	0.0000189	0.0000178	0.0000185	0.00025	0.00023	0.00025
C ₂	1.113036	0.685952	1.1146	1.11	0.685	0.6878	1.106918	1.111518	1.108436	0.6878	0.68688	0.6878
C ₃	0	-0.18669	0	0	-0.59	0.5962	0	0	0	0.5962	0.20475	0.5962
C ₄	0	92.4	0	0	140	0	0	0	0	0	46.2	0
C ₅	0	0	0	0	0	0	0	0	0	0	0	0
C ₆	1.2952	-243.543	0.01	3.79	-259.2	-213.15	6.3226	2.5426	5.0752	-213.15	-228.347	-213.15
C ₇	775.129	1870.05	800	726.85	2726.85	206.85	677.8395	750.9895	701.979	206.85	1038.45	206.85
PLXANT (Extended Antoine equation for vapour pressure) $\ln p^l [bar] = C_1 + \frac{C_2}{T[{}^{\circ}C] + C_3} + C_4 T[{}^{\circ}C] + C_5 \ln T[{}^{\circ}C] + C_6 T[{}^{\circ}C]^{C_7}$ for $C_8 \leq T[{}^{\circ}C] \leq C_9$												
C ₁	64	6	62	67	6	7	70	65	69	7	6	7
C ₂	-7375	-138	-7258	-7601	-113	-159	-7831	-7488	-7718	-185	-148	-171
C ₃	0	0	0	0	0	0	0	0	0	0	0	0
C ₄	0	0	0	0	0	0	0	0	0	0	0	0
C ₅	-8	0	-7	-8	0	0	-8	-8	-8	0	0	0
C ₆	0	0	0	0	0	0	0	0	0	0	0	0
C ₇	2	2	2	2	2	2	2	2	2	2	2	2
C ₈	-5	-269	0	-15	-269	-269	-26	-10	-21	-269	-269	-269
C ₉	373	-235	374	371	-235	-235	369	372	370	-235	-235	-235

Table (4.2) properties of tritium and deuterium isotopologues in water and hydrogen with temperature

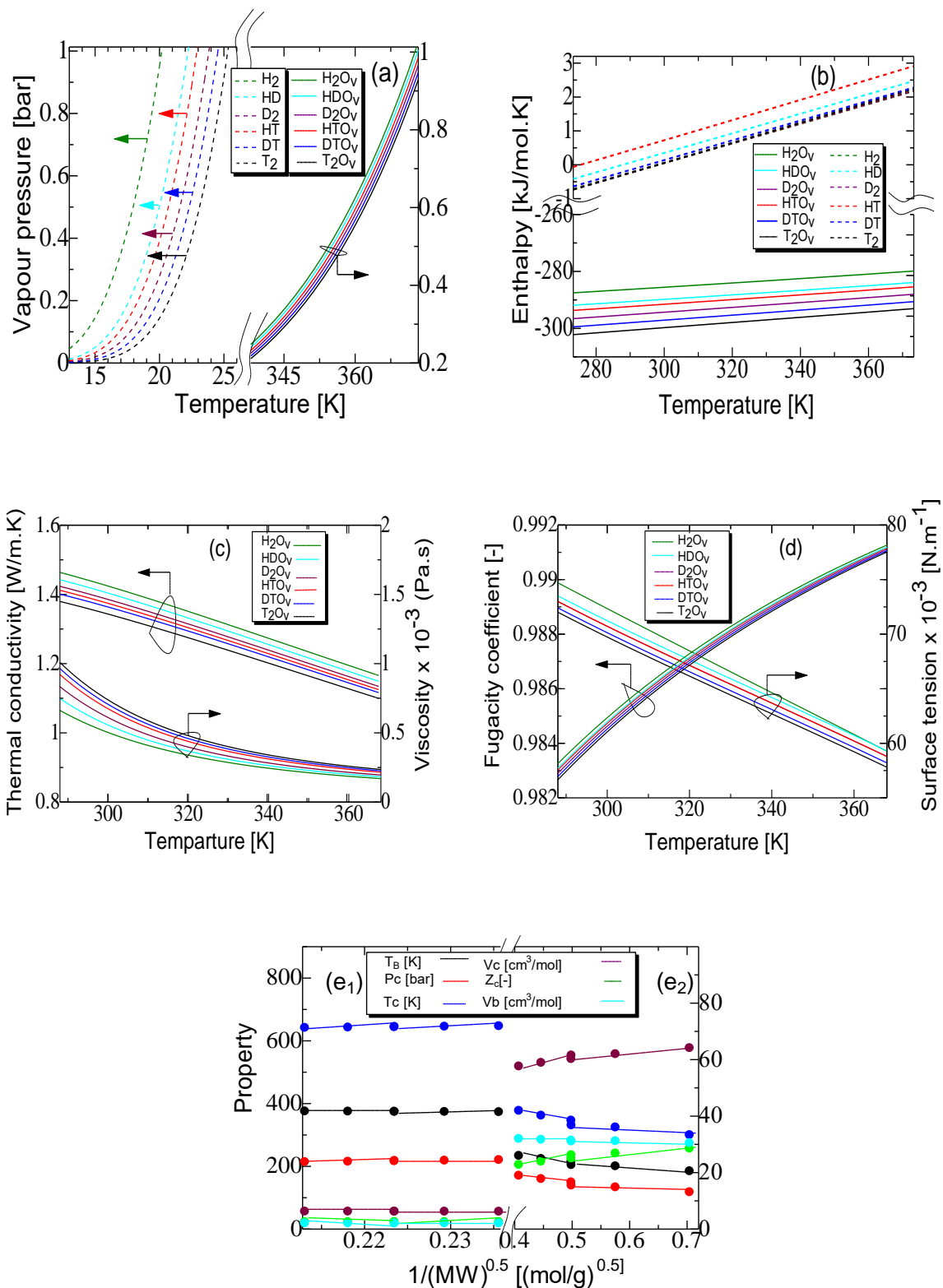


Figure (4.5) deuterium and tritium isotopologue properties in both hydrogen gas and water phases. (a-d) Changes with temperature, (e) Extension of deuterium isotopologue properties to analogous tritium isotopologues: (e₁) H_2O isotopologues, (e₂) H_2 isotopologues.

4.3.2.2 Equilibrium model

The equilibrium model was first investigated as it does not require detailed information on properties of both hydrophobic catalytic packing and hydrophilic inert packing but requires information on thermodynamic properties of the physical and chemical equilibrium boundaries. The equilibrium model, which relies on the assumption of ideal mixing between the liquid and the gaseous phases, would anticipate, according to Eq. 4.12, the highest separation factor $Sep_{D,eq}$ of deuterium relevant to hydrogen isotopologues.

$$Sep_{D,eq} = \frac{x'_{D,eq}(1-y'_{D,eq})}{(1-x'_{D,eq})y'_{D,eq}} \quad (4.15.1)$$

$$x'_{D,eq} = \frac{x_{D_2O,eq} + \frac{1}{2}x_{HDO,eq}}{x_{H_2O,eq}} \quad \text{and} \quad y'_{D,eq} = \frac{y_{D_2O,eq} + \frac{1}{2}y_{HDO,eq}}{y_{H_2O,eq}} \quad (4.15.2)$$

Where $x'_{D,eq}$ and $y'_{D,eq}$ represent the atom fractions of deuterium in the liquid water and hydrogen phases, respectively, at equilibrium conditions.

4.3.2.2.1 CEPE Model

The phase equilibrium model (CEPE), commonly known as MESH (Material balance, vapour–liquid equilibrium equations, mole fraction summations, and heat balance), along with the gas phase hydrogen catalytic exchange reaction (as expressed by Eqs. (4.4-4.6)) was used. Several assumptions have been made for formulating and solving the model equations: (1) equilibrium controlled reactions, (2) equilibrium controlled mass transfer between bulk gas and liquid phases and (3) negligible flow dispersion and pressure drops in the column.

The MESH model for steady-state operations at the j^{th} theoretical stage is given by Eqs. 4.16.1-4.16.4, where the index j counts downwards.

- Mass balance

$$L'_{j-1}x_{i,j-1} - L'_jx_{i,j} + G'_{j+1}y_{i,j+1} - G'_jy_{i,j} + r_{i,j}m_{c,j} = 0 \quad (4.16.1)$$

- Energy balance

$$L'_{j-1}h_{j-1} - L'_jh_j + G'_{j+1}H_{j+1} - G'_jH_j = 0 \quad (4.16.2)$$

Where, $i=1-6$ (number of components), $j=1-N$ (number of stages) and $m_{c,j}$ is catalyst load at stage j . The heat associated with the process was assumed to be driven by liquid H and vapour/gas h enthalpies which were estimated in section 4.3.2.1 and shown in Figure (4.1, b). L' and G' are the flow rates of liquid and gas phase, respectively and i is the reactive

component. The reaction kinetic rates $r_{i,j}$ were set to zero for the CEPE model and to Eqs. 4.7-4.9 for CKPE model.

- Equilibrium between bulk phases

Good mixing between the phases is assumed between leaving streams at each stage, leading to equilibrium assumption between bulk phases as illustrated by Eq. 4.16.3.

$$y_{i,j} - K_{i,j}x_{i,j} = 0 \quad (4.16.3)$$

The gas/liquid equilibrium constant K values of H₂O, HDO, D₂O, HTO and T₂O were calculated from non-ideal gas/liquid fugacity equilibrium models where Antoine model and NRTL model were used for the saturated vapour pressures and fugacity coefficients, respectively.

- Summations

$$\sum_{i=1}^N x_{ij} = 1, \sum_{i=1}^N y_{ij} = 1 \quad (4.16.4)$$

4.3.2.2.2 Model validation

The base case of the reactive stripping model was developed in accordance with the experimental run conditions and modelling provided by Ye et al. [128] who investigated the steady-state catalytic exchange of deuterium between HDO and water. As no data on kinetics were reported, we assume that the catalytic exchange (reaction 4.1) and gas/liquid scrubbing (reaction 4.2) under control of the chemical equilibrium and the bulk phase equilibrium, respectively, that is, the vapour leaving any stage was in physical equilibrium with the liquid at that stage, leading to maximum separation efficiency. The influence of the temperature, pressure, vapour to liquid flow ratios and catalyst loading on the distribution of deuterium at the top of the column was investigated. Thus, the stripping column was simulated by assuming chemical equilibrium controlled conditions of the reverse reaction 4.1, which was expressed by the reaction mechanism of Eqs. 4-6, and by assuming that the wet scrubbing (reaction 4.2) takes place under gas/liquid bulk phase equilibrium or negligible mass/heat transfer control. A mixed deuterium-enriched water of 0.2 mol % and a high-purity natural hydrogen gas were counter-currently passed through the column. Typical operating conditions were run under a molar ratio of hydrogen gas to water flowrate of one, flow rate of H₂O_L of 3.5 mol/h, number of theoretical stages in the column of 5, and operated at atmospheric total pressure and temperature of 323 K. In order to maintain isothermal operations along the axial profile of the column and in absence of a heating jacket, a reboiler was added at the bottom of the column as

a humidifier. The value of the reboiler heat duty for each run was not predicted but tuned until a constant profile of the desired temperature along the column height was achieved. The set of mass balance Eqs. 4.16.1-4.16.4 was computed by using the embedded Newton- Raphson's method based solver in Aspen plus. This method required setting of the initial values of temperatures and flowrates which were obtained from similar process and operations of stripping process without the catalytic exchange. The computation of this later allowed solutions with no convergence difficulty. The solutions by the Newton-Raphson method however, needed large computation efforts for the numerical evaluation of the element of the Jacobian matrix and calculation of its inverse matrix when the reactive stripping was added. This was caused by the small compositions of deuterium isotope, resulting in the minimization of the residuals to be more sensitive to such small amounts than the large compositions of water and hydrogen, and thus to inadequate stability in achieving convergence.

4.3.2.2.1 Effects of temperature and pressure

For deuterium removal from liquid water, the simulation was conducted at temperatures ranging between 293.3 and 353.3 K. The deuterium in D_2O_L was converted into HDO_V , D_2 and HD as shown by Eqs. 4.4–4.6. The top column released a non-condensable hydrogen gas mixture (i.e. H_2 , HD and D_2) and a condensable water vapour mixture (i.e. H_2O_V , HDO_V and D_2O_V). Since the vapour phase is commonly condensed and recycled back to the column, the separation of deuterium from liquid water relies on its presence in the hydrogen gas mixture (D_2 , HD in H_2) only. The composition of the condensable vapour phase (i.e. D_2O_V and HDO_V) and relevant atom fraction of deuterium in the vapour phase, x'_D as well as the composition of hydrogen phase (i.e. D_2 and HD) and relevant atom fraction of deuterium in hydrogen phase, y'_D , at the top exit are shown in Figure (4.6, a). Similar to the results reported by Ye et al. [128] At atmospheric pressure the concentration of deuterium in the hydrogen gas increased with temperature until about 348 K and then decreased owing to increased presence of H_2O_V at high temperatures, promoted by the higher relative volatility of H_2O_V compared with HDO_V , as illustrated in Figure (4.6, a), leading to more condensation of HDO_V than H_2O_V , favouring a shift of the chemical equilibrium of reaction 4.12.1 and 4.12.2 towards H_2O_V production. The trends of increase or decrease in HDO_V production was thus dominated by relevance of chemical equilibrium of reactions 4.4-4.6 and reaction 12. The CEPE model was first validated by the separation factor $Sep_{D,e}$ of deuterium from water to hydrogen gas as computed by Eq.

4.15.1. The values of separation factor at atmospheric pressure is within a reasonable agreement (i.e. deviation of 1.2 %) with the model proposed by Rolston et al. [103].

The effect of total pressure was investigated by the CEPE model while a negligible deactivation by pore condensation of water was assumed. Increasing the total pressure, as suggested by Sugiyama et al. [153], would maintain high H_2O_L levels in the liquid phase at high temperatures. This is confirmed by Figure (4.6, a), which validates that reducing the pressure leads to increased proportion of H_2O_V and a reduced concentration of deuterium in the hydrogen gas. Thus, operating at high pressures promoted the presence of deuterium, mainly in HD form, in the hydrogen gas at reduced H_2O_V and D_2O_V compositions but extending to temperatures beyond maximum HD compositions favoured relevance of reaction 4.12 over reactions 4-6 at reduced HD and HDO_V productions.

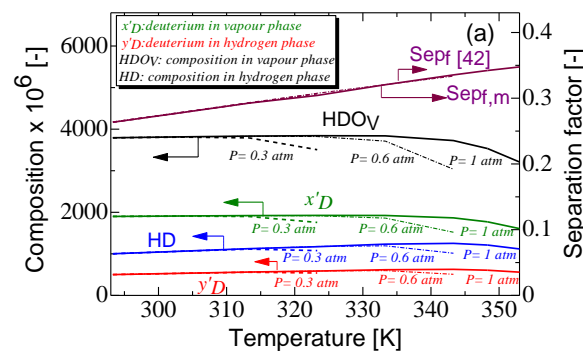


Figure (4.6, a) Effect of pressure and temperature.

4.3.2.2.2.2 Effect of feed flow ratio of hydrogen to water (G'/L')

Since operations were carried out under chemical and physical equilibrium of reactions 4.2 and 4.4-4.6, changing the feed flowrate ratio of H_2 to H_2O_L affected exclusively the equilibrium compositions of reactions 4.2 and 4.4-4.46. Trends of HD again has shown maximum values with operating temperatures for each value of G'/L' ratio. These temperature for maximum HD production were approximately 353, 343, 323 and 293 K at G'/L' values of 0.2, 1, 2 and 4, respectively, as shown in Figure (4.7, b). High G'/L' ratios produced less pure deuterium in the hydrogen phase due to higher loads of hydrogen feed. Other potential advantages of increasing the feed rate of hydrogen, such as mass transfer rates and flow dynamics in the packing, were not accessible owing to assumption of bulk gas/liquid equilibrium operations.

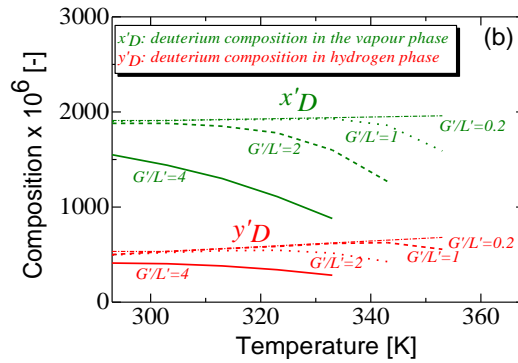


Figure (4.7, b) Effect of gas to liquid flowrate ratio

4.3.2.2.3 Effect of number of stages

Alternatively, rather than reducing gas flowrates, increasing the number of stages or packing height would instead present similar trends of deuterium separation, as observed in Figure (4.8, c), which shows the effect of the number of stages ($N = 2-8$) on the concentration of deuterium at the top of the column. A set of simulations were run to determine the effect of packing height on deuterium capture at a constant value of unity for G'/L' ratio. It is clear that the deuterium capture increased with increasing column height, up to a packing height of five theoretical stages and then remained reasonably unchanged thereafter. This may be due to attainment of maximum separation efficiency which was driven the chemical equilibrium compositions of both reactions 4.12.1-4.12.2 and 4.4-4.6.

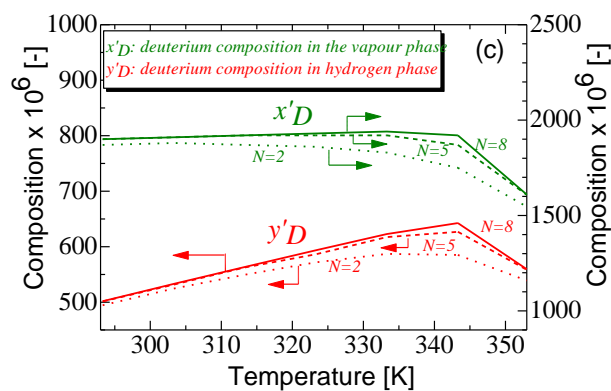


Figure (4.8, c) Effect of reactive stages.

4.3.2.2.2.4 Effect of mass of catalyst

Under chemical kinetic operations, the reaction time of the catalytic exchange (Eqs. 4.4-4.6) would affect the overall gas/liquid mass transfer boundaries. Thus, the chemical kinetic module in Aspen plus was then turned on and added to the phase equilibrium module. The chemical kinetic module included chemical kinetics of reaction 4.4 and 4.6. The CKPE model is thus used instead of CEPE that has been used in sections 4.3.2.2.1-4.3.2.2.3. Figure (4.9, d) shows the benefit of using reactive stripping when compared with gaseous phase catalytic exchange only in section (4.3.1). Unlike the results in Figure (4.4, c), which were obtained by operating the isotopic exchange under a gaseous phase only, the results of the reactive stripping process as illustrated in Figure (4.9, d) shows an increase in conversion into HD gas when the mass of catalyst was increased. Increasing the mass of catalyst promoted the rate of conversion of D_2O_L into HD gas compared with HDO_V as shown in Figure (4.9, d). Since the resistance to gas/liquid mass transfer was ignored in the phase equilibrium model, the amount of catalyst for HD conversion was over-predicted owing to rapid counter-current mass transfer of H_2O_L into the hydrogen gas phase and HDO_V into the liquid water phase compared with relevant chemical kinetics. At high values of catalyst mass, the conversion reached asymptotic values close to the equilibrium ones obtained in Figure (4.6, a).

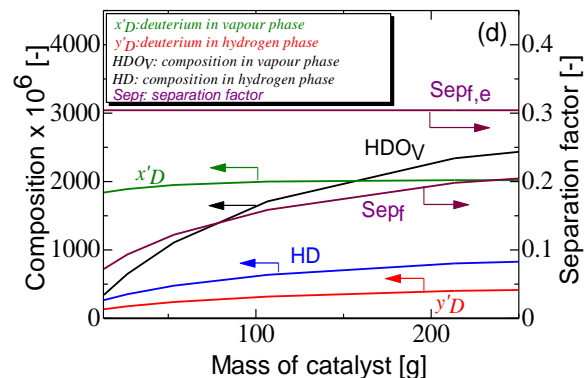


Figure (4.9, d) product distribution at the top of the LPCE column. Liquid feed composition: 0.2 mol % of D_2O , Pure hydrogen gas, liquid flow are L' : 3.5 mol/h, column ID: 0.025 m, height: 1.2 m, packing type: Dixon ring of 1.5 mm. Effect of mass of catalyst per stage, $T=333$ K, $G'/L'=1$, $P= 101.3$ kPa.

In addition, the composition profiles of isotopologues and corresponding reaction rates inside the column, as shown in Figure (4.10, e), clearly indicates that most of the conversion into HD took place throughout the bottom part of the column (stages 4–6). Maximum values of HD composition were achieved over the packing height, justifying the role of HD as an intermediate towards HDO_V production as shown in Eqs. 4.4-4.6 and the efficient condensation

of this later (Eq. 4.11) as assumed in the CEPE model, and thus demonstrating an excess use of reactive stages when the full column is packed with reactive packing.

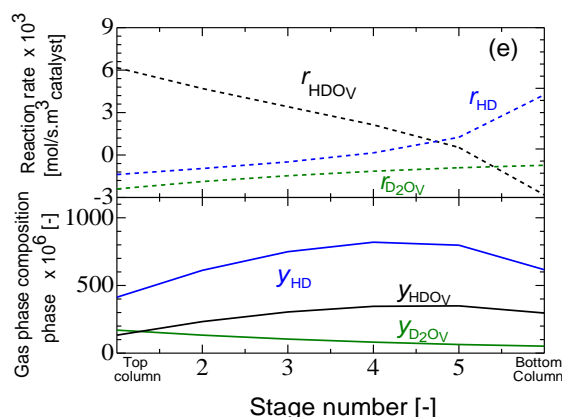


Figure (4.10, e) product distribution inside the LPCE column, $T=333$ K, $G'/L'=1$, $P=101.3$ kPa.

4.3.2.3 Rate-based non-equilibrium model

Assuming well defined mass transfer inside the catalyst packing, the mass transfer rate of deuterium from the liquid water to hydrogen gas phase depends on the external mass transfer, which is a function of fluid dynamics. The fluid dynamics consist of an upflowing hydrogen gas, which gets saturated with water vapour at the operating temperature and offers a holdup equivalent to the open space of the reactor while the liquid water trickles down and covers the wettable surface of both the inert and reactive packings. Thus, the mass transfer is a function of the exposed surface area of the down-flowing H_2O_L and shaped by the packing material. The overall mechanism of mass transfer herein includes, according to the two-film theory, transport of D_2O_L reactant to the liquid film interface through the down-flowing H_2O_L , diffusion of D_2O_L through the film, evaporation at surface interphase into D_2O_V , diffusion of D_2O_V in the gas film and transport in the up-flowing gas, and opposite mass transfer pathway applies to condensation of produced HDO_V , transport of D_2O_V in the core of the gas phase and surface reactions in the hydrophobic reactive packing. Thus, mass transfer is a function of the chemical kinetics, packing properties and flow dynamics (accessible surface area, wettability, holdup and pressure and temperature).

The rate-based module of Aspen plus was used as a basis for simulating the reactive stripping process of hydrogen isotopic exchange. The module combines CKRN-E models and thus is a powerful tool for the design and scale-up analysis of the hydrogen exchange process, as it has the capability of employing real reactive stripping configurations of internals, multi-component

mass and heat transfer methods, actual chemical kinetic and thermodynamic models. However, this model requires good underlying models for kinetics, thermodynamics and hydrodynamics.

4.3.2.3.1 CKRN-E Model

The CKRN-E model uses separate mass balance models for each phase along with rate of mass and heat exchanges between the gas and liquid phases. The set of mass and heat balance equations for bulk phases and interphases is illustrated in Eqs. 4.17.1-4.17.10 while the set of mass transfer equations at the interphase, mixing rules of properties, correlations for mass and heat transfer coefficients and pressure drops is illustrated in Appendix A.

- Mass balance:

- Material balance for bulk liquid

$$L'_{j-1}x_{i,j-1} + NM_{i,j}^L - L'_jx_{ij} = 0 \quad (4.17.1)$$

- Material balance for bulk gas

$$G'_{j+1}y_{i,j+1} - NM_{i,j}^G + r_{ij}^G - G'_jy_{ij} = 0 \quad (4.17.2)$$

- Material balance for liquid interphase film

$$NM_{ij}^I = NM_{ij}^L \quad (4.17.3)$$

- Material balance for gas interphase film

$$NM_{ij}^I = NM_{ij}^G \quad (4.17.4)$$

Where NM is the rate of mass transfer between the liquid and gaseous phases

- Energy balance

- Energy balance for bulk liquid

$$L'_{j-1}H_{j-1} + q_j^L - L'_jH_j = 0 \quad (4.17.5)$$

- Energy balance for bulk gas

$$G'_{j+1}h_{j+1} - q_j^G - G'_jh_j = 0 \quad (4.17.6)$$

- Energy balance for liquid interphase film

$$q_j^I = q_j^L \quad (4.17.7)$$

- Energy balance for gas interphase film

$$q_j^I = q_j^G \quad (4.17.8)$$

Where q is the heat transfer associated with the mass transfer between the phases

- Phases equilibrium at gas/liquid interphase

$$y_{ij}^I - K_{ij}x_{ij}^I = 0 \quad (4.17.9)$$

- Summations

$$\sum_{i=1}^N x_{ij} = 1, \sum_{i=1}^N y_{ij} = 1, \sum_{i=1}^N x_{ij}^I = 1, \sum_{i=1}^N y_{ij}^I = 1$$

(4.17.10)

4.3.2.3.2 Model validation

The thermodynamic model, physicochemical properties and chemical kinetic modules package were similar to those used in the equilibrium model, whereas the mass and heat transfer models were switched to the mass and heat transfer rate-based model. This model included a transport rating module for the column used. The column rating allowed access to flow dynamic properties (i.e. liquid holdup, maximum liquid velocity before flooding and pressure drops) as well as to mass and heat transfer properties (i.e. interfacial area, heat and mass transfer coefficients, composition and temperature at gas/liquid interface and height equivalent to a theoretical plate (HETP)). The rate-based model, which is based on the two film theory, included the mass and heat transfer rates between the contacting phases and was based on a detailed description of the combined diffusion and advection processes taking place in both the liquid and gaseous phases, while phase equilibrium existed at the gas and liquid interface and a relevant transfer model was used to calculate the gas/liquid phase resistances.

The “VPLUG” flow model (Eqs. A.1-A.10 in Appendix A) in which the bulk properties for each phase were assumed to be the same as the outlet conditions for that phase leaving that stage model, was used to calculate the bulk properties, including the reaction, energy and mass rates. Mass transfer coefficients and interfacial area were calculated using Onda’s model [154] (Eqs. A.11-A.17 in Appendix A) as it is recommended for the Dixon packing used. In addition, the pressure drop model presented by Billet and Schultes [155] (Eqs. A.18-A.20 in Appendix A) was assumed applicable to the Dixon packing and the heat transfer coefficient was predicted by the Chilton and Colburn analogy. [156] The absorber heat loss was assumed negligible.

The results of Ye et al. [128] first validated this model as a means to investigate the actual separation efficiency of the mass transfer based non-equilibrium model. The reactive stripping column was set with a size of 0.025 m I.D. and 1.20 m length, resulting into five to six HETP depending on the operated flow rates used. This HETP corresponds approximately to a single section of packing inside Ye’s column which was equally filled with inert hydrophilic packing and reactive hydrophobic packing. The model was validated as well with results from Kumar et al. [139] and a sensitivity analysis was then applied which utilized the packing configuration, kinetic models, gas and liquid mass transfer coefficients, and the effective interfacial area to

determine the effects of different design parameters on performance of separation of deuterium into HD gas at the top of the reactive stripper.

Figure (4.11, a₁) shows the trends of product profiles with temperature for the combined chemical kinetics and the rate-based gas/liquid non-equilibrium model (CKRN-E) along with the two previously discussed the chemical equilibrium and the bulk gas/liquid physical equilibrium (CEPE) model and the chemical kinetics and the bulk gas/liquid physical equilibrium (CKPE) model. The profiles of deuterium in the hydrogen phase, by inference HD compositions, by the rate-based model were favoured at high temperatures owing to increase of both mass transfer rates and chemical kinetic rates. These trends are similar to those observed by Ye et al. [128] and the deviations from the chemical equilibrium model are more pronounced at low temperatures where conversion into HD was not significant. At high temperatures, these deviations were about one third those observed by Ye and about one half those observed in the CKPE equilibrium model, leading are to conclude that the kinetic rate model would fit the results of Ye well if the catalyst was more active.

The results were as well compared with those from Kumar et al. [139] who simplified the hydrogen exchange process into a single reaction involving the conversion of deuterated water into HD to facilitate the use of a two-phase model, and the sensible heat transfer between phases and back absorption of hydrogen gases by water were as well ignored. The trend of composition of deuterium at the top of column in hydrogen gas as shown in Figure (4.11, a₂) shows negative deviation about 20 %, which is reasonable, considering the catalytic activity of present packing along with the errors associated with the physical properties, fluid flow model, Onda's mass transfer correlations and experimental runs.

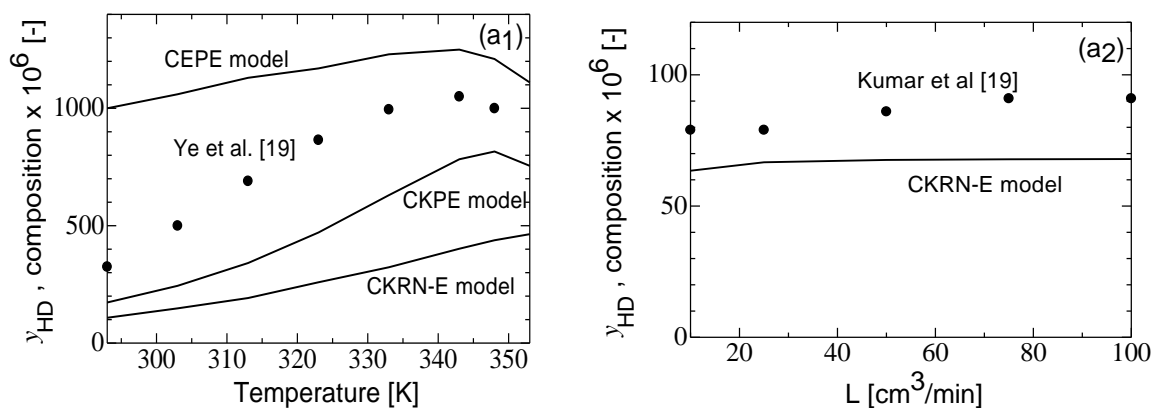


Figure (4.11, a₁) product distribution by rate-based non-equilibrium phase model: (a₁, a₂) at the top of the LPCE column.

The trends observed using the equilibrium-based model (CEPE or CKPE) were also observed in the non-equilibrium model (CKRN-E), but with a significant deviation of HD composition at the top of the column, particularly at low temperatures. The contribution of gas/liquid mass transfer limitation at low temperature is also validated by the deviation of the rate constant of the gaseous catalytic exchange (Eq. 4.4) from the overall gas/liquid rate constant as shown in Figure (4.12, b₁) and ratio of gaseous reaction rate to gas/liquid mass transfer rate (Figure (4.12, b₂)). This would demonstrate that the non-equilibrium model predicts mass transfer resistance between the gas phase and the liquid water phase, particularly the counter-current mass transfer of D₂O_L and H₂O_L mixture from the liquid to H₂ phase, and HDO_v from the gas phase to the liquid water phase.

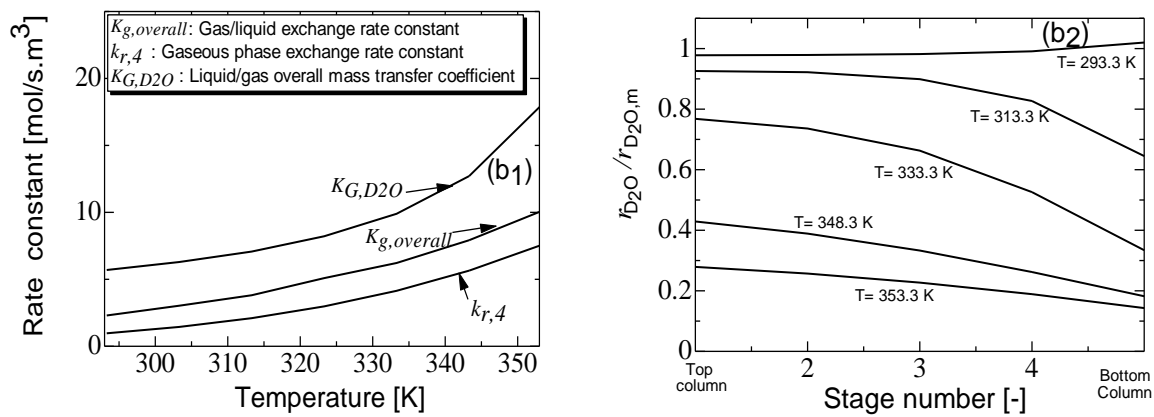


Figure (4.12, b₁, b₂) product distribution by rate-based non-equilibrium phase model: at the top of the LPCE column. (b₁) profiles of kinetic rate constants $k_{r,4}$, liquid/gas overall mass transfer coefficient based on the gaseous phase for D₂O species $K_{G,D2O}$, and gas/liquid exchange rate constant $K_{g,overall}$. (b₂) Ratio of kinetic rates of D₂O to mass transfer rate of D₂O.

The mass transfer at liquid/gas interphase boundary and the overall mass transfer from the H₂O_L to the catalytic packing were investigated and the model parameters, including mass transfer coefficients and relevant rates were validated by experimental tests of Kumar et al. [139]. Increasing the feed flow ratio (G'/L') of hydrogen to water at constant liquid flowrate was effective on mass transfer coefficients in the gaseous phase only (Figure (4.13, c₁)) while increasing the liquid flowrate (L'/G') was relevant for both liquid and gas mass transfer coefficients (Figure (4.13, c₂)), demonstrating the relevance of transport resistance inside the film on the gas phase side at present operating conditions. These values of mass transfer coefficients were in the range of those obtained by Kumar et al. [139], validating the use of Onda's model.

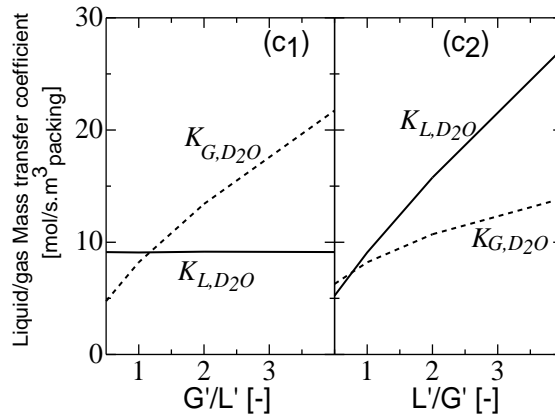


Figure (4.13, c1, c2) product distribution by rate-based non-equilibrium phase model: at the top of the LPCE column. (c1 and c2) effect of gas to liquid flow rate at L' : 3.5 mol/h and liquid to gas flow rate at G' : 3.5 mol/h, respectively.

Unlike the equilibrium model (CKEP), where the temperature affected the chemical rate constants of reactions, saturation of hydrogen phase by water vapours (D_2O_V , HDO_V and H_2O_V) and flow enthalpies, the rate-based model ((CKRN-E) was even more sensitive to temperature due to the dependency of additional physical property parameters on temperature, including the solubility of isotopologues in water, diffusivity in both gaseous and liquid phases, viscosity, surface tension, thermal conductivity and heat capacity.

Figure (4.14, d) compares the profiles of compositions of HDO_V and HD components along the column height obtained using either the rigorous mass transfer CKRN-E model or the equilibrium CKEP model which were illustrated in Figure (4.10, e). Literature on experimental data of compositions profiles of deuterium inside the column is limited and the following results were validated by those obtained by Kumar et al. [139] as well as by those derived from the top or bottom of the column. The equilibrium model significantly overestimates the stripping of D_2O as well as the scrubbing of HDO, and thus provides non-reliable results, leading to lower packing heights and hence to incorrect process designs. This is contrary to the rigorous rate-based model which produced less HD and HDO_V , particularly towards the top of the column, owing to lower chemical conversion of D_2O_L with the later model. The CKRN-E model exhibited steady trends of HD and HDO compared to the curvy trends observed in CEPE and CKEP models owing to inhibited counter-current mass transfer of D_2O_L and HDO_V to the H_2 and H_2O_L phases, respectively.

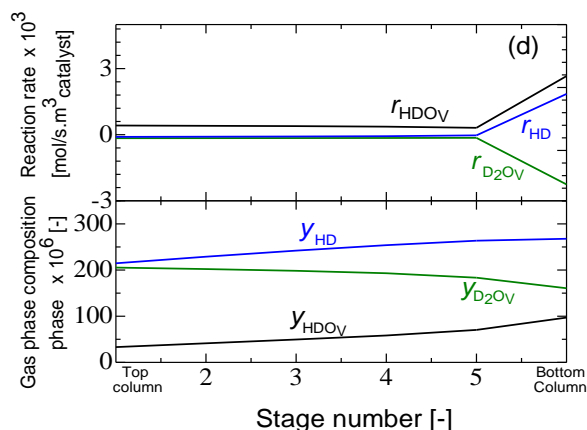


Figure (4.14, d) product distribution and relevant reaction rates inside the LPCE column.

4.4 Summary of the chapter

This chapter extends applicability of the equilibrium and rate-based models of commercial Aspen plus modular package to hydrogen catalytic exchange by using a reactive stripping column packed bed of Pt/SDBC resin catalyst. Compared with the equilibrium model, the rate-based model, which governs the coupling of mass and heat transports and specific features of the reaction mixture of hydrogen isotope exchange, simulated more realistically the synergic effect of these on the de-deuteration efficiency. The kinetic model confirmed a single into HD and HDO_V and double de-deuteration into D_2 and H_2O_V when D_2O_L was used as the starting feed. The kinetic model fitted the experimental data well and relevant parameters were estimated based on data generated using deuterium. The missing physical properties of deuterium and tritium isotopologues in hydrogen gas and water forms were predicted and validated within acceptable agreement with existing literature data. These physical data were needed for the bulk gas/liquid equilibrium model and even more for the rate-based non-equilibrium model. The equilibrium model (CEPE), which is independent of types of packing and catalysts but function of thermodynamic boundaries of underlying chemical reactions and gas/liquid physical exchange, allowed access to trends of maximum separation efficiency of deuterium isotope into HD that would ideally be reached under assumptions of efficient gas/liquid mixing and efficient reactive packing. The concentration of deuterium in the hydrogen gas increased with temperature and then decreased owing to increased presence of H_2O_V at high temperatures, leading to more condensation of HDO_V . Other operating parameters such as the operating pressure was effective to separation owing to reduced H_2O_V compositions, gas to liquid flow rate ratio reduced maximum separation efficiency and column

height promoted local separation efficiency until a height where it remained unchanged. Under kinetic control, the phase equilibrium model (CEPE) indicated maximum values of deuterium in hydrogen over the packing height, demonstrating efficient condensation of HDO_v intermediate by the ideal mixing and limiting further de-deuteriation of this later into H_2O_v . The rate-based model (CKRN-E) presented results close to real pilot scale data and relevant deviations of CKRN-E model from the equilibrium model allowed predictions of mass transfer rates, reactive mass transfer rates and separation efficiency of the reactive stripping column. Compared with equilibrium model, the rate-based model simulated the reactive stripping/scrubbing process more accurately, including the effects of temperature, type and properties of the packing and pressure drops. The mass transfer control of D_2O_L into the gaseous phase reduced overall production of HD compared with the equilibrium model. Maximum trends of HD over the packing height in the equilibrium model however were not observed in the rate-based model owing mass transfer control of HDO_v condensation, inhibiting further de-deuteriation into H_2O_v and HD. The gas to liquid flow ratios demonstrated that the gas/liquid mass transfer was mainly driven by gas film side and this control was even more promoted at high temperatures, which was illustrated by overall mass transfer coefficients and isotopic exchange rate constants.

Chapter 5

Analysis of fluid flow in a 3D trickle bed reactor

Computational fluid dynamics (CFD) studies provide identification of the hydrodynamic characteristics and multiphase flow in the TBR by numerical modelling. [157-165] There are two modelling approaches to simulate of trickle bed reactors by using CFD computation; the porous media and packed bed concepts. There is a number of published studies [159-162 and 164] dealing with packed bed flow simulations by use of a three-phase Eulerian model in which the solid velocity is identically set to zero. Such calculations are nevertheless computationally demanding. The alternative approach [157] deals with the porous media concept, which is more computationally intensive and use two-phase Eulerian model along within the solid phase as porous zone.

In this chapter, influence of the fluid velocity and the particle size at low aspect ratios of tube to particle diameters of a three-phase reactor is investigated by a 3D CFD modelling. CFD has proven to be a powerful tool to simulate the detailed flow and scalar transport in trickle bed to provide improved understanding and quantitative information in developing the effective medium models that are the basis for chemical reactors. The implementation of the 3D model is expected to offer more understanding of various underlying phenomena taking place at local scale. The setting methodology of the CFD model is presented. The independent experimental data sets analysed by researchers [159-160, 166-169 and 198] are selected to validate the predictions of the CFD modelling. Along with these, the results are as well compared with those from literature work on numerical simulations such as Gunjal et al. [159] and Atta et al. [157] who used 2D two-phase Eulerian model combined with a the porous media concept.

5.1 Introduction

Trickle bed reactors (TBRs) are among the most used multi-phase (gas/liquid/solid) systems where the trickling flow regime dominates in them. [157, 170] Application of the TBRs include petroleum refining, chemical and process industries, pollution abatement and biochemical. [170] Typical trickle bed reactors hold a fixed-bed of solid catalytic particles in which gas and liquid phase reactants flow in co-currently downward direction (toward the direction of gravity). [159-160] The gas phase as continuous media may flow as well in counter-currently upward direction depending on the kind of application. The liquid flows intermittently over the solid particles in the form of films or rivulets or drops through the operational characteristics

which it describes the word “TRICKLE”. [171] Co-currently downward operation of TBR is usually preferred because it provides better radial distribution and high throughput of liquid phase without flooding. However, for applications where equilibrium limited reactions take place, the counter-current operation of TBR is preferred as it provides a better driving force and thus higher gas-liquid mass transfer rates between the gaseous and the liquid phases over the entire length of the bed. [172]

The design and scale up of trickle beds continues to be a considerable challenge owing to the complex nature of key hydrodynamic variables and subsequent influences associated with the heat and mass transfer phenomena. Major factors affecting the state of flow are the fluid properties (e.g. density, viscosity, and surface tension), the fluid velocity (gas and/or liquid), the liquid hold-up and the reactor geometry (e.g. reactor diameter, packing properties and aspect ratio). Three common parameters describing fluid dynamics are the pressure drop, liquid holdup and catalyst wetting efficiency. [173-174] The first-mentioned parameter is a major design parameter for process plants as it determines an important part of the energy balance and consequently the operating effectiveness. The second one gives details on the flow behaviour and controls the liquid residence time in the reactor, and hence the presence of dead zones which can be problematic for expressing conversion and selectivity. The last one is important in determining local reaction rates, and thus essential in determining the degree of catalyst utilization and reactor performance. [174-175]

Several studies reported experimental data on pressure drop and liquid holdup in trickle-bed reactors. [166, 170, 176 and 177] The previous attempts for describing trickle bed hydrodynamics can be categorized into two different classes of work [157]. The traditional method is empirical wherein correlations are developed to fit the experimental data. [178-181] Another method is to describe hydrodynamics in phenomenological manner, i.e., assuming a simple image of a dedicated the scale flow pattern, and subsequently integrating that depiction to process the entire bed. [182-183]

TBRs are typically built by using randomly packed beds due to their simplicity in construction and loading process. Randomly packed catalyst particles are mostly spherical, cylindrical, extrudates, trilobes, or quadrilobes. [171] From phenomenological perspective, the structure of solid packing within the packed bed plays a significant role. Several physical phenomena involving dispersion, pressure drop, interstitial velocity, and local boundary layer formation over particle surfaces can be affected by the complex geometry and are often hard to identify. [175] Varied local packing arrangements exist in randomly packed bed reactors and the nature of voids formed between particles affects the flow structure inside the void and therefore

controls the mixing, heat, and mass transport rates. Besides, it affects the static and dynamic liquid holdup in the bed. When particles are packed randomly in a column, the characteristic of packing depends considerably on the ratio of tube-to-particle diameter and on the shape of particles. [171]

5.2 Model equations and packed bed generation

5.2.1 Model equations

In order to study the hydrodynamic characteristics of a trickle bed reactor, the commercial CFD software COMSOL Multiphysics® 5.0 was employed. The program presents a platform to solve the differential equations of the Navier-Stokes equations in combination with component material balances by means of the Finite Element Method (FEM). Numerical simulation of fluid flow is based on the laws of conservation for mass, momentum and energy. [174] In the simulation the two-phase flow model was used. To simplify the corresponding system of differential equations, the following assumptions were made:

- Isothermal system.
- Both fluids are Incompressible (constant density).
- Newtonian fluid.
- Reactor is operating under trickling flow regime, i.e., gas-liquid interaction is low so capillary pressure force can be neglected. This means that the same pressure for both phases at any point in time and space.
- The pressure drop across the bed is due to gas phase only, as liquid undergoes trickle flow and plays a little role.

The two phase model is based on a Cahn-Hilliard equation, for which two second order partial differential equations are decomposed and solved. The model tracks a diffuse interface separating the immiscible phases and ensures that the total energy of the system diminishes correctly. The tracking of the interface between the two fluids is governed by the so-called phase field variable (ψ).

Based on the assumptions above, we used the Phase Field Method (PFM) to study the interfacial motion of the multiphase flow. This method allows to notice the geometric evolution of the fluidic interface with an Eulerian formulation. As a result, the Laminar Two-Phase Flow, Phase Field module of Comsol package Multiphysics®5.0 was selected to execute this simulation. Although there are other methods such as level set to simulate the laminar two-phase flow, the phase field method has a more vigorous coupling with other physics in Comsol.

This advantage can be utilized to model several physics such as: chemical diffusion, heat transfer, electric field and other related phenomena associated with the system. [184]

In the phase field method, the multiphase flow is described by the parameter ϕ . Here one fluid element is defined with $\phi = 1$, whereas the second fluid element is defined with $\phi = -1$.

The phase field module in COMSOL Multiphysics®5.0 uses the continuity equation in order to satisfy the condition of conservation of mass for the incompressible flow:

$$\nabla \cdot \mathbf{u} = 0 \quad (5.1)$$

In the same way it considers the conservation of momentum for an incompressible flow solving the Navier-Stokes equations to describe the fluid evolution in the multiphase model:

$$\rho \frac{\partial \mathbf{u}}{\partial t} + \rho (\mathbf{u} \cdot \nabla) \mathbf{u} = \nabla \cdot [-p \mathbf{I} + \mu (\nabla \mathbf{u} + (\Delta \mathbf{u})^T)] + \mathbf{F}_g + \mathbf{F}_{st} + \mathbf{F} \quad (5.2)$$

Where \mathbf{u} is the velocity vector (m/s), p is the pressure (Pa), ρ is the density (kg/m³), μ is the dynamic viscosity (Pa.s), and F_g is the gravitational force, F_{st} is the surface tension force (N/m³), and F is any additional volume other force (N/m³) in the model.

Two additional equations are solved to track the interface. These arise from the use of the phase field method and comprise the phase-field variable (ϕ) and phase-field help variable (ψ):

$$\frac{\partial \phi}{\partial t} + \mathbf{u} \cdot \nabla \phi = \nabla \cdot \frac{\gamma \lambda}{\varepsilon_{pf}^2} \nabla \phi \quad (5.3)$$

$$\psi = -\nabla \cdot \varepsilon_{pf}^2 \nabla \phi + (\phi^2 - 1) \phi + \frac{\varepsilon_{pf}^2}{\lambda} \frac{\partial f}{\partial \phi} \quad (5.4)$$

Where (γ) is the mobility (m), (λ) is the mixing energy density (N) and (ε_{pf}) is the interface thickness parameter (m). The density ρ (kg/m³) and dynamic viscosity μ (Pa.s) of the mixture are defined to vary smoothly over the interface with the following equations:

$$\rho = \rho_1 (1 - V_{f2}) + \rho_2 (V_{f2}) \quad (5.5)$$

$$\mu = \mu_1 (1 - V_{f2}) + \mu_2 (V_{f2}) \quad (5.6)$$

In the above equations, density (ρ) and dynamic viscosity (μ) of the two fluids, where the subscripts 1 and 2 refer to the liquid and gas phases, respectively.

$$\mathbf{F}_g = \rho \mathbf{g} \quad (5.7)$$

$$\mathbf{F}_{st} = \left(G - \frac{\partial f}{\partial \phi} \right) \nabla \phi \quad (5.8)$$

In equation (5.8), G is the chemical potential (J/m³) defined in terms of (λ) and proportional to (ε_{pf}) as:

$$G = \lambda \left(-\nabla^2 \phi + \frac{\phi(\phi-1)}{\varepsilon_{pf}^2} + \frac{\partial f}{\partial \phi} \right) \quad (5.9)$$

V_{f2} , is the volume fraction of second fluid defined as:

$$V_{f2} = \frac{1+\phi}{2} \quad (5.10)$$

The interface between them (phase field) are the set of values:

$$0 \leq V_{f2} \leq 1 \quad (5.11)$$

$$-1 \leq \phi \leq 1 \quad (5.12)$$

The relation between λ and ε_{pf} is defined by means of the surface tension (σ) in this model:

$$\sigma = \frac{2(2)^{1/2}\lambda}{3\varepsilon_{pf}} \quad (5.13)$$

The relation between mobility γ , ε_{pf} and the mobility tuning parameter (χ) is defined by equation (5.14):

$$\chi = \frac{\gamma}{\varepsilon_{pf}} \quad (5.14)$$

In the simulations, the following are used as inputs:

$$\chi = 1(m.\frac{s}{kg}), \varepsilon_{pf} = tpf.\frac{hmax}{2} (m), \frac{\partial f}{\partial \phi} = 0 (J/m^3)$$

Transient with initialization study type consisting of Phase Initialization and time dependent steps is applied in the model. During the Phase Initialization step, the distance to the initial interface (D_{wi}) is solved. Next, a time dependent step initializes the phase field variable according to the following expressions:

In fluid (1):

$$\phi_0 = -\tanh\left(\frac{D_{wi}}{\sqrt{2}\varepsilon_{pf}}\right) \quad (5.15)$$

In fluid (2):

$$\phi_0 = \tanh\left(\frac{D_{wi}}{\sqrt{2}\varepsilon_{pf}}\right) \quad (5.16)$$

These expressions are obtained from a steady, analytic solution of equations (5.3) and (5.4) for a straight, non-moving interface. The initial condition for (ψ) is 0. A more detailed discussion of the theory related to the laminar phase field method can be found elsewhere. [184-187]

5.2.2 Packing generation by discrete element method (DEM) and packed bed design

A granular packing of densely spherical particles was built by means of DEM in order to mimic experimental samples. [125] The DEM program of particle flow code 3D (PFC^{3D}) was used to generate realistic packing samples of random structures with AR2 and AR4, as shown in Figure (5.1). The structure of the packing was the function of properties of both the container and the particles, including the stiffness, the density, and the friction coefficients between the particles or the particles and the confining wall. The compaction process was carried out until the

maximum unbalanced contact force between particles reached a value of the order 10^{-7} N, resulting in a packing at static equilibrium. The stiffness coefficients of the wall and the particles were varied for maximum density of the packing. The overall setting parameters have been enlisted as shown in Chapter 3 in Table (3.1). The packing geometry, which was defined by the 3D coordinates of particle centres, was then embedded into the commercial CFD package COMSOL Multiphysics 5.0 via 3D AutoCAD (Autodesk) processing, allowing a dedicated meshing to take place by using a computer with 512 GB RAM.

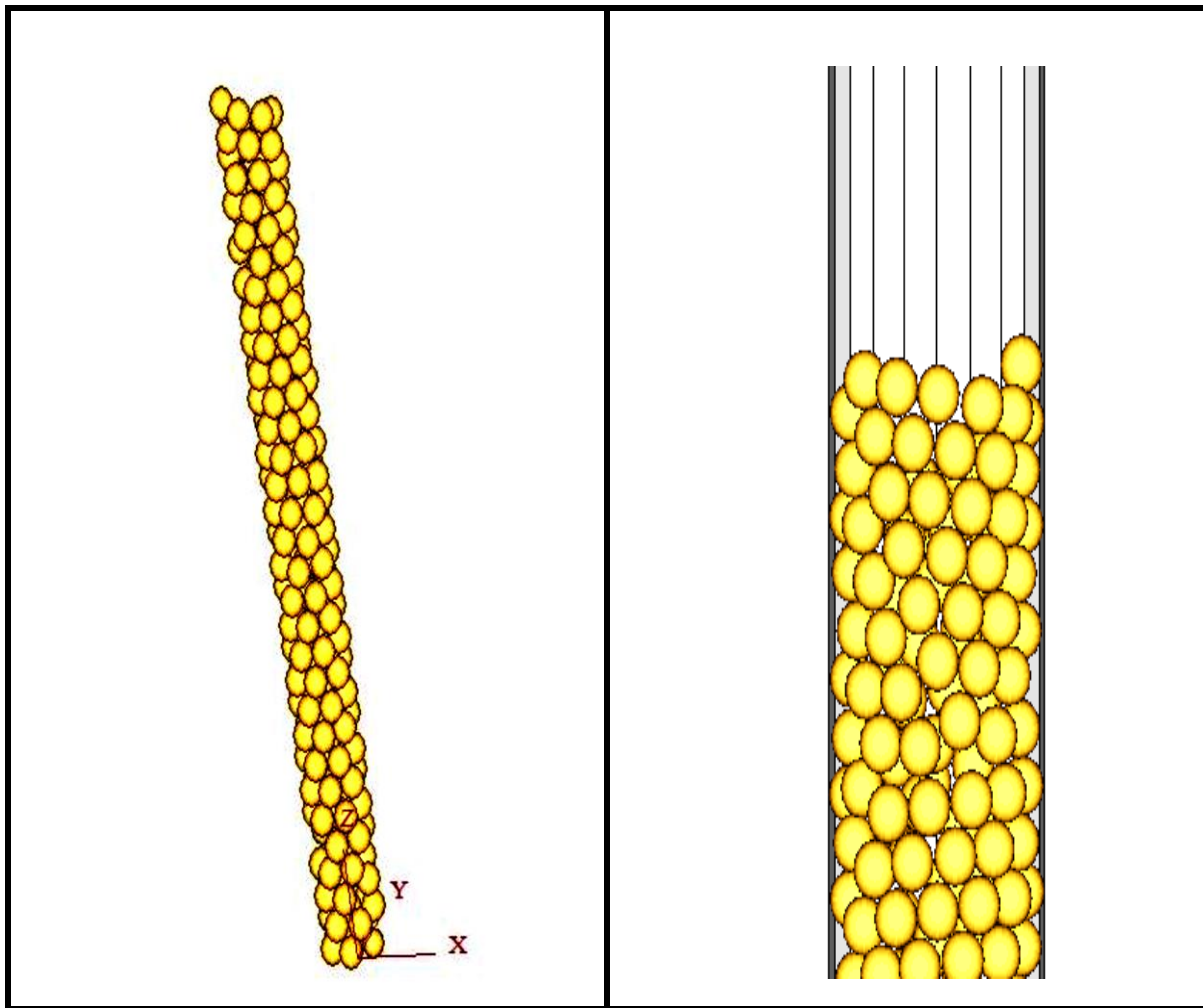


Figure (5.1) Generated packing by DEM

The packed bed reactor was designed as shown in Figure (5.2). Two volume domains were assembled to contain the gaseous and the liquid phase separately, allowing well-defined interphase at the start of the simulation.

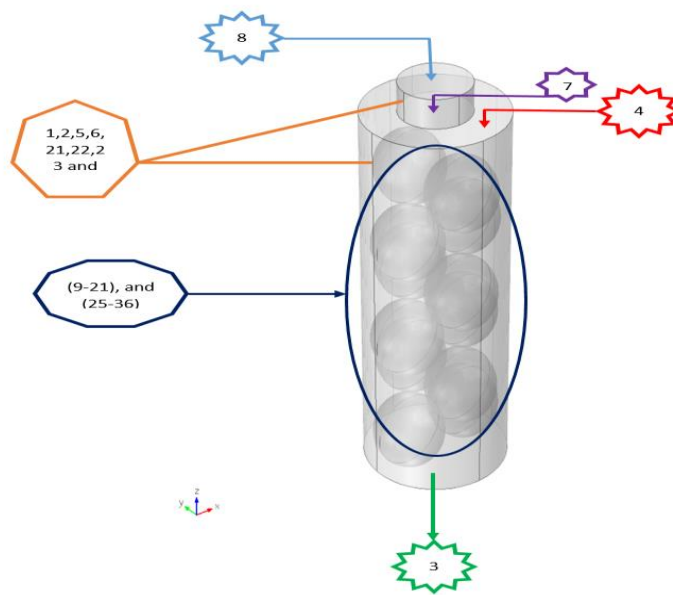


Figure (5.2) simulation domain.

5.2.3 Boundary conditions

In order to solve a system of differential equations, initial and boundary conditions must be given. In the model different boundaries exist and each boundary has to be set by one boundary condition for the momentum balance. At the inlet, boundary conditions were specified, as the system parameters were known or could be estimated easily. Here the inlet velocity u_0 was set. The outlet boundary conditions were clearly harder to estimate. The velocity was defined by an outlet pressure, because of the connection of velocity and pressure in the continuity and Navier-Stokes equation. [174] A summary of the simulation setup with boundary and initial conditions is presented in Table (5.1-a) and (5.1-b).

Table (5.1a). Boundary and subdomain condition for CFD model

	inlet	outlet	AR	No. of particle	free fluid
momentum balance	u_0 (m/s)	P_0 (Pa)	2, 4	12, 118	Navier-Stokes

Table (5.1-b). Simulation domain and its description

Domain, Boundary	Type, Specified Values
Laminar two-phase flow, phase-field interface (1=gas, 2=liquid)	
1,2	Both initial values (velocity and pressure) for fluids are zero.
7	Initial interface
4	Inlet of fluid (1): Normal inflow velocity= u_0 Volume fraction of gas=0
8	Inlet of fluid (2): Normal inflow velocity= u_0 Volume fraction of water=1
3	Outlet for both
1,2,5,6,21,22,23 and 24	Column wall
(9-21), and (25-36)	Particle

The phase initialization and transient solver of the Comsol package with default settings was used. The domain of interest between the solid particles was divided into numerous cells where the governing equations were integrated across the volume of each cell. The integrals converted the governing equations into a set of difference equations which were solved numerically using the generalized minimal residual method (GMRES) with the Geometric Multigrid preconditioner. The GMRES algorithm is an iterative method for the numerical solution of a non-symmetric system of linear equations. The method approximates the solution by the vector in a Krylov subspace with minimal residual. Trial studies with a variety of solvers (FGMRES, conjugate gradient, BiCgStab) indicated that in these particular cases, the simulation result was fairly insensitive to the exact one. The convergence was evaluated based on relative tolerance which was set to 0.0001. [125, 188]

The discretisation was carried out by the built-in meshing module of Comsol using the Adaptive Mesh Refinement Method which generated predominantly tetrahedral domain elements and triangular surfaces. The effects of the size of these elements on the viscous forces, particularly in area where potential skewed meshes could be generated such as particle contact points were investigated. This was insured by a mesh convergence check for each packed bed

by increasing the number of mesh elements and monitoring the pressure values at three arbitrary locations from the CFD simulation. It was observed that the packed beds of high AR required refined meshing than the low AR to reach approximately stable values of pressure. This result was subsequently confirmed by using the Grid Convergence Index (GCI) as described in Appendix B. The GCI reached values below 2%, validating the reasons to trust the accuracy of the present numerical simulations and to ensure that the solution is independent of the mesh size. [125, 188]

In addition, the quality of the mesh was analysed by the minimum element quality statistics method which expresses the contribution of the skewed elements. The spherical particles in the packed bed were expected to release skewed elements which were extensively reported in literature. These dealt with such elements by increase or the decrease of particle sizes as well as using the range of features available in commercial CFD to smooth these skewed elements. Herein, the diameter size of particles was reduced by 0.3% in all our tests. Such shrinkage was found necessary to prevent highly-skewed meshes at single-point contacts between particles while maintaining reasonable computation time. A shrinkage lower than this value would yield no advantage in producing more accurate results and would be computationally more expensive. [125, 188]

5.3 TRB structure and non-uniform porosity distribution

The difficulties in modelling flow in catalytic packed beds are mostly because the complicated nature of the flow domain that is formed by passages around randomly packed particles. [162] As a result of the random packing of pellets of specific shape almost always leads to non-uniform porosity distribution along the bed. The structure of this interstitial space inside the packed bed is generally determined by particle size (d_p), particle shape (φ), tube-to-particle diameter ratio (AR), and the packing method. Experimental measurement and computer simulation carried out on porosity distribution in packed beds have been the subject of several studies investigating for a considerable period of time. [162] These experimental and computational studies have shown that the longitudinally averaged radial porosity profile is higher near the vicinity of the wall and oscillates significantly in the near wall zone (of width of about 4 to 5 particle diameters), whereas the cross-sectional averaged porosity over the entire length of the bed, $\varepsilon(z)$, is distributed randomly. The magnitude of vacillations is a strong function of tube-to-particle diameter ratio (for aspect ratio (AR)>15, vacillations are within 1% while for lower values of AR, fluctuations may rise up to 30%). [159, 160, 162, 171]

Before computing the two-phase flow, one needs to generate a multidimensional porosity distribution at a certain sectional size for radial and axial profile. Therefore, the procedure of this work used available data in the 3D matrix that defines coordinates of particles inside the packed bed. The porosity profiles of packed beds of different AR were calculated by using the data of various spatial domains, which are denoted as ‘Domain Index’ in COMSOL Multiphysics 5.0 software. Domain index is a single integer number and is allocated to mesh boundaries of a single domain area (solid particle or between particles). This method allowed access to porosity distribution at any 3D coordinate with a spatial resolution at mesh size limits. Just like the distribution shown in Figure (5.3-a), the cylinder container of the packed bed of 25 mm length was cut into number of slices allowing a spatial resolution along the axial direction of 25 mm. The exported data files were then processed for porosity distribution of the packed bed by a Matlab code for the procedure illustrated in Figure (5.3-b). First, the domain index of the area between the particles was considered fully porous with an integer number of unity, and the remaining domain indexes that belong to solid particles were considered non-porous with an integer number of zero. The 3D data were angularly averaged into 2D data, which in turn, were subsequently reduced into 1D axially averaged porosity and global or averaged porosity of the full packed bed. Table (5.2) illustrates the porosity data obtained in the present simulation for various aspect ratios. A comparison with a model from Zou et al. [189] shows a good agreement, particularly for low AR. More insights into the loose structure have been shown in the 2D maps of the circumferentially averaged porosity in Figure (5.4). The loose structure along the axial coordinate is confirmed along the axial coordinate of the packed bed for AR2 and AR4. The packing porosity of a selected location of the packed bed could be larger or smaller than the entire corresponding bed, depending on where the location was selected and how many particles were included in the selected location. Moreover, Figure (5.4) shows the porosity of the selected locations and how it deviated from the entire packed bed when the numbers of particles in the segments varied. The periodic variations corresponded to the layer changes in the packing. The porosity deviation suffered from a small jump when additional particles constituted a new layer of packing. For AR4, the particle number further increased. The local porosity could be either larger or smaller than the entire bed, but the deviation was relatively small. The larger AR was, the more particles were needed to reach this low-level deviation of packing porosity. This is because sufficient layers were required to represent the entire packed bed, and a packing with a larger AR contains more particles per layer. Taking the axially averaged porosity for these Figures (5.4), which represent the distribution of porosity along the radial coordinate within the packing system, was the next step

to compare simulation results with the semi-analytical model of the radial porosity distribution by Mueller [190] who has suggested a correlation for radial variation of axially averaged porosity as a function of particle diameter (d_p), column diameter (D), and average porosity (ε_B). This correlation is fairly general and represents the available experimental data with sensible accuracy. In this work, we have used this correlation as shown below in Mueller [190] equation to prescribe bed porosity.

$$\varepsilon(r) = \varepsilon_B + (1 - \varepsilon_B)J_0(ar^*)e^{-br}, \text{ for } 2.61 \leq D/d_p \quad (5.17)$$

Where,

$$a = 8.243 - \frac{12.98}{(D/d_p + 3.156)}, \text{ for } 2.61 \leq D/d_p \leq 13.0 \quad (5.18)$$

$$a = 7.383 - \frac{2.932}{(D/d_p + 3.156)}, \text{ for } 13.0 < D/d_p \quad (5.19)$$

$$b = 0.304 - \frac{0.724}{(D/d_p)} \quad (5.20)$$

$$r^* = r/d_p, \text{ for } 0 \leq r/d_p \quad (5.21)$$

$$\varepsilon_p = 0.379 + \frac{0.078}{(D/d_p - 1.80)} \quad (5.22)$$

In Figure (5.5), it can be seen that the radial distribution of porosity obtained was in good agreement with the models of Mueller [190], especially close to the wall, because the porosity at low AR lead to high porosity near the wall in packed beds. Such property distribution of porosity impacts the flow dynamics and mass transfer, as described in the following sections. Additional assumptions on how the porosity varies in the axial direction are however required to complete the prescription of bed porosity. Jiang et al. [161] observed that porosity variation in the axial direction at any radial location is near to Gaussian distribution, and this was followed in this work. Hence, for any radial position, axially averaged porosity was calculated as shown in Figure (5.6).

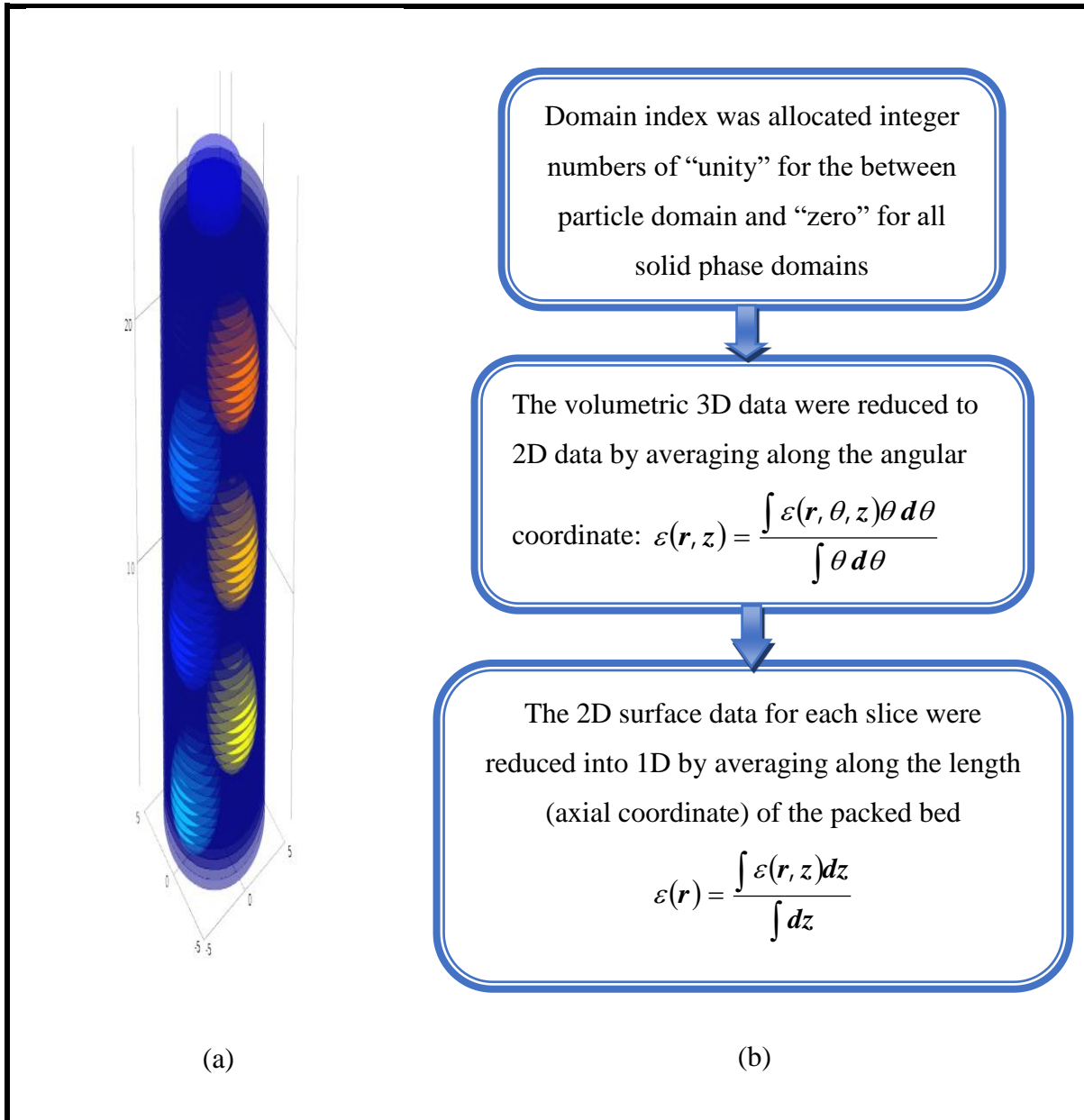


Figure ((5.3-a) and (5.3-b)) Reduction procedure of volumetric 3D data of porosity.

Table (5.2). Porosity trends for AR2 and AR4.

Aspect Ratio (AR)	Porosity $\epsilon(r)$ by CFD	Porosity $\epsilon(r)$ data by Zou et al
2	0.575	0.578
4	0.547	0.532

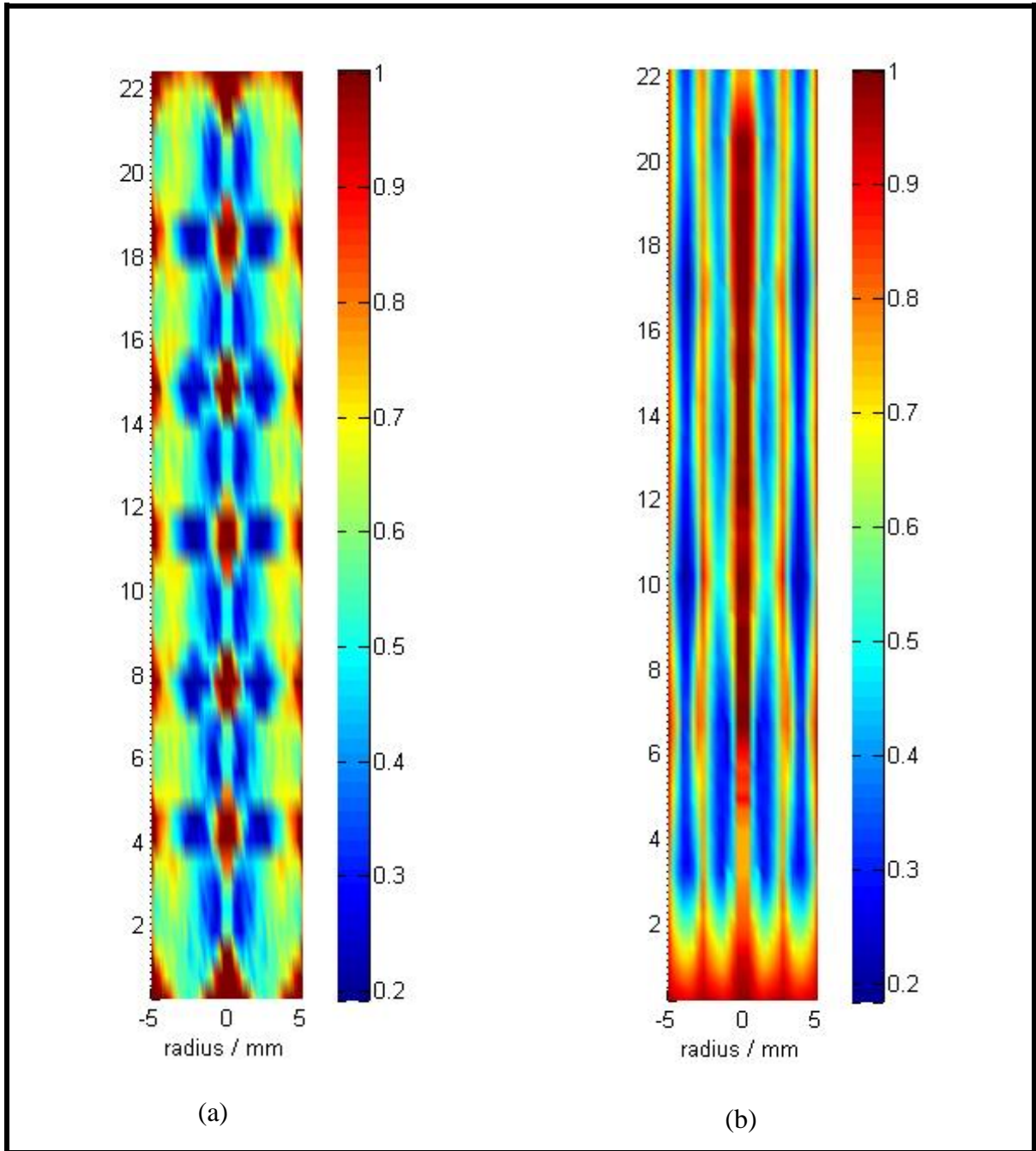


Figure (5.4) spatial distribution of angularly averaged porosity inside the packing for (a) AR2; (b) AR4.

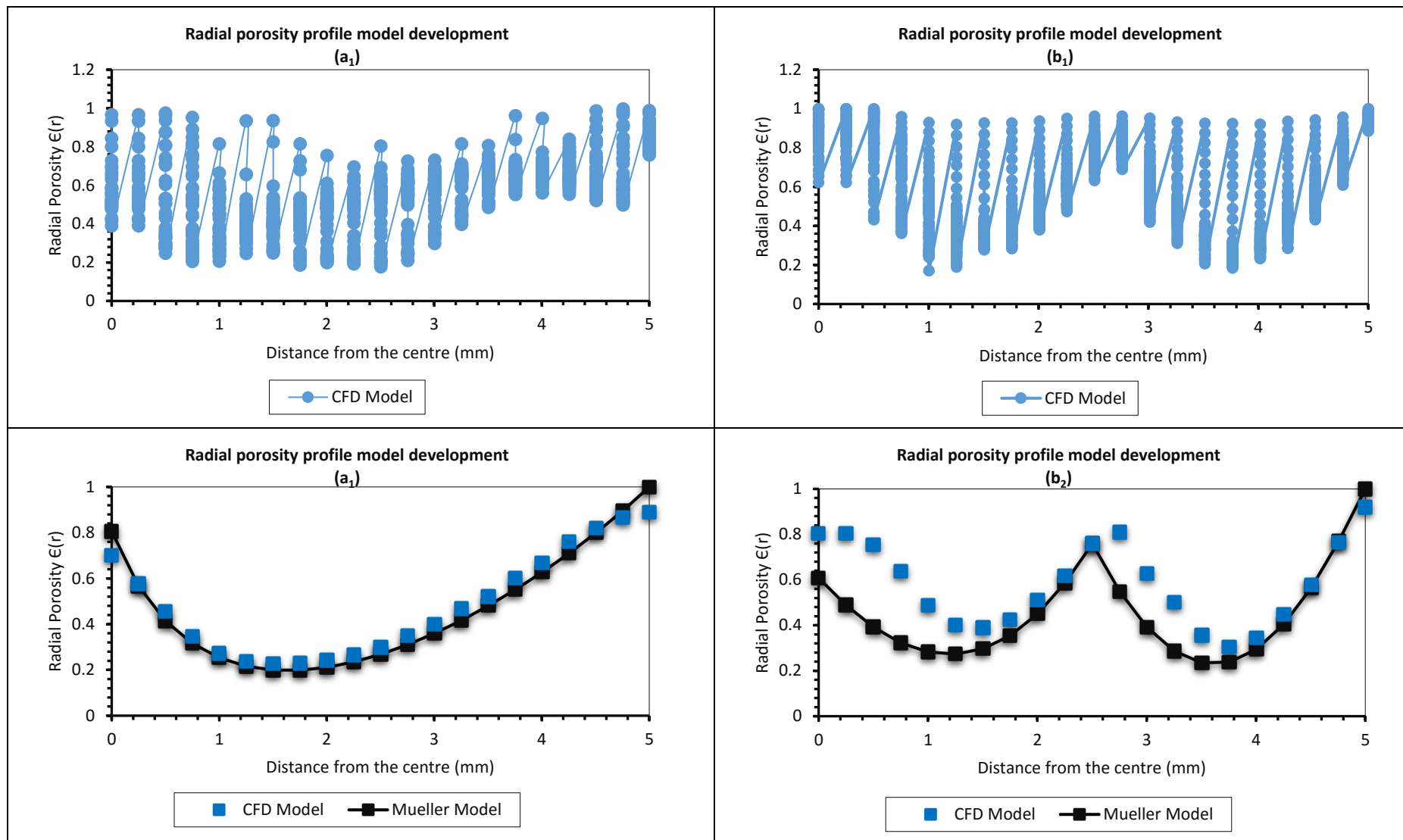


Figure (5.5). Radial porosity profile, $\epsilon(r)$ before averaging at (a₁) and (b₁) and after averaging (a₂) and (b₂) compared with Mueller's model; AR2 (left) and AR4 (right).

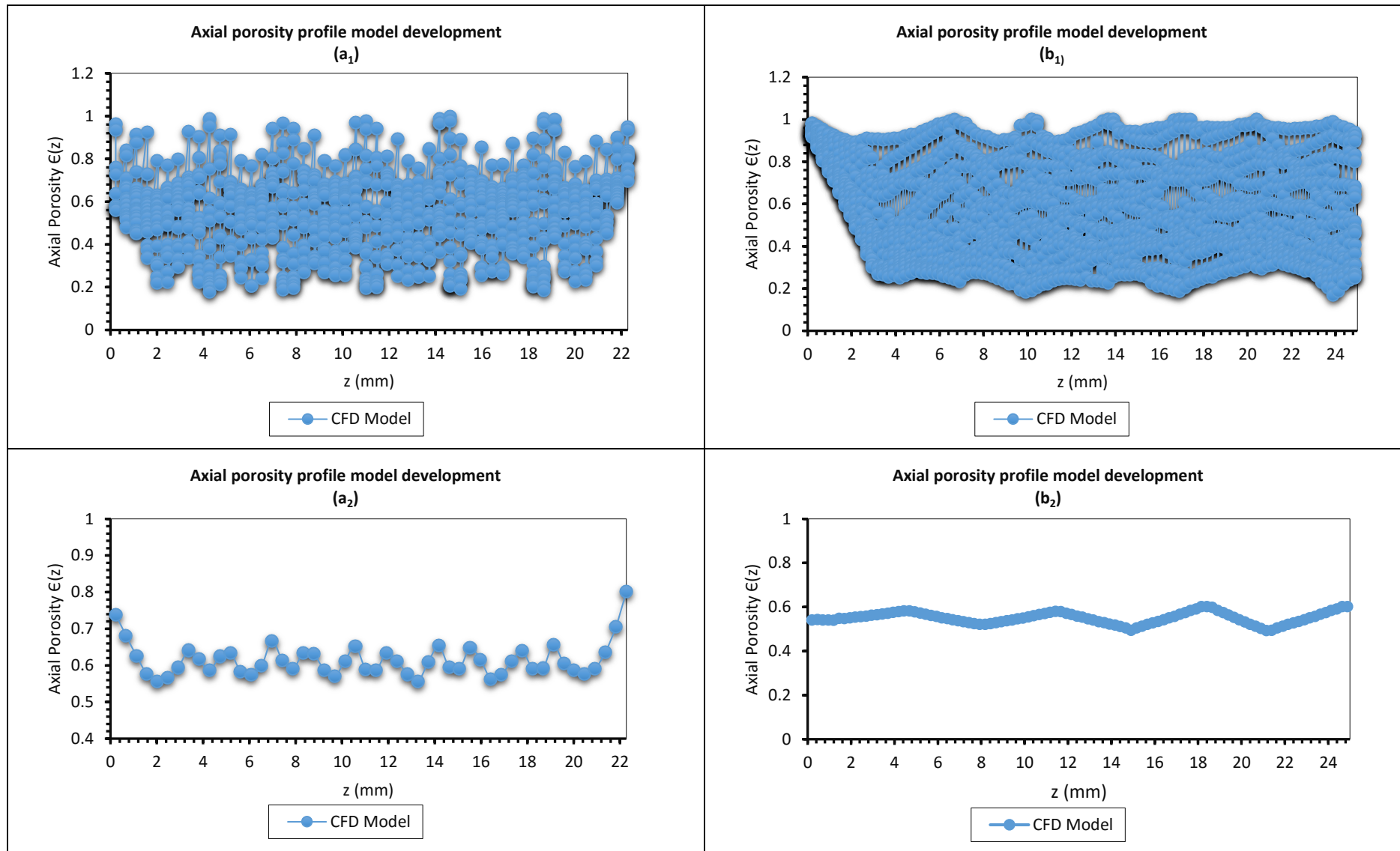


Figure (5.6). Axial porosity profile, $\epsilon(z)$ before averaging at (a₁) and (b₁) and after averaging (a₂) and (b₂); AR2 (left) and AR4 (right).

5.4 Pressure drop

Pressure drop estimation in trickle bed reactors is one of the very essential design parameters. It is one of the key interaction indices for the overall system and provides information on required feed pressures, therefore is useful in evaluation and prediction of other design parameters such as transport coefficients, wetting efficiency, and heat transfer coefficient. Two-phase pressure drop throughout the length of the bed is a function of (1) the reactor equipment such as column diameter, particle size and shape, and interiors; (2) operating variables such as gas/liquid velocity (flow regime); and (3) general properties of fluid such as density and viscosity of flowing fluid, surface tension, and surface characteristics. [171, 175] Operating pressure and temperature indirectly influence the pressure drop through fluid properties. [171]

Column diameter (D) has relatively lower impact on pressure drop as compared with the particle diameter (d_p). This impact is more significant for low aspect ratios (AR). For high (AR), variation of pressure drop with column diameter is almost negligible. For low (AR), variation of porosity close to the wall plays an important role. Owing to high porosity near wall, fluid bypassing happens, leading in a lower pressure drop [159, 171].

In large diameter columns, uniform distribution of liquid phase is to some extent difficult. Liquid maldistribution through the bed cross-section may result in lower interaction among the phases and consequently lower pressure drop. [171] Trickle bed reactors are often operated at low liquid velocity which results in incomplete wetting of particles. Pressure drop for incompletely wetted particles is often less than completely wetted particles. [171, 175]

The starting point in pressure drop estimation is most often the Ergun equation (5.23), this is widely used for calculating single-phase pressure drop in packed beds. This has been extended to the two-phase flow through packed beds in many studies [175, 191-192]:

$$\frac{\Delta P}{l} = \frac{150(1-\varepsilon_B)^2}{\varepsilon_B} \frac{u\mu}{d_p^2} + \frac{1.75(1-\varepsilon_B)u^2\rho}{\varepsilon_B^3 d_p} \quad (5.23)$$

The $\left(\frac{\Delta P}{l}\right)$ term in equation (5.23) is the effect of porous media on each phase pressure drop which is based on the relative permeability concept developed by Sàez and Carbonell [193]. The concept of relative permeability is very frequently investigated, and has been widely applied to the problems of multiphase flow pass through porous media. Basically, it is a concept that stems from the traditional Darcy's Law, a macroscopic equation based on average quantities for evaluating pressure drop through a porous medium at a fixed superficial velocity for the case of one phase flow. [157] Whether a fluid of viscosity μ is crossing through an

isotropic porous medium of absolute permeability κ in a homogeneous gravitation domain with the flow rate \mathbf{q} , then the pressure gradient ∇p towards the medium is given by Darcy's law;

$$\mathbf{q} = -\frac{\kappa}{\mu}(\nabla p - \rho \mathbf{g}) \quad (5.24)$$

Where \mathbf{g} indicates the acceleration due to gravitational forces and ρ is the density of that single phase fluid. For fluid flow in a horizontal direction, the term \mathbf{g} can be neglected. Whereas describing two phase flow in porous media, it becomes necessary to modify the equation referred to above, in order that while two fluids are simultaneously present in a porous medium, one fluid's ability to flow will be guided by the microscopic configuration of the second fluid. [157] To calculate the two-phase flow pressure drop which can be represented in dimensionless form with the help of Reynolds and Galileo numbers [157, 159 and 193-194]:

$$\left(\frac{\Delta P}{l}\right) = \frac{1}{k_\alpha} \left[A \frac{Re_\alpha}{Ga_\alpha} + B \frac{Re_\alpha^2}{Ga_\alpha} \right] \rho_\alpha \mathbf{g} \quad (5.25)$$

The constants A and B in equation (5.25) are the Ergun equation coefficients for single-phase flow in the packed bed and subscript α refers to either the gas (g) or the liquid (l) phases. The Reynolds and Galileo numbers are defined as:

$$Re_\alpha = \frac{\rho_\alpha \mathcal{U}_\alpha d_\alpha}{\mu_\alpha (1-\varepsilon)} \quad (5.26)$$

$$Ga_\alpha = \frac{\rho_\alpha^2 \mathbf{g} d_e^3 \varepsilon^3}{\mu_\alpha^2 (1-\varepsilon)^3} \quad (5.27)$$

$$d_e = \frac{6V_p}{A_p} \quad (5.28)$$

In order to consider the microscopic/local configuration of the second fluid and to define the ability to flow of one fluid in presence of other fluid, the term relative permeability (k_α) was introduced. Since the relative permeability parameter has been incorporated to accommodate the presence of a second phase, essentially it will be a function of phase saturation or holdup of that corresponding phase. [157, 159] To determine the dependence of the relative permeability on the saturation for each phase, Sàez and Carbonell [193], analysed several data sets for liquid holdup and pressure drop through a wide range of Reynolds and Galileo numbers in packed beds available in the literature until that time. They made the hypothesis that liquid relative permeabilities are only a function of reduced saturation (δ_l) which is represented by the ratio of effective volume of flow of the liquid phase to the available volume of flow considering that the static liquid holdup ($\varepsilon_{l,stat}$) represents a portion of the void fraction occupied by stagnant liquid. [159, 194]

$$\delta_l = \frac{\varepsilon_l - \varepsilon_{l,stat}}{\varepsilon - \varepsilon_{l,stat}} \quad (5.29)$$

The gas phase relative permeability was correlated as a function of the gas phase saturation. The empirical correlations were reported by Sàez and Carbonell [193]:

$$k_l = \delta_l^{2.43} \quad (5.30)$$

$$k_g = S_g^{4.80} \quad (5.31)$$

Where

$$S_g = 1 - \frac{\varepsilon_l}{\varepsilon} \quad (5.32)$$

The static liquid holdup can be calculated by the following correlation given by Sàez and Carbonell [193]:

$$\varepsilon_{l,stat} = \frac{1}{(20+0.9E_0)} \quad (5.33)$$

$$E_0 = \frac{\rho_l g d^2 \varepsilon^2}{\sigma_l (1-\varepsilon)^2} \quad (5.34)$$

After simplifying these expressions for a given particle diameter and the velocity of gas and liquid flows, the equation (5.25) can be used to compute the pressure drop.

5.5 Liquid holdup

Liquid holdup in trickle bed reactors is expressed in two ways: (1) total liquid holdup (ε_l) is the fraction of the bed volume occupied by liquid and (2) liquid saturation (δ_l) which is the fraction of external bed voidage occupied by liquid. Total liquid holdup (ε_l) is usually divided in two categories: dynamic liquid holdup ($\varepsilon_{l,dyn}$) and static liquid holdup ($\varepsilon_{l,stat}$). [175 and 195-196] Static liquid holdup which is a function of the particle diameter and properties of liquid, could not be measured and was estimated from the equations (5.33-5.34). [157, 159, 171 and 175]

The knowledge of liquid holdup, as a function of system's properties and operating variables is important to evaluate the extent of liquid-solid contact, average film thickness, gas-liquid-solid mass transfer, liquid residence time in the reactor, and hence, conversion of the reactants. It is consequently necessary to understand how liquid holdup could be different with (1) reactor equipment such as column diameter, particle size, and internals, (2) operating variables such as gas and liquid flow rates, and (3) general physico-chemical properties of fluids. [157, 159-162, 171 and 175]

Liquid holdup is sensitive to alteration in bed diameter at low aspect ratio (AR) and increases with the bed diameter for particle size [159, 171]. For smaller column diameters, flow bypassing findings in lower pressure drop which lead to low gas-liquid interaction. Accordingly, liquid holdup is higher for the lower diameter columns where flow bypassing

happens. Nevertheless, for larger diameter columns, liquid holdup is less sensitive to the column diameter because of the wall impact is negligible [171, 175]. Liquid holdup is significantly sensitive to particle diameter than bed diameter due to higher specific area of solid particles for smaller sized particles which lead to higher liquid phase retention and holdup [159, 171 and 176].

5.6 Particle wetting and liquid-solid covering

The state of particles wetting by flowing liquid is another important parameter required for design calculations in trickle bed reactors. Among the varied types of multiphase reactors, this phenomenon is unique in the trickle bed reactors and its quantification is a hard task to some extent [175]. Non-uniform liquid distribution on the catalyst particles leads to liquid maldistribution and therefore causes various degrees of wetting. Two types of wetting phenomenon are normally observed in the trickle bed reactors: external and internal wetting of the catalyst particles. [171] External wetting (η_{CE}) of the particles is the fraction of the catalyst external area that is covered by flowing liquid, while internal wetting (η_I) is the fraction of the internal pore volume in the catalyst particles that are liquid-filled. Away from liquid maldistribution effects, porosity and particle size of the bed have an impact on the wetting efficiency of the bed. [171, 173 and 175] Wetting efficiency decreases with increase in particle diameter. This trend could be ascribed to two parameters: liquid holdup and capillary pressure. To make efficient wetting, it is critical to use smaller-sized particles, but this eventually will be at the expense of increase in pressure drop [159, 171 and 175]. For small laboratory reactors, dependency of wetting efficiency on liquid velocity is represented by the following correlation which is based on the available literature data in the low gas-liquid interaction regime [167-169 and 197]:

$$\eta_{CE} = 1.617 Re_L^{0.146} Ga_L^{-0.0711} \quad (5.35)$$

The above correlation can as well be represented as a relation between external wetting efficiency and the dynamic liquid saturation defined by:

$$\omega_{d=\varepsilon_{l, dyn}}/\varepsilon \quad (5.36)$$

$$\eta_{CE} = 1.02 \omega_D^{0.224} \quad (5.37)$$

5.7 Results and Discussion

5.7.1 Impact of liquid velocity on pressure drop at different gas velocity

Figure (5.7) shows the relationship between pressure drop in the bed and the liquid velocity at a various gas velocity values. The results validate that any increase of velocity of the liquid or the gaseous phases would promote pressure drop and demonstrates both liquid and gaseous friction. Pressure drop increases with increase in liquid velocity and at a particular gas velocity and it is higher for higher gas velocity, as a result of local flow path for gas phase which is blocked by liquid pockets/plugs and results in the formation of high gas-liquid interfacial zones.

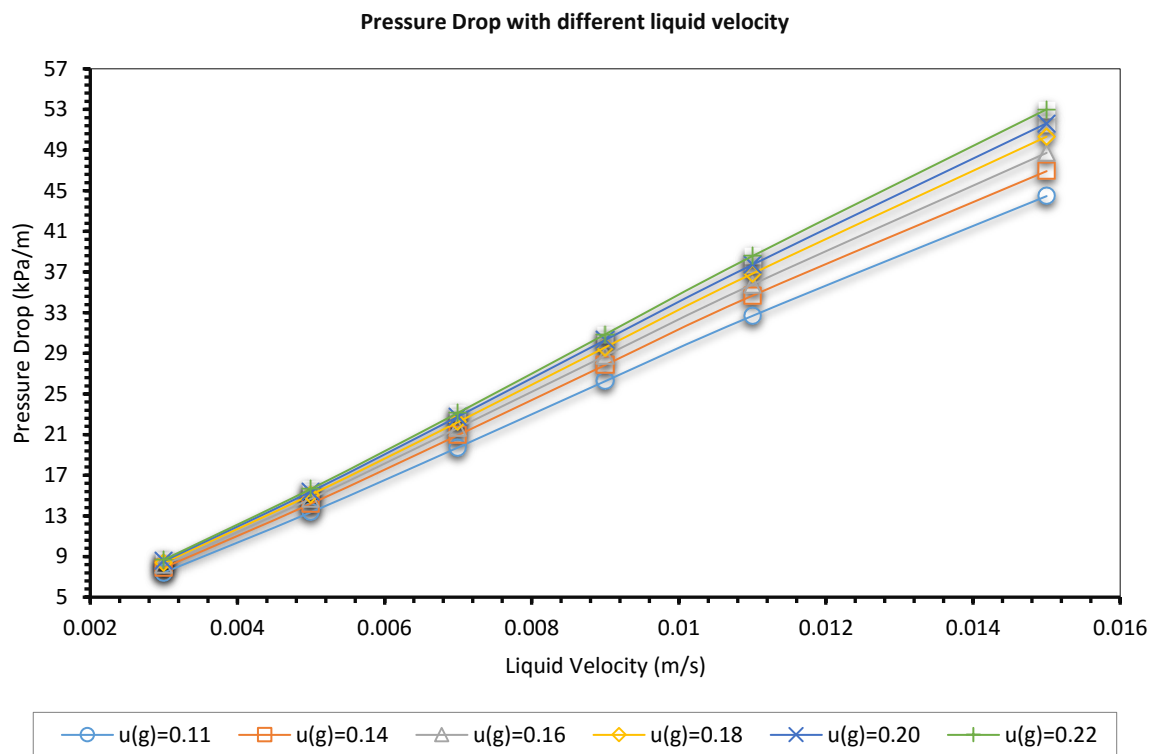


Figure (5.7) Effect of liquid velocity on pressure drop at different gas velocity.

5.7.2 Impact of particle diameter on pressure drop at different liquid velocities

Pressure drop is sensitive to the particle packing characteristics. Influence of particle size on pressure drop is shown in Figure (5.8). It can be clearly seen that the pressure drop increases with a decrease in the particle diameter due to extended zigzag path of fluid in the bed, particularly with the smaller-sized particles. Accordingly, the particles should be used for a range that is convenient to achieve suitable balance of pressure drop and catalyst usage. Similar trend results were reported Gunjal et al. [159] by using 2D modelling of the three-phase

Eulerian concept of interaction between the phases of Attou and Ferschneider's theory [158] and relying on a drag force model for the film shape regime [159].

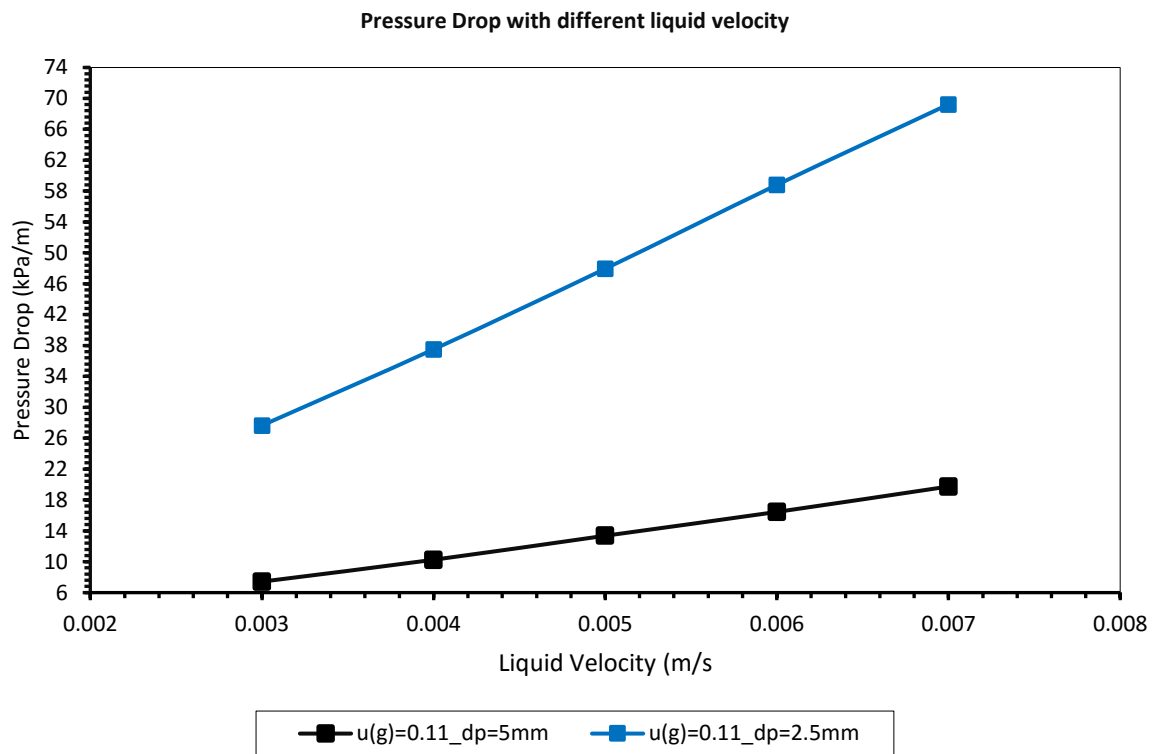


Figure (5.8) Effect of particle diameter on pressure drop at different liquid velocity.

5.7.3 Impact of particle diameter and gas velocity on pressure drop at different liquid velocity

The effect of gas velocity on pressure drop is shown in Figure (5.9). It can be seen that when the gas velocity increases, the transition from trickle flow to pulse flow occurs at a lower liquid velocity. At higher gas velocity, transition starts early and there is a much increment in pressure drops, and this phenomenon related to the instability occurring in the liquid film due to the shear exerted by the gas phase. In other words, accumulated excess liquid generates blockage to the gas flow passage which finally causes pulse formation. Besides, by through visible observations on a change in slope of measured pressure drop or liquid holdup with respect to gas or liquid velocities might as well appear the transition to the pulse flow regime. In addition, it should be noticed that the transition to pulse flow gets delayed for larger-sized particles. Similar trend results were reported Gunjal et al. [159].

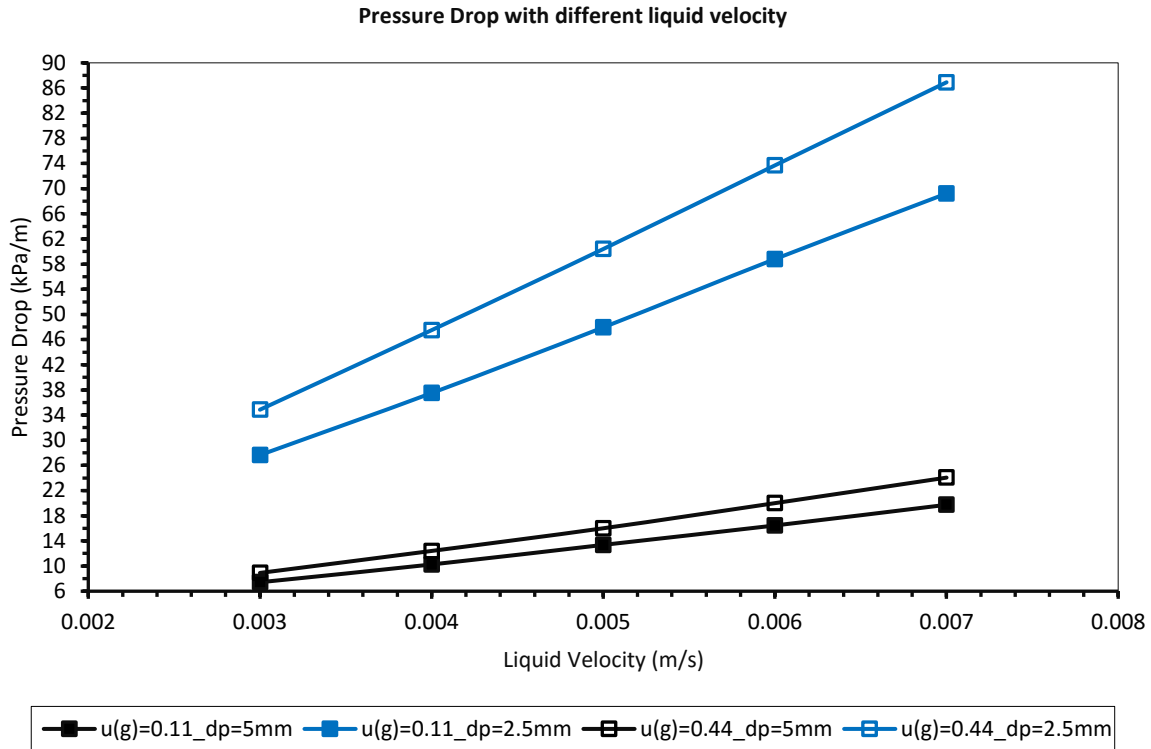


Figure (5.9) Effect of particle diameter and gas velocity on pressure drop at different liquid velocity.

In Figure (5.10) comparison between the CFD results of pressure drops with the experimental data from Szady and Sundaresan [166] and numerical simulations from Atta et al. [157] and Abdolkarimi [194] are presented. Based on the experimental data chosen from Szady and Sundaresan [166], only the upper branch of pressure drop curve was taken, corresponding to conditions of bed where capillary pressure can be neglected. The results are consistent with Abdolkarimi [194] and agrees relatively less with those obtained by Szady and Sundaresan [166] as well as by Atta et al at a constant gas superficial velocity of 0.22 (m/s) and these results are even more consistent at low liquid velocity values due to that with increase of liquid velocity, the regime moves gradually towards the transition zone.

In addition, the results of simulation were compared with experimental and model prediction data by Gunjal et al. [159] as shown in Figure (5.11). It can be seen that the proposed model predictions holds fairly good agreement with those predicted by Gunjal's simulation. [159] The reason behind this deviation could attributed to that Gunjal's simulation was based on three-phase Eulerian concept in which the interaction between the phases was developed theoretically by Attou and ferschneider, and also, they have used the definition of modified Eötvos number (E_0) while calculation static liquid holdup, $E_0 = \frac{\rho_l g d^2 \varepsilon^2}{\sigma_l (1 - \varepsilon^2)^2}$ in which ε^2 has been used as an alternative of ε in the denominator. Moreover, this observation showed that at higher

velocities, transition regime occurred in flow system, leading to a larger amount of gas-liquid interfacial interaction, which results in higher pressure drop values. [159]

Finally, in Figure (5.12), model prediction was also studied against the experimental data of Specchia and Baldi [198] for different gas superficial velocities at a constant liquid velocity of 0.003 (m/s). It shows that the predictions are satisfactory. It is interesting to see that through these comparisons, this model validates well the low interaction regime of gas-liquid phase of the trickling flow.

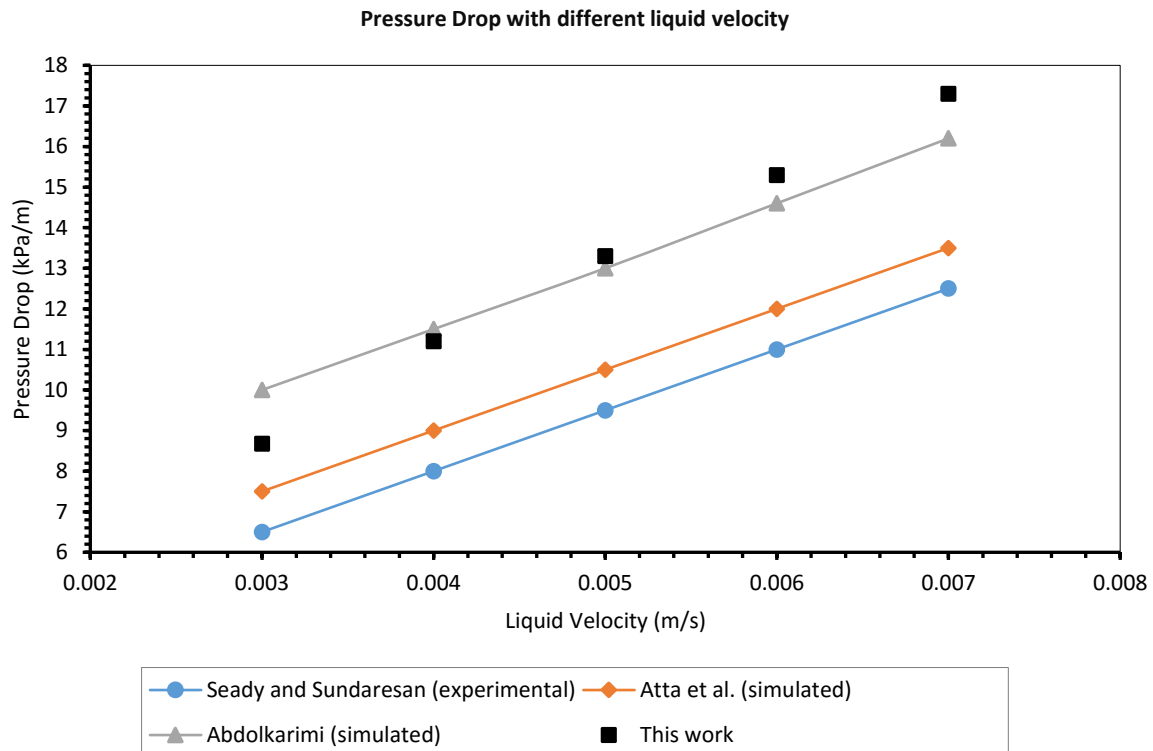


Figure (5.10) Comparison of effect of liquid velocity on pressure drop with literature data at gas velocity 0.22 (m/s).

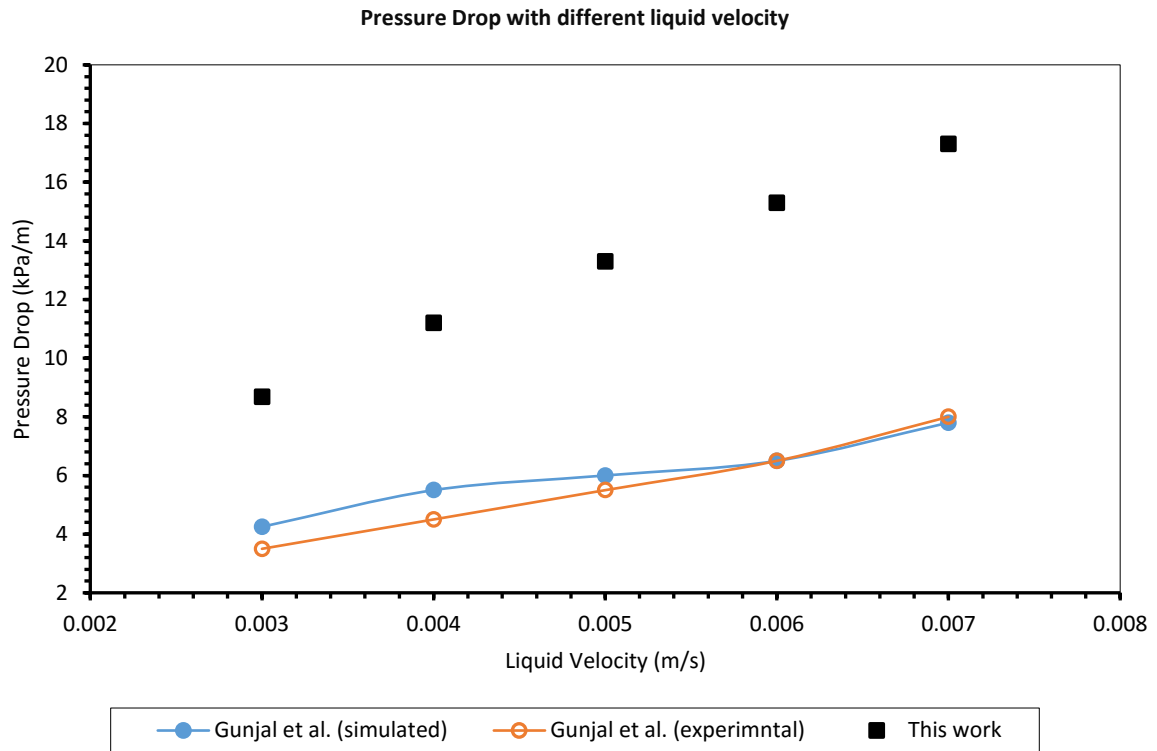


Figure (5.11) Comparison of effect of liquid velocity on pressure drop with data of Gunjal et al. (at gas velocity 0.22 (m/s)).

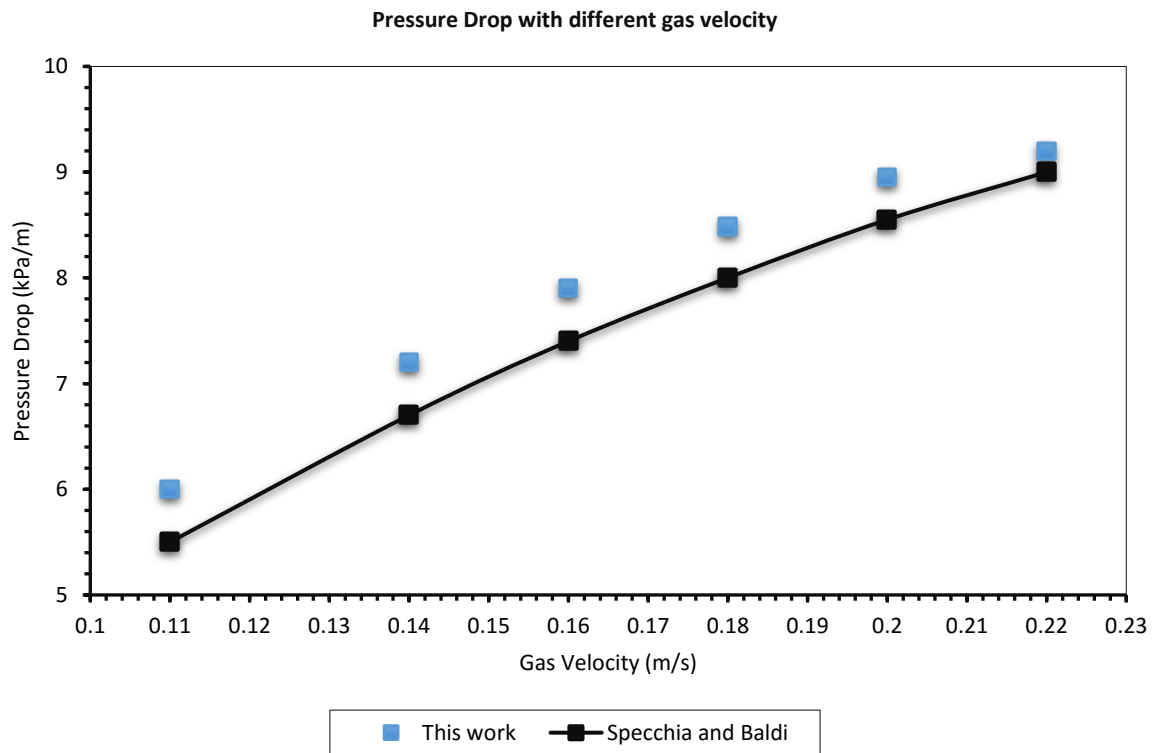


Figure (5.12) Comparison of effect of gas velocity on pressure drop with Specchia and Baldi (at liquid velocity 0.003 (m/s)).

5.7.4 Impact of variation in liquid and gas velocities on liquid holdup

Figures (5.13) and (5.14) indicate the variation of liquid holdup with variation in liquid and gas velocities. The liquid holdup increased with liquid velocity and decreased with increase in gas velocity. The increase of liquid holdup with liquid velocity was driven by the displacement of gas phase by the liquid. In a trickle flow regime, this displacement occurs until liquid occupies the maximum possible region. When the gas velocity increases the mean residence time of the liquid decreases necessarily because of the greater shear at the gas liquid interface, leading thus to a decrease in liquid fraction in the column. The rate of decrease in liquid holdup is more rapid at low gas velocity than at high gas velocity. For a particular liquid velocity, the sudden increase in the gas velocity drives expansion into the space limiting the liquid velocity. But at a higher gas velocity, the liquid holdup is almost constant. The liquid holdup is seen to be more sensitive to gas velocity than the liquid velocity. Similar trends were reported earlier by Atta et al., Gunjal et al. and al Jiang et al [157, 159 and 199].

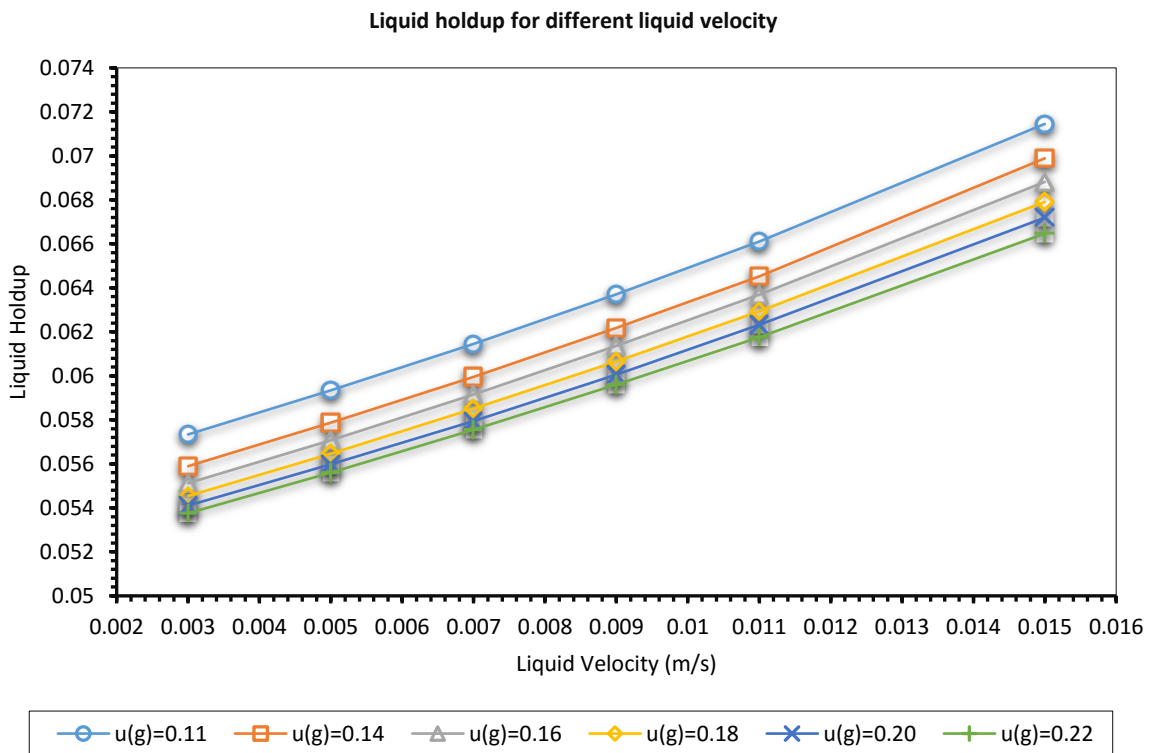


Figure (5.13) Effect of liquid velocity on liquid holdup at different gas velocity.

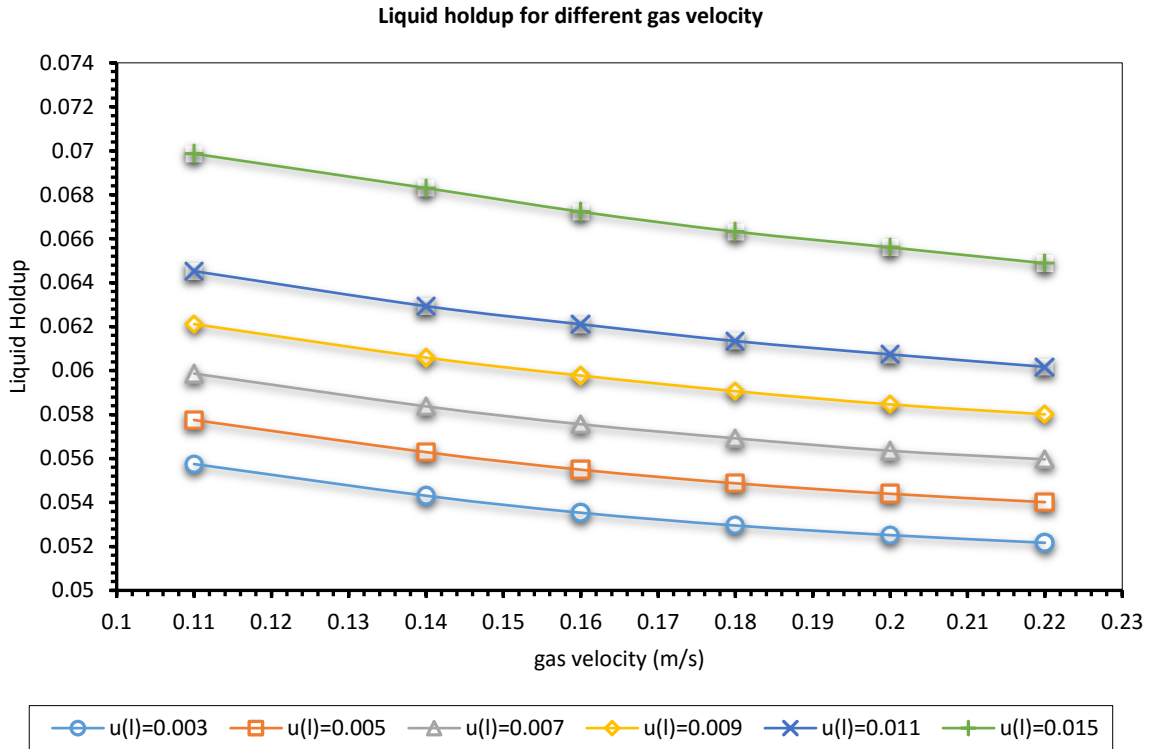


Figure (5.14) Effect of gas velocity on liquid holdup at different liquid velocity.

5.7.5 Impact of gas velocity on liquid holdup with column height at a particular liquid velocity

Figure (5.15) and (5.16) show the variation of liquid holdup with column height at gas velocity ranging from 0.11 to 0.22 (m/s) and two liquid velocities at 0.003 (m/s) and 0.015 (m/s), respectively. It is noticed that liquid holdup follows first a relatively steady trends from the bottom of the column and along the packing region and then increased values at the region above the packing, and thus accumulation of the liquid takes place at the gaseous region located at the front of packing. The gradient of such increase is more prominent for lower liquid velocity and almost equal distribution is noticed at higher liquid velocity. The liquid holdup shows a noticeable gradient value when the liquid velocity is operated at 0.003 (m/s). Nevertheless, it shows a relatively flat profile along the length of the column when the velocity is increased to 0.015 (m/s).

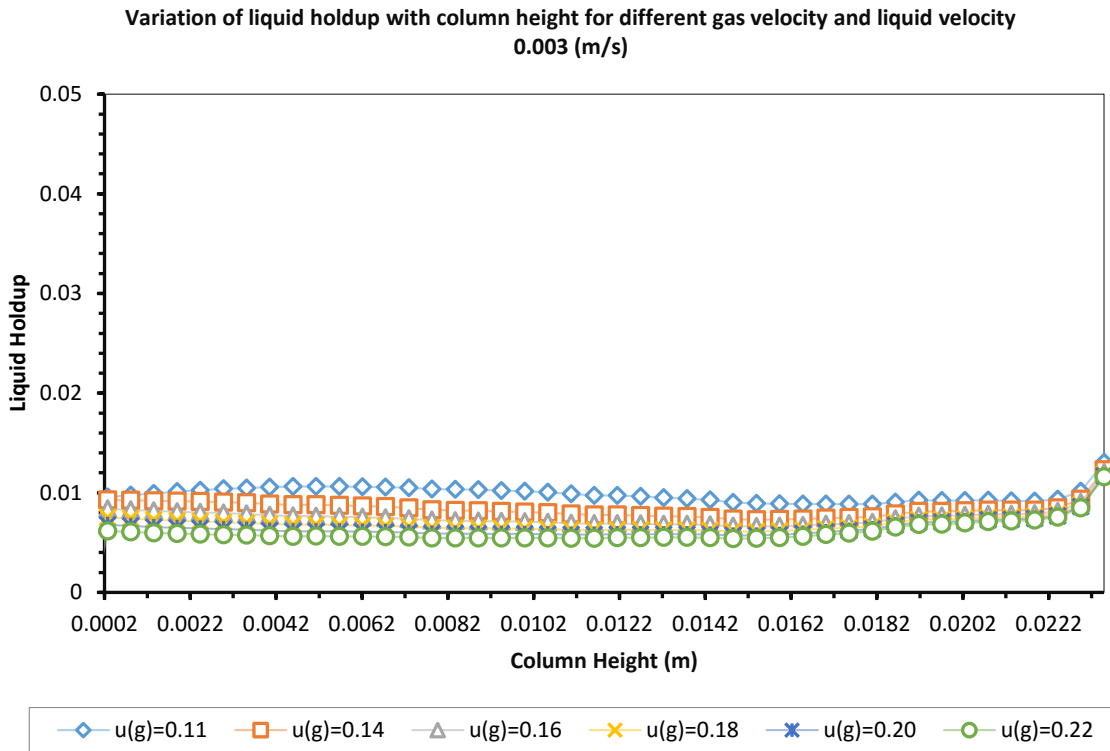


Figure (5.15) Effect of gas velocity on liquid holdup with column height (at liquid velocity 0.003).

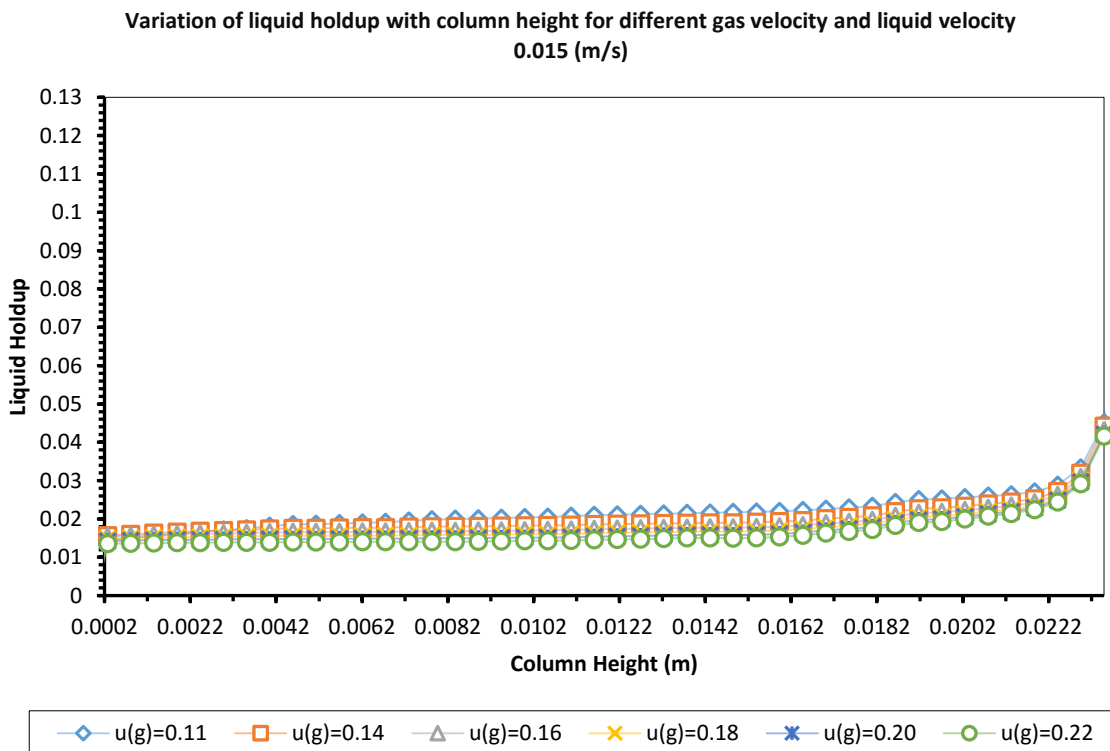


Figure (5.16) Effect of gas velocity on liquid holdup with column height (at liquid velocity 0.015).

5.7.6 Impact of gas velocity on liquid holdup with radial variation at a particular liquid velocity

Figures (5.17) and (5.18) show the radial variation of liquid holdup at a particular bed height for different gas velocities and liquid velocities of 0.003 (m/s) and 0.015 (m/s), respectively. The Figures show that the liquid holdup is low near the wall and then increases toward the central part of the column and then once more decreases at the other end of the wall. This is due to high porosity near the wall for low AR packed bed allowing more gas to flow in the vicinity of these regions. In addition, the liquid holdup shows a noticeable gradient value at central part of the column when the liquid velocity is operated at 0.003 (m/s). Nevertheless, it remains nearly constant at the same part when the velocity is increased to 0.015 (m/s).

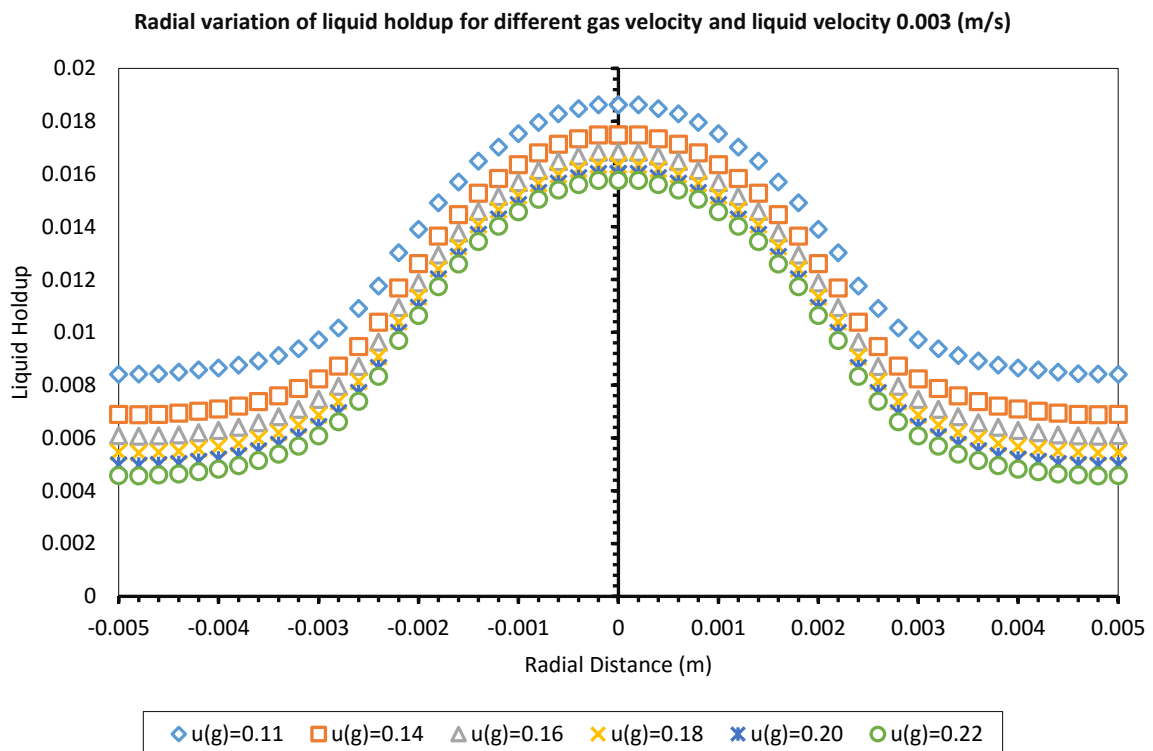


Figure (5.17) Effect of gas velocity on liquid holdup with radial variation (at liquid velocity 0.003).

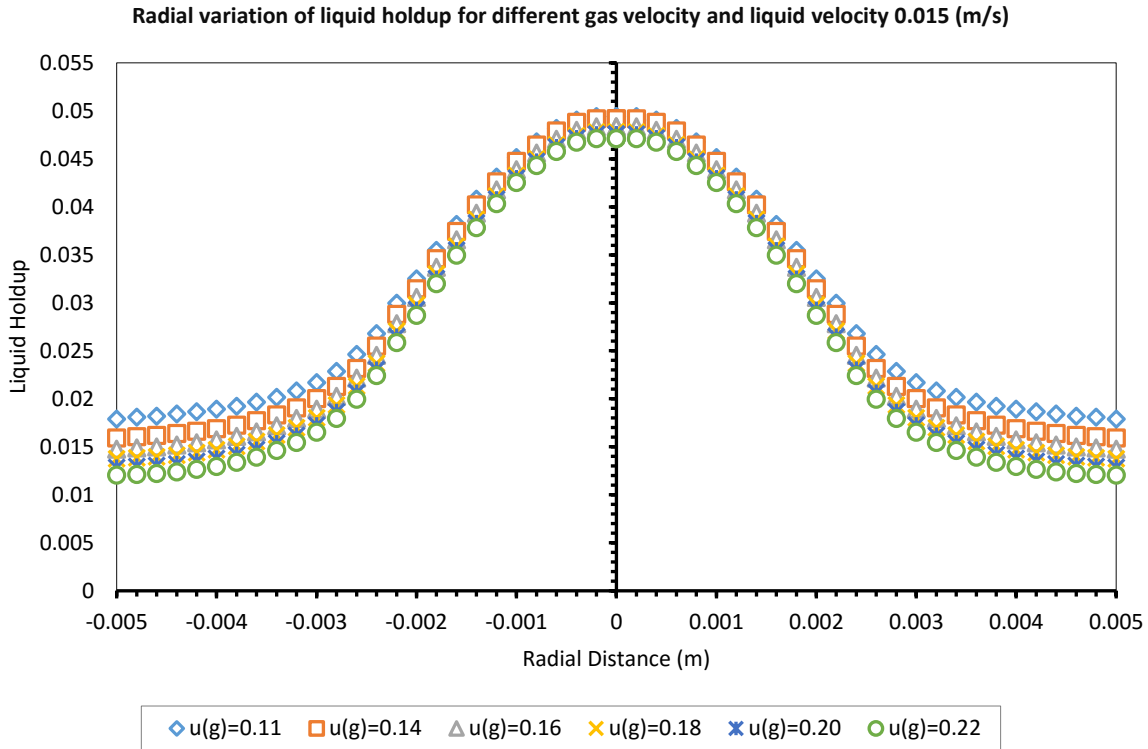


Figure (5.18) Effect of gas velocity on liquid holdup with radial variation (at liquid velocity 0.015).

5.7.7 Impact of particle diameter on liquid holdup and wetting efficiency

Figure (5.19) show the influence of particle size on liquid holdup. It can be seen that there is significant change in the observed liquid holdup with particle size due to a specific area of solid particles which is higher for the small size particles, leading to a better spreading and to higher liquid phase retention and holdup. For larger diameter particles, capillary forces are less dominant than gravitational forces and the liquid holdup is then substantially lower. Furthermore, particle diameter effects on the wetting efficiency of the bed are illustrated in Figure (5.20). The wetting efficiency decreased with increase in particle diameter. Besides particle diameter, external wetting efficiency is highly sensitive to the gas-liquid velocities. Liquid is insufficient to cover the particle surface especially at low velocities and therefore, partial wetting is unavoidable under such conditions. The effect of liquid velocities is significant on wetting efficiency of the bed as shown in the same Figure. The rate of decrease of wetting efficiency is significant at high liquid velocities.

These results of wetting efficiency were validated with those calculated using various correlations which are proposed by Mills and Dudukovic [167], Ring and Missen [168] and El-Hisnawi et al. [169] as shown in Figure (5.21) with averaged deviations of 4.08 %, 5.76 % and 3.89 %, respectively.

In Figures (5.22), (5.23) and (5.24), the flow distribution on an iso-surface with a liquid volume fraction for AR 2 and 4, at velocities, 0.003 (m/s) and 0.11 (m/s), for liquid and gas, respectively are visualized. The colour scale in same figures refers to the phasic volume fraction of fluid in which a blue colour is 100 vol. % of gas and red colour represents 100 vol. % of liquid. It can be clearly seen that the flow distribution such as droplets with time progressing until trickle flow gradually engulfed the whole domain and the all particles were wetted as shown in these Figures. The liquid distribution is sensitive to alteration in bed diameter at low aspect ratio and increases with the bed diameter for particle size. Consequently, Figure (5.24) indicates the trickle flow engulfed the whole domain and the particles with increasing time, which is clear even more at small diameters than large ones due to more coverage of the liquid distribution.

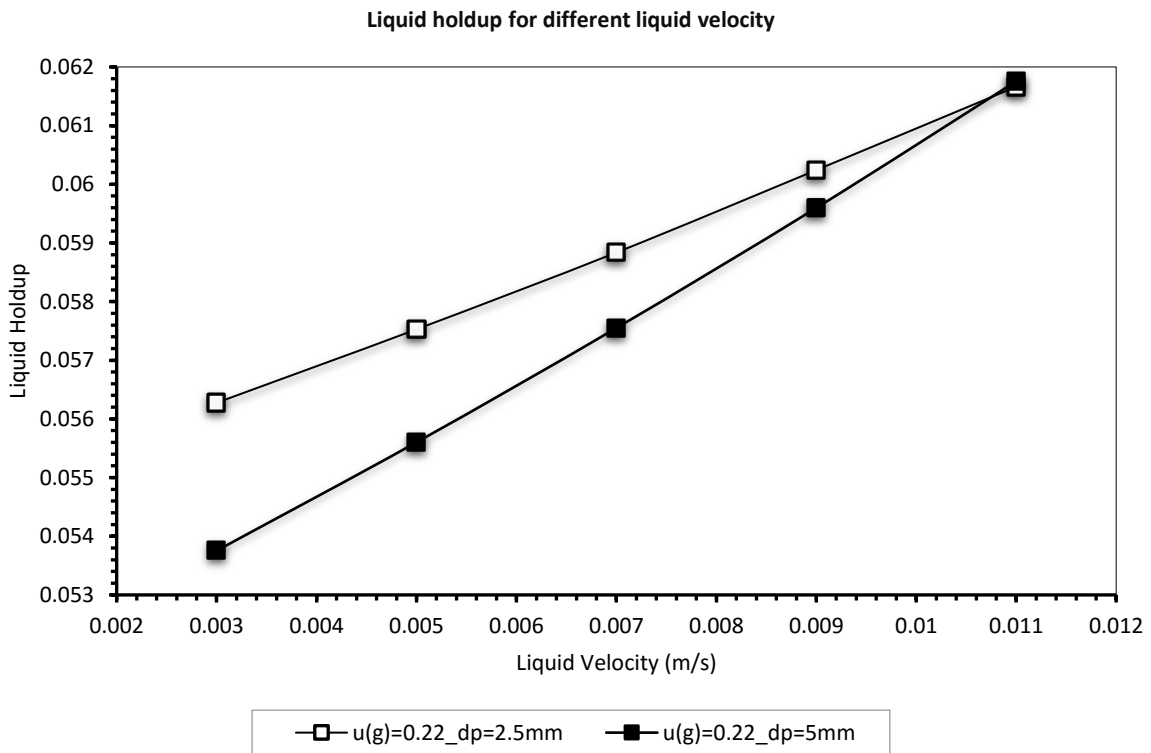


Figure (5.19) Effect of particle diameter on liquid holdup at different liquid velocity.

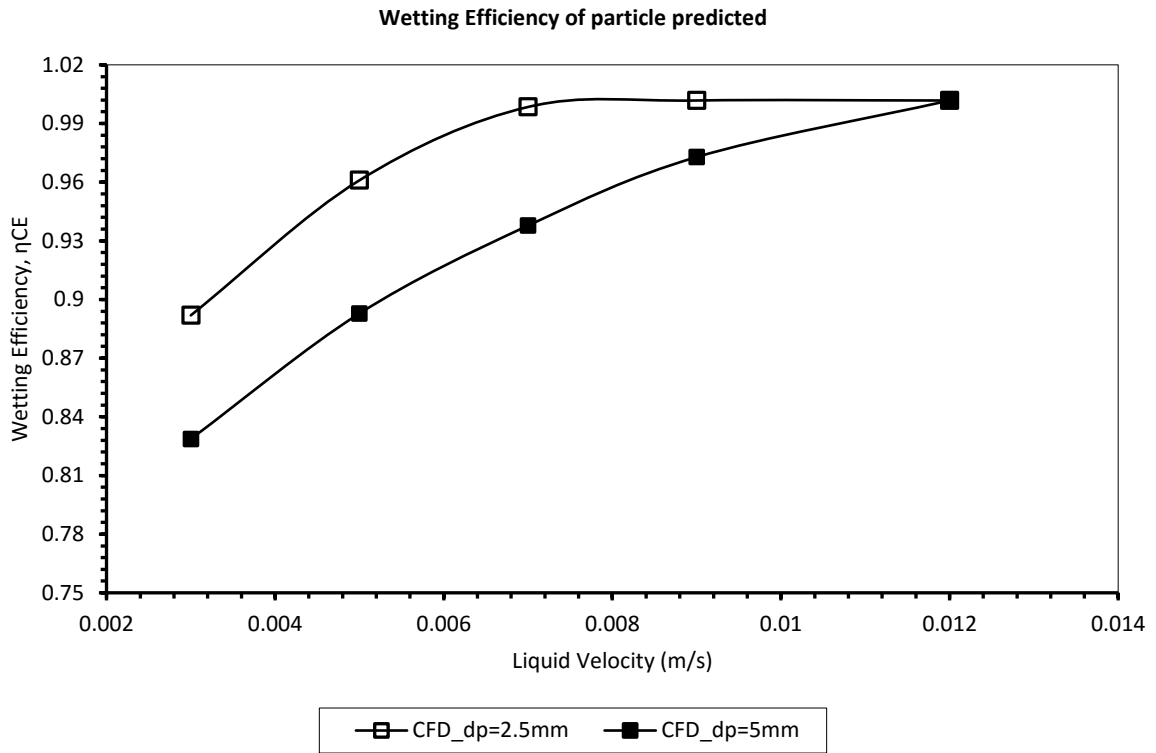


Figure (5.20) Effect of particle diameter on wetting efficiency at different liquid velocity.

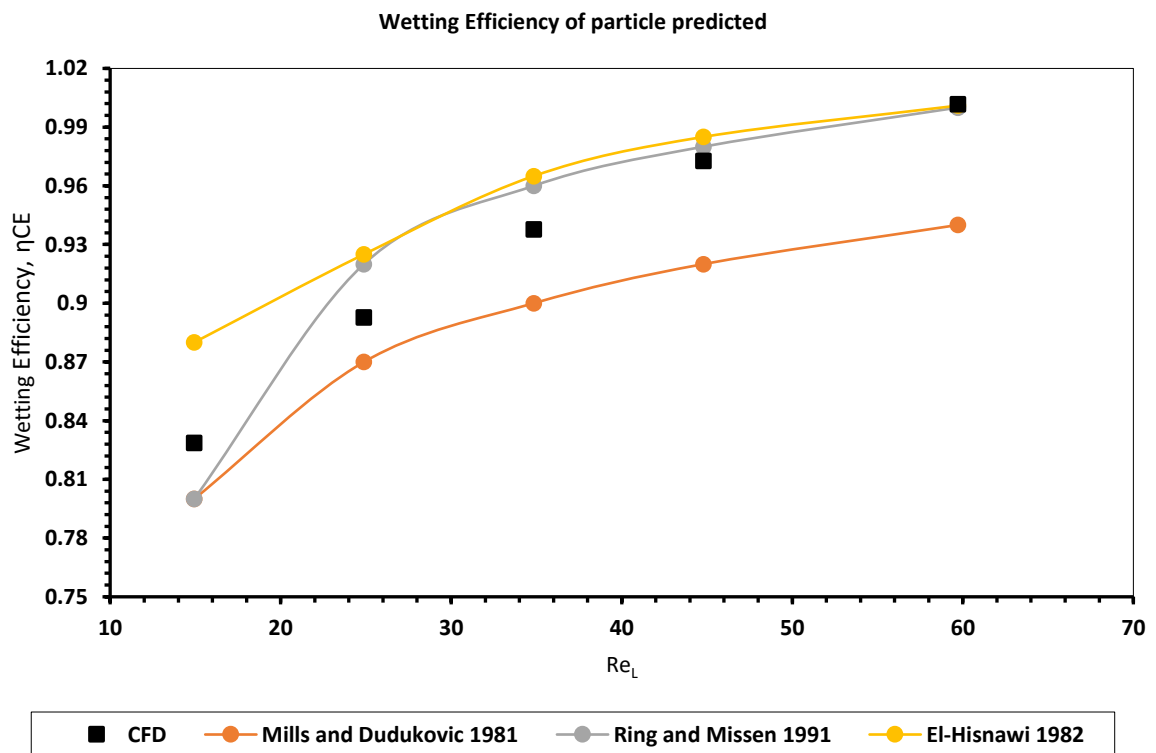


Figure (5.21) Comparison of effect of liquid velocity on wetting efficiency with literature data.

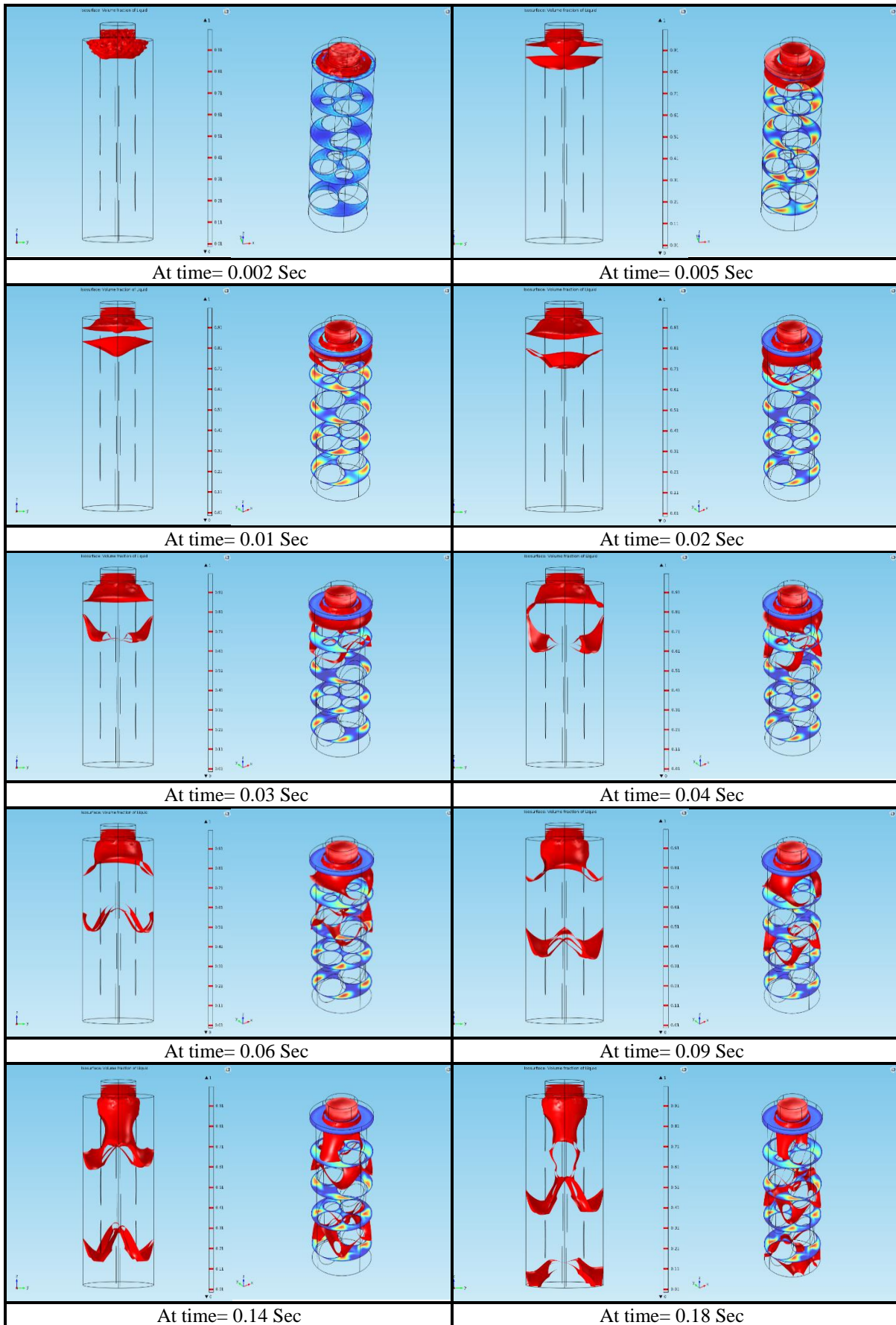


Figure (5.22) liquid flow distribution of iso-surface at liquid and gas velocity of 0.003 (m/s) and 0.11 (m/s), respectively; AR2.

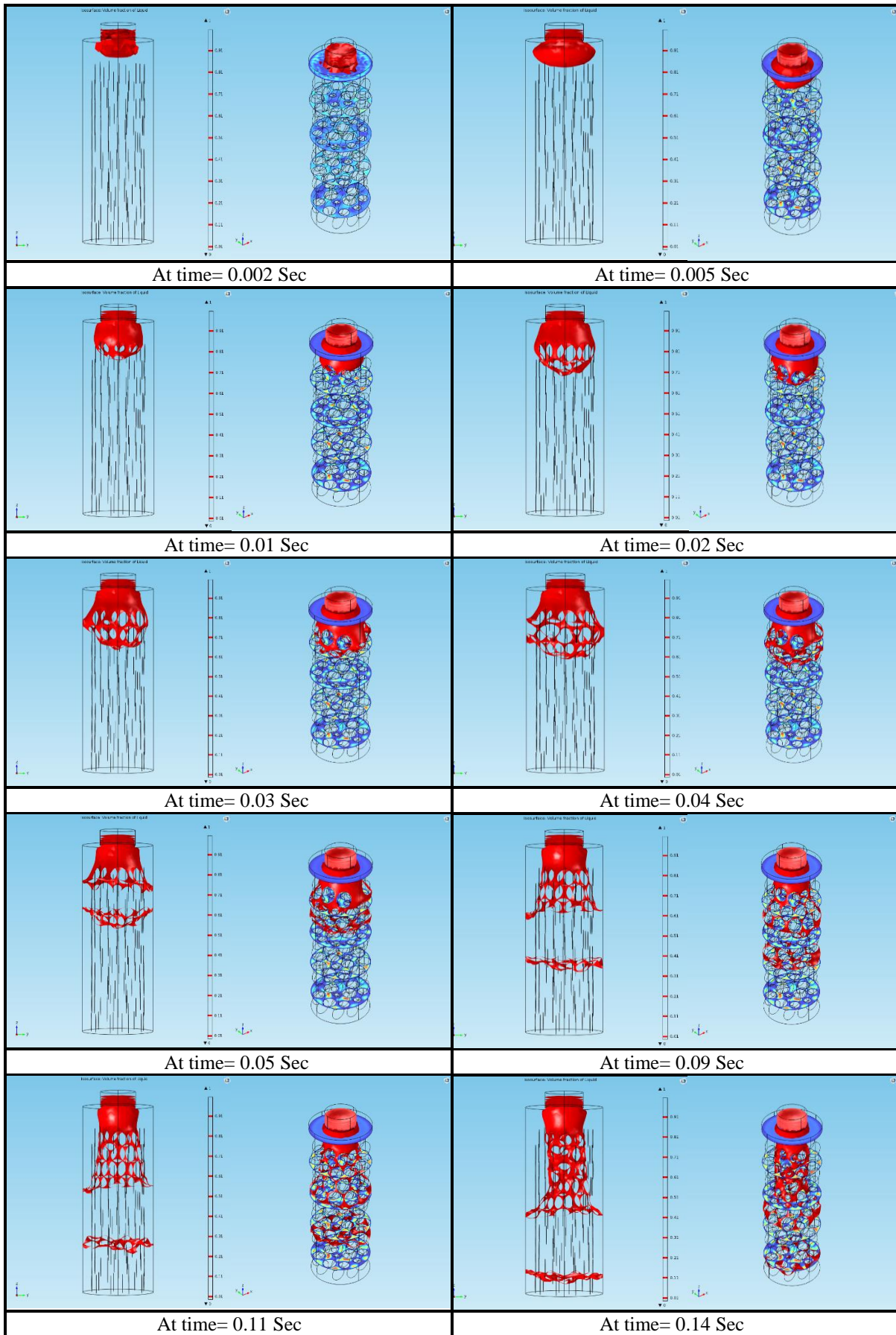


Figure (5.23) liquid flow distribution of iso-surface at liquid and gas velocity of 0.003 (m/s) and 0.11 (m/s), respectively; AR4.

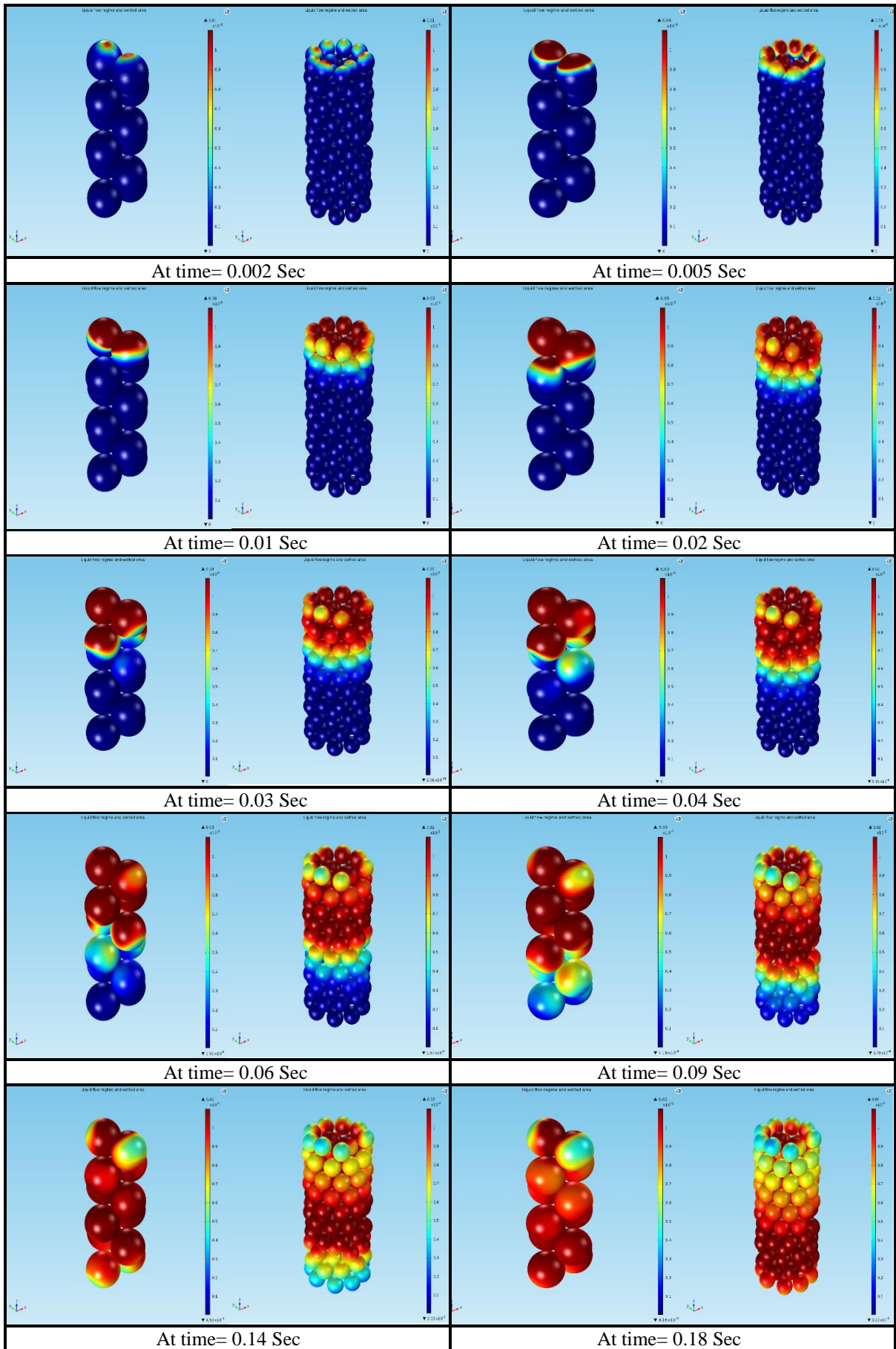


Figure (5.24) Liquid flow regime and wetted area at liquid and gas velocity of 0.003 (m/s) and 0.11 (m/s), respectively; AR2 and AR4.

5.7.8 Impact of flow mode operation on liquid holdup

From our knowledge, there are a few published works on CFD modelling of liquid holdup of gas/liquid flow operated in counter-current flow mode. The 3D modelling by CFD is even more problematic than the co-current owing to design issues including the packed beds, inlet and outlet geometries, boundaries setting conditions and requirements for transient operations. Liquid holdup and surface efficiency of the solid particles plays a significant role in the conversion of gas/liquid/solid catalytic reactors as shown in Chapter 6, and therefore it is worthwhile to investigate the mode of operations gas to liquid flow directions. Thus, it is necessary to study counter-current flow mode under realistic random packing to understand impact of liquid holdup and flow dynamics on mass transfer phenomena or conversion efficiency of the TBR. Herein in Figure (5.25), the results of the numerical simulation indicate that the liquid holdup in counter-current flow mode was higher than co-current owing to higher driving force and hence, it is expected to lead to promoted mass transfer rates as illustrated in Chapter 6.

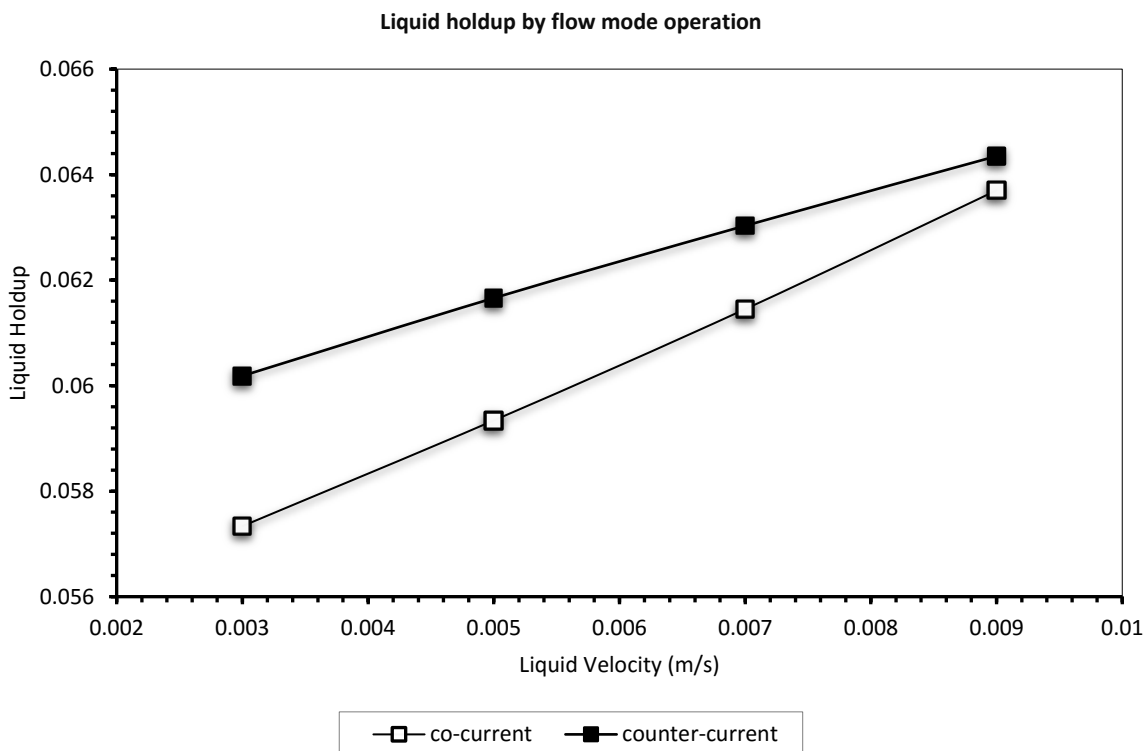


Figure (5.25) Effect of flow mode operation on liquid holdup, at gas velocity 0.11 (m/s).

5.7.9 Dispersion profiles by CFD particle tracking

Since the liquid holdup and surface wetting efficiency were observed to follow uneven distribution in the packed beds (Figures 5.15 -5.18 and 5.22-5.24), it is important to understand the dispersion and thus the down-flow trajectories taken by the liquid. These trajectories were investigated by 3D Lagrangian particle tracking procedure, which relies on the macroscopic mixing of tracer particles along the axial and the radial directions of the PBR. Herein, the particle tracking module of Comsol was coupled with the 3D fluid flow model to give trajectories to individual particles of similar trends to those developed by the carrying fluid. The particles were assumed to be of negligible mass and subject to bounce conditions at the fluid-solid interphase. The design of the packed bed required addition of an inlet for particle flow by using a small cylinder of 0.25 mm I.D. and 2 mm height at the top center of the packed bed. The size of the small cylinder was effective in terms of meshing requirements. About 100,000 particles were released, and the displacement of these particles was followed with time. Quantitative values of dispersion coefficients were then computed by accessing first the trends of individual particle positions with time. These positions were used to compute trends of the second moment or mean square deviation of positions of these particles along axial and radial directions according to equations described in Appendix C. These values served to calculate the asymptotic values of dispersion coefficients. The profiles of axial and radial dispersion coefficients normalized to molecular diffusion were added to Figure (5.26) along with those computed by the semi-analytical models of Freund and Delgado. [200-201] The prediction of axial and radial dispersion is in a good agreement with those obtained by literature models. It can be seen that axial dispersion values were between the two models of Freund. Unlike axial dispersion, radial dispersion is in good agreement with Freund model 1. Figure (5.27) shows horizontal and vertical maps of particle tracers in the packed bed.

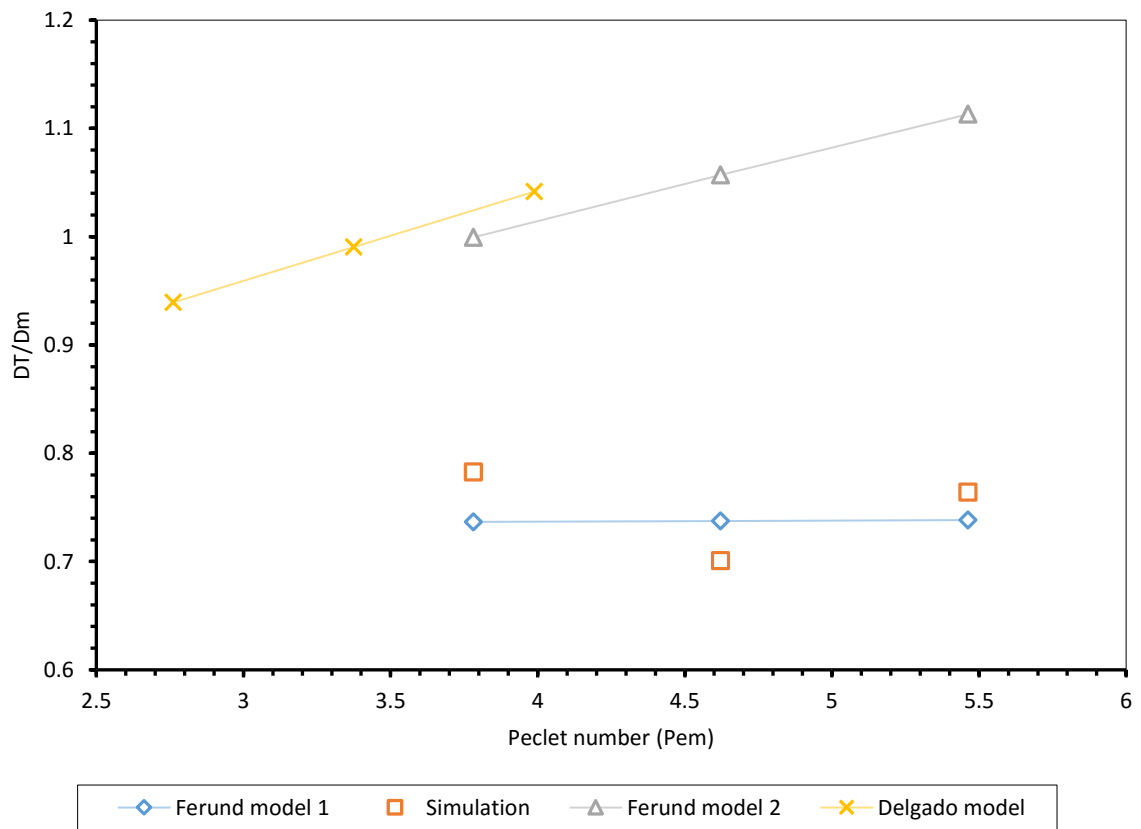
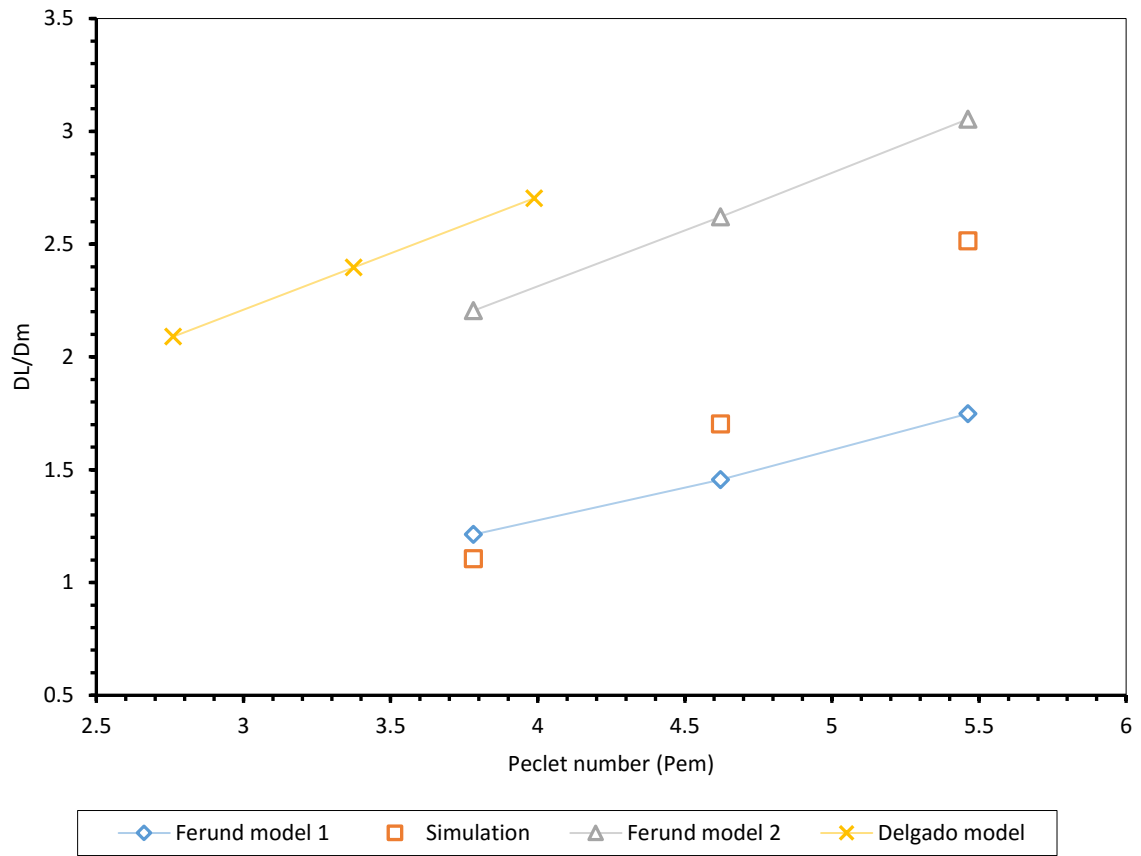


Figure (5.26) axial and radial dispersion along with flow dynamics; (a_1 , a_2), respectively for AR2.

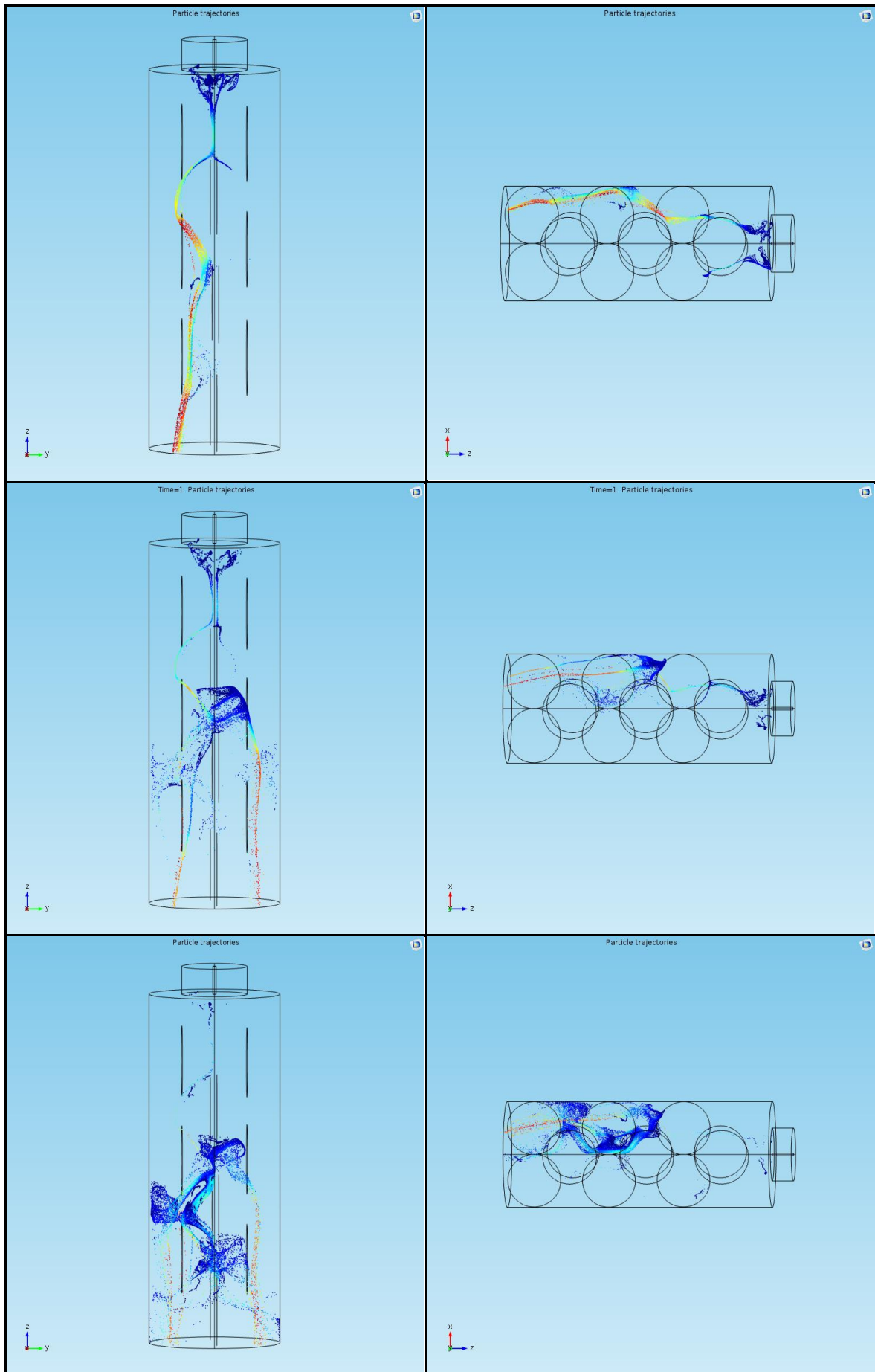


Figure (5.27) vertical slices of particle tracers at P_e of 3.78, 4.62 and 5.46, respectively for AR2.

5.8 Summary of the chapter

In this chapter, a two-phase Eulerian formulation model based on the porous media concept to simulate gas-liquid flow through trickle bed was carried out to investigate the behaviour of two-phase flow by using COMSOL Multiphysics® 5.0 using a transient 3D modelling. The following conclusions can be drawn from the results:

1. The 3D CFD modelling can provide a reliable data of the bed structure, including porosity, an averaged radial, axial porosity and porosity distribution profiles.
2. The structural porosity trends (3D, 2D and 1D) were compared with semi-analytical models the porosity profiles and were in a good agreement with the semi-analytical models such as Mueller's expression, especially in the zone near the wall. Similar oscillation trends with damping profiles towards the centre of the packed beds were observed. In addition, the average porosity obtained by CFD simulation was in reasonable agreement with Zou's model.
3. The CFD model was validated under the trickling flow regime and its predictions were compared with different sets of independent experimental liquid holdup and two-phase pressure drop data. The results were compared with the numerical results of Atta et al. which are based on two phase Eulerian formulation and the porous media concept and Gunjal et al. which are based on interaction between the three phases. The model was optimized in terms of mesh size and time step, and hence give sensible and good agreement for both hydrodynamic parameters.
4. A number of computational runs were performed to investigate axial and radial profiles of liquid holdup. The liquid velocity had more prominent effect on liquid holdup at higher values. Alternatively, the gas velocity had a pronounced impact at lower interaction regimes.
5. The CFD model was able to capture the influence of particle diameter on liquid holdup and pressure drop. Furthermore, it provided a wetting efficiency that was in a good agreement with data obtained by using relevant literature correlations.
6. The profiles of axial and radial dispersion coefficients normalized to molecular diffusion were compared with the semi-analytical models of Freund and Delgado. The prediction of axial and radial dispersion coefficients were in a good agreement with those obtained by literature models.
7. The simulation results by 3D modelling validated the promoted liquid holdup under counter-current mode operations and were compared with co-current mode operations

owing to higher driving force and hence, leading to a potential increase in the mass transfer as demonstrated in chapter 6.

The results by CFD predictions under both co-current and counter-current operations will be coupled with the catalytic reaction of H₂-H₂O exchange in the chapter 6, and local phenomena issues from interactions of fluid flow, mass transfer and reactions inside the TBR will be investigated, and impacts on conversion assessed.

Chapter 6

Analysis of hydrogen-water isotope exchange in a 3D trickle bed reactor

In chapter 4, the commercial Aspen Plus modular package, was found to be a promising tool to investigate the coupling of mass and heat transport, specific features of the reaction mixture and the synergic impact on isotope separation of the catalytic exchange process in a reactive stripping column. The results of modelling of reactive stripping process, including effects of significant design and operating parameters on the column performance were presented. Since the process simulation package however is still not able to offer local information at a particle catalyst level on fluid flow, gas/solid mass transfer and chemical reactions, 3D CFD modelling is a promising method to investigate interactions of flow, mass transfer and chemical reactions in a porous media of a catalytic packing. The isotopic exchange process is investigated by passing the hydrogen gas and liquid counter-currently as well as co-currently through a trickle bed catalytic column. Different simulation conditions of mass transfer with chemical reaction (Chapter 4) and fluid flow (Chapter 5) result in changes in the concentrations at the outlet of the isotopic exchange column and are discussed. These changes are assessed by looking at process performance in terms the conversion rate of HD gas into HDO_L. The process to be investigated is therefore the reactive scrubbing of HD from a contaminated H₂ gas by H₂O_L. Impacts of operating conditions such as the flow rate of hydrogen, flow rate of water, reaction temperature and height of catalytic bed are investigated and validated by experimental data and literature models in published works. The main objective of this chapter is to investigate local activity of the gaseous phase catalytic exchange and therefore the gas/liquid mass transfer was assumed to be fast enough to allow for sufficient mixing between the two phases. This assumption is justified by the results of Chapter 4 (section 4.3.2.3.2) where the mass transfer limitation between the gas and liquid phases was found relevant only at temperatures less than 310 K. Also, this assumption reduced the complexity of the 3D modelling by avoiding empirical models of gas/liquid mass transfer to be used. This chapter is divided into three main sections: The first introduces the models associated with mass transfer inside an LPCE process taking place in a reactive scrubbing column under both co-current and counter-current operations. The second chapter looks at the 3D modelling of

two-phase flow inside the LPCE column under both co-current and counter-current operations. The third section presents impacts of various design and operating parameters on process performance and the results are discussed and validated by literature data and models.

6.1 Introduction

Separation of hydrogen isotopes is one of the most significant matters in the field of heavy water production. [101] The topic of separation and purification of deuterium and tritium has attracted considerable interest of scholars in the whole world. [71] Several advanced technologies have been developed for separation of hydrogen isotopes like; chemical exchange, liquid hydrogen distillation, cryogenic adsorption, palladium or palladium membrane diffusion, thermal diffusion, laser separation and electrochemical isotope separation and so on. [71] Among them, chemical exchange has been vastly applied to production and upgrading of heavy waters along with tritium removal from light waters or heavy waters, and recovering tritium for fusion reactors. [71] As a result of various research activities, the hydrogen isotopic exchange process by using liquid phase catalytic exchange (LPCE) is recognized as one of the most suitable process for water detritiation and heavy water production. [202] The separation of deuterium, by hydrogen-water exchange process (LPCE), due to its very high separation factor and relatively mild operating conditions, makes it a viable alternative to the hydrogen sulphide-water ($\text{H}_2\text{S}-\text{H}_2\text{O}$) and ammonia-hydrogen (NH_3-H_2) exchange processes. [64 and 230-204] This process was formerly developed by the Atomic Energy of Canada and applied to various hydrogen isotope applications. [205] A laboratory-scale LPCE method was built and operated at Chalk River Nuclear Laboratories and some other countries. [202] Thereafter, Romania and Korea independently developed a comparable processes based on a trickle-bed reactor packed with a hydrophobic catalyst. [202] LPCE columns with different structures have been developed. Nevertheless, the designs of these exchange columns have not been reported. [202] The trickle-bed-type reactor has an important advantage in that the structure of the column is quite simple. [69] In the case of the trickle-bed-type reactor, hydrophobic catalysts and hydrophilic packings are packed within the column, based on this structure, it leads to a smaller column height than the multistage type. [69] This mixture is key element for LPCE, and called mixed catalytic parking and was ascertained to be more efficient than the layered or separated bed. [101]

The heart of the LPCE process is that it contains a hydrophobic catalyst because traditional catalysts lose their activity owing to contact with liquid water. [85] On the other hand, hydrophobic catalysts, which allow the transport of gaseous reactants to and from active centres

and prevent the passage of liquid water, allow for the success of the LPCE process. Therefore, the use of a hydrophobic catalyst for the hydrogen-water isotope exchange reaction was first proposed as patent by Steven in 1972. [102] Since this initial development, and by during several of decades of research and development, there have been mainly three types of hydrophobic catalysed which were developed and selected to promote isotopic exchange by liquid phase catalytic exchange including: (a) Pt/C/inert carrier (Pt/C/IC); (b) Pt/C/polytetrafluoroethylene (Pt/C/PTFE) developed and used in different ways in Germany, Belgium, Romania and Canada; and (c) Pt/styrene-divinylbenzene copolymer (Pt/DSB) developed and applied in Japan, Russia and Korea [101] .

6.2 LPCE Mathematical Model

6.2.1 H₂-H₂O exchange reaction

When D₂O is mixed with H₂O, there will be HDO molecules in the water. The transfer between isotope molecules is called isotopic exchange reaction. Hydrogen isotopic exchange reaction includes simple exchange and disproportionation reactions as will be discussed later. The reaction of H₂- H₂O isotopic exchange proceeds through a similar path with H-D, H-T and D-T exchanges. In this chapter the H-D exchange is considered owing to abundant literature compared to the two others, helping thus the validation of the simulation results.

6.2.1.1 Kinetics of H₂-H₂O liquid exchange reaction

The kinetics of the isotopic exchange plays an important role for the prediction of mass transfer rate. In this section the kinetics model of the exchange of deuterium between the liquid phase and the gaseous phase is defined by a simple expression.

The exchange is simplified by a single reaction between deuterated water and hydrogen gas as expressed by reaction (6.1),



The kinetic model relevant to the exchange process is expressed by equation (6.2),

$$\frac{dC_{HD}}{dt} = k_1 C_{HDO} C_{H_2} - k_{-1} C_{HD} C_{H_2O} \quad (6.2)$$

Where C_{HDO} and C_{H₂O} represent concentrations of HDO and H₂O in water, respectively, and C_{H₂} and C_{HD} represent concentrations of H₂ and HD in hydrogen gas mixture, respectively. *k*₁ and *k*₋₁ represent reaction rate constants of forward and backward reactions, respectively. To expand usability of the kinetic model, concentrations of HD and HDO are defined in terms of

C and C' , respectively. The exchange kinetic equation is then rewritten as illustrated by equation (6.3),

$$\frac{dC_{HD}}{dt} = k_1 C' C_{H_2} - k_{-1} C C_{H_2O} \quad (6.3)$$

When the exchange reaction reaches equilibrium $\frac{dC}{dt} = 0$, concentration C and C' are replaced by relevant concentration at equilibrium C_e and C'_e , respectively. Equation (6.3) is rewritten into equation (6.4),

$$k_1 C'_e C_{H_2} = k_{-1} C_e C_{H_2O} \quad (6.4)$$

The exchange process to meet the material balance is then, expressed by equation (6.5),

$$C' + C = C'_e + C_e \quad (6.5)$$

Substituting equation (6.4) and equation (6.5) in equation (6.3), yield equation (6.6),

$$\frac{dC}{dt} = (k_1 C_{H_2} + k_{-1} C_{H_2O}) \times (C_e - C) \quad (6.6)$$

Because hydrogen gas and water are typically operated at high concentrations compared with those of HD and HDO : $C_{H_2} > C, C_{H_2O} > C'$, flow rate ratio of H_2O and H_2 is then consistent during the exchange process, leading C_{H_2O} and C_{H_2} to be treated as constants. Therefore,

$(k_1 C_{H_2} + k_{-1} C_{H_2O})$ can be approximated as constant. Taking $k_1 C_{H_2} = k'_1, k_2 C_{H_2O} = k'_2$

$$\frac{dC}{dt} = k'_1 C' - k'_2 C \quad (6.7)$$

$$\frac{dC}{dt} = k'_1 C_{H_2O} [C' / C_{H_2O} - \left(\frac{k_2}{k_1}\right) C / C_{H_2}] \quad (6.8)$$

The reaction rate of HDO and HD can be expressed as:

$$-r_{HDO} = r_{HD} = R \left(x - \frac{y}{K} \right) \quad (6.9)$$

Where $x = \frac{C_{HDO}}{C_{H_2O}}, y = \frac{C_{HD}}{C_{H_2}}, R = k'_1 C_{H_2O}, K = \frac{k_1}{k_2}$

Also, equation (6.6) is expressed as follow,

$$\frac{dC}{dt} = K (C_e - C) \quad (6.10)$$

Where

$$K = k_1 C_{H_2} + k_{-1} C_{H_2O} \quad (6.11)$$

Equation (6.10) is the expression of the kinetic model of the isotopic exchange. It is interesting to see that the rate of the kinetic model is proportional to concentration of HD at any time with reference relevant values at the equilibrium conditions ($C - C_e$). This expression is useful to gain

access to the kinetic rate constant/mass transfer coefficient K' (equation 6.11) and thus to evaluate activity of catalyst.

6.2.1.2 Equilibrium constant and separation factor of H₂-H₂O liquid exchange reaction

Equation (6.1) represents hydrogen-deuterium exchange between H₂-H₂O and relevant equilibrium constant K can be expressed by equation (6.12),

$$K = \frac{C_{HDO(liquid)} C_{H_2(gas)}}{C_{H_2O(liquid)} C_{HD(gas)}} \quad (6.12)$$

Which can be rewritten as;

$$K = K_{gas} K_{phase} \quad (6.13)$$

$$\text{Where, } K_{gas} = \frac{C_{HDO(gas)} C_{H_2(gas)}}{C_{HD(gas)} C_{H_2O(gas)}} \quad \text{and} \quad K_{phase} = \frac{C_{HDO(liquid)} C_{H_2O(gas)}}{C_{H_2O(liquid)} C_{HDO(gas)}} \quad (6.14)$$

K_{gas} is equilibrium constants for the gaseous phase reaction and K_{phase} is the equilibrium constant of the phase exchange reaction. The isotopic exchange reaction between gas and liquid phase for H₂-H₂O (equation 6.1) includes therefore two steps; isotope exchange (6.15) and phase exchange (6.16).



The value of separation factor of deuterium or tritium isotope Sep_{eq} for H₂-H₂O gas-liquid phase isotope exchange reaction, as defined by equation 4.15.1 in chapter 4, is related to the abundance of heavy isotope. We have obtained in the Chapter 4 through the Aspen plus modular package a value of the separation factor for H-D separation that fitted well literature data [140]. Here are some selected models for H-D, H-T and D-T separation factors.

Canadian literature based empirical equations 6.17.1-3 [20];

$$\ln Sep_{D,eq} = -0.2143 + \frac{368.9}{T} + \frac{27870}{T^2} \quad (6.17.1)$$

$$\ln Sep_{T,eq} = -2.426 + \frac{774}{T} + 0.292 \ln T \quad (6.17.2)$$

$$\ln Sep_{D/T,eq} = -0.1474 + \frac{191.5}{T} \quad (6.17.3)$$

Russian literature used empirical equations 6.18.1-3 (when the concentration of one of the isotopes is less than 8%) [20, 71].

$$\ln Sep_{D,eq} = -0.1636 + \frac{333.7}{T} + \frac{33840}{T^2} \quad (6.18.1)$$

$$\ln Sep_{T,eq} = -2.4264 + \frac{718.2}{T} + \frac{24589}{T^2} + 0.292 \ln T \quad (6.18.2)$$

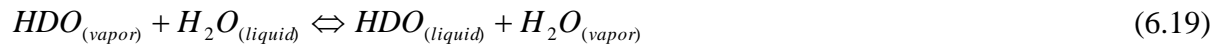
$$\ln Sep_{D/T,eq} = -0.1974 + \frac{211.1}{T} \quad (6.18.3)$$

The biggest difference among these empirical models is less than 5%.

6.2.1.3 H₂-H₂O liquid phase exchange reaction

H₂-H₂O liquid phase catalytic exchange reaction system is gas-liquid-solid three phase system and associated with complex mass transfer process between these phases. The reaction mainly includes two reactions: isotope exchange and vapour-water phase exchange. The catalytic reaction that happens on surface of catalyst is actually a gas-liquid-solid multi-phase catalytic reaction through the following processes [100]:

(1) Vapour-water exchange,



(2) Diffusion inside the catalyst and adsorption.

(3) Gaseous phase isotopic catalytic exchange,



(4) Desorption and inverse diffusion

Because of hydrophobicity of catalyst, water would not reach active catalytic centres. Water has to be transferred through phase exchange into a vapour phase on the surface of a hydrophilic packing by diffusion through the liquid/gaseous film, core of the gaseous phase the outer surface of catalyst, the inner surface and then to spread towards adsorption sites for the isotopic exchange reaction.

Hydrogen isotopic exchange is the exchange of deuterium from hydrogen gas to water vapour and the reaction only happens on the surface of the catalyst. The process that determines the rate for the whole reaction is rate-determining step. In chapter (4), we determined operating conditions where the isotopic exchange process was assessed under a rate controlling step of the overall reaction as well as chemical equilibrium operations. When the catalyst had a high activity such as at high temperature, then the phase exchange was competitive and thus relevant within the whole reaction kinetics mechanism.

6.2.2 Mass Transfer model and expression of activity of catalyst

6.2.2.1 gas-liquid flow exchange in co-current bed

According to the kinetics of H₂-H₂O liquid exchange as demonstrated in equation (6.10);

$$\frac{dC}{dt} = K(C_e - C) \quad (6.10)$$

Mass transfer coefficient K is expressed as equation (6.11),

$$K = k_1 C_{H_2} + k_{-1} C_{H_2O} \quad (6.11)$$

After being integrated, equation (6.21) is obtained,

$$K = \frac{1}{t} \ln \frac{C_e - C_0}{C_e - C_t} \quad (6.21)$$

So total volume of the mass transfer coefficient K_{ya} for exchange reaction under co-current operations of gas and liquid flow could be expressed by equation (6.22),

$$K_{ya} = \frac{G}{V} \ln \frac{C_e - C_0}{C_e - C_t} \quad (6.22)$$

In equation (6.22), G is the flow rate of gas (m³ s⁻¹); V is volume of catalytic bed (m³); C_0 is the initial concentration of HD in hydrogen; C_t is HD concentration in hydrogen when exchange reaction reaches time t ; C_e is HD concentration in hydrogen when exchange reaction reaches equilibrium conditions.

In the engineering field, molar fraction based concentration are typically used. If y represents the mole fraction of species in the gaseous phase, the mass transfer coefficient under a co-current exchange reaction could be expressed by equation (6.23)

$$K_{ya} = \frac{G}{V} \ln \frac{y_e - y_0}{y_e - y_t} \quad (6.23)$$

The mass transfer coefficient K_{ya} for exchange reaction is used to represent activity of catalyst.

6.2.2.2 gas-liquid flow exchange in counter-current bed

For gas-liquid counter-current exchange, the mass transfer coefficient K_{ya} can be expressed by conventional concepts of number of transfer units and height of transfer units (m), as illustrated equation (6.24),

$$K_{ya} = \frac{G}{V} NTU \quad (6.24)$$

The height of a transfer unit is expressed by equation (6.25),

$$HTU = \frac{h}{NTU} \quad (6.25)$$

In equation (6.25), h is the height of catalyst in the catalytic bed (m).

The number of a transfer unit NTU is expressed as equation (6.26),

$$NTU = \int_{C_t}^{C_0} \frac{dC}{C - C_e} \quad (6.26)$$

After integration, equation (6.27) is obtained,

$$NTU = \frac{C_0 - C_t}{(C_0 - C_{e0})(C_t - C_{et})} \ln \frac{C_0 - C_{e0}}{C_t - C_{et}} \quad (6.27)$$

If the liquid phase had very low deuterium concentration, C_e could be expressed by equation (6.28),

$$C_e = \frac{C'}{Sep} \quad (6.28)$$

For the gas-liquid counter-current exchange, when the reaction is using a high purity hydrogen gas, C_0 can be considered approximately equal to 0.

Based on a mass balance, equation (6.29) is obtained,

$$G(C_t - C_0) = L(C'_t - C'_0) \quad (6.29)$$

In equation (6.29), G is the flow rate of hydrogen and L is the flow rate of water.

Equation (6.29) could be rewritten into equation (6.30),

$$C'_0 = C'_t - \lambda C_t \quad (6.30)$$

In equation (6.30), λ is the molar ratio of hydrogen and water.

Substituting equation (6.30) in equation (6.28), equation (6.31) is obtained,

$$C_{e0} = \frac{C'_0}{Sep_{D,eq}} = \frac{1}{Sep_{D,eq}} (C'_t - \lambda C_t) \quad (6.31)$$

Substituting equation (6.31) in equation (6.27), equation (6.32) is obtained,

$$NTU = \frac{1}{1 - \frac{1}{Sep_{D,eq}} \lambda} \ln \frac{C'_t - \lambda C_t}{C'_t - Sep_{D,eq} C_t} \quad (6.32)$$

Substituting equation (6.32) in equation (6.24), equation (6.33) is obtained,

$$K_{ya} = \frac{G}{V} \frac{1}{1 - \frac{1}{Sep_{D,eq}} \lambda} \ln \frac{C'_t - \lambda C_t}{C'_t - Sep_{D,eq} C_t} \quad (6.33)$$

In the engineering field, y represented composition in the gas phase and x represents composition in the liquid phase. Thus, the overall mass transfer coefficient for counter-current exchange reaction could be expressed by equation (6.34),

$$K_{ya} = \frac{G}{V} \frac{1}{1 - \frac{1}{Sep_{D,eq}} \lambda} \ln \frac{x_t - \lambda y_t}{x_t - Sep_{D,eq} y_t} \quad (6.34)$$

The activity of catalyst could be expressed by conversion rate of HD into HDO, α_{HD} as equation (6.35),

$$\alpha_{HD} = \frac{y_0 - y_t}{y_0} \quad (6.35)$$

The activity of catalyst in this study was expressed by conversion rate α_{HD} .

6.3 Modelling Description

6.3.1 Model equations (Eulerian formulation)

In Computational fluid dynamics (CFD), numerical methods and algorithms were used to solve and analyse the problems that involve fluid flows. To describe the 3D flow field between the particles inside the trickle bed reactor, the momentum and the continuity equations were solved. The flow through the trickle bed was considered incompressible and the solid particles would not move and the void between them remains constant. The simulation was performed under laminar two-phase flow condition. In addition to the overall mass balance for the system (continuity equation), material balances for each component were required to describe the local concentration profiles. The Transport of diluted species (Chemical Reaction Engineering Module) was applied and included diffusion and convection terms to model the component concentrations in the fluids (gas or liquid). In addition, the fluid properties were assumed constant during the course of the reactive process.

In this chapter, a 3D mass transfer model was developed to simulate the operation of an isothermal trickle bed. The LPCE process with a counter-currently and co-currently operated gas-liquid flow was assessed in terms of conversion and relevant interactions with local fluid flow.

6.3.1.1 Fluid flow model

This model for fluid flow combines the fluid flow model of gas and liquid phases, the Cahn-Hilliard model for interphase assessment and the mass transfer model with chemical reaction. The Cahn-Hilliard model, as described in Chapter 5, tracks the diffuse interface separating the immiscible gas/liquid phases and ensures that the total energy of the system diminishes correctly. Briefly, the tracking of the interface between the two fluids is governed by the so-called phase field variable (ψ).

$$\frac{\partial \phi}{\partial t} + \mathbf{u} \cdot \nabla \phi = \nabla \cdot \frac{\gamma \lambda}{\varepsilon_{pf}^2} \nabla \phi \quad (6.36)$$

$$\psi = -\nabla \cdot \varepsilon_{pf}^2 \nabla \phi + (\phi^2 - 1)\phi + \frac{\varepsilon_{pf}^2}{\lambda} \frac{\partial f}{\partial \phi} \quad (6.37)$$

In the above equations, (γ) is the mobility (m), (λ) is the mixing energy density (N) and (ε_{pf}) is the interface thickness parameter (m).

The Cahn-Hilliard model was combined with conservation of mass and momentum equations (6.38 and 6.39), and with the transport of diluted species model expressed by equations (6.40-6.45) and can be written as follows:

$$\nabla \cdot \mathbf{u} = 0 \quad (6.38)$$

$$\rho \frac{\partial \mathbf{u}}{\partial t} + \rho (\mathbf{u} \cdot \nabla) \mathbf{u} = \nabla \cdot [-p \mathbf{I} + \mu (\nabla \mathbf{u} + (\Delta \mathbf{u})^T)] + \mathbf{F}_g + \mathbf{F}_{st} + \mathbf{F} \quad (6.39)$$

Where \mathbf{u} is the velocity vector (m/s), p is the pressure (Pa), ρ is the density (kg/m³), μ is the dynamic viscosity (Pa.s), and \mathbf{F}_g is the gravitational force, \mathbf{F}_{st} is the surface tension force (N/m³), and \mathbf{F} is any additional volume for other forces (N/m³) in the model.

6.3.1.2 Mass balance model

The diffusion of reaction species in hydrogen gas was considered as molecular (Fickian) due to low values of velocity and concentration used (turbulent diffusion and concentration based diffusion coefficients were neglected). Mass transfer in the catalytic phase was assumed to be driven by diffusion and free of convection (negligible velocity) and the chemical reaction to occur in the catalytic phase only.

Hydrogen gaseous phase

$$\frac{\partial c_{i,g}}{\partial t} + \nabla \cdot (-D_{i,g} \nabla c_{i,g}) + \mathbf{u} \cdot \nabla c_{i,g} = 0 \quad (6.40)$$

$$\mathbf{N}_{i,g} = -D_{i,g} \nabla c_{i,g} + \mathbf{u} c_{i,g} \quad (6.41)$$

Water liquid phase

$$\frac{\partial c_{i,l}}{\partial t} + \nabla \cdot (-D_{i,l} \nabla c_{i,l}) + \mathbf{u} \cdot \nabla c_{i,l} = 0 \quad (6.42)$$

$$\mathbf{N}_{i,l} = -D_{i,l} \nabla c_{i,l} + \mathbf{u} c_{i,l} \quad (6.43)$$

Reactive packing phase

$$\frac{\partial c_{i,s}}{\partial t} + \nabla \cdot (-D_{i,s} \nabla c_{i,s}) = R_i \quad (6.44)$$

$$\mathbf{N}_{i,s} = -D_{i,s} \nabla c_{i,s} \quad (6.45)$$

Where $D_{i,g}$, $D_{i,l}$ and $D_{i,s}$ denotes the diffusion coefficient (m²/s), c_i is the species concentration (mol/m³), R_i is the reaction rate expression for the species (mol/(m_{cat}³ s)), and N_i is the molar flux (mol/(m² s)). The first term on the left-hand side of Equation (6.40, 6.42 and 6.44) represent the accumulation or consumption of the species. The second term accounts for the

diffusion transport (interaction between the dilute species and solvent) ($u \cdot \nabla c$). The third term accounts for the convective transport due to a velocity field (u). Lastly, the first term on the right-hand side represents a source or sink term, usually due to a chemical reaction. The kinetic model of the gaseous phase isotopic exchange in Chapter 4 was used. In addition phase transfer between phases were assumed to take place under equilibrium conditions (ideal mixing or no mass transfer resistance between phases). To solve the overall space-dependent model, the equations of motion and the material balance equations were coupled and solved for velocity, concentration and pressure.

6.3.2 Boundary conditions and solver details

The equations (6.36-6.45) were subject to the following boundary conditions. At the inlet of the reactor, we used a constant velocity inlet boundary condition. At the outlet of the reactor, we used a pressure outlet boundary condition with zero gauge pressure. The wall boundaries were assumed to be stationary with no slip boundary condition. All particles were modelled as packing of randomly distributed bed with no slip boundary condition. Mass and momentum equations were combined with the transport of diluted species model and solved in 3D transient formulations. Convergence limits of the sum of the absolute residuals for all the equations were set to 10^{-5} . Unsteady simulations with a time step of 0.005 second were continued until steady-state at the outlet velocity was reached. In all simulations, liquid and gas were observed flowing co-currently or counter-currently. In the liquid phase, water content was set to 99.97 mole % and deuteriated water (HDO) to 0.03 mole %. In the hydrogen gas mixture, hydrogen content was set to 99.9716 mole % and hydrogen deuterated gas (HD) to 0.0284 mole %. These operating conditions were selected with reference to those used by Huang et al. [71] The volume fraction of the liquid was set to 1 at the inlet of the liquid phase and was set to zero at the inlet of the gaseous phase. A summary of the simulation setup with boundary and initial conditions is presented in Table (6.1).

Table (6.1). Boundary and subdomain condition for CFD model

	inlet	outlet	AR	No. of particle	free fluid
momentum balance	u_0	P_0	2	12	Navier-Stokes
component mass balance	c	convective flux	2	12	Convection and diffusion

6.3.3 Kinetic model of the gaseous phase exchange and analysis

The kinetic model investigated in Chapter 4 was used for 3D two-phase modelling. Herein, detailed mechanism of the kinetic of isotopic exchange reaction between hydrogen and water vapour is introduced taking into account literature models and validating the use of kinetic model used for the reactive stripping simulation in Chapter 4. The isotopic exchange on Pt/SDBC catalyst was assumed to proceed via the following steps: [137]



Water vapour was assumed not to prevent dissociative chemisorption of hydrogen [137] and the rate limiting step was assumed to take place at the surface reaction (step, iii) between chemisorbed hydrogen atom and water vapour molecules. The isotopic exchange rate is then written as:

$$-r_{HDO} = r_{HD} = k_{r1}\theta'_{HDO}\theta_H - k_{r2}\theta'_{H_2O}\theta_D \quad (6.46)$$

When the adsorption-desorption steps (i), (ii), (iv) and (v) are in equilibrium, the surface coverages for each component are given by following equations:

$$\theta'_{HDO} = K_{H_2O}p_{HDO}\theta'_v \quad (6.47)$$

$$\theta_D = \left(\frac{K_{H_2}p_{HD}}{\sqrt{K_{H_2}p_{H_2}}} \right) \theta_v \quad (6.48)$$

$$\theta'_{H_2O} = K_{H_2O}p_{H_2O}\theta'_v \quad (6.49)$$

$$\theta_H = \sqrt{K_{H_2}p_{H_2}}\theta_v \quad (6.50)$$

Substitution of these equations into equation (46) results in:

$$-r_{HDO} = r_{HD} = k_{r1}\sqrt{K_{H_2}p_{H_2}}K_{H_2O}p_{H_2O}\theta_v\theta'_v \left(\frac{p_{HDO}}{p_{H_2O}} - \frac{1}{K} \frac{p_{HD}}{p_{H_2}} \right) \quad (6.51)$$

$$-r_{HDO} = r_{HD} = \frac{k_{r1}\sqrt{K_{H_2}p_{H_2}}K_{H_2O}p_{H_2O}}{(1+\sqrt{K_{H_2}p_{H_2}})(1+\sqrt{K_{H_2O}p_{H_2O}})} \left(x - \frac{y}{K} \right) \quad (6.52)$$

Where, $x = \frac{p_{HDO}}{p_{H_2O}}$, $y = \frac{p_{HD}}{p_{H_2}}$, $K = \frac{k_{r1}}{k_{r2}}$. In deriving equation (6.52), the following assumption are made: $\theta_v = 1 - \theta_H$ at $p_{H_2} \gg p_{HD}$ and $\theta'_v = 1 - \theta'_{H_2O}$ at $p_{H_2O} \gg p_{HDO}$.

At highly diluted liquid and gaseous phases, equation (6.52) reduces to first-order reversible kinetics given by equation (6.7) and validated by the kinetic model study in chapter 4.

The catalytic effectiveness factor for a spherical porous solid catalyst is given by:

$$\eta = \frac{1}{\phi_s} \left[\frac{1}{\tanh(3\phi_s)} - \frac{1}{3\phi_s} \right] \quad (6.53)$$

With the Thiele modulus defined as:

$$\phi_s = \frac{d_p}{6} \sqrt{\frac{R_i \rho_p R_g T}{D_{HDO} \rho_{H_2O}} + \frac{R_i \rho_p R_g T}{K D_{HD} \rho_{H_2}}} \quad (6.54)$$

Where D_e is the effective diffusivity in the pore of catalyst.

Thus, the apparent kinetic expression for the total exchange reaction could be given by:

$$R = \eta R_i \quad (6.55)$$

Equation (6.57-6.67) includes the five unknown parameters $k_{r1}, K_{H_2}, K_{H_2O}, D_{HD}, D_{HDO}$. These parameters were determined as follows:

The first parameters k_{r1} was obtained from the kinetic model presented in the chapter (4). The temperature dependences of k_{r1} is expressed by the Arrhenius equation as:

$$k_{r1} = k_{r1}^0 \exp\left(\frac{E_r^0}{RT}\right) \quad (6.56)$$

Where k_{r1}^0 and E_r^0 are the pre-exponential factor and activation energy for the surface reaction, respectively and the values of equation is listed in Table (6.2). The higher values of surface adsorption constants K_{H_2}, K_{H_2O} and the higher partial pressures of these gases ensure that the surface is saturated, and therefore, the surface adsorption steps would have negligible influences on the reaction rate. As a result, the reaction kinetics were modeled by neglecting the surface adsorption parameters, and hence equation (6.52) is rearranged in terms of molar concentration of the reacting species as mentioned it before in equation (6.7).

Table (6.2) kinetic parameters.

Parameters	Values
k_{r1}^0 (mol/m ³ .s)	217510
E_r^0 (J/mole)	27350

The last two unknown parameters are the diffusivity coefficient of each reactive species into multicomponent gases mixture available inside the solid catalyst, $D_{i,s}$, which is also denoted effective diffusivity. The diffusivity coefficients were calculated by using the binary diffusivity data and correlations developed by Wilke [206] along with Wakao and Smith model [207]. The application of Wilke model to bulk diffusion coefficient of $D_{H_2,mix}, D_{H_2O,mix}, D_{HDmix}, D_{HDO,mix}$ is expressed as follows:

$$D_{H_2,mix} = (1 - y_{H_2}) \left[\frac{y_{H_2O}}{D_{H_2,H_2O}} + \frac{y_{HDO}}{D_{H_2,HDO}} + \frac{y_{HD}}{D_{H_2,HD}} \right]^{-1} \quad (6.57)$$

$$D_{H_2O,mix} = (1 - y_{H_2O}) \left[\frac{y_{HDO}}{D_{H_2O,HDO}} + \frac{y_{HD}}{D_{H_2O,HD}} + \frac{y_{H_2}}{D_{H_2O,H_2}} \right]^{-1} \quad (6.58)$$

$$D_{HD,mix} = (1 - y_{HD}) \left[\frac{y_{H_2O}}{D_{HD,H_2O}} + \frac{y_{HDO}}{D_{HD,HDO}} + \frac{y_{H_2}}{D_{HD,H_2}} \right]^{-1} \quad (6.59)$$

$$D_{HDO,mix} = (1 - y_{HDO}) \left[\frac{y_{H_2O}}{D_{HDO,H_2O}} + \frac{y_{HD}}{D_{HDO,HD}} + \frac{y_{H_2}}{D_{HDO,H_2}} \right]^{-1} \quad (6.60)$$

Where y_{H_2O} , y_{HDO} , y_{HD} and y_{H_2} are the mole fraction of H₂O, HDO, HD and H₂, respectively in the bulk fluid. $D_{H_2O,HDO}$, D_{HDO,H_2O} , D_{HD,H_2O} and D_{H_2,H_2O} are the respective binary diffusion coefficients. The binary diffusivities were calculated by using the following correlation developed by Fuller et al [208]:

$$D_{AB} = D_{BA} = \frac{CT^b \left(\frac{1}{M_A} + \frac{1}{M_B} \right)^{\frac{1}{2}}}{P[(\sum_A v_i)^{\alpha_1} + (\sum_B v_i)^{\alpha_2}]^{\alpha_3}} \quad (6.61)$$

Where;

D_{AB} = binary diffusion coefficient of A into B (cm²/s).

$C = 1 \times 10^{-3}$, an arbitrary constant.

T = temperature (K).

P = pressure (atm).

M_A , M_B = molecular weight (g/ mole).

$b = 1.75$, temperature power dependence.

$\alpha_1 = \alpha_2 = \frac{1}{3}$, $\alpha_3 = 2$ = arbitrary exponents to the $\sum_A v_i$ and $\sum_B v_i$.

$\sum_A v_i$ = summation of atomic diffusion volumes of A. Diffusion volumes for H₂O = 12.7 and for H₂ = 7.02. The atomic diffusion volumes of HDO and HD were taken similar to those of H₂O and H₂, respectively, in the absence of available data. Table (6.3) and table (6.4) illustrate the numerical values of various binary diffusivities and effective diffusivities calculated by equations 6.61 and 6.57-6.60, respectively, at different temperature from 298.15 to 363.15 K.

Table (6.3) binary diffusion coefficient.

Temp (K)	$D_{HDO,HD}$ (cm ² /s)	D_{HDO,H_2O} (cm ² /s)	D_{HDO,H_2} (cm ² /s)	D_{H_2,H_2O} (cm ² /s)	D_{HD,H_2O} (cm ² /s)	D_{HD,H_2} (cm ² /s)
298.15	0.50463194	0.222491679	0.603619117	0.605232471	0.506560667	0.90946879
303.15	0.51953471	0.229062292	0.621445165	0.623106165	0.52152039	0.936327175
313.15	0.54989598	0.242448542	0.657762015	0.659520082	0.551997701	0.991045523
323.15	0.58099326	0.256159301	0.694959254	0.696816742	0.58321384	1.047090348
333.15	0.61282080	0.270192027	0.733029989	0.734989232	0.615163022	1.104451265
343.15	0.64537304	0.284544277	0.77196759	0.774030906	0.647839683	1.163118281
353.15	0.67864466	0.299213695	0.811765669	0.813935357	0.681238462	1.223081774
363.15	0.71263049	0.314198013	0.852418068	0.854696412	0.715354191	1.284332466

Table (6.4) effective diffusion coefficient.

TEMP	D _{H2O} (cm ² /s)	D _{HDO} (cm ² /s)	D _{H2} (cm ² /s)	D _{HD} (cm ² /s)
298.15	0.016701606	0.568324542	0.016868443	0.042084229
303.15	0.017194837	0.439018144	0.017366601	0.042449812
313.15	0.018199692	0.268531468	0.018381493	0.043154759
323.15	0.019228907	0.169324887	0.019420989	0.043826715
333.15	0.02028229	0.109766414	0.020484895	0.044467868
343.15	0.021359659	0.072977691	0.021573026	0.045080226
353.15	0.022460837	0.049653589	0.022685204	0.045665631
363.15	0.023585653	0.034508149	0.023821256	0.04622578

The Wakao and smith model for effective diffusivities of each species was applied as follows:

$$D_{e,i} = \bar{D}_{M,i} \varepsilon_M^2 + \frac{\varepsilon_\mu^2 (1 + 3\varepsilon_M)}{1 - \varepsilon_M} \bar{D}_{\mu,i} \quad (6.62)$$

Where $\bar{D}_{M,i}$ and $\bar{D}_{\mu,i}$ are the mean effective pore diffusivities of component i in macro- and micropore regions, respectively. ε_M and ε_μ are the void fractions in macro- and microregions, respectively. The values $\bar{D}_{M,i}$ and $\bar{D}_{\mu,i}$ were obtained by applying the following expressions in macro- and microregions.

$$\frac{1}{\bar{D}_{M,i}} = \frac{1}{D_{i,mix}} + \frac{1}{(\bar{D}_K)_{M,i}} \quad (6.63)$$

$$\frac{1}{\bar{D}_{\mu,i}} = \frac{1}{D_{i,mix}} + \frac{1}{(\bar{D}_K)_{\mu,i}} \quad (6.64)$$

Where, $D_{i,mix}$ is the bulk diffusivity of the component i in the gas mixture. $(\bar{D}_K)_{M,i}$ and $(\bar{D}_K)_{\mu,i}$ are the mean Knudsen diffusivity of component i in the macro- and microregions, respectively and expressed as follows:

$$(D_K)_i = 9700 r_e \sqrt{\frac{T}{M_i}} \quad (6.65)$$

Where, r_e is the mean pore radius, T is the temperature in Kelvin, and M_i is the molecular weight of component i in grams per mole.

The effective diffusion coefficient generally increases with increase in temperature; nevertheless, in the present case the difference of effective diffusion coefficient with temperature is very small and for the case of HDO it has even shows reverse trend for

temperatures 333 and 363 K, as noticeable in Table (6.4). This is because of the change in composition of gas mixture in the column. As the hydrogen gas gets saturated with water vapour into the exchange column at higher temperature the partial pressure of water vapour is increased greatly with an increase in operating temperature.

6.4 H₂-H₂O catalytic exchange processing:

6.4.1 Counter-current flow exchange

The trickle bed reactor system consists of solid catalyst, with gas and liquid flowing in between them. A schematic representation of H₂-H₂O liquid exchange processing and catalytic bed is illustrated in the Figure (6.1) and more detailed representation that was used for the 3D modelling was introduced in Chapter 5.

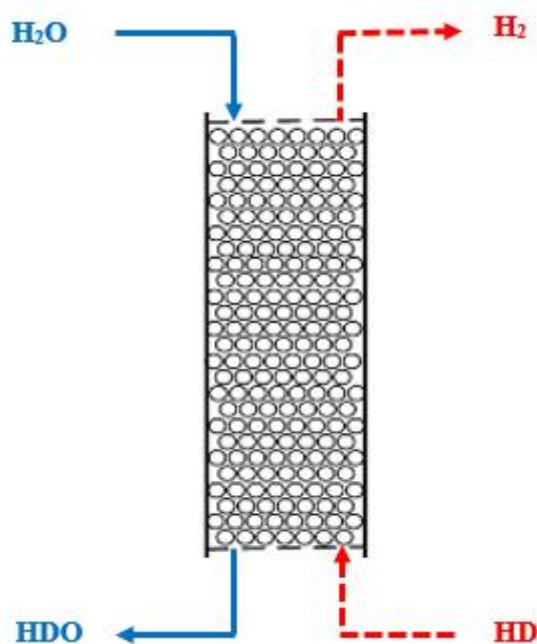


Figure (6.1) Schematic representation of hydrogen-water exchange in the counter-current mode operation.

Hydrogen flowed from the bottom of catalytic bed and water flowed from the top of catalytic bed. Hydrogen and water of a counter-current flow conducted the hydrogen isotope exchange reaction and associated mass transfer of involved reactive species through the gas/liquid phases. The operating temperature and inlet velocities of both phases were set at different values while the total length and diameter of the TBR were set to 25 mm and 10 mm, respectively. Typical process data and liquid and gas properties are listed in Table (6.5) and (6.6). In the process of H₂-H₂O liquid catalytic exchange, activity of catalyst can be fully assessed if a certain reaction scale is achieved. The performance of the reactor and activity of the catalyst can be described by measuring the conversion values throughout the catalytic bed. Effects of flow rate, temperature and bed height on conversion rate was investigated to assess

local efficiency of interactions of flow, mass transfer and chemical reactions and thus optimize operating conditions of H₂-H₂O liquid catalytic exchange process. These operating conditions were selected based on experimental data of Huang et al. [71].

Table (6.5) Operating data for 3D CFD modelling.

Parameter	Unit	Quantity
Operating pressure	kPa	101.325
Operating temperature	K	303.15, 313.15, 323.15, 333.15, 343.15, 353.15 and 363.15
Flow rate of liquid	ml/h	12, 18, 24, 26.4, 30, 36, 42, 48, 60 and 75
Flow rate of gas	ml/s	2, 2.55, 4.55, 5, 6.5, 8, 8.63, 9.9, 11.5, 12.9 and 13.33
Gravity	m/s ²	9.8

Table (6.6) Physical properties of the liquid and gas phases.

Parameter	Liquid		Gas	
	Temp	Density	Temp	Density
Density (kg/m ³)	303.15	995.7	303.15	0.081028912
	313.15	992.2	313.15	0.078441369
	323.15	988.1	323.15	0.076013971
	333.15	983.1	333.15	0.073732297
	343.15	977.8	343.15	0.071583607
	353.15	971.8	353.15	0.069556604
	363.15	965.3	363.15	0.067641236
Viscosity (Pa.s)	303.15	0.0007978	303.15	8.95163E-06
	313.15	0.0006531	313.15	9.15423E-06
	323.15	0.0005471	323.15	9.35339E-06
	333.15	0.0004658	333.15	9.54928E-06
	343.15	0.0004044	343.15	9.74204E-06
	353.15	0.000355	353.15	9.93178E-06
	363.15	0.000315	363.15	1.01186E-05

6.4.1.1 Impact of flow rate

The liquid catalytic exchange H₂-H₂O reaction is a gas-liquid-solid reaction, where the exchange occurs at the solid catalytic bed. Effects of flow rates of the feed, liquid (i.e. water) or gas (i.e. H₂), gas-to-liquid flowrate ratio were demonstrated in Chapter 4 to be effective on the conversion rate of the catalytic exchange, and thus the separation efficiency of deuterium (or tritium).

6.4.1.1.1 Impact of flow rate of gas

Trends observed of effect of gas flow rate on conversion are conflicting in different studies, owing particularly to various design and operating parameters that were discussed on Chapter 4. Figure (6.2) show the effect of flow rate of hydrogen on conversion rate of HD in counter-current mode operation by a reactive packing (operating conditions; temperature= 333.15 K and flow rate of water=30 ml/h).

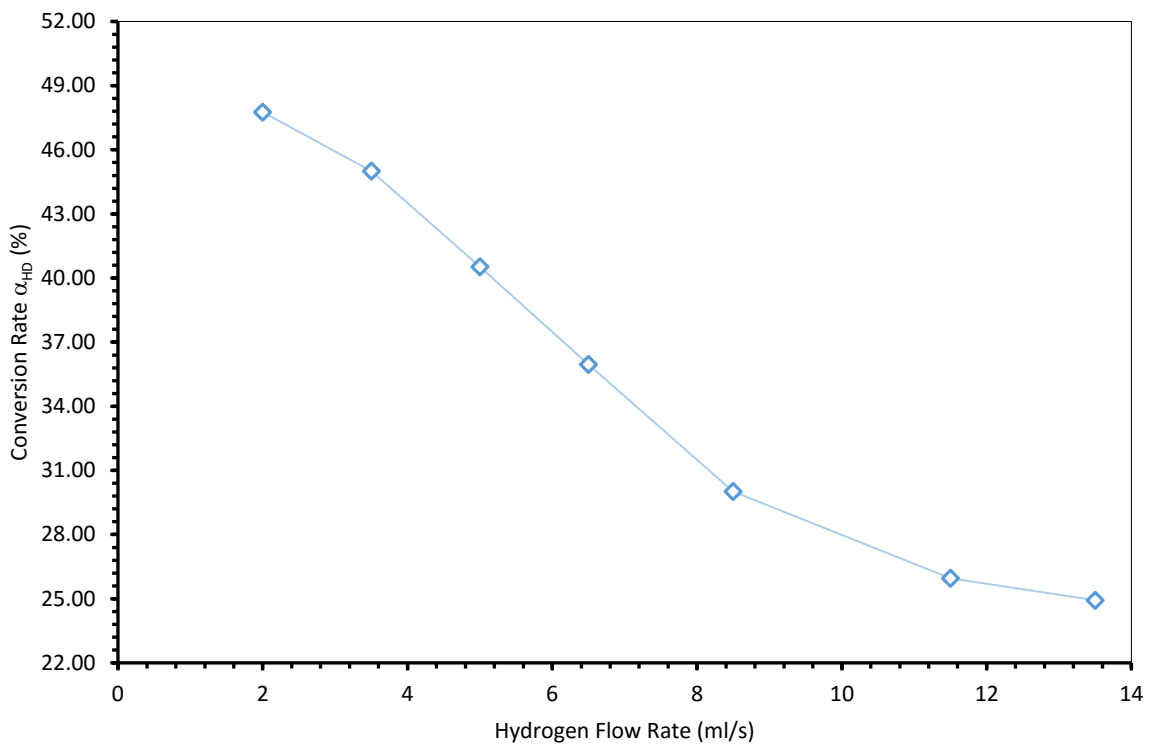


Figure (6.2) Influence of hydrogen flow rate on conversion rate, water flow rate 30 ml/h, temperature 333.15K.

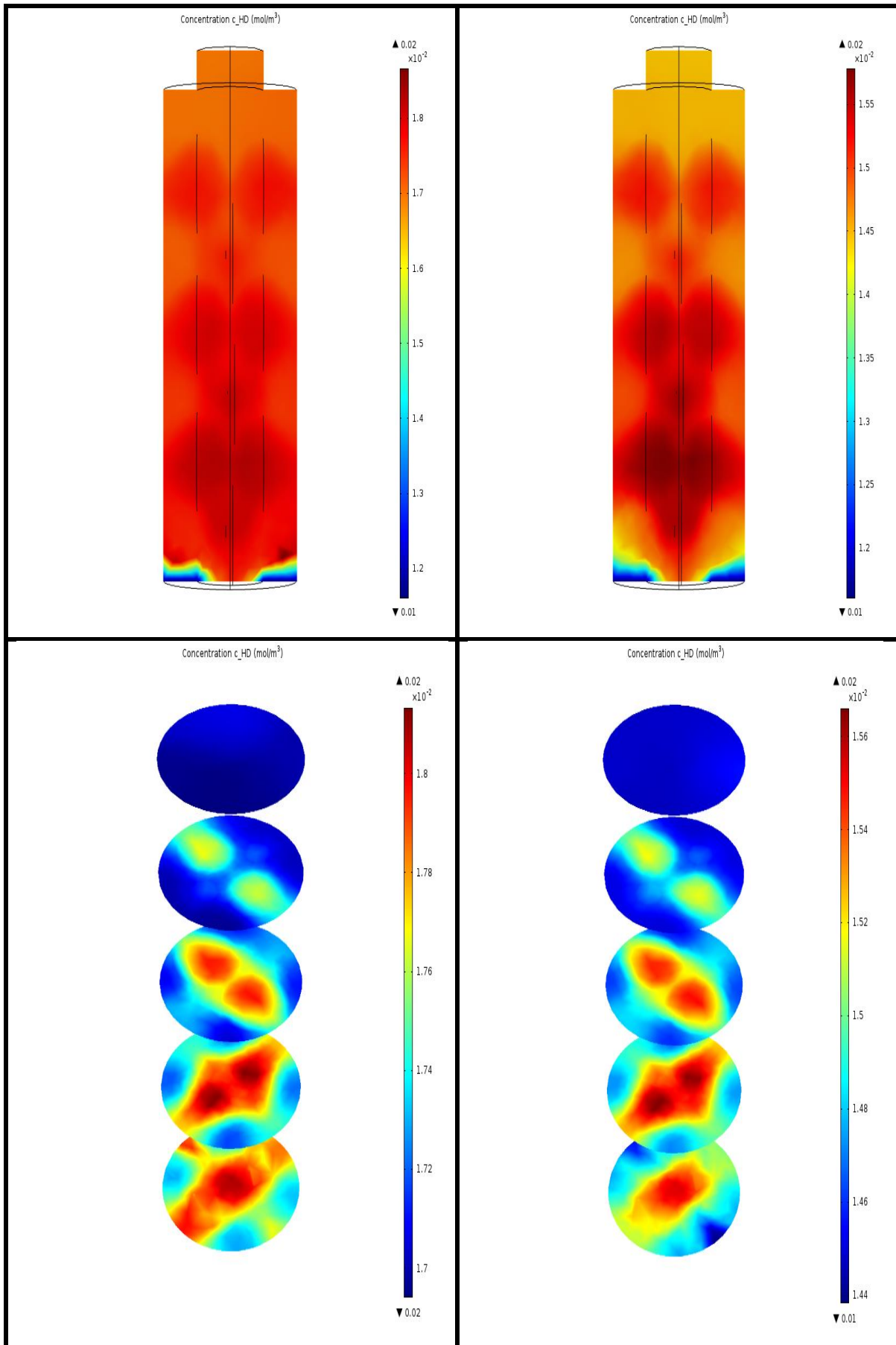
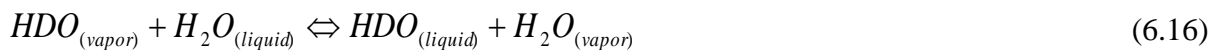


Figure (6.3) Colour map of HD concentration over catalyst surface in counter-current mode operation at gas velocity; 2.55 (ml/s) (left - 3D on cross-sectional and vertical planes) and 12.9 (ml/s) (right - 3D on cross-sectional and vertical planes).

It can be clearly seen that increasing the flow rate of hydrogen reduced conversion rate of HD. Higher values than those cited in the Figures (6.2) and (6.3) reached conditions of pressure drop boundaries when liquid flooding happened. It is expected that with the increasing the flow rate of hydrogen gas, and thus the load of deuterium, would lead to reduced conversion of HD into HDO if a constant amount of catalyst or packing size was used. By comparing two particle sizes of catalyst (5mm and 2.5mm), the later was found more effective, because of the denser accumulation of the packing. Smaller diameter of the packing would drive however higher pressure drops and thus would offer a narrower range for hydrogen load before the flooding would take place. It is therefore important to control the particle size as discussed that in chapter (5). In addition, the smaller particle size beds offered a higher conversion owing to more efficient mass transfer inside the pores of the catalytic particles and thus the rate of gas/liquid exchange should be closer to the gaseous phase intrinsic rate of the gaseous phase catalytic exchange. Figure (6.3) shows the cross-sectional and vertical maps of concentration in the packed bed and demonstrates how deep the local concentration of HD inside the catalytic beads is.

6.4.1.1.2 Impact of liquid flow rate

As introduced in section 6.2.1.2, the reaction of H₂-H₂O liquid catalytic exchange includes two reactions: vapour water-hydrogen exchange reaction (6.15) and phase change reaction (6.16):



Even though the overall degree of separation depends mainly on the transfer of deuterium between hydrogen and water vapour represented by equation (6.15), the vapour-liquid equilibrium as expressed by equation (6.16) plays a role in mass transfer between the gas/liquid phases and thus efficiency of gas/liquid mixing as demonstrated in chapter (4). Figure (6.4) illustrates the relationship of water flow rate and conversion rate (operating conditions: hydrogen flow rate= 12.9 ml/s and reaction temperature= to 333.15 K).

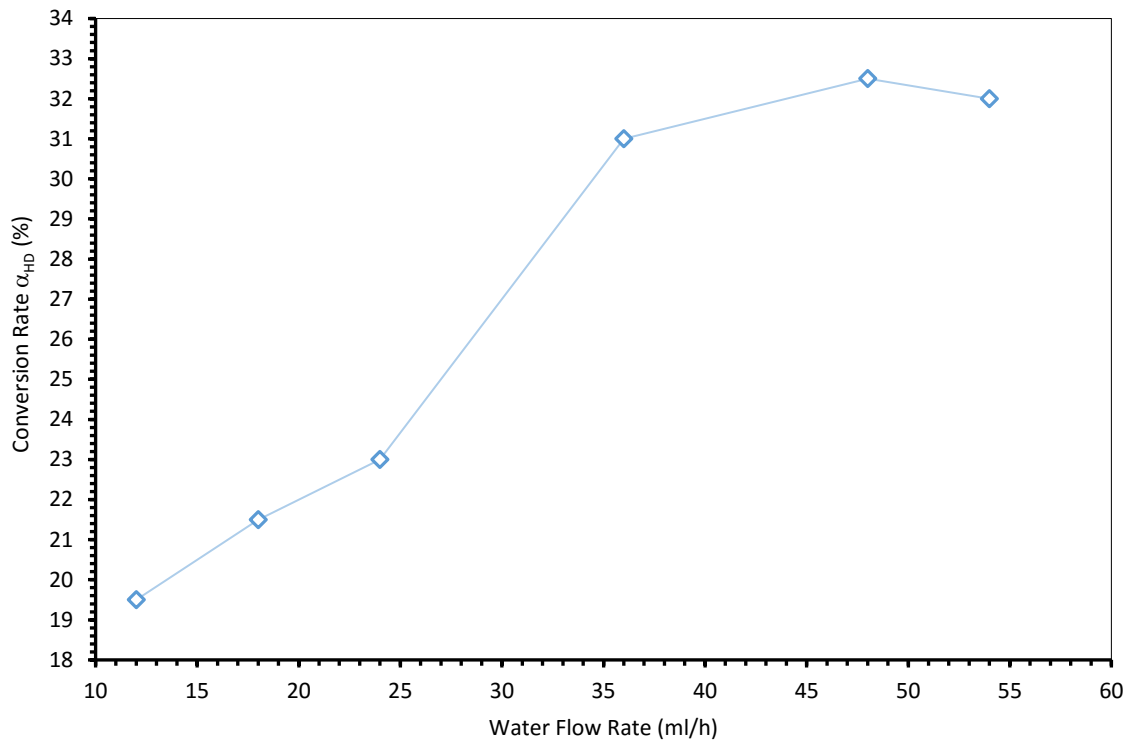


Figure (6.4) Influence of water flow rate on conversion rate, hydrogen flow rate 12.9 ml/s, temperature 333.15 K.

The effect of water flow rate on conversion rate is shown in Figure (6.4). It can be seen that with increased water flow rate, the conversion rate increased. The increase in the conversion was significant at low values of liquid flowrates likely due to promoted wetting of the catalytic surface as will be discussed in the following sections. At high liquid flow rates, the conversion rate then gradually slowed down at high values of liquid flow rates. When the flow rate of water increased, the entire amount of water vapour inside the reactor increased by phase exchange, which promoted the isotope exchange between hydrogen and vapour, resulting in an increased conversion rate of HD. It is clear that thermodynamic boundaries of the reaction (6.16) plays an important role here and the mass transfer between phases was not considered but the surrounding the catalyst (gas/solid mass transfer) played a reduced role at high liquid flow rates compared with the gaseous phase catalytic exchange rate and caused trends of conversion to follow those of the intrinsic gaseous catalytic exchange.

6.4.1.2 Impact of temperature

The reaction of H_2 - H_2O exchange of deuterium presents kinetics rate and separation factors (i.e. equilibrium constants) that are sensitive to temperature, therefore relevant conversion rates would be affected by temperature. A lower temperature leads to a greater separation factor as expressed by equations (6.17) and (6.18), which means that the lower the temperature, the more appropriate and beneficial the system is to H_2 - H_2O isotope exchange. However, in practical

conditions, H₂-H₂O isotope exchange rarely reaches theoretical separation factors, which are just driven by the thermodynamic boundaries of the two aforementioned reactions, but reach values of conversions, and by inference separation factors that are driven by kinetically controlled rates of the gaseous catalytic exchange.

Figure (6.5) represents the relationship between temperature and the conversion rate of HD in a counter-current exchange reaction (operating conditions, water flow rate= 24 ml/h, hydrogen flow rate= 4.5 ml/s and gas/liquid flow ratio, $\lambda=0.5$).

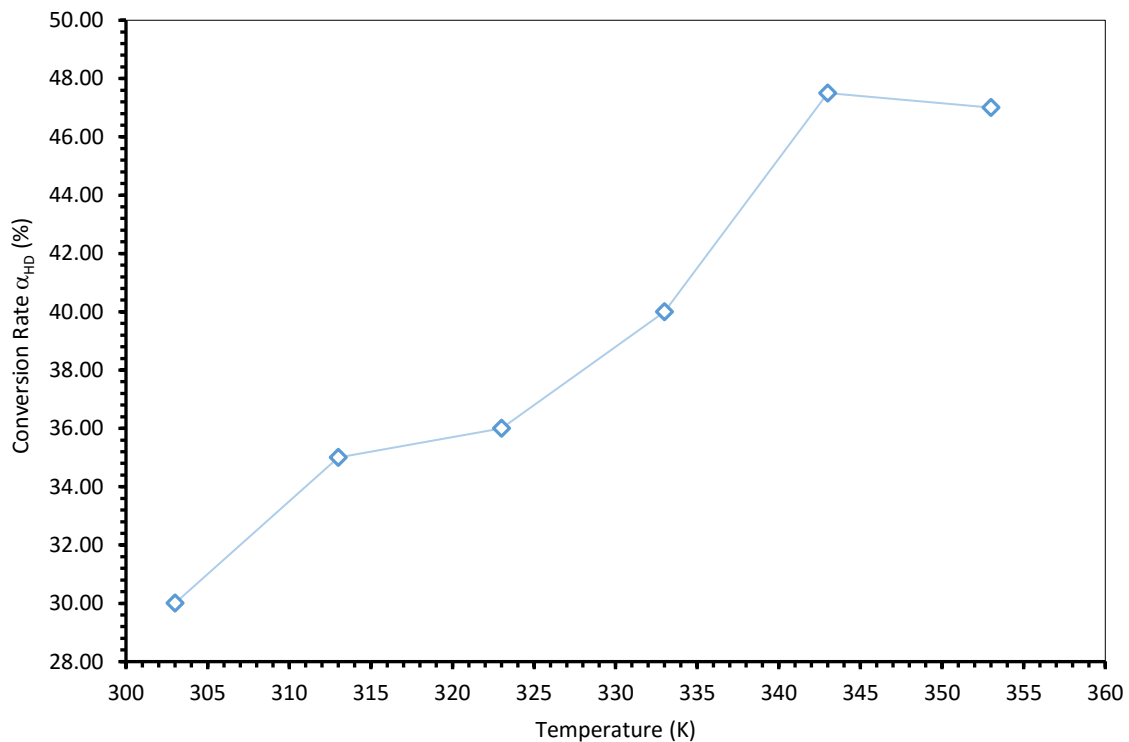


Figure (6.5) Influence of the temperature on conversion rate, hydrogen flow rate 4.5 ml/s, molar flow ratio of hydrogen gas to water ($\lambda=0.5$).

The general trend is that by increasing reaction temperature, the conversion rate will increase owing to acceleration of the kinetic rate of the gaseous reaction by temperature. It can be noticed that the conversion rate first increased with increased operating temperature until about 343.15 K and then decreased, confirming the profiles observed in the CKPE model Figure (4.11.a1) Chapter 4 on effect of temperature on isotopic exchange. The decreased conversion after a maximum value have been explained by the competitive presence of HDO vapour along with H₂O vapour at high temperatures, promoting the reverse reaction rate of the isotopic exchange. The isotope exchange has a temperature optimum of 343.15 K. This value is close to the one obtained by Aspen plus simulation (348 K in Figure 4.11a1). The vapour-water phase

exchange and isotope exchange were affected differently by temperature. The former under kinetic control was indeed accelerated by high temperature while the second, under chemical equilibrium control (efficient gas/liquid mixing) was favoured by low temperature due to higher relative volatility of H₂O vapour compared with HDO vapour, leading to more condensation of HDO vapour. To ensure sufficient conversion of HD into HDO, it is necessary therefore to locate the optimum temperature where both the kinetic rate of H₂-H₂O vapour exchange and the chemical equilibrium of the gas/liquid exchange are sufficiently high to reach maximum conversions. Figure (6.6) shows the projections of HD concentration profiles over catalyst surface by cross-sectional and vertical planes along the bed length and demonstrates how deep the local concentration of HD inside the catalytic beads is.

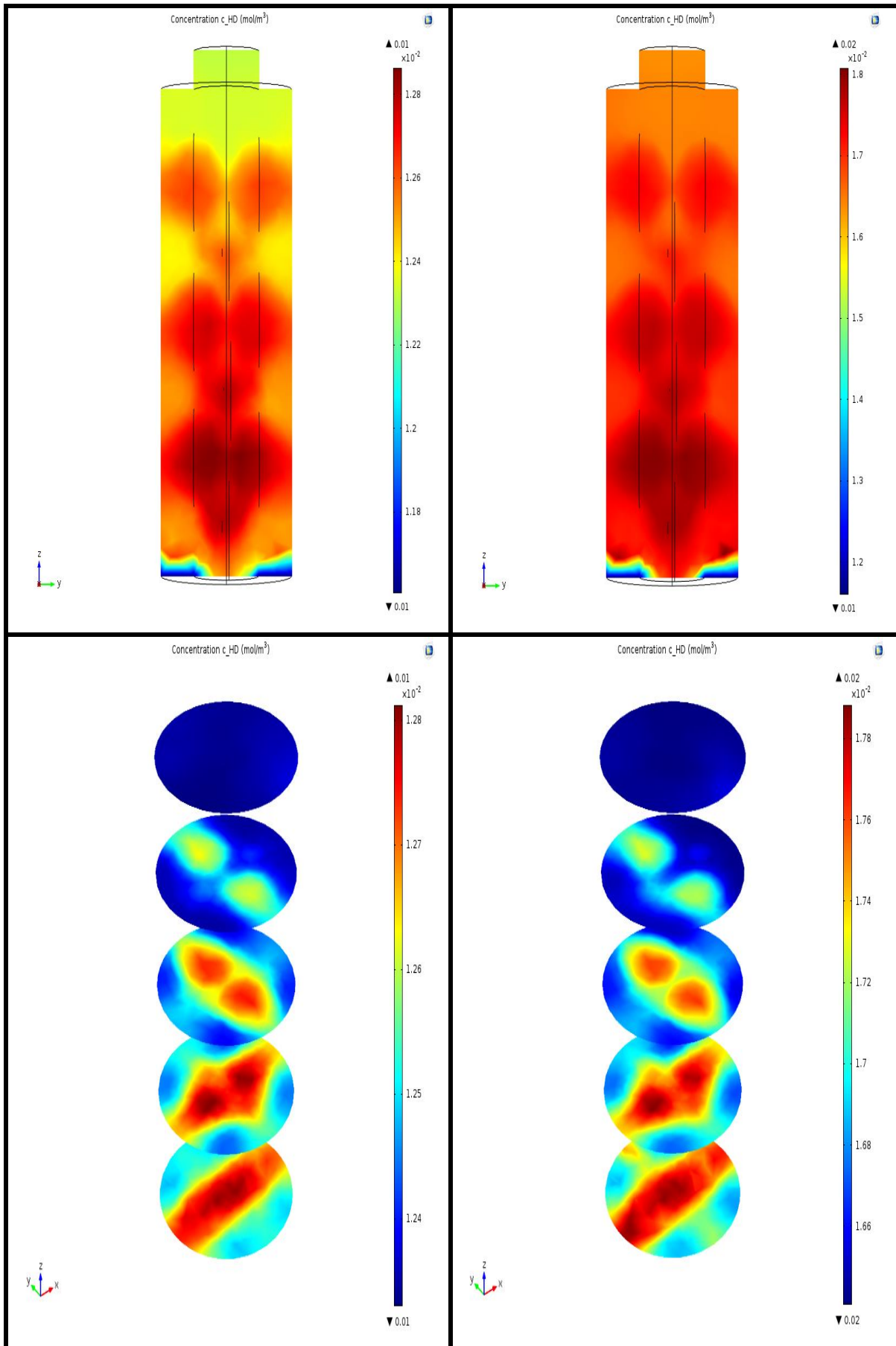


Figure (6.6) Colour map of HD concentration over catalyst surface in counter-current mode operation at temperature; 303.15 (K) (left - 3D on cross-sectional and vertical planes) and 343.15 (K) (right - 3D on cross-sectional and vertical planes).

Figure (6.7) presents the impact of temperature at varied values of the gas/liquid ratio (λ) on the conversion rate of HD. The general trends show a decrease in the conversion of HD with gas-to-liquid flow rate ratio and reproduce the profile of Figure (6.2). Unlike Figure (6.5), where both reactions were set under chemical equilibrium control, this figure shows that under chemical kinetic control, low temperature values of conversion are not the same at various gas-to-liquid flow rate ratios.

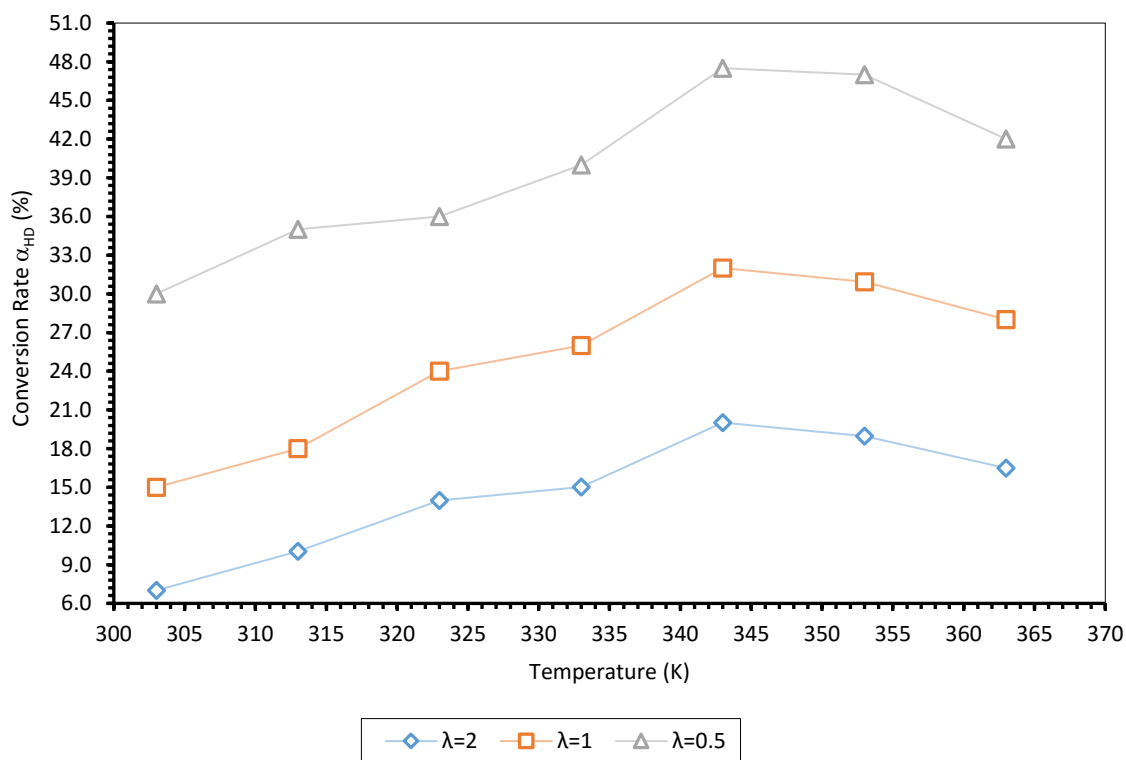


Figure (6.7) Influence of reaction temperature and varied gas/liquid ratio on conversion rate.

6.4.1.3 Impact of the height of catalytic bed

In a counter-current exchange, the height of catalytic bed, and by inference the mass of catalyst, would affect the contact time and reaction depth of reactants. Figure (6.8) shows impact of the height of catalytic bed on the conversion rate (design and operating conditions; heights of catalytic bed=5 mm to 40 mm, reaction temperature= 333.15 K, flow rate of hydrogen= 8.63 ml/s and gas-liquid flow ratio (λ) was 0.5).

Figure (6.8) shows that increasing the height of catalyst bed led to higher conversion and beyond 35 mm, conversion rate slowed down towards asymptotic values close to the chemical equilibrium ones. In addition, the profiles of HD conversion clearly indicate that most of the conversion into HD took place throughout the bottom part of the column. Maximum conversion at 35 mm justifies the role of efficient condensation of HDO by gas/liquid mixing. These results

confirm those obtained by the CEPE model in Chapter 4 by using Aspen plus modular package and thus demonstrate an excess height of the packing after 35 mm.

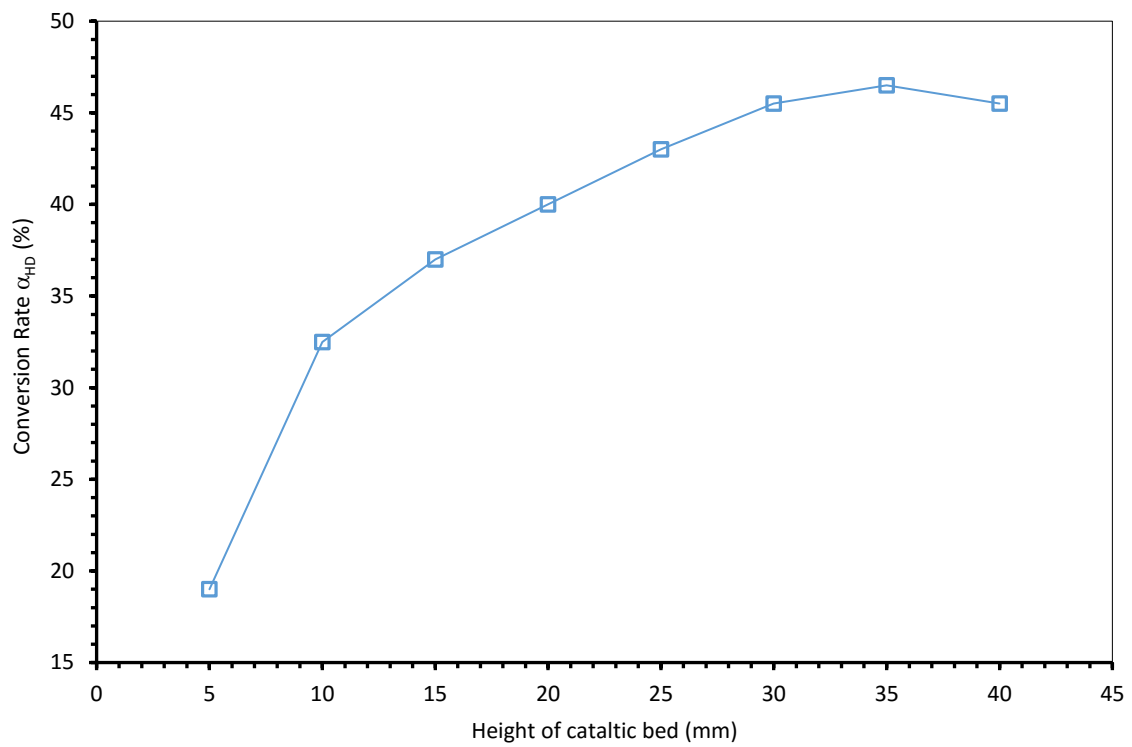


Figure (6.8) Influence of column height on conversion rate with a molar flow ratio ($\lambda=0.5$).

6.4.2 Co-current exchange

Figure (6.9) shows the process of H₂-H₂O in a co-current flow exchange. Hydrogen and water entered the catalyst bed from the top to conduct the co-current exchange. Hydrogen isotope chemical exchange is conducted in the catalytic bed and water-vapour phase exchange happened in the inter packing. Hydrogen and water simultaneously flow from the top of the catalytic bed and when liquid water changed into vapour, hydrogen brought water vapour to go through catalytic bed and conducted the catalytic exchange on the surface of the hydrophobic packing.

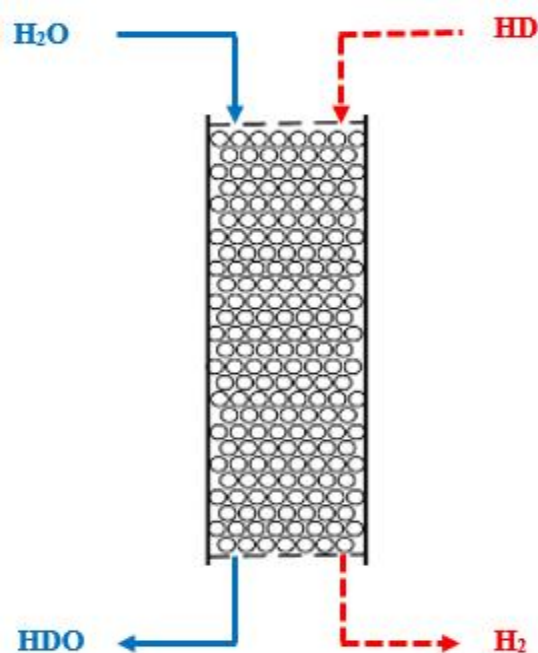


Figure (6.9) Schematic representation of hydrogen-water exchange in the co-current mode operation.

6.4.2.1 Impact of flow rate

Flow rates of hydrogen gas and liquid water and ratios of these flow rates were carried out to investigate impact of flow dynamics on conversion rate. At a constant height of the catalytic bed, the flow rate of the both gas and liquid streams would impact flow dynamics, wettability of the packing and mass transfer in the catalytic packing. Similar to the counter-current mode operations, the mass transfer resistance between the gas/liquid phases was assumed negligible.

6.4.2.1.1 Impact of flow rate of gas

Figure (6.10) illustrates the impact of the flow rate of hydrogen on conversion rate in co-current flow operation (operating conditions; reaction temperature= 333.15 K and water flow rate= 24 ml/h). As shown in Figure (6.10), the conversion rate decreased with increased flow rate of hydrogen, when the height of catalytic bed and flow rate of water were fixed. Higher flow rate

of gas means faster interstitial velocity of the gaseous phase, leading to a shorter contact time with water, causing a reduction in the conversion rate. Figure (6.11) shows the projections of HD concentration profile over catalyst surface by cross-sectional and vertical planes along the bed length. HD concentration maps are well distributed inside the packing beads, demonstrating mass transfer resistance inside the catalytic beads.

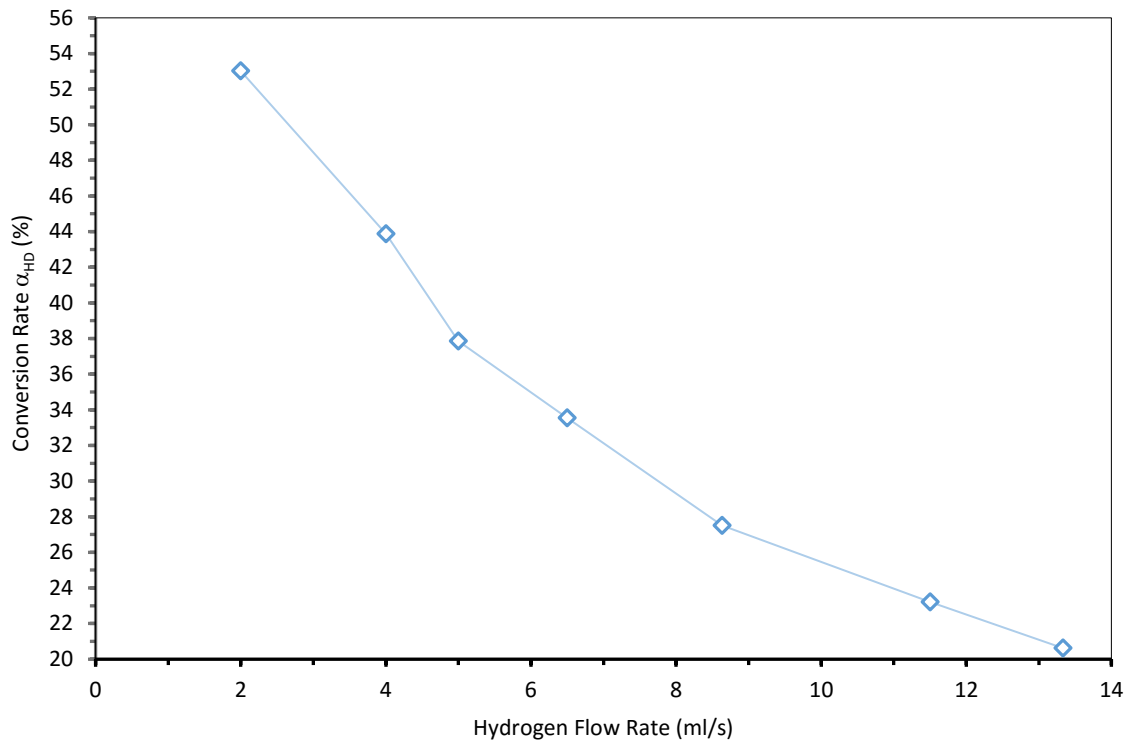


Figure (6.10) Influence of hydrogen flow rate on conversion rate, water flow rate 24 ml/h, temperature 333.15 K.

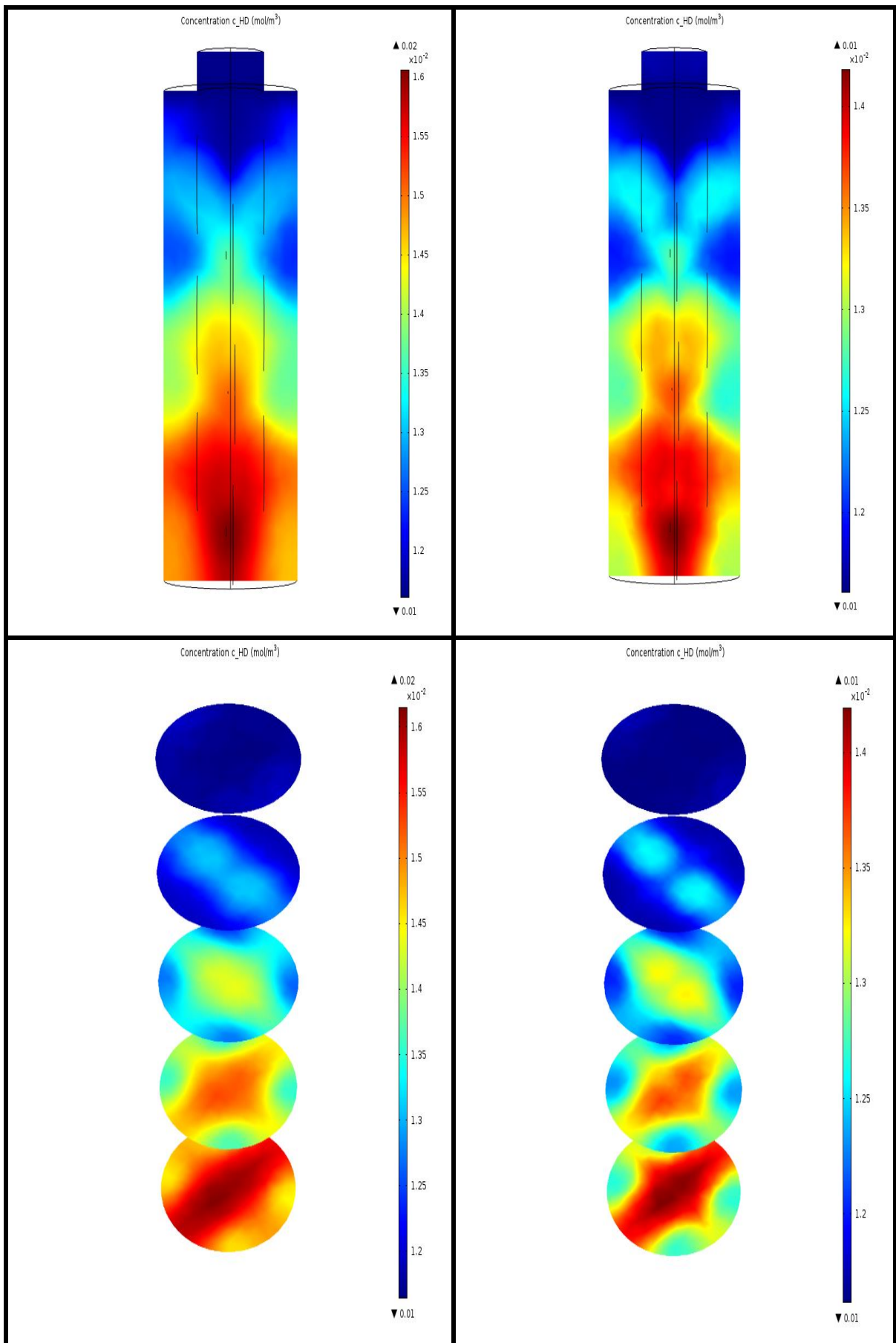


Figure (6.11) Colour map of HD concentration over catalyst surface in co-current mode operation at gas velocity; 5 (ml/s) (left - 3D on cross-sectional and vertical planes) and 13.33 (ml/s) (right - 3D on cross-sectional and vertical planes)

6.4.2.1.2 Impact of the flow rate of liquid

Figure (6.12) shows effect of the flow rate of water on conversion rate (operating conditions; flow rate of hydrogen=13.33 ml/s and reaction temperature= 333.15K). The conversion increased with flow rate of water, owing to more wetting of the catalyst surface and promoted the driving force of both mass transfer and gaseous phase catalytic exchange and increasing contact between the vapour and hydrogen, and therefore the conversion rate.

When the flow rate of water reached certain values, the rate of the conversion rate gradually slowed down toward steady state. This trend was observed as well in the modelling of liquid/gas flowrate effect on separation efficiency when the column was modelled by Aspen plus package (see Chapter 4) and was explained by the efficient mixing at high liquid flow rates, promoting mass transfer more presence of water vapour in the vapour phase and thus decreasing HDO conversion rate into HD. The gaseous phase isotope exchange reaction plays a key role for the whole reaction, therefore the increasing the velocity of the liquid phase at large values slowed down the conversion rate.

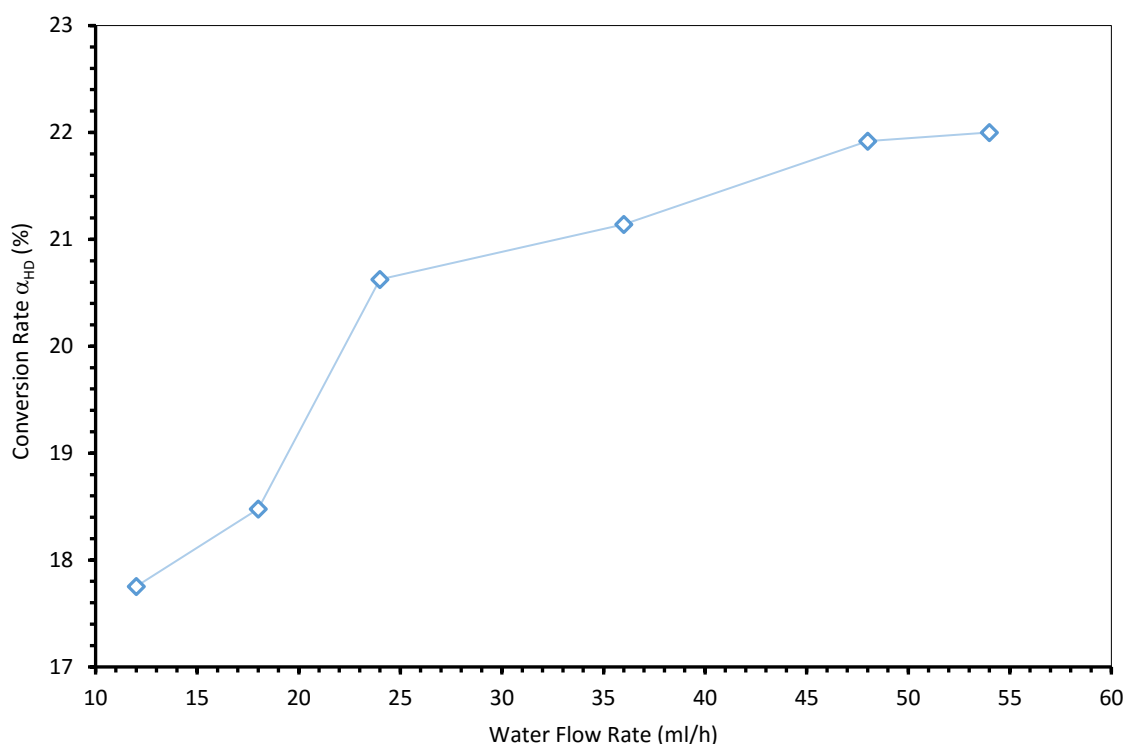


Figure (6.12) Influence of water flow rate on conversion rate, hydrogen flow rate 13.33 ml/s, temperature 333.15K.

6.4.2.2 Impact of temperature

Figure (6.13) illustrates impact of temperature on the conversion rate of HD in the co-current flow exchange reaction (operating conditions; flow rate of water: 48 ml/h, hydrogen flow rate: 8.63 ml/s and gas/liquid flow rate ratio $\lambda=0.5$). It can be clearly seen that, with increased temperature, the conversion rate increased, demonstrating the acceleration of both mass transfer rate and catalytic rate. When the temperature rises, vapour-water phase exchange was promoted, and the conversion rate increased continuously. It is interesting to see that under co-current mode operation, the trend of conversion into HD do not show maximum values which was observed in the counter-current operation. In fact, the isotope exchange did not reach high conversion rates compared with the counter-current flow. Although the separation factor (by inference the chemical equilibrium) of the isotopic exchange under low temperature is higher, it was still operated under kinetic control. Figure (6.14) shows the projections of HD concentration profile over catalyst surface by cross-sectional and vertical planes along the bed length and clearly show how deep is the conversion inside the core of the catalytic beads, demonstrating non relevance of internal mass transfer limitation on the overall liquid/gas hydrogen exchange.

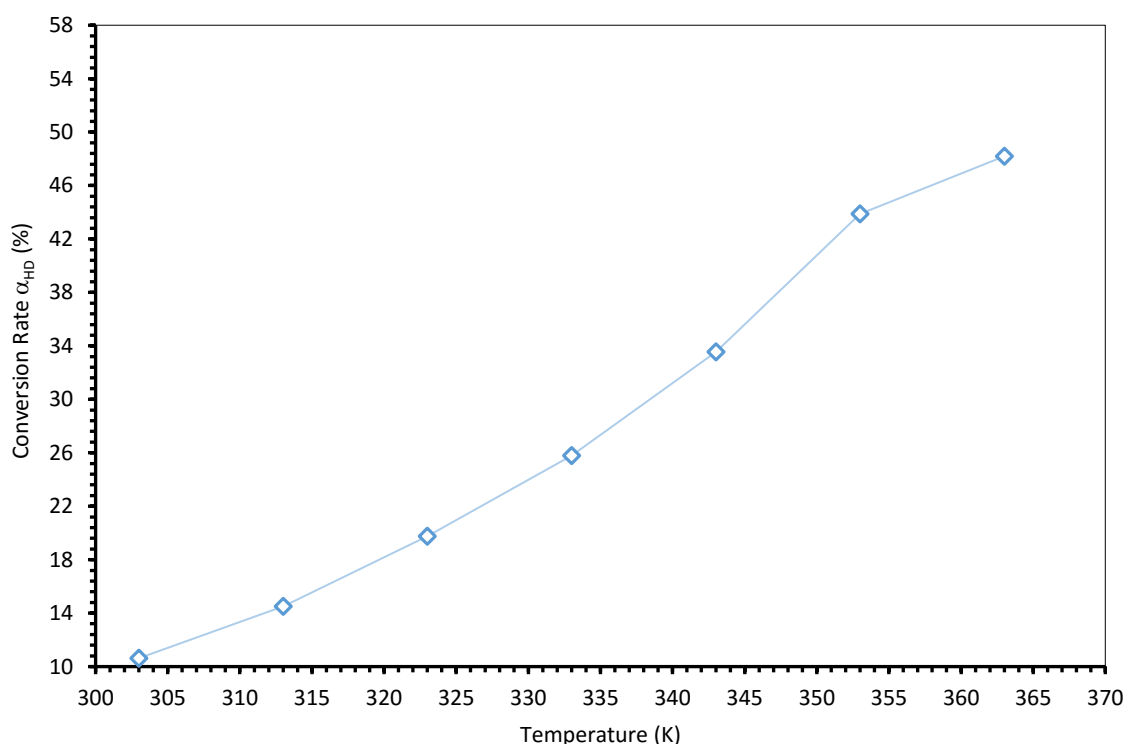


Figure (6.13) Influence of the temperature on conversion rate, hydrogen flow rate 8.63 ml/s, molar flow ratio of hydrogen gas to water ($\lambda=0.5$).

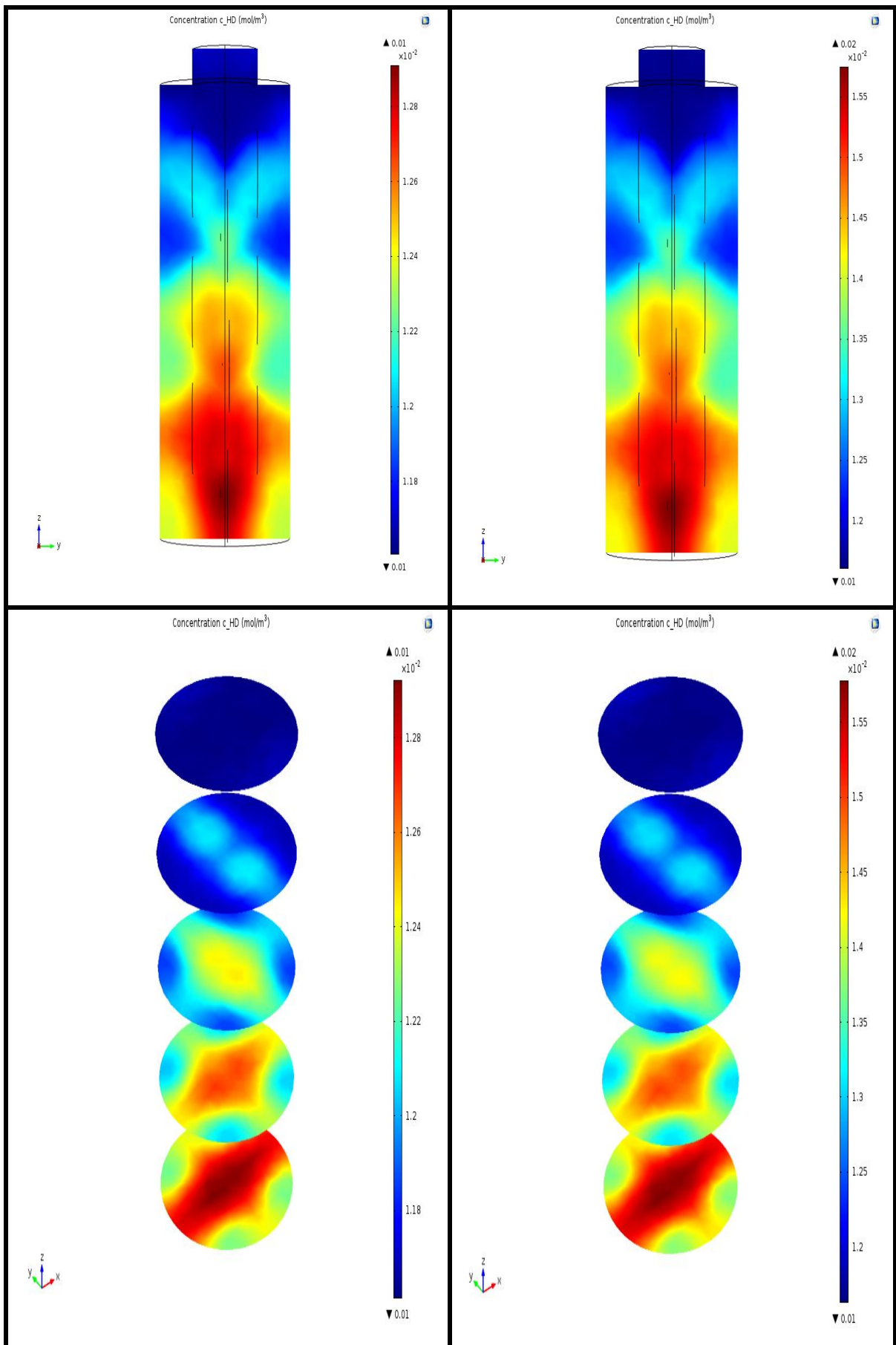


Figure (6.14) Colour map of HD concentration over catalyst surface in co-current mode operation at temperature; 303.15 (K) (left 3D on cross-sectional and vertical planes) and 343.15 (K) (right - 3D on cross-sectional and vertical planes).

Figure (6.15) shows effect of temperature and gas/liquid flow rate ratio (λ) on conversion rate in a co-current flow of gas/liquid of the isotopic exchange reaction. Similar to the counter-current flow operation, the conversion rate decreased with the increased molar flow ratio of hydrogen to water. In the co-current exchange reaction, phase exchange played a key role and high temperature are effective on the vapour-water phase exchange. When the gas phase in the catalytic bed was sufficiently saturated with water vapour, the conversion rate gradually slowed down.

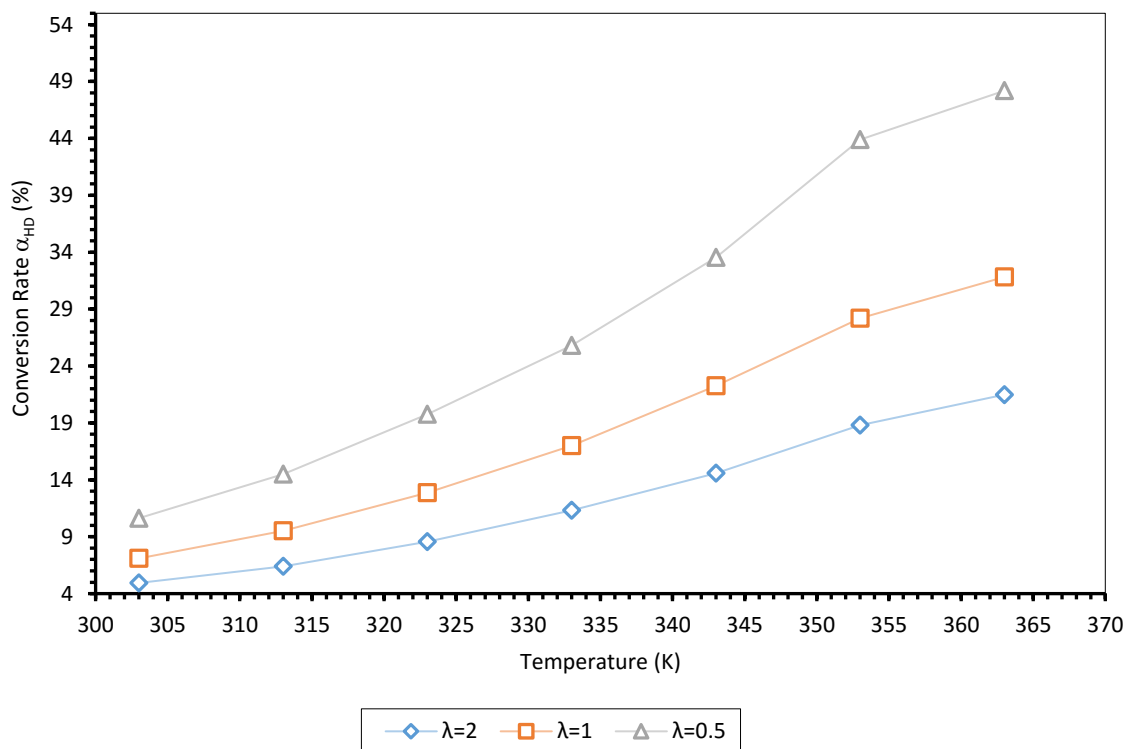


Figure (6.15) Influence of the temperature on conversion rate with different molar flow ratio (λ).

6.4.2.3 Impact of the height of catalytic bed

Figure (6.16) shows the impact of the height of catalyst bed (mass of catalyst) on conversion rate in a co-current flow exchange (operating conditions; the height of catalytic bed= 5 mm to 40 mm, reaction temperature= 333.15 K, hydrogen flow rate= 8.63 ml/s and gas-liquid flow rate ratios (λ) to 0.5).

The conversion rate increased linearly with the height of the packing bed. At a given height value, herein about 35 mm, the conversion rate reached steady values and even some decrease when the height of the packing was extended. Similar trends were observed with the counter-current flow catalytic exchange and was explained by the reversible process of the isotopic exchange which is less favoured in presence of increased amounts of water vapour at the

expense of reagent HDO vapours. The H₂-H₂O isotope exchange is reversible, and hence increased height of catalyst means more catalyst usage, which increased contact time of reacting species and reaction depth, as well as time for vapour-water phase exchange. The height of the packing thus increased the conversion rate but decreased the conversion as well at a given height of the reactive packing. Thus the maximum values observed are those achieved under maximum conversion (equilibrium conversion).

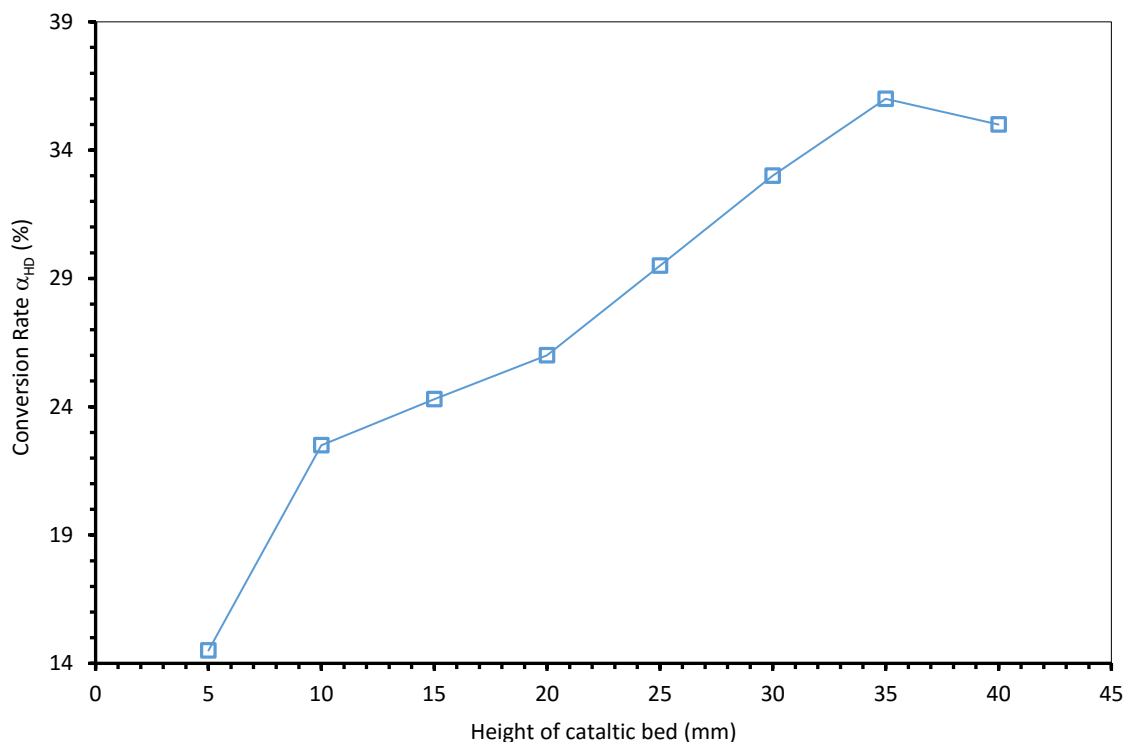


Figure (6.16) Influence of column height on conversion rate with molar flow ratio ($\lambda=0.5$).

6.4.3 Impact of flow mode operation for the isotopic exchange process

H₂-H₂O isotope exchange could be obtained by two methods: co-current flow exchange and counter-current flow exchange. The performance of separation was evaluated by investigating impacts of relevant design and operating parameters.

Figure (6.17) shows the trend of conversion rate under varied gas flow rate and co-current as well as counter-current operations. The conversion rate decreased with increased flow rate of hydrogen under different exchange methods. Increasing flow rate of hydrogen reduced reaction depth, and hence, caused reduction of the conversion rate. Figure (6.18) shows the relationship between the flow rate of water and conversion rate under different exchange methods. In co-current exchange, the conversion rate increased with increased flow rate of water while in the counter-current exchange, the conversion rate increased and then decreased with increased flow rate of water. Increased flow rate of water brought more vapour, promoted the exchange

reaction by a higher conversion rate. In counter-current exchange, when the flow rate of water reached a certain value, mass transfer resistance and pressure drops were relevant, developing flooding and limited efficiency of the exchange. Figures (6.19) and (6.20) illustrate the trends of conversion rate with temperature and height of the packed bed, respectively. The counter-current mode achieved higher conversion than the co-current mode at similar operating conditions owing to improved gas/liquid mass in the former mode.

In addition, the effect of fluid flow and impact of flow mode operation on the overall (volumetric) mass transfer coefficient based on the gaseous phase $K_y a$ is shown in Figures (6.21 and 6.22). K_y is the overall mass transfer coefficient and a is the interfacial area between the gaseous and liquid phases. According to the film theory, the mass transfer coefficient is function of the diffusion through the interphase film and the thickness of the interphase film and this later is strongly function of the flow dynamics (see for instance Onda model in Chapter 4). The mass transfer coefficients for the co-current and counter-current mode operations were calculated according to equations (6.23 and 6.34), respectively. It is seen that from Figure (6.21), the mass transfer coefficient increases with increase hydrogen flow rate in the range of 2-13.5 ml/s. The relationship of volumetric mass transfer coefficient $K_y a$ with gas flow rate has been reported by a number of works. At conditions of normal temperature and pressure, countercurrent operations and a hydrogen flow rate in the range 0.05~1.4m/s, Butler et al. [203] reported an increase of $K_y a$ to approximately the ~0.3 power of hydrogen flow rate. Enright and Chuang [209] reported an increase to in the range 0 to 0.64 power of hydrogen flow rate at a pressure of 5.27 MPa and they believe that 0.64 corresponds to the maximum value of fully turbulent regime. In Figure (6.21), the counter-current operation shows an increase of mass transfer coefficient to the 0.69 power of gas flow rate and this value is within the range of literature values, including Onda model (power of 0.7) as expressed in equation (A.11-A.17) in Appendix A. This result clearly shows that mass transfer between the gas and liquid phases dominated the overall mass transfer with chemical reaction.

The mass transfer coefficient changes slightly with liquid flow rate as illustrated Figure (6.22), (i.e. $K_y a$ increased approximately to the ~0.32 power of water flow rate). However, some discrepancies with Butler's [203] results are observed who reported an increase of $K_y a$ increase to the ~0.08 power of the water flow rate. This minor dependence on liquid flow was explained by the increased turbulences and liquid holdup in the bed at high liquid flow, leading to reduced efficiency of isotopic exchange compared with the trickle bed operations. As a result of the liquid flow rate and distribution slightly improved the mass transfer as demonstrated in Chapter

4, demonstrating the relevance of transport resistance inside the film on the gas phase side at present operating conditions.

The effect of temperature on mass transfer coefficient was investigated in the range from between 303.15 K to 363.15. The results show that the reaction temperature affected significantly the mass transfer coefficient under both co-current and counter-current operation. The mass transfer coefficient followed the trends observed with the conversion rate. For instance, under counter-current operations, an increase with temperature until 343.2 K and decreased at higher temperatures due to higher relative volatility of H₂O vapour compared with HDO vapour, leading to more condensation of HDO vapour (see section 6.4.1.2).

Figures (6.17-6.23) illustrated therefore that the conversion rate and mass transfer coefficient of gas-liquid counter-current exchange reaction were significantly higher than that of the co-current exchange reaction owing to high mass transfer driving forces (concentration gradients) available in the counter-current mode operations. In the absence of mass transfer limitation between the gas and liquid phases (temperatures higher than 310 K), the CFD results showed that the vapour-water phase exchange was very important for the whole exchange process. In gas-liquid counter-current exchange, water that was added from the top of the column went through the catalytic bed by drops and because of the hydrophobicity of the catalytic packing, water was distributed unevenly, leading to inefficient contact and to limited efficiency of the overall separation. The advantages of gas-liquid counter-current exchange were however associated with more complex flow dynamics (i.e. changes in the flow regimes, pressure drops and flooding potential).

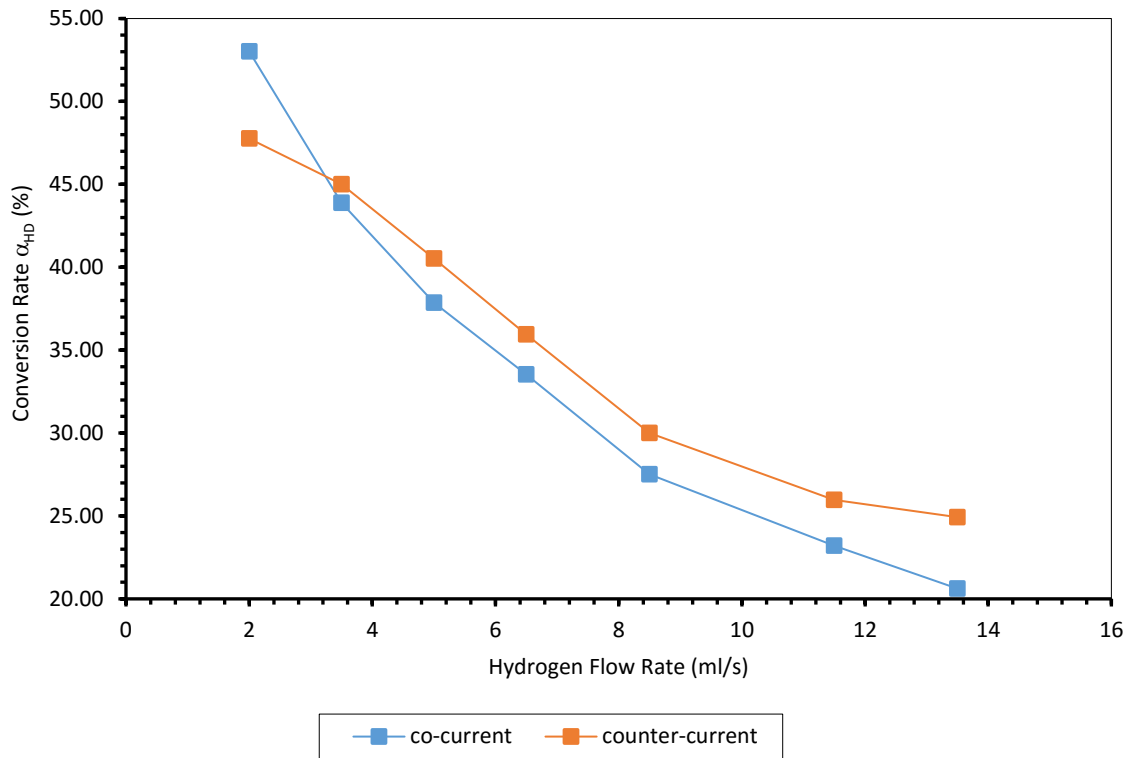


Figure (6.17) Influence of hydrogen flow on conversion rate in co-current and counter current modes, water flow rate 24 ml/h, temperature 333.15 K.

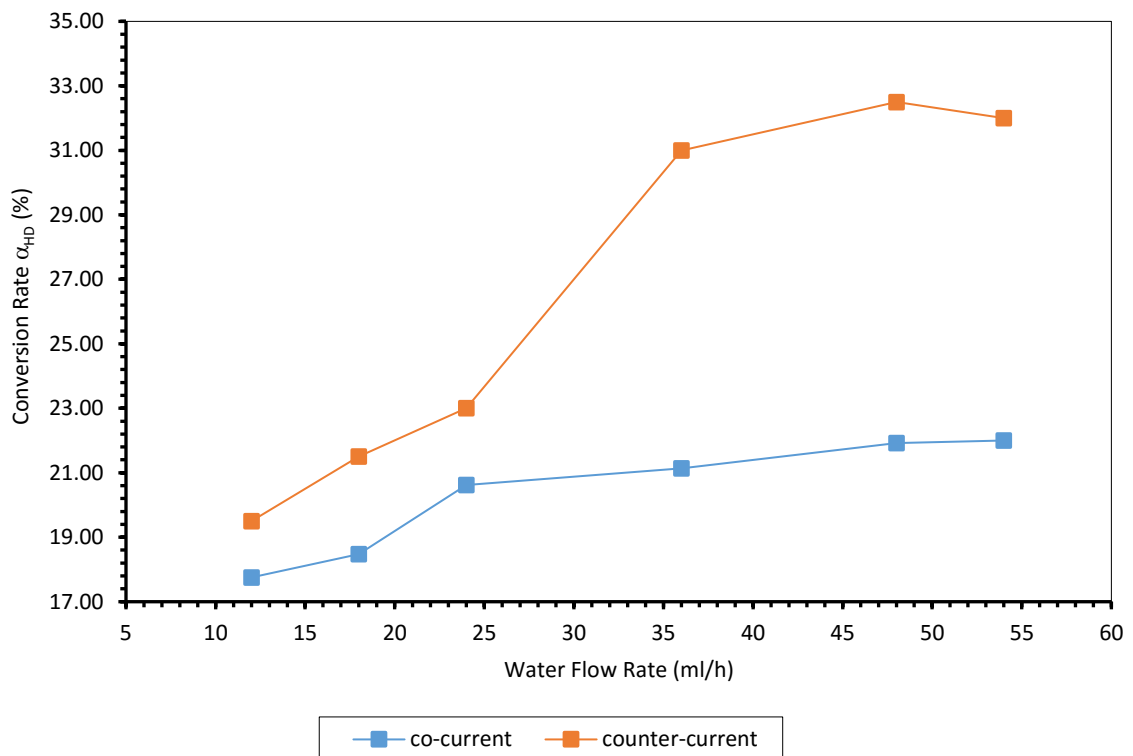


Figure (6.18) Influence of water flow rate on conversion rate in co-current and counter current modes, hydrogen flow rate 13.5 ml/s, temperature 333.15 K.

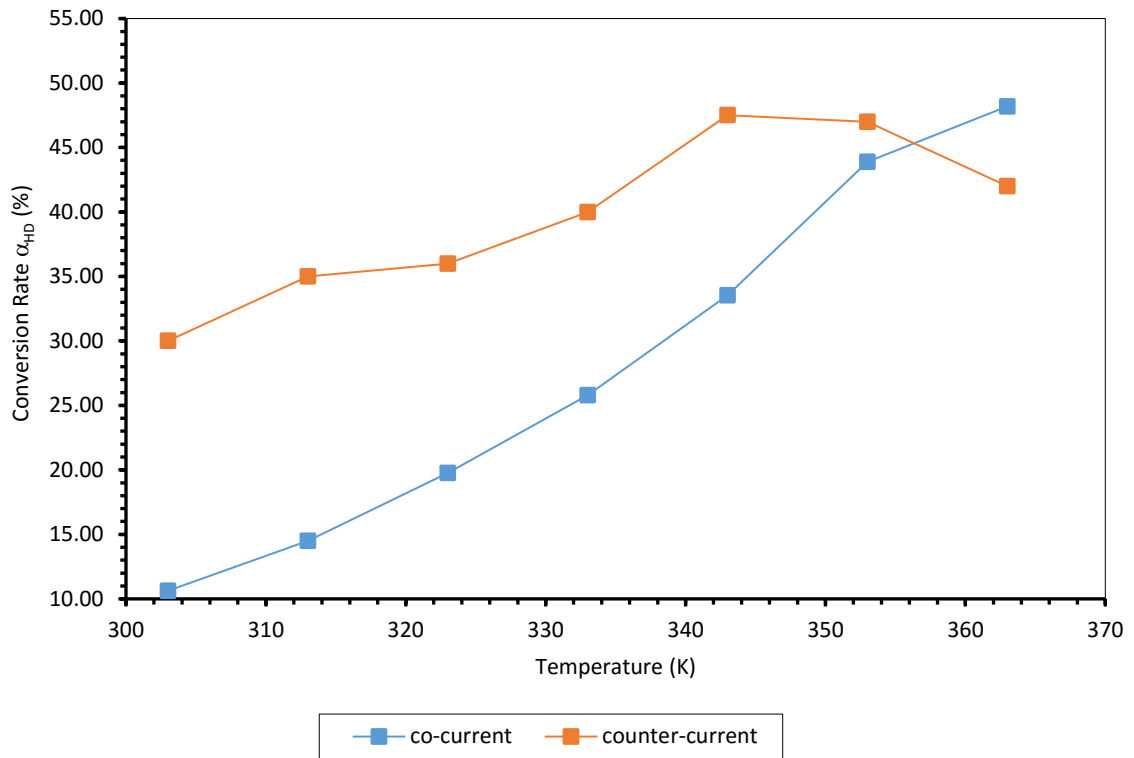


Figure (6.19) Influence of the temperature on conversion rate in co-current and counter current modes with molar flow ratio ($\lambda=0.5$).

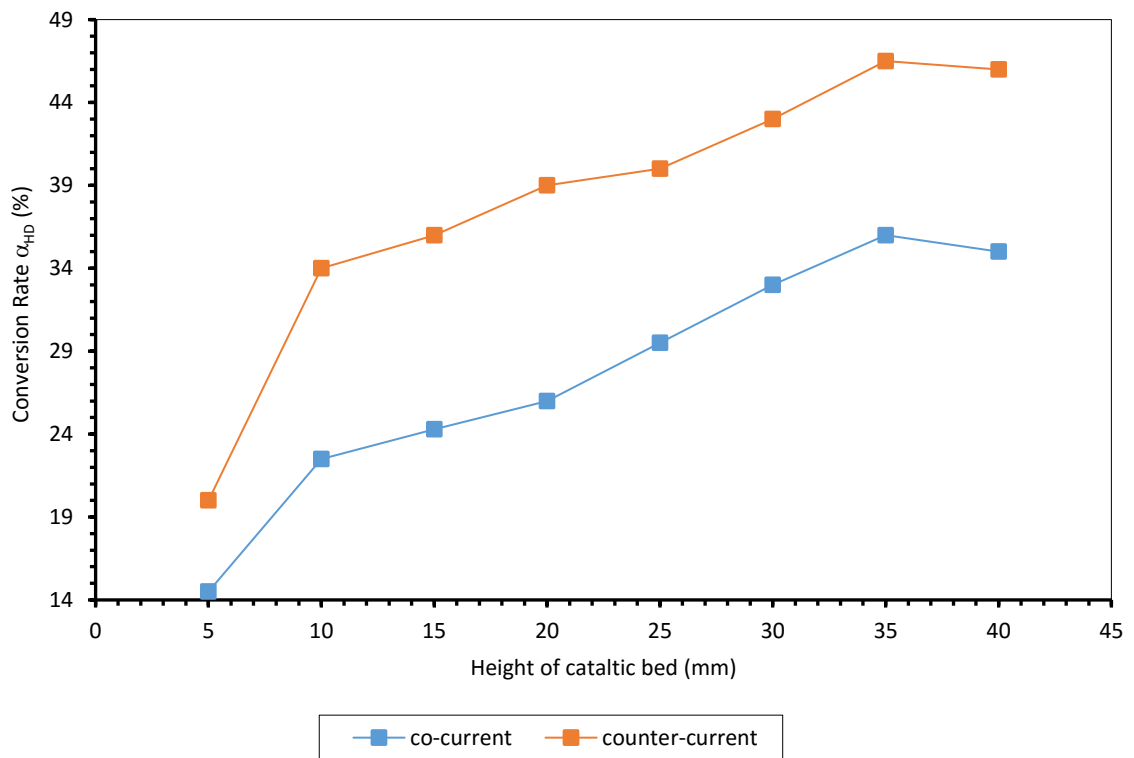


Figure (6.20) Influence of the catalytic bed height on conversion rate in co-current and counter current modes, molar flow ratio ($\lambda=0.5$).

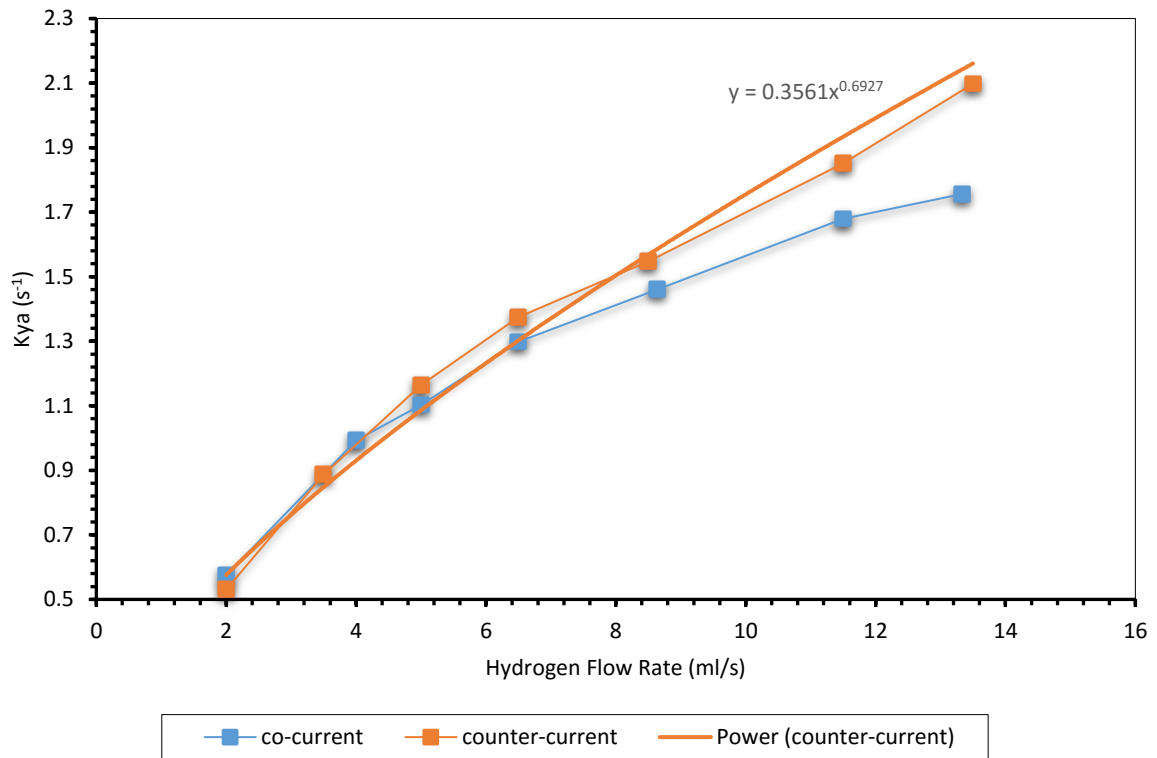


Figure (6.21) Influence of hydrogen flow rate on mass transfer coefficient in co-current and counter current modes, water flow rate 24 ml/h, temperature 333.15 K.

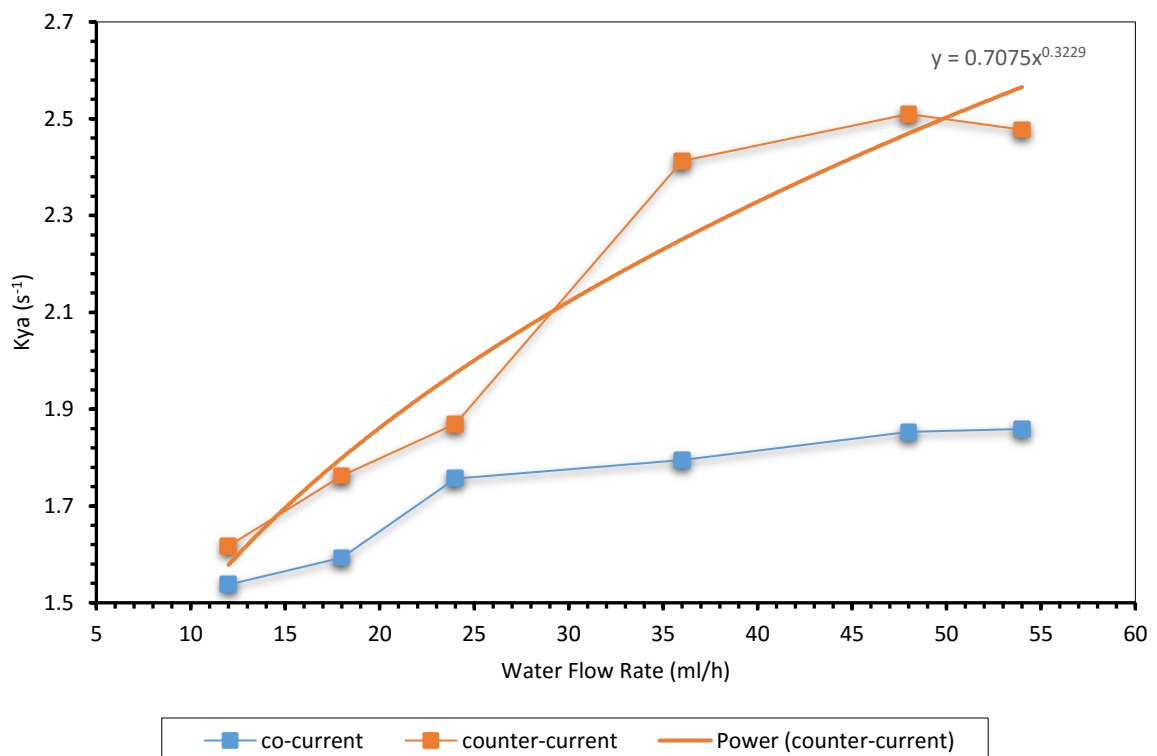


Figure (6.22) Influence of water flow rate on mass transfer coefficient in co-current and counter current modes, hydrogen flow rate 13.5 ml/s, temperature 333.15 K.

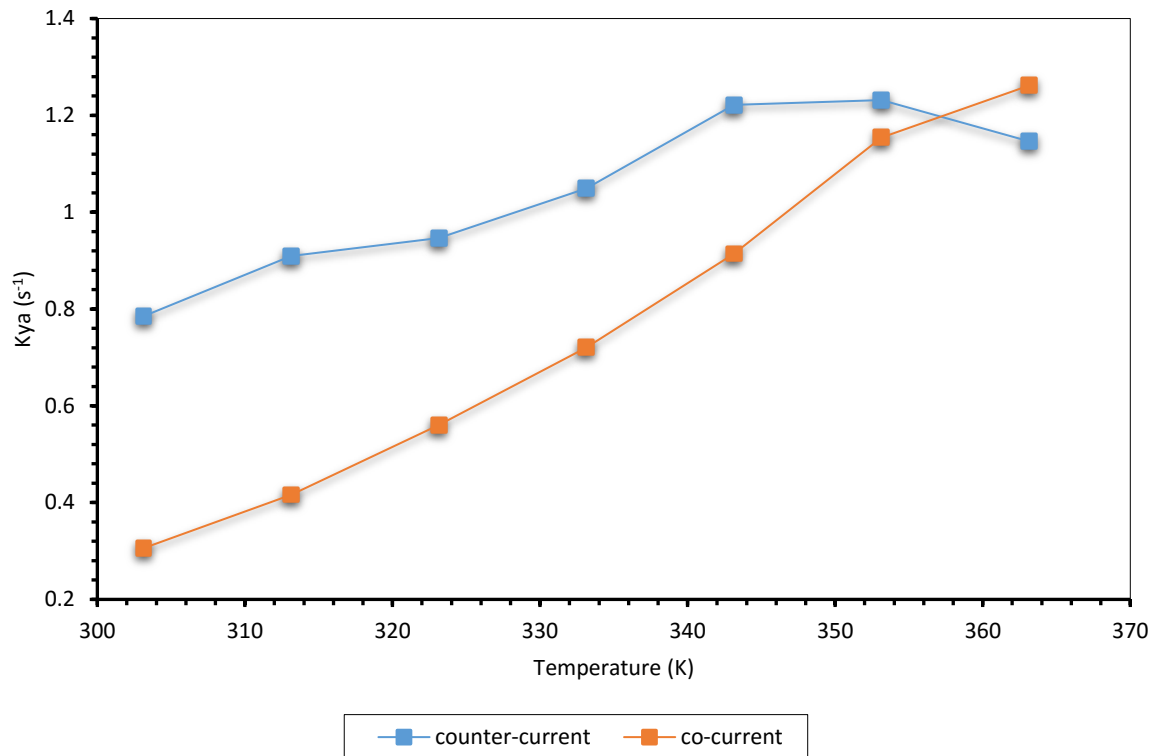


Figure (6.23) Influence of temperature on mass transfer coefficient in co-current and counter current modes with flow ratio ($\lambda=0.5$).

6.5 Stability of the steady-state operations

An important parameter to validate the 3D simulation results, particularly for solving both fluid flow and mass transfer equations under transient operations, is the numerical stability of the solution. This is particularly the case herein due to the non-linearity of the correlation of gas/liquid models and combined fluid flow and mass transfer models. Therefore, the solving algorithm which was defined in the previous section (6.3.1) was validated by looking at the solutions of conversion rate of HD for a long running simulation time. This is particularly important as output results (i.e. flow velocity and concentrations) should be not sensitive to the integration time and integration step used. The default setting of the upwind technique allowed the time step to be modified accordingly at high values of flow rates and low compositions used.

The activity profile of the catalyst was simulated based upon the time-on-stream theory. The time-on-stream was used to look at behaviour of the stability of the computational method based on the conversion rate. The evaluation of conversion rate was set for a period ranging from one hour to 24 hours of computation running time. Figure (6.24) shows the numerical simulation running time along with the conversion rate (operating conditions; gas/liquid flow

rate ratio $\lambda=0.5$, temperature= 333.15 K, flow rates of water and hydrogen= 24ml/h and 4.5 ml/s, respectively). As shown in Figure (6.24), the values of conversion rates remained steady for an extended period of 24 hours, no significant change in the stability of the simulation were observed. This result is important to validate previous results where changes in trends were observed on conversion rates with temperature and height of the packing, particularly the counter-current mode operations, after long-time simulation runs.

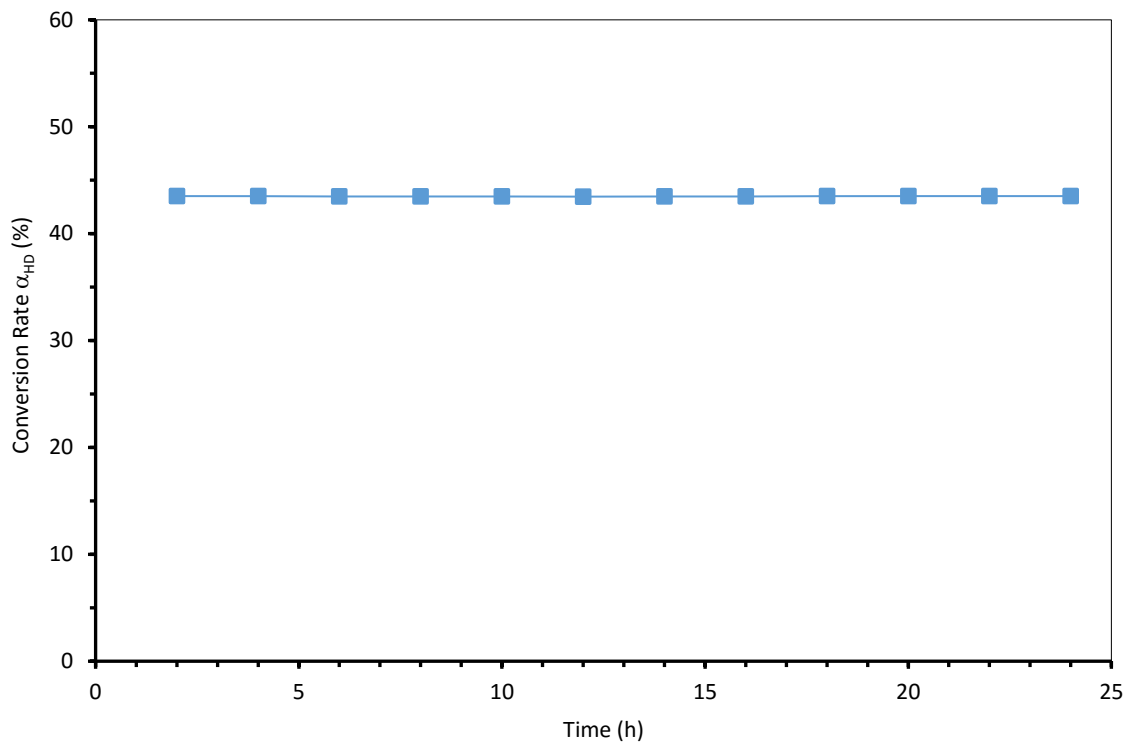


Figure (6.24) Influence of the time on stability, hydrogen flow rate 4.55 ml/s, molar flow ratio of hydrogen gas to water ($\lambda=0.5$).

6.6 CFD model validation

Despite the fact that numerical simulations are well developed and have been applied vastly to providing accurate replications of phenomena inside catalytic reactors, it is understood that the CFD model and its results have to be validated by comparisons against experimental data available from literature related to TBR operation under similar operating conditions. Accordingly, the results of CFD assessments of H_2 - H_2O liquid phase exchange reaction were validated by comparing the simulation results with a recent experimental results reported by Huang et al. [71].

Comparison between the CFD results with the experimental data on influence of flow rate and temperature on conversion rate are shown in Figures (6.25), (6.26) and (6.27). As shown in Figure (6.25), the impact of the gas flow rate on conversion rate fits well with the results

obtained by Huang et al. [71]. In addition, it appears from Figure (6.26) that there is an acceptable agreement as well of our model predictions and those obtained by Huang et al. [71] on impact of water flow rate on conversion rate. In Figure (6.27) on impact of temperature on conversion rate, it is clearly observed how the conversion rates reach maximum values before they decline. The predictions are satisfactory, particularly at low temperatures where both vapour/gas rate and liquid/gas mass transfer limitations took place simultaneously. The maximum optimal temperature obtained by simulation was close to the one achieved by Aspen plus simulation on reactive stripping modelling in chapter (4). However, some discrepancy is observed with those obtained experimentally as reported by Huang et al. [71] Even though there is a difference on optimal temperature, the general trends of influence of temperature are still well confirmed by literature data [128].

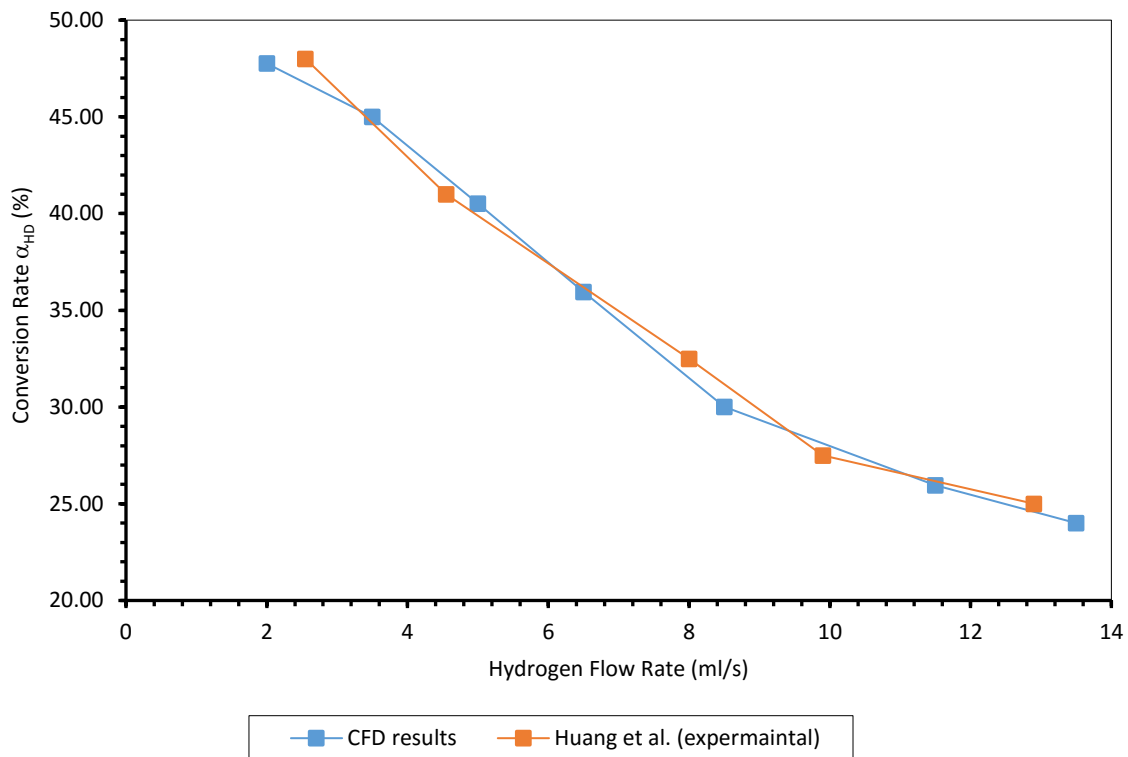


Figure (6.25) Comparison of the influence of hydrogen flow rate on conversion rate, water flow rate 24 ml/h, temperature 333.15 K.

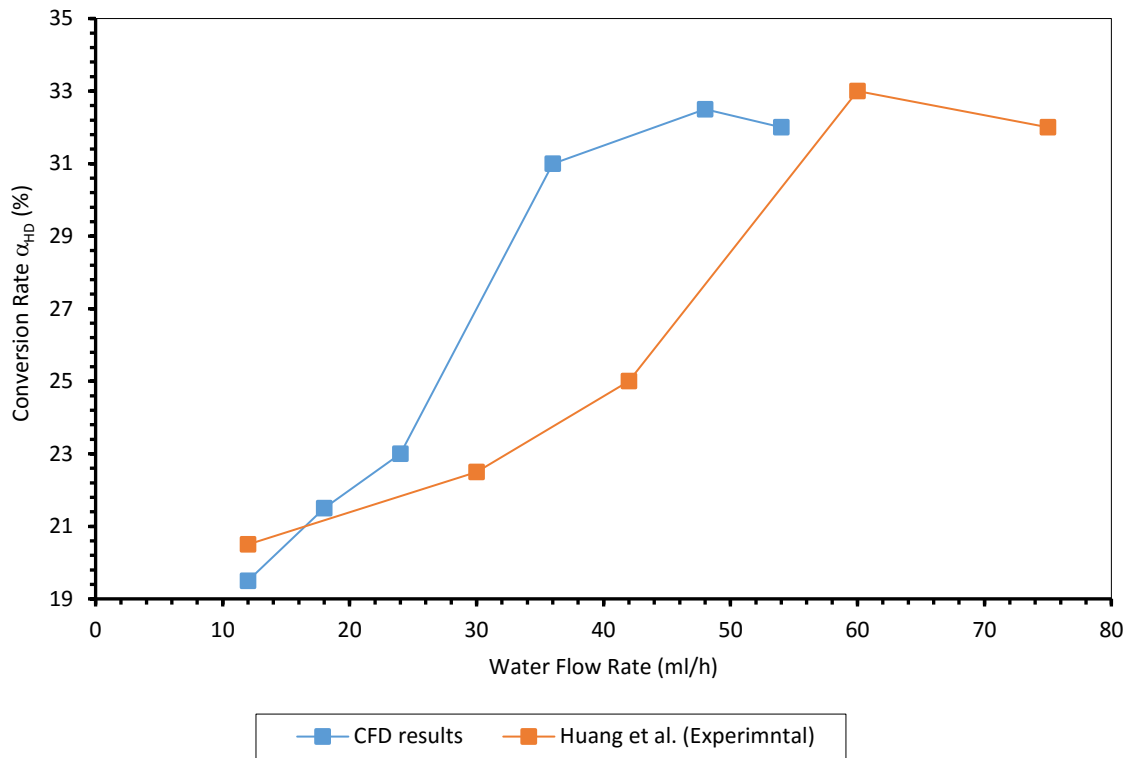


Figure (6.26) Comparison of the influence of water flow rate on conversion rate, hydrogen flow rate 13.3 ml/s, temperature 333.15 K.

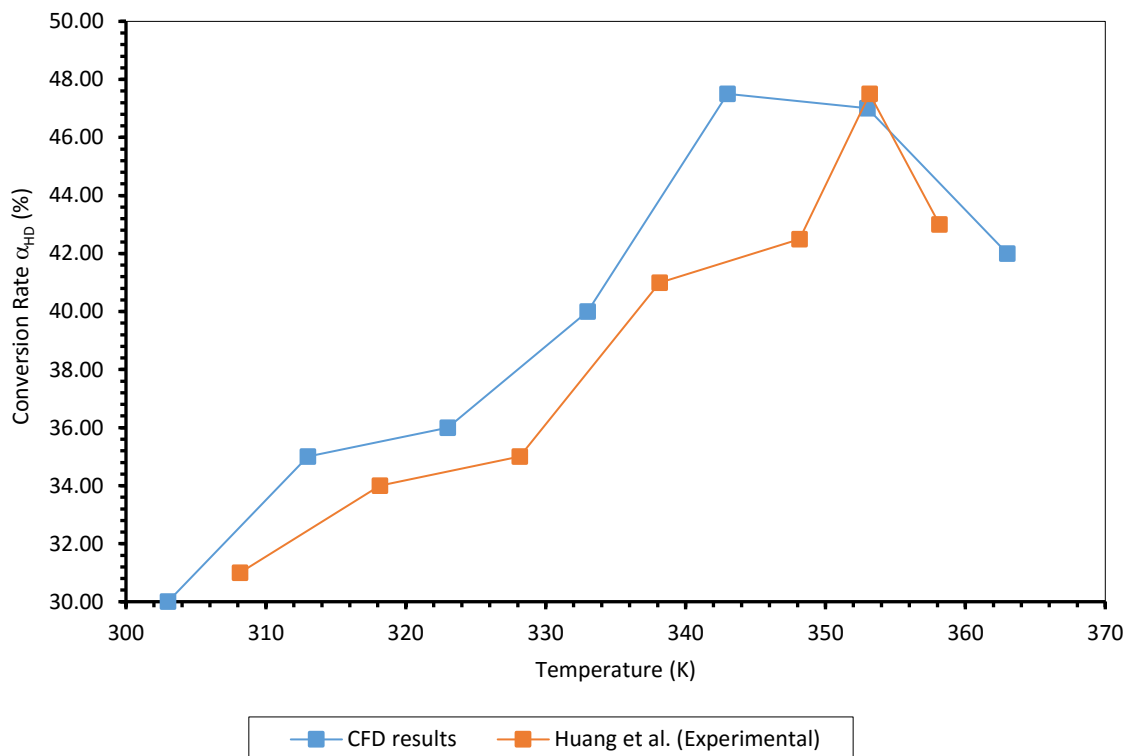


Figure (6.27) Comparison of the influence of the temperature on conversion rate, hydrogen flow rate 8.63 ml/s, molar flow ratio of hydrogen gas to water ($\lambda=0.5$).

6.7 Summary of the chapter

The behaviour of a trickle-bed reactor for the H₂-H₂O liquid catalytic exchange was studied by using 3D CFD modelling. The CFD based Eulerian model has been applied for the prediction of fluid flow and conversion rates that are associated with running the H₂-H₂O liquid catalytic exchange in a trickle-bed reactor. The vapour-water phase exchange was assumed to be the rate controlling step for the whole reactive scrubbing process owing to operating temperature used. We investigated impacts of design and operating factors on the separation factor, herein the conversion rate for H₂-H₂O liquid catalytic exchange. The Eulerian model was able to give good predictions. Flow rate of reagents, temperature, height of the catalytic bed, flow model and behaviour of the stability of the computational method were investigated. Major conclusions were as follows:

1. In the co-current flow exchange, the greater flow rate of hydrogen led to; (i) shorter residence time of reagents, and (ii) less complete conversion of the isotopic exchange. In counter-current flow exchange, increased flow rate of hydrogen was limited by the flooding constraints, pressure drops and mass transfer resistance between the solid/gas phases. In general, however, the trends have shown a reduced conversion in both mode of flow (co-current or counter-current) when the gas flow rate was increased.
2. Increased flow rate of water brought more water vapour in the reactor, promoting contact between the solid and gaseous phase and this the catalytic exchange.
3. Increased temperature promoted the vapour-water phase exchange and increased the conversion rate. In the counter-current flow exchange, both vapour-water phase exchange reaction and isotope exchange reaction affected the overall conversion rate. Temperature had opposite impact on the two reactions. At low temperature, vapour-water phase exchange was the rate-determining step, and increased temperature promoted the rate of this reaction and the overall conversion rate. When the temperature increased to a certain degree, the catalytic isotopic exchange approached equilibrium asymptotes and became competed by the isotope exchange reaction. This later is favoured at low temperature under equilibrium operations in counter-current exchange reaction, the best usage temperature was found at 343.15 K and low gas/liquid flow ratio, validating previous findings in chapter (4).
4. Increased height of the catalytic bed provided enough contact time for the exchange reaction to take place and beyond a height of 35mm (operating conditions; gas/liquid flow rate ratio of 0.5, temperature of 333.15K and gas flow rate of 8.63 ml/s), the catalytic reaction achieved equilibrium conditions and even some decrease was observed, which

was likely due weak interactions between the fluid flow, mass transfer and catalytic reactions.

5. Under the same CFD simulation condition, the conversion rate of the co-current exchange was significantly lower than that of the counter-current exchange owing to lower driving force of mass transfer taking place.
6. The stability of simulation was well demonstrated after a long running time (24 hours). The CFD result showed that the solution provided stability at low concentrations of deuterium in both gas and liquid phases and significant flow rates of both phases.
7. The CFD model was validated under trickling flow regime and its predictions were compared with different sets of independent experimental data from literature as well as those obtained by process simulation by using Aspen plus package observed in chapter (4). The results were satisfactory and fitting well existing correlation models.

Chapter 7

Conclusions and Recommendations

7. Conclusions and Recommendations

The final chapter of this thesis summarises the main results and achievements in section 7.1 and gives recommendations for future research in section 7.2.

7.1 Review of the work

This thesis presents a simulation study of the liquid catalytic isotopic exchange of H₂-H₂O in a three-phase (gas, liquid and solid) trickle bed reactors under both co-current and counter-current operations. Important issues associated with local information was investigated and relevant impact on the overall performance of the reactive process was discussed. Performed experimental data along with those obtained from literature were used to design the process simulation study and 3D CFD modelling. We performed numerical simulations to determine the optimum operating parameters and predict the exchange performance of the column. The simulation results were verified through the experiments available from literature. Two different methods, process simulation by Aspen Custom Modeler and the Eulerian 3D CFD formulation of multi-phase flow were used in this research.

The missing physical properties of deuterium and tritium isotopologues for hydrogen and water were predicted by using existing thermodynamic models, geometric mean interpolation and linear correlation of the critical properties. The rate-based model of Aspen plus modular package was used to model the reactive stripping of the hydrogen isotopic exchange. This model, which governs the coupling of mass and heat transports and specific features of the reaction mixture, was used to investigate the synergic impact on isotope separation by catalytic exchange. The model was then extended to a sensitivity analysis on the effects of significant design and operating parameters on the column performance. Local transfers of momentum and mass, and relevant interactions with the chemical reaction were next investigated in a three-phase trickle flow reactive column. The performance of the trickle bed reactor was assessed by looking at underlying phenomena between catalyst particles as well as inside solid particles and how these affect the overall efficiency.

To perform the above mentioned simulations, commercial process simulation package Aspen plus and commercial CFD package Comsol Multiphysics were used.

The research undertaken in this thesis achieved the following results:

- The properties of hydrogen isotopes gases as well as liquids were first predicted with rigorous models and then compared with some experimental data available in the open literature, implemented and further used for performance simulation to determine optimum operating parameters of temperature and gas/liquid flow ratios. The parameters affecting the separation characteristics of the column were discussed in detail by observing the trends of the following parameters on process performance (i.e. temperature, overall pressure, number of stages, feed flow ratio of hydrogen to water (G/L) and pressure drop per stage).
- 3D Representative bed geometries of different particle to tube diameter ratios were used by DEM and the bed structure properties such as average porosity and spatial distribution of porosity were compared with literature models.
- A comprehensive 3D CFD model helped to understand the local hydrodynamics inside trickle beds during the transient operations. The design of trickle bed reactors is depended on key hydrodynamic parameters such as liquid volume fraction, overall gas-liquid distribution and pressure drop.
- The 3D CFD modelling was extended to axial and radial dispersions of liquid by using a Lagrangian approach. Particles were released at the centre of the trickle bed and their propagation along the radial and axial directions was examined. The profiles of axial and radial dispersion coefficients which were normalised to molecular dispersion were compared those computed by the semi-analytical models of Freund and Delgado. The prediction of axial and radial dispersion of liquid has a good agreement with literature models.
- Formulation of 3D gas-solid-liquid model of mass including the chemical reaction and visualization of concentration distributions in trickle beds was also extended to :
 - Calculation and analysis of the conversion rate at different feed flow rate in (co/counter) current exchange.
 - Calculation and analysis of the conversion rate at different feed temperature in (co/counter) current exchange.
 - Calculation and analysis of the conversion rate at different height of bed in (co/counter) current exchange.
 - Impact of exchange method (co/counter) current on liquid catalytic exchange processing.

Chapters 4 reports a rigorous model to simulate the characteristics of a multistage-type column for the water/hydrogen isotopic exchange reaction. The solutions from the model equations, formulated of a component material balance and equilibrium relationships on any scrubbing

and catalyst bed, were effectively determined out by using a successive iteration mode into the simulation software Aspen plus Modeler. Parametric investigations were implemented to study the influence of design and operating variables on the multicomponent hydrogen isotopic compositions at each scrubbing stage. It was observed that the maximum performance on the concentration of deuterium at outlet of the column was obtained at the temperature conditions giving an equimolar composition ratio of the water vapour to the given hydrogen stream in the column. The optimum exchange temperature decreases with increased hydrogen flow rate. The originality in the work in this chapter is the applicability of commercial packages such as Aspen plus modular software to catalytic isotopic exchange of hydrogen inside a reactive stripping column. Many features of the heat and mass transfer associated with reactive stripping inside the column, including local bulk properties (compositions, temperatures, enthalpies, fluid flow, holdup, pressure drops, etc.) as well as local gas/liquid interphases properties (mass and heat transfer coefficients, compositions, temperature, mass and heat transfer rates of heat and mass transfer rates), could be computed or predicted for a rigorous design. The development of the module was demonstrated to be flexible and applicable to many similar processes including the water detritiation by reactive scrubbing processing.

Chapter 5 reports a 3D CFD study to help understand local hydrodynamics parameters of trickle bed reactor for gas-liquid system with transient operations. Impacts of packing structure, flow of liquid and gas on liquid holdup, pressure drops and solid wetting were investigated. The structures of the packed bed were varied by changing the AR of the PBR (i.e. AR of 2 and 4). The velocity profile inside the packed bed was function of the porosity and arrangement of particles. In the zones where the values of porosity were lower, the local velocity was also lower in comparison with the regions of higher values of porosity. In the later zones, velocities were even higher than the inlet velocity as flow channelling was observed. Channelling existed in packed beds close the wall but also in the bulk regions, depending on the porosity distribution and arrangement of the particles. An Eulerian formulation approach was used for the 3D flow modelling. For this approach, the mass and momentum equations were solved by the finite element method. According to the simulation results, the effective liquid holdup in the three-phase (gas, liquid and solid) system was function of the velocity of the liquid and gas phases. In the trickle flow regime, an increase of the liquid velocity was an effective way to increase the liquid holdup rate. Contrary to this trend, the liquid holdup rate decreased with increase in gas velocity. In addition, liquid holdup with smaller-sized particles was higher because it led to better spreading and therefore higher liquid phase retention. Prediction of pressure drop in trickle bed reactors is an important design parameter. It is sensitive to the flowing fluids as well

as to the particle packing characteristics. Pressure drop increased with increasing liquid velocity and decreased in packing of smaller particle size owing to zigzags of extended path in the bed. The results offered perspective to visualise the phenomenological interactions of the fluid flow and packing structure inside a trickle bed are occur, and hence to anticipate favoured operating parameters for performance of the process when mass transfer and the catalytic isotopic exchange of H₂-H₂O reactions were added in Chapter 6.

In chapter 6, results of process design of chapter 4 and 3D modelling of flow of chapter 5 were used to perform 3D CFD modelling of H₂-H₂O liquid phase catalytic exchange process inside a trickle bed reactor. Impacts of design and operating parameters on process performance have roles of flow rates of hydrogen gas and liquid water and ratios of these flow rates, temperature, bed height and (co/counter)-current flow mode operations on conversion rate of HD gas into liquid HDO. These results, which were validated by data available in literature, help us to could provide data for design and operating parameters of H₂-H₂O liquid catalytic exchange process for scrubbing contaminated H₂ by HD.

7.2 Recommendations for future research

Even though the research related to this thesis has come to end and considering the limitations and capability of the numerical software packages, computation time, mesh generation and complexity of the modelling the three-phase packed beds, the model, methodology and simulations results discussed in the thesis are new as demonstrated by published papers and others anticipated for publication. The research in this study has generated many interesting and promising ideas and some of these are worth exploring further. In this section, we describe some aspects for future research:

- For the case of the Aspen Plus, the missing physical properties of deuterium, and particularly of tritium, isotopologues in hydrogen gas and water forms were predicted and validated with limited existing literature data. It is worthwhile to extend thermodynamic studies of tritium isotopologues. It is understood that dedicated facilities are indeed needed
- For the case of the 3D CFD multiphase flow, the structural bed was simplified to a limited number of catalytic particles to reduce the computation time and power. It would be worthwhile to extend the simulation to a larger number of particles, or real packing geometries obtained modern visualization techniques, to mimic to some extend large size packed beds and reproduce behaviours of industrial packed beds.
- The contribution of mass transfer through the gas/liquid phases was not investigated as it was assumed to take place under equilibrium conditions between the bulk phases.

There is so far no literature to our knowledge that has approached by CFD modelling, mass transfer studies owing to fluctuating surfaces between the gas and liquid phases.

- It should be noticed that there is more than one reaction in the system of trickle bed reactors for the isotopic exchange. The simple model used in this study is worthwhile to be extended to complex reactions taking place, including complex kinetics of non-linear model (i.e. Langmuir Hinshelwood). It is anticipated to see the modelling computationally expensive.

Appendix

Appendix A

The equations below for flux demonstrate the so-called “mixed flow model” where outlet conditions are used for the bulk properties in each phase.

- Mass flux for liquid film

$$\left[\Gamma_{i,k,j}^L\right](x_j^I - x_j) - \left[R_j^L\right](N_j^L - N_t^L x_j) = 0 \quad (\text{A.1})$$

$$\Gamma_{i,k,j}^L = \delta_{i,k} + x_{i,j} \left. \frac{\partial \ln \phi_{ij}^L}{\partial x_{i,j}} \right|_{T_j^L, P_j, \Sigma} \quad (\text{A.2})$$

Where the symbol Σ means fixing the mole fractions of all components except the n th while evaluating the differentiation

$$R_{i,i,j}^L = \frac{x_{ij}}{\rho_j^L a_j^I k_{i,m,j}^L} - \sum_{\substack{m=1 \\ m \neq i}}^N \frac{x_{i,j}}{\rho_j^L a_j^I k_{i,m,j}^L} \quad \text{for } i = 1, 2, \dots, n_c - 1, i \neq k \quad (\text{A.3})$$

$$R_{i,k,j}^L = -x_{i,j} \left(\frac{1}{\rho_j^L a_j^I k_{i,k,j}^L} - \frac{1}{\rho_j^L a_j^I k_{i,m,j}^L} \right) \quad \text{for } i = 1, 2, \dots, n_c - 1, i \neq k \quad (\text{A.4})$$

- Mass flux for gas film

$$\left[\Gamma_{i,k,j}^G\right](y_j^I - y_j) + \left[R_j^G\right](N_j^G - N_t^G y_j) = 0 \quad (\text{A.5})$$

$$\Gamma_{i,k,j}^G = \delta_{i,k} + x_{i,j} \left. \frac{\partial \ln \phi_{ij}^G}{\partial y_{i,j}} \right|_{T_j^L, P_j, \Sigma} \quad (\text{A.6})$$

Where the symbol Σ means fixing the mole fractions of all components except the n th while evaluating the differentiation

$$R_{i,i,j}^G = \frac{G_{ij}}{\rho_j^G a_j^I k_{i,m,j}^G} - \sum_{\substack{m=1 \\ m \neq i}}^N \frac{y_{i,j}}{\rho_j^G a_j^I k_{i,m,j}^G} \quad \text{for } i = 1, 2, \dots, n_c - 1, i \neq k \quad (\text{A.7})$$

$$R_{i,k,j}^G = -y_{i,j} \left(\frac{1}{\rho_j^G a_j^I k_{i,k,j}^G} - \frac{1}{\rho_j^G a_j^I k_{i,m,j}^G} \right) \quad \text{for } i = 1, 2, \dots, n_c - 1, i \neq k \quad (\text{A.8})$$

- Heat flux for the liquid film

$$a_j^I H_j (T_j^I - T_j^L) - q_j^L + \sum_{i=1}^N N_{i,j}^L \bar{H}_{i,j} = 0 \quad (\text{A.9})$$

- Heat flux for gas film

$$a_j^I h_j (T_j^G - T_j^I) - q_j^G + \sum_{i=1}^N N_{i,j}^G \bar{h}_{i,j}^L = 0 \quad (\text{A.10})$$

The rate-Based model uses well-known and accepted correlations to calculate binary mass transfer coefficients for the vapour and liquid phases, interfacial areas, heat transfer coefficients and liquid holdup. In general, these quantities depend on column diameter and operating parameters such as vapour and liquid flow rates, densities, viscosities, surface tension, and binary diffusion coefficients in both liquid and gaseous phases. Mass transfer coefficients, interfacial areas and liquid holdup also depend on the type, size, specific surface area, and construction material of packing and flow path length (packing tortuosity). Most parameters can vary by stage, but only depend on the properties for that stage. The subscript j on each variable is omitted in the equations for readability.

The Onda model [154] predicts mass transfer coefficients and interfacial area for random packing.

$$k_{i,k}^L = 0.0051 \text{ Re}^{0.667} Sc_{L,i,k}^{-0.5} (a_F d_F)^{0.4} \left(\frac{\mu^L g}{\rho_i^L} \right)^{0.333} \quad (\text{A.11})$$

$$k_{i,k}^G = \begin{cases} 2.0 \text{ Re}_G^{0.7} Sc_{G,i,k}^{0.333} a_F D_{i,k}^G (a_F d_F)^{-2} & \text{for } d_F < 0.015 \\ 5.23 \text{ Re}_G^{0.7} Sc_{G,i,k}^{0.333} a_F D_{i,k}^G (a_F d_F)^{-2} & \text{for } d_F > 0.015 \end{cases} \quad (\text{A.12})$$

$$a^I = a_w A h_F$$

$$a_w = a_F \left[1 - \exp \left(-1.45 \left(\frac{\sigma_c}{\sigma} \right)^{0.75} \text{Re}_L^{0.1} Fr_L^{-0.05} We_L^{0.2} \right) \right] \quad (\text{A.13})$$

The heat transfer coefficient h was estimated by Chilton–Colburn method [156]

$$h_j = \bar{k}_j \bar{\rho}_j C_{p,j} \left(\frac{\lambda_j}{\bar{D}_j \bar{\rho}_j C_{p,j}} \right)^{2/3}$$

$$\text{where } \bar{D}_j = \frac{\sum_{i=1}^{nc-1} \sum_{k=i+1}^{nc} (x_{i,j} + \delta)(x_{k,j} + \delta) D_{i,k,j}}{\sum_{i=1}^{nc-1} \sum_{k=i+1}^{nc} (x_{i,j} + \delta)(x_{k,j} + \delta) D_{i,k,j}} \quad (\text{A.14})$$

$$\text{and } \bar{k}_j = \frac{\sum_{i=1}^{nc-1} \sum_{k=i+1}^{nc} (x_{i,j} + \delta)(x_{k,j} + \delta) k_{i,k,j}}{\sum_{i=1}^{nc-1} \sum_{k=i+1}^{nc} (x_{i,j} + \delta)(x_{k,j} + \delta) D_{i,k,j}}$$

Where C_p is the specific molar heat capacity, \bar{D} is the average diffusivity, \bar{k} is the average mass transfer coefficient, $\bar{\rho}$ is the averaged density, M is the molecular weight, u is the average flow velocity, ρ is the molar density, λ is the thermal conductivity, n_c is the number of components and d is the Chilton-Colburn averaging parameter specified on the Rate-Based Setup Specifications sheet with a default recommended value of 0.0001. This parameter

provides stability when compositions change, especially in reactive systems when some compositions may go to zero at the boundary.

The pressure drops through the Dixon packing were estimated using literature models applied to random Raschig packing as follows [141].

$$\begin{aligned} \Delta P/L &= C_{P,0} \left(\frac{64}{\text{Re}_v} + \frac{1.8}{\text{Re}_v^{0.08}} \right) \frac{a u_v^2 \rho}{\varepsilon^3} \frac{1}{2} \left(1 + \frac{2}{3} \frac{1}{1-\varepsilon} \frac{d_p}{d_s} \right) \\ \frac{1}{\text{Re}_v} &= \frac{(1-\varepsilon) \nu_v}{u_v d_p} \left(1 + \frac{2}{3} \frac{1}{1-\varepsilon} \frac{1}{a} \frac{1}{d_s} \right) \\ d_p &= 6 \frac{1-\varepsilon}{a} \end{aligned} \quad (\text{A.15})$$

Appendix B

The numerical errors of the simulation were assessed by guidelines provided by Celik et al. [188] to ensure if the results are independent of mesh size. First the representative grid size h procedure is defined as;

$$h = \left(\frac{1}{N} \sum_{i=1}^N \Delta V_i \right)^{1/3} \quad (\text{B.1})$$

Where ΔV is the cell volume and N is the number of cells. A three grids grid refinement factor higher than 1.3 was used for the ultimate refinements. The apparent order m of the method is defined by eqs (B.2) to (B.4):

$$m = \left| \ln \left| \frac{\Theta_{32}}{\Theta_{21}} \right| + q(m) \right| / \ln(r_{21}) \quad (\text{B.2})$$

$$q(m) = \ln \left(\frac{r_{21}^m - s}{r_{32}^m - s} \right) \quad (\text{B.3})$$

$$s = 1. \text{sgn}(\Theta_{32}/\Theta_{21}) \quad (\text{B.4})$$

Where, $h_1 < h_2 < h_3$, $r_{21} = h_2/h_1$, $r_{32} = h_3/h_2$, $\Theta_{32} = P_3 - P_2$, and $\Theta_{21} = P_2 - P_1$ and P_k ($k = 1, 2, 3$) expresses the pressure values taken at three arbitrary grid locations in the packed bed, and also, sgn is the function signum. Equation (B.3) should be solved numerically for m . This is then used to find the extrapolated value for the pressure (eq B.5), the relative error (eq B.6), and the fine grid convergence GCI (eq B.7)

$$P_{ext}^{21} = \frac{r_{21}^m P_1 - P_2}{r_{21}^m - 1} \quad (\text{B.5})$$

$$e_a^{21} = \frac{P_1 - P_2}{P_1} \quad (\text{B.6})$$

$$GCI = \frac{1.25 e_a^{21}}{r_{21}^m - 1} \quad (\text{B.7})$$

Appendix C

The Lagrangian method by following distinct particles along a trajectory in a steady-state velocity field. The method of moments, as shown in (eq C.1), is used to calculate axial and radial dispersion coefficients.

$$D_{ax/rad} = \frac{1}{2} \frac{d\sigma_{ax/rad}^2}{dt} \quad (\text{C.1})$$

Here, $D_{ax/rad}$ is axial or radial dispersions coefficients and $\sigma_{ax/rad}$ is the second moment or mean square deviation, as defined by equations (C.2) and (C.3) as shown below:

$$\sigma_{ax}^2(t) = \frac{1}{NP} \sum_{n=1}^{NP} (x_n(t) - \bar{x}(t))^2 \quad (\text{C.2})$$

$$\sigma_{rad}^2(t) = \frac{1}{NP} \sum_{n=1}^{NP} (r_n(t) - \bar{r}(t))^2 \quad (\text{C.3})$$

Here, n is the particle index, NP is the total number of tracked particles, t is the time and x and r are displacements of particles along the axial and radial coordinates, respectively. \bar{x} and \bar{r} are the averaged displacements of all particles along the axial and radial coordinates, respectively.

References

- [1] Souers, P. C. Hydrogen Properties for Fusion Energy. Berkeley Los Angeles London: University of California Press. 1986.
- [2] Korakianitis T, Namasivayam A M, Crookes R J. Hydrogen dual-fuelling of compression ignition engines with emulsified biodiesel as Pilot fuel. International journal of hydrogen Energy, 2010, 35(24), 3329-13344.
- [3] Verstraete, D., et al., Hydrogen fuel tanks for subsonic transport aircraft." International Journal of Hydrogen Energy. 2010, 35(20), 11085-11
- [4] Kruger, P. and J. D. Leaver, Comparative requirements for electric energy for production of hydrogen fuel and/or recharging of battery electric automobile fleets in New Zealand and the United States. International Journal of Hydrogen Energy. 2010, 35(20), 11284-11290.
- [5] Roebuck, A. K. and B. Evering. Hydrocracking an Aromatic Extract to Naphthalene and 100-Octane Gasoline. Industrial & Engineering Chemistry, 1958, 50(8), 1135-1138.
- [6] Kozlov, I., et al. Hydrocracking /hydrotreating of high-sulfur straight-run naphtha. Chemistry and Technology of Fuels and Oils; September 1981, 17(9) p 493-496.
- [7] Teles, U. M. and Fernandes, F. A. N. Hydrocracking of Fischer-Tropsch Products. Optimization of Diesel and Naphtha Cuts. Chemical and Biochemical Engineering Quarterly. 2008, 22 (2) 227–231.
- [8] Ju, K. S. and Rebecca E. P., Nitroaromatic Compounds, from Synthesis to Biodegradation. Microbiology and Molecular Biology Reviews : MMBR 74.2. 2010, 250-272.
- [9] C. A. Pirrie and H. Menown, The evolution of the hydrogen thyatron. Marconi Applied Technologies Ltd, Chelmsford, U.K.
- [10] Anderson, D. A., Moddel, G., Paul, W. An assessment of the suitability of rf sputtered amorphous hydrogenated Si as a potential solar cell material. Journal of electronic material, 1980, 9,141-152.
- [11] Castellanos, A. R., et al. Solar-Hydrogen-Fuel Cell Prototype as a Source of Renewable Energy Generation. Journal of the Mexican Chemical Society, 2007, 5(2), 55-58.
- [12] Lee, C. H., et al. Material properties of microcrystalline silicon for solar cell application. Solar Energy Materials and Solar Cells. 2011, 95(1), 207-210.
- [13] Jacobs, M. J., The impact of Hydrogen on optical fibers. Corning White Paper, WP, WP9007. 2004.

- [14] Choe, E. and Min, D. B. Mechanisms and factors for edible oil oxidation. *Comprehensive Reviews in Food Science and Food Safety*. 2006, 5(4), 169-186.
- [15] JET Team, Fusion energy production from a deuterium-tritium plasma in the JET tokamak. *Nuclear fusion*, 1992, 32(2): 187-203.
- [16] Alcántara-Núñez, J. A., et al. investigating the intra-nuclear cascade process using the reaction ^{136}Xe on deuterium at 500 AMeV. *EPJ Web of Conferences*, 8, 6-12.
- [17] Kozioziemski, B. J., et al. Deuterium-tritium fuel layer formation for the National Ignition Facility. *Fusion Science and Technology*. 2010, 59(1), 14-25.
- [18] Das Gupta, J. B., et al., *Science, Technology, Imperialism, and War*, Pearson Longman. 2007.
- [19] Mahdavi, M. and Jalaly, B. Effects of Deuterium-Lithium Fusion Reaction on Internal Tritium Breeding. *International Journal of Modern Physics E*, (2010), 19(11), 2123-2132.
- [20] Andreev, B. M., et al., *Separation of Isotopes of Biogenic Elements in Two-Phase Systems*. Amsterdam: Elsevier Science, 2007.
- [21] Chernysheva, M. G and Badun, G. A. In vitro study of proteins surface activity by tritium probe. *Journal of Radioanalytical and Nuclear Chemistry* December 2010, 286(3), 835-840.
- [22] Fan, A. M., Public health goal for tritium in drinking water. Office of environmental health hazard and assessment California environmental protection agency, 2006.
- [23] Nickerson, S. B. The tritium monitoring requirements of fusion and the status of research. Canadian fusion fuel technology project. 1982.
- [24] Arita, T. and et al., Tritium recovery system from waste water of fusion reactor using CECE and cryogenic-wall thermal diffusion column. *Fusion technology*, 1996, 30(3), 864-868.
- [25] Goodall, K. B., In Search of the Fountain of Youth Preliminary Analysis of Deuterium's Role in DNA Degradation. *The Nutrition Notebook*, 2003.
- [26] Gross P.R. and Spindel, W. Mitotic arrest by deuterium oxide. *Science*. 1960, 131(3392), 37-39.
- [27] Gross, P. R. and Spindel, W. The inhibition of mitosis by deuterium. *Annals of the New York academy of sciences*. 1960, 25(84), 745-754.
- [28] Gross, P. R. and Spindel, W. heavy water inhibition of cell division: an approach to mechanism. *Annals of the New York academy of sciences*. 1960, 90(2), 500-522.
- [29] Vasilescu, V. and Mărgineanu, D. D₂O effect on active transport through frog skin. *Naturwissenschaften*. 1970, 57(3), 126-127.
- [30] Vasilescu, V. and Mărgineanu, D. Investigations on the effects of deuteration on some functions of biological membranes. *Revue roumaine physiologie*, 1971, 8(3), 217-226.

- [31] Katona, E. and Vasilescu, V. Dynamics and compartmentation of water in certain biosystems. *Physiologies*, 1989, 26(4), 285-296.
- [32] Currier, S.F. and Mautner, H.G. On the Mechanism of Action of Choline Acetyltransferase. *Biochemistry*. 1974, 71(9), 3355-3358.
- [33] Katz, J. J., et al. Some observations on biological effects of deuterium, with special reference to effects on neoplastic processes. *Journal of the national cancer institute*. 1957, 18(5), 641-659.
- [34] Katz, J. J. The biology of heavy water. What happens to experimental organisms that have been raised on water in which the hydrogen is not the common isotope of mass one but the heavy isotope of mass two? *Scientific American*, 1960, 203, 106-116.
- [35] Czajka, D. M., et al. Physiological effects of deuterium on dogs. *American Journal of Physiology*, 1961, 201, 357-362.
- [36] Vasaru, G., *Tritium Isotope Separation*. CRC Press, 1993.
- [37] Jones, R. C. and Furry, W. H. The Separation of Isotopes by Thermal Diffusion. *Reviews of modern physics*, 1946, 18(2), 151-244.
- [38] Rutherford, W. M. and Lindsay, C. N. Separation of Hydrogen Isotopes by Thermal Diffusion. *Fusion Science and Technology*, 1985, 8(2), 2278-2284.
- [39] Kobayashi, N et al. Isotope Separation of H₂-HD Gas Mixture with “Cryogenic-Wall” Thermal Diffusion Column with a Heated Tube. *Journal of Nuclear Science and Technology*, 2002, 39(4), 431-434.
- [40] Yeh, H. M. Improvement in recovery of deuterium from water–isotopes mixture in inclined thermal-diffusion columns. *International Journal of Hydrogen Energy*, 2003, 28(8), 873-879.
- [41] Huang, F., et al. Isotope fractionation in silicate melts by thermal diffusion. *Nature*, 2010, 464(7287), 396-400.
- [42] Naito, T. et al., Design study of fuel circulating system using Pd-alloy membrane isotope separation method. *The International Journal of Applied Radiation and Isotopes*, 1980, 31(8), 480.
- [43] Bellanger, G. Optimization for the tritium isotope separation factor and permeation by selecting temperature and thickness of the diffusion Pd-Ag alloy cathode. *Fusion engineering and design*, 2009, 84(12), 2197-2205.
- [44] Izumoji, Y., et al. separation of hydrogen isotope by Pd-alloy membrane. *The International Journal of Applied Radiation and Isotopes*, 1980, 31(8), 495.

- [45] Burger, L.L. et al., The separation and control of tritium, state-of-the-art study, 211B00990, Battelle pacific northwest laboratory, Richland, WA, 1972.
- [46] Urey, H., et al., A Hydrogen Isotope of Mass 2. *Physical Review*. 1932, 39, 164-165.
- [47] Denton, W. H. The production of deuterium by the distillation of hydrogen, *Angewandte chemie international edition*, 1957, 59 (17), 565.
- [48] Embury, M.C. et al. A low temperature distillation system for separating mixtures of protium, deuterium, and tritium isotopes. *Fusion Science and Technology*, 1985, 8(2), 2168-2174.
- [49] Enoeda, M., et al. Hydrogen isotope separation characteristics of cryogenic distillation column. *Fusion Engineering and Design*, 1989, 10, 319-323.
- [50] Busigin, M., et al. Installation and early operation of a complex low inventory cryogenic distillation system for the Princeton TFTR, *fusion technology*, 1995, 28(3), 1312-1316.
- [51] Langming, L., et al. Separation of H-D mixtures by cryogenic distillation. *Nuclear techniques*, 2007, 30(10), 833-836.
- [52] Bornea, A., et al. Investigation related to hydrogen isotopes separation by cryogenic distillation. *Fusion science and technology*. 2008, 54(2), 426-429.
- [53] Zhang, D., et al. Equilibrium Modeling for Hydrogen Isotope Separation by Cryogenic Adsorption. *Chinese Journal of Chemical Engineering*, 2006, 14(4), 526-531.
- [54] Zhang, D., et al. Kinetics in hydrogen isotopes cryogenic adsorption. *Separation and Purification Technology*, 2004, 37(1), 1-8.
- [55] Kumar, A. V. A., et al. Quantum Effects on Adsorption and Diffusion of Hydrogen and Deuterium in Microporous Materials. *The Journal of Physical Chemistry B*, 2006, 110(33), 16666-16671.
- [56] Munakata, K., et al. Adsorption of hydrogen isotopes on various adsorbents at cryogenic temperature. *Fusion science and technology*. 2009, 56(1), 153-157.
- [57] Broom, D. P., et al., Outlook and challenges for hydrogen storage in nanoporous materials. *Applied Physics A*, 2016, 122(3), 1-21.
- [58] Marling, J. B., laser isotope separation of deuterium. *Chemical physics letters*, 1975, 34(1), 84-89.
- [59] Atabek, M. C. and Lefebvre, R. Isotope separation using intense laser fields. *Physical Review A*, 1994, 49(1), 8-11.
- [60] Dutt, P. K. Heavy water electrolysis unit for generator of deuterium gas provided with automatic switch off and safety devices. *Journal of scientific instruments*, 1960, 37(9), 352-353.

- [61] Keil, K and Erdle, E. Tritium-Enrichment via CECE-Process with High Temperature Steam Electrolysis. *Fusion Science and Technology*, 1988, 14(2), 513-517.
- [62] Ying, S., et al. Study on the technology of CECE-GC system for water detritiation. *Fusion Engineering and Design*, 2008, 83(10-12), 1400-1404.
- [63] Ovcharov, A.V. et al. Simulation of CECE Facility for Water Detritiation. *Fusion Science and Technology*, 2009, 56(4), 1462-1470.
- [64] Rae, H. K., Separation of hydrogen isotopes. American chemical society. 1978.
- [65] Cristescu, I., et al. Simultaneous tritium and deuterium transfer in a water detritiation CECE facility at TLK. *Fusion Engineering and Design*, 2008, 69(1-4), 109-113.
- [66] Cristescu, I., et al. Investigation of simultaneous tritium and deuterium transfer in a catalytic isotope exchange column for water detritiation. *Fusion Engineering and Design*, 2002, 61-62, 537-542.
- [67] Cristescu, I., et al. Investigation of Separation Performances of Various Isotope Exchange Catalysts for the Deuterium-Hydrogen System. *Fusion Science and Technology*, 2002, 41(3), 1087-1091.
- [68] Belapurkar, A. D., et al. PTFE Dispersed Hydrophobic Catalysts for Hydrogen-Water Isotopic Exchange I. Preparation and Characterization. *Applied catalysis*, 1998, 43(1), 1-13.
- [69] Paek, S., et al. The performance of a trickle-bed reactor packed with a Pt/SDBC catalyst mixture for the CECE process. *Fusion Engineering and Design*, 2007, 82(15), 2252-2258.
- [70] Song, K. M., et al. Installation of liquid phase catalytic exchange columns for the Wolsong tritium removal facility. *Fusion Engineering and Design*, 2007, 82(15-24), 2264-2268.
- [71] Huang, F. and Meng, C. Hydrophobic platinum-polytetrafluoroethylene catalyst for hydrogen isotope separation. *International Journal of Hydrogen Energy*, 2010, 35(12), 6108-6112.
- [72] Moore, W. R. and Ward, H. R. gas-solid chromatography of H₂, HD, and D₂ Isotopic separation and heats of adsorption on alumina. *The Journal of Physical Chemistry*, 1960, 64(6), 832.
- [73] Sayeed, A. and Hilton, A. S., Separation and analysis of various forms of hydrogen by adsorption and gas chromatography. *Chemical Reviews*, 1964, 64 (3), 261-276.
- [74] KWU-nuclear power plant with pressurized heavy water reactor, 1979, 10.
- [75] Busigin, A., et al. FLOSHEET: microcomputerized flowsheeting/simulation program for simulating hydrogen isotope separation processes. *Separation science and technology*, 1987, 22(2-3).

- [76] Busigin, A. and Sood, K., Optimization of Darlington tritium removal facility performance: effects of key process variables. Nuclear journal of Canada. 1987, 1(4), 368-371.
- [77] Pautort, P. and Damiani, M. Operating experience with the tritium and hydrogen extraction plant at the laue-langevin institute. Separation of hydrogen isotopes, 1978, chapter 12, 163-17.
- [78] Okuno, K., et al. Tritiated Water Processing Using Liquid Phase Catalytic Exchange and Solid Oxide Electrolyte Cell. Fusion Science and Technology. 1995, 28(3), 1591-1596.
- [79] Hammerli, M. and Butler, J. P. Apparatus for finishing and upgrading of heavy water. US4191626 A, 1980.
- [80] Miller, A. I. Deuterium pilots new hydrogen technology. International Journal of Hydrogen Energy, 1984, 9(1-2), 73-79.
- [81] Jun-hua, L. I., Detritiation from heavy water by H₂-H₂O liquid phase catalytic exchange. Atomic Energy Science and Technology. 2001, 35(1), 91-96.
- [82] Andreev, B. M., et al. Installations for separation of hydrogen isotopes by the method of chemical isotopic exchange in the `water-hydrogen` system. Fusion Technology, 1995, 28(3), 515-518.
- [83] Bruggeman, A., et al. Development of the ELEX process for tritium separation at reprocessing plants. Radioactive waste management and the nuclear fuel cycle, 1985, 6(3-4), 237-254.
- [84] Pautrot, G. P. The Tritium Extraction Facility at the Institute Laue-Langevin Experience of Operation with Tritium. Fusion Science and Technology, 1988, 14(2), 480-483.
- [85] Spagnolo, D. A. and Miller, A. I. The CECE Alternative for Upgrading/Detritiation in Heavy Water Nuclear Reactors and for Tritium Recovery in Fusion Reactors. Fusion Science and Technology, 1995, 28(3), 748-754.
- [86] Dautovich, D. P. and Miller, J. M. Overview of Canadian Activities in Tritium. Fusion Science and Technology, 1995, 28(3), 439-448.
- [87] Sienkiewicz, C. J. and Lentz, J. E. Recovery of Tritium from Water, Fusion Science and Technology, 1988, 14(2), 444-449.
- [89] Shimizu, M., et al. Hydrogen isotope enrichment by hydrophobic Pt-catalyst in Japan and western countries Proceedings of International Symposium on Isotope Separation and Chemical Exchange Uranium Enrichment, Tokyo (1990).
- [90] Eckardt, B. and Hill, A. Apparatus for the recombination of hydrogen in a gas mixture, US 6356613 B1, 2002.

- [91] Eckardt, B. and Hill, A. Catalyst system and recombination device for recombining hydrogen and oxygen, in particular for a nuclear power station and method for operating a catalyst system, US 6054108 A, 2000.
- [92] Alekseev, I. A., et al. Heavy water detritiation by combined electrolysis catalytic exchange at the experimental industrial plant. *Fusion Engineering and Design*, 2007, 69(1-4), 33-37.
- [93] Jung, M. and Winsel, A. Hydrophobic catalyst for recombiners. US 4350610 A, 1982.
- [94] Burch, R. and Ellis, P. R. An investigation of alternative catalytic approaches for the direct synthesis of hydrogen peroxide from hydrogen and oxygen. *Applied Catalysis B: Environmental*, 2003, 42(2), 203-211.
- [95] Chuang, K. T., et al. Supported catalyst and process for catalytic oxidation of volatile organic compounds. US 5851948 A, 1998.
- [96] Lavelle, K. and Mcmonagle, J. B. Mass transfer effect in the oxidation of aqueous organic compounds over a hydrophobic solid catalyst. *Chemical Engineering Science*, 2001, 56(17), 5091-5102.
- [97] Chuang, K. T. and Fu, L. Reduction of nitrogen oxides, US 4981659 A, 1991.
- [98] An, W., et al. A Hydrophobic Pt/Fluorinated Carbon Catalyst for Reaction of NO with NH₃. *Industrial & Engineering Chemistry research*, 2002, 41(1), 27-31.
- [99] Huang, T. L., et al. Nitrogen removal from wastewater by a catalytic oxidation method. *Water research*, 2001, 35(9), 2113-2120.
- [100] YE, L., et al., Improved catalysts for hydrogen/deuterium exchange reactions. *International journal of hydrogen energy*, 2013, 38(31), 13596-13603.
- [101] Ionita, G., et al. An assessment on hydrogen isotopes separation by liquid phase catalytic exchange process. *Journal of Radioanalytical and Nuclear Chemistry*, 2015, 305(1), 117-126.
- [102] Stevens, W. H. Process and catalyst for enriching a fluid with hydrogen isotopes. CA 907292 A, 1972.
- [103] Rolston, J. H., et al. The deuterium isotope separation factor between hydrogen and liquid water. *The Journal of Physical Chemistry*, 1976, 80 (10), 1064-1067.
- [104] Den, H. J., et al. An ordered bed packing module. EP 0068862 A2, 1983.
- [105] Butler, J. P., et al. Process for the exchange of hydrogen isotopes using a catalyst packed bed assembly. US 4126667 A, 1978.
- [106] Hammerli, M., et al. Heavy water recovery from combined electrolytic and non-electrolytic hydrogen streams. *International Journal of Hydrogen Energy*, 1981, 6(2), 167-179.
- [107] Chuang, K. T., et al. Development of a wetproofed catalyst recombiner for removal of airborne tritium. *Applied catalysis*, 1987, 30(2), 215-224.

- [108] Asakura, Y. Numerical analysis of hydrogen isotope separation characteristics in improved dual temperature exchange reaction system between water and hydrogen gas. *Journal of Nuclear Science and Technology*, 1983, 20(5), 422-432.
- [109] Shimizu, M., et al. numerical analysis on heavy water separation characteristics for a pair of dual temperature multistage-type H₂/H₂O-exchange columns. *Journal of nuclear science and technology*, 1980, 17(6), 448-460.
- [110] Isomura, S., et al. Separation and Recovery of Tritium by Hydrogen-Water Isotopic Exchange Reaction. *Fusion Science and Technology*, 1988, 14(2), 518-523.
- [111] Andreev, B. M., et al. Prospects for using chemical isotopic exchange for separation of hydrogen isotopes. *Atomic energy*, 1998, 86(3), 200-205.
- [112] Ionitã, G. and Ștefãnescu, I. The separation of deuterium and tritium on PT/SDB/PS and PT/C/PTFE hydrophobe catalysts. *Fusion Science and Technology*, 1995, 28(3), 641-646.
- [113] Carlson, E. C., Don't Gamble with Physical Properties for Simulations. *Chemical engineering progress*, 1996, 92(10), 35-46.
- [114] Aspen Technology, Aspen physical property system. *Physical property methods*. 2011
- [115] Cho, J., Estimation of physical properties for hydrogen isotopes using aspen plus simulator. *Transactions of the Korean Nuclear Society Spring Meeting, Jeju, Korea, May 2009*, 22, 135-136.
- [116] Aldehani, M., Alzahrani, F., tSaoir, M. N. A., Fernandes, D. L. A., Assabumrungrat, S. and Aiouache, F., Kinetics and reactive stripping modelling of hydrogen isotopic exchange of deuterated waters. *Chemical engineering and processing: process intensification*. 2016, 108, 58-73.
- [117] Dixon, A.; Taskin, M.; Nijemeisland, M.; Stitt, E. CFD method to couple three-dimensional transport and reaction inside catalyst particles to the fixed bed flow field. *Ind. Eng. Chem. Res.* 2010, 49, 9012-9025.
- [118] Vortmeyer, D.; Schuster, J. Evaluation of steady flow profiles in rectangular and circular packed beds by a variational method. *Chem. Eng. Sci.* 1983, 38, 1691-1699.
- [119] Giese, M.; Rottschäfer, K.; Vortmeyer, D. Measured and modeled superficial flow profiles in packed beds with liquid flow. *AIChE J.* 1998, 44, 484-490.
- [120] Gladden, L.; Akpa, B.; Anadon, L.; Heras, J.; Holland, D.; Mantle, M.; Matthews, S.; Mueller, C.; Sains, M.; Sederman, A. Dynamic MR Imaging of single- and two-phase flows. *Chem. Eng. Res. Des.* 2006, 84, 272-281.
- [121] Freund, H.; Bauer, J.; Zeiser, T.; Emig, G. Detailed simulation of transport processes in fixed-beds. *Ind. Eng. Chem. Res.* 2005, 44, 6423-6434.

- [122] Theuerkauf, J.; Witt, P.; Schwesig, D. Analysis of particle porosity distribution in fixed beds using the discrete element method. *Powder Technol.* 2006, 165, 92–99.
- [123] Hao, R., Local fluid flow and transports inside a thin packed reactor. MPhil Thesis. Queen's University of Belfast; U.K. 2012.
- [124] Delenne, J.-Y., et al., Mechanical behaviour and failure of cohesive granular materials. *International Journal for Numerical and Analytical Methods in Geomechanics*, 2004, 28(15), 1577-1594.
- [125] Alzahrani, F., Aldehani, M., Aiouache, F., et al., Gas Flow visualization in low aspect ratio packed beds by three-dimensional modeling and near-infrared tomography. *Industrial & engineering chemistry research*. 2015, 54(51), 12714-12729.
- [126] Fedorchenko, O., et al., Water-Hydrogen Isotope Exchange Process Analysis. *Fusion science and technology*. 2008, 54(2), 450-453.
- [127] Yamanishi, T. and Okuno, K., A computer code simulating multistage chemical exchange column under wide range of operating conditions. Japan Atomic Energy Research Institute, 1996, JAERI-Data Code, 96-028.
- [128] Ye, L., et al., Process simulation for hydrogen/deuterium exchange in a packed column. *International journal of hydrogen energy*, 2014, 39(12), 6604-6609.
- [129] Taylor, R. and Krishna, R., *Multicomponent mass transfer*. John Wiley & Sons, New York, 1993.
- [130] Kinoshita, M., An Efficient Simulation Procedure Especially Developed for Hydrogen Isotope Distillation Columns. *Fusion science and technology*. 1984, 6(3), 574-583.
- [131] Perevezentsev, A. N., et al., Wet scrubber column for air detritiation. *Fusion science and technology*. 2009, 56, 1455-1461.
- [132] Perevezentsev, A. N. and Bell, A. C., Development of water detritiation facility for JET, *Fusion science and technology*. 2008, 53, 816-829.
- [133] Huang, F. and Meng, C., Method for the production of deuterium-depleted potable water. *Industrial & engineering chemistry research*. 2011, 50(1), 378-381.
- [133] tSaoir, M. N., et al., Three dimensional water vapour visualization in porous packing by near-infrared diffuse transmittance tomography. *Industrial & engineering chemistry research*. 2012, 51(26), 8875-8882
- [134] tSaoir, M. N., et al., Visualization of water vapour flow in a packed bed adsorber by near-infrared diffused transmittance tomography. *Chemical engineering science*. 2011, 66(24) 6407-6419.

- [135] tSaoir, M. N., et al., Transient distributions of composition and temperature in a gas–solid packed bed reactor by near-infrared tomography. *Chemical engineering journal*, 2012 189-190, 383-392.
- [136] Roland, T. F., et al., Surface mediated isotope exchange reactions between water and gaseous deuterium, *Journal of Nuclear Materials*, 2006, 353, 193-201.
- [137] Kawakami, K., et al., Kinetics of isotopic exchange reaction between hydrogen and water vapor over platinum supported on a hydrophobic carrier. *The Canadian journal of chemical engineering*. 1986, 64(3), 432-439.
- [138] Sagert, N. H. and Pouteau, M. L., The production of heavy water: hydrogen-water deuterium exchange over platinum metals on carbon supports. *Platinum metals review*, 1975, 19(1), 16-21
- [139] Kumar, R., et al., Reactive Stripping for the Catalytic Exchange of Hydrogen Isotopes. *Industrial & engineering chemistry research*. 2013, 52(32), 10935-10950.
- [140] Yamanishi, T. and Okuno, K., Simulation code treating all twelve isotopic species of hydrogen gas and water for multistage chemical exchange column. *Japan Atomic Energy Research Institute*, 1994, JAERI-Data Code, 94-019.
- [141] Billet, R. and Schultes, M., Prediction of mass transfer columns with dumped and arranged packings: updated summary of the calculation method of billet and schultes. *Chemical engineering research and design*, 1999, 77(6), 498-504.
- [142] Bruggeman, A., et al., Water Detritiation: better catalysts for liquid phase catalytic exchange. 7th Tritium Science and Technology Conference, Baden, Germany 12-17 September 2004.
- [143] Richardson, A. and Leachman, J. W., Thermodynamic properties status of deuterium and tritium, *Advances in Cryogenic Engineering*, AIP conference proceeding. 2012, 1434, 1841-1848
- [145] Van Hook, W. A., Isotope effects on VLE properties of fluids and corresponding states: Critical point shifts on isotopic substitution, *Fluid Phase Equilibria*, 2007, 257(1), 35-52.
- [146] Cho, J., Estimation of physical properties for hydrogen isotopes using aspen plus simulator. *Transactions of the Korean Nuclear Society Spring Meeting*, Jeju, Korea, May 2009, 22, 135-136.
- [147] Sanggyun, N., et al., Cryogenic Distillation Simulation for Hydrogen Isotopes Separation, *Journal of the Korea Academia-Industrial cooperation Society*, 2013, 14(9), 4643-4651.

- [148] Salomon, M., Thermodynamic properties of liquid H₂O and D₂O and their mixtures. Electronics research centre Cambridge, mass. National aeronautics and space administration, NASA TN D-5223, Washington, D. C. 1969.
- [149] Durmayaz, A., Approximate functions for the fast computation of the thermodynamic properties of heavy water. Nuclear engineering and design, 1997, 178(3), 309-329.
- [150] Xianga, H. W., Vapor pressure and critical point of tritium oxide. Journal of physical and chemical reference data, 2003, 32(4), 1707-1711.
- [151] Matsunaga, N. and Nagashima, A., Saturation vapor pressure and critical constants of H₂O, D₂O, T₂O, and Their Isotopic Mixtures. International journal of thermophysics, 1987, 8(6), 681-694.
- [152] Friedman, A. S., et al., Critical constants, boiling points, triple point constants, and vapor pressures of the six isotopic hydrogen molecules, based on a simple mass relationship. The journal of chemical physics, 1951, 19, 126-127.
- [153] T. Sugiyama, Y. Asakura, Y. Udaa, T. Shiozaki, Y. Enokida, I. Yamamoto, Present status of hydrogen isotope separation by CECE process at the NIFS. Fusion engineering and design, 2006, 81(1-7), 833-838.
- [154] Onda, K., et al., Mass transfer coefficients between gas and liquid phases in packed columns. Journal of chemical engineering of Japan. 1968, 1(1), 56-62.
- [155] Billet, R. and Schultes, M., Prediction of mass transfer columns with dumped and arranged packings: updated summary of the calculation method of billet and schultes. Chemical engineering research and design, 1999, 77(6), 498-504
- [156] Chilton, T. H. and Colburn, A. P., Mass transfer (absorption) coefficients prediction from data on heat transfer and fluid friction. Industrial and engineering chemistry, 1934, 26(11), 1183-1187.
- [157] Atta, A., et al., Prediction of pressure drop and liquid holdup in trickle bed reactor using relative permeability concept in CFD. Chemical Engineering Science. 2007, 62, 5870-5879.
- [158] Attou, A. and Ferschneider, G., A two-fluid model for flow regime transition in gas-liquid trickle bed reactors. Chemical Engineering Science. 1999, 54, 5031-5037.
- [159] Gunjal, P.R., et al., Hydrodynamics of trickle-bed reactors: experiments and CFD modeling, Industrial & Engineering Chemistry Research. 2005, 44, 6278-6294.
- [160] Gunjal, P.R., et al., Liquid distribution and RTD in trickle bed reactors: experiments and CFD simulations. Canadian Journal of Chemical Engineering. 2003, 81, 821-830.
- [161] Jiang, Y., et al., CFD of multiphase flow in packed-bed reactors: I. k-fluid modeling issues, AIChE. Journal. 2002a, 48,701-715.

- [162] Jiang, Y., et al., CFD modeling of multiphase flow distribution in catalytic packed bed reactors: scale down issues. *Catalyst today*. 2001, 66, 209-218.
- [163] Propp, R.M., et al., A numerical model for trickle bed reactors. *Journal of computational physics*. 2000, 165, 311-333.
- [164] Rodrigo J.G., et al., Trickle-bed CFD studies in the catalytic wet oxidation of phenolic acids. *Chemical Engineering Science*. 2007, 62, 7045-7052.
- [165] Souadnia, A. and Latifi, M.A.; Analysis of two-phase flow distribution in trickle-bed reactors, *Chemical Engineering Science*. 2001, 56, 5977–5985.
- [166] Szady, M.J. and Sundaresan, S., Effect of boundaries on trickle-bed hydrodynamics, *AIChE Journal*, 1991, 37, 1237-1241.
- [167] Mills, P. L. and Dudukovic, M. P., Evaluation of liquid-solid contacting in trickle-bed reactors by tracer methods. *AIChE Journal*, 1981, 27, 893-904.
- [168] Ring, Z. E. and Missen, R. W. Trickle-bed reactors: tracer study of liquid holdup and wetting efficiency at high temperature and pressure. *Canadian journal of chemical engineering*, 1991, 69, 1016-1020.
- [169] El-Hisnawi, A. A., et al., Trickle-bed reactors: dynamic tracer tests, reaction studies and modelling of reactor performance. *ACS Symposium Series*, 1982, 196, 421-440.
- [170] Al-Dahhan, M., et al., High-pressure trickle bed reactors: a review. *Industrial & Engineering Chemistry Research*. 1997, 36, 3292-3314.
- [171] Ranade, V.V.; Chaudhari, R.; Gunjal, P.R., *Trickle Bed Reactors: Reactor Engineering & Applications*. Book, (2011), 1-284.
- [172] Kumar, R., et al., Investigation of hydrodynamic behaviour of a pilot-scale trickle bed reactor packed with hydrophobic and hydrophilic packings using radiotracer technique. *Journal of Radioanalytical and Nuclear Chemistry*. 2012, 294, 71-75.
- [173] Maiti, R., et al., Effect of Particle Porosity on Hysteresis in Trickle-Bed Reactors. *Industrial and Engineering Chemistry Research*, 2008, 47, 8126-8135.
- [174] Muller, A., et al., model-based investigation of a pellet string reactor. *Procedia engineering*, 2012, 42, 1189-1201
- [175] Dudukovic, M. P., et al., Three-Phase Trickle-Bed Reactors. *Ullmann's Encyclopedia of Industrial Chemistry*. 2014, 1–40.
- [176] Rao, V.G., et al., Hydrodynamics of two-phase concurrent down-flow in packed beds. Part II: experiment and correlation. *AIChE Journal*. 1983, 29,467-483.
- [177] Sun, Y. and Beckermann, C., Sharp interface tracking using the phase-field equation. *Journal of Computational Physics*, 2007, 220, 626–653.

- [178] Ellman, M.J., et al., A new improved pressure drop correlation for trickle-bed reactors. *Chemical Engineering Science*. 1988, 43, 2201-2206.
- [179] Ellman, M.J., et al., A new improved liquid holdup correlation for trickle bed reactors. *Chemical Engineering Science*. 1999, 45, 1677-1684.
- [180] Larachi, F., et al., Experimental study of a trickle bed reactor operating at high pressure: two-phase pressure drop and liquid saturation. *Chemical Engineering Science*. 1991, 46, 1233-1246.
- [181] Larkins, R. P., et al., Two-phase concurrent flow in packed beds. *AIChE Journal*., 1961, 7, 231-239.
- [182] Holub, R.A., et al., A phenomenological model for pressure drop, liquid holdup, and flow regime transition in gas-liquid trickle flow. *Chemical Engineering Science*. 1992, 47, 2343-2348.
- [183] Iliuta, I., et al., Double-slit model for partially wetted trickle flow hydrodynamics. *AIChE. Journal*. 2000, 46, 597-609.
- [184] Conchouso, D., et al., Simulation of a 3D flow-focusing capillary-based droplet generator. *Proceedings of the Comsol conference in Rotterdam*. 2013
- [185] Yue, P., et al., A diffuse-interface method for simulating two-phase flows of complex fluids. *Journal of Fluid Mechanics*, 2004, 515, 293-317.
- [186] Sun, Y. and Beckermann, C., Sharp interface tracking using the phase-field equation. *Journal of Computational Physics*, 2007, 220, 626–653.
- [187] Galdamez, R. G., et al., Numerical simulations of pulsed-air mixing technology using multiphase computational fluid dynamics methods. *WM 2011 Conference*, February 27- March 3, 2011. Phoenix, AZ.
- [188] Celik, I., et al., Procedure for Estimation and Reporting of Uncertainty Due to Discretization in CFD Applications. *Journal of fluids engineering*. 2008, 130 (7), 078001, 1-4.
- [189] Zou, R. P. and Yu, A. B., The packing of spheres in a cylindrical container: the thickness effect. *Chemical engineering science*. 1995, 50 (9), 1504-1507.
- [190] Muller, G. E., Prediction of radial porosity distributions in randomly packed fixed beds of uniformly sized spheres in cylindrical containers. *Chemical engineering science*. 1991, 46 (2), 706-708.
- [191] Benkrid, K., et al., Prediction of pressure drop and liquid saturation in trickle-bed reactors operated in high interaction regime. *Chemical Engineering Science*, 1997, 52, 4021-4032.
- [192] Wammes, W. J. A. and Westerterp, K. R., Hydrodynamics in a pressurized cocurrent gas-liquid trickle-bed reactor. *Chemical Engineering Technology*, 1991, 14, 406-413.

- [193] Sàez, A. E. and Carbonell, R.G., Hydrodynamic parameters for gas-liquid cocurrent flow in packed beds. *AIChE. Journal*. 1985, 31, 52-62.
- [194] Abdolkarimi, V., Hydrodynamics modeling of a bench scale trickle bed reactor using CFD. *Petroleum and Coal*, 2013, 55, 188-195.
- [195] Goto, S. and Simth, J. M., Trickle-bed reactor performance. Part I. Holdup and mass transfer effects. *AIChE Journal*. 1975, 21, 706-713.
- [196] Shulman, H.L., et al., Performance of packed columns: II. Wetted and effective-interfacial areas, gas-and liquid-phase mass transfer rates. *AIChE. Journal*, 1955, 1, 253–258.
- [197] Alicilar, A., et al., The relation between wetting efficiency and liquid holdup in packed columns. *Chemical Engineering Communications*, 1994, 128, 95-107.
- [198] Specchia, V. and Baldi, G., Pressure drop and liquid holdup for two phase concurrent flow in packed beds. *Chemical Engineering Science*, 1977, 32, 515-523.
- [199] Jiang, Y., et al., CFD of multiphase flow in packed-bed reactors: II. Results and applications. *AIChE. Journal*, 2002, 48, 716-730.
- [200] Delgado, J. M. P. Q. Longitudinal and transverse dispersion in porous media. *Chemical engineering research and design*. 2007, 85, 1245-1252.
- [201] Freund, H., Bauer, J., Zeiser, T. and Emig, G., Detailed simulation of transport processes in fixed-beds. *Industrial & engineering chemistry research*. 2005, 44, 6423-6434.
- [202] YE, L., et al., Hydrogen isotope separation in hydrophobic catalysts between hydrogen and liquid water. *Fusion Engineering and Design*. 2015, 100, 576-580.
- [203] Butler, J. P., Hydrogen isotope separation by catalyzed exchange between hydrogen and liquid water. *Separation science and technology*. 1980, 15 (3), 371-396.
- [204] Miller, A., *Heavy Water: A Manufacturers' Guide for the Hydrogen Century*. *Canadian Nuclear Society Bulletin*, 2001, 22(1), 1-14.
- [205] Holtslander, W. J., The chalk river tritium extraction plant. *Fusion Engineering and Design*. 1990, 12, 357-363.
- [206] Wilke, C. R. *Diffusional Properties of Multicomponent Gases*. *Chemical engineering progress*. 1950, 46, 95-104.
- [207] Wakao, N. and Smith, J. M. *Diffusion in Catalyst Pellets*. *Chemical engineering science*. 1962, 17(11), 825-834.
- [208] Fuller, E. N., et al., A New Method for Prediction of Binary Gas Phase Diffusion Coefficients. *Industrial & Engineering Chemistry*. 1966, 58, 19-27.
- [209] Enright, J. T. and Chuang, T. T., Deuterium exchange between hydrogen and water in a trickle bed reactor. *Canadian journal of chemical engineering*. 1978, 56, 246-250.